Studienrichtung Vermessungswesen
Technische Universität Wien

GEOWISSENSCHAFTLICHE
MITTEILUNGEN

Heft 49

# Soil Moisture Retrieval from ERS Scatterometer Data

von

**Wolfgang Wagner**

Veröffentlichung des Institutes für Photogrammetrie und Fernerkundung

Geowiss. Mitt.
49, 1998

Wien, im December 1998

Studienrichtung Vermessungswesen
Technische Universität Wien

GEOWISSENSCHAFTLICHE
MITTEILUNGEN

Heft 49

# Soil Moisture Retrieval from ERS Scatterometer Data

von

**Wolfgang Wagner**

Veröffentlichung des Institutes für Photogrammetrie und Fernerkundung

Geowiss. Mitt.
49, 1998

Wien, im December 1998

**Herausgeber und Verleger: o. Prof. Dr.-Ing. Karl Kraus**
Vorstand des Institutes für Photogrammetrie und Fernerkundung
der Technischen Universität Wien
A-1040 Wien, Gußhausstraße 27-29

Die Kosten für den Druck wurden aus eigenen Einnahmen des Institutes für Photogrammetrie und Fernerkundung der Technischen Universität Wien getragen.

This work has been submitted as Ph.D. dissertation to the "Technisch-Naturwissenschaftliche Fakultät" of the Vienna University of Technology, Karlsplatz 13, A-1040 Wien, Austria

Referees: Prof. Dr. Karl Kraus
Institute for Photogrammetry and Remote Sensing, Vienna University of Technology, Gusshausstr. 27-29, A-1040 Wien, e-mail: kk@ipf.tuwien.ac.at.
Prof. Dr. Helmut Rott
Institute for Meteorology and Geophysics, University of Innsbruck, Innrain 52, A-6020 Innsbruck, e-mail: helmut.rott@uibk.ac.at.

It has also been published by the Joint Research Centre of the European Commission as Publication EUR 18670 EN. This publication contains some minor corrections with respect to EUR 18670-EN.

Druck: Laser-Print-Express
Auflage: 200 Stück
ISBN 3-9500791-1-4

## Abstract

Although soil moisture constitutes only about 0.005 % of the global water resources, it is an important component of the hydrological cycle. It is a limiting factor in agricultural production, puts an important control on ecosystems, influences runoff, affects weather patterns, and is a crucial element in climate change studies. Currently, soil moisture can only be reliably measured on the ground, which is expensive and does not provide a good spatial representation of the soil wetness conditions due to the high variability of soil moisture on a local scale. Remote sensing may resolve these problems since it naturally provides areal measurements and because soil moisture maps of large regions could be produced at relatively low costs. However, the problem is that soil moisture is only one of the many factors that affects the remotely sensed signal.

The objective of this work was to develop a method to retrieve soil moisture from ERS Scatterometer data. The ERS Scatterometer is a C-band radar with a spatial resolution of about 50 km, and has been flown on board of the European Remote Sensing Satellites ERS-1 and ERS-2. It measures the backscattering coefficient that, over land surfaces, is a function of vegetation, surface roughness, soil moisture content, and incidence angle. To estimate soil moisture the other influencing factors need to be accounted for. How this is achieved is described in this thesis.

The retrieved soil wetness values are a relative measure of the moisture content in the remotely sensed soil surface layer which, in C-band, is in general 0.5 – 2 cm deep. In most applications, however, one is interested in the water content in the soil profile, and therefore an algorithm to estimate the profile soil moisture content from ERS Scatterometer and soil data is developed. A validation of the method based on an extensive data set of gravimetric soil moisture measurements from the Ukraine shows that the soil moisture content in the first meter of the soil can be estimated with a r.m.s. error of 4.9 % volumetric units. Soil moisture maps of a number of other regions with diverse climatic conditions (Mali, Iberian Peninsula, Illinois, England and Wales) were produced. A qualitative analysis suggests a good quality of the derived soil moisture maps for a wide range of climate and vegetation types.

## Zusammenfassung

Obwohl das im Boden gespeicherte Wasser nur zirka 0.005 % der globalen Wasserressourcen ausmacht, ist es eine wichtige Komponente des hydrologischen Kreislaufes. Der Bodenwassergehalt beeinflußt das Wettergeschehen, den Wasserabfluß, die landwirtschaftliche Produktion, die Art und Funktionsweise von Ecosystemen, und ist ein kritisches Element in Klimastudien. Derzeit erlauben nur bodengestütze Methoden eine verläßliche Messung der Bodenfeuchte. Sie sind allerdings relativ teuer und sind oft aufgrund der hohen kleinräumigen Variabilität der Bodenfeuchte nicht repräsentativ für die umliegenden Gebiete. Die Fernerkundung könnte diese Probleme lösen da sie räumliche Messungen liefert, und weil Karten von größeren Gebieten relativ kostengünstig erstellt werden könnten. Das Problem ist allerdings, daß der Bodenwassergehalt nur ein Faktor von vielen ist, der das Fernerkundungssignal beeinflußt.

Das Ziel dieser Arbeit war es, eine Methode zur Bestimmung des Bodenwassergehaltes basierend auf ERS Scatterometer Daten zu entwickeln. Das ERS Scatterometer ist ein C-Band Radar mit einer räumlichen Auflösung von 50 km, das an Bord der Europäischen Fernerkundungssatelliten ERS-1 und ERS-2 geflogen wurde und wird. Es mißt den Rückstreukoeffizienten, der über Landflächen von der Vegetation, der Bodenrauhigkeit, der Bodenfeuchte, und dem Einfallswinkel beeinflußt wird. Um den Bodenwassergehalt zu bestimmen, müssen die anderen Einflußgrößen berücksichtigt werden. Wie das erzielt werden kann ist in dieser Dissertation beschrieben.

Die erhaltenen Bodenfeuchtigkeitswerte sind ein relatives Maß des Wassergehaltes in den obersten 0.5 – 2 cm des Bodens. In den meisten Anwendungen will man allerdings den Wassergehalt im Bodenprofil kennen, und daher wurde eine Methode zur Abschätzung dieser Größe anhand von ERS Scatterometer und Bodendaten entwickelt. Eine Validierung der Methode anhand von umfangreichen Bodenfeuchtigkeits-Messungen aus der Ukraine zeigt, daß der Wassergehalt im ersten Meter des Bodens mit einem Fehler von 4.9 % volumetrische Bodenfeuchte bestimmt werden kann. Bodenfeuchtigkeitskarten wurden für eine Anzahl von Gebieten (Mali, Iberische Halbinsel, Illinois, England und Wales) mit unterschiedlichen klimatischen Bedingungen erstellt. Eine qualitative Analyse dieser Karten deutet auf eine gute Qualität für unterschiedlichste klimatische und vegetative Verhältnisse hin.

## Acknowledgements

The work was carried out at the Institute for Photogrammetry and Remote Sensing of the Vienna University of Technology, the Space Applications Institute of the Joint Research Centre of the European Commission, and the Electromagnetics Division of the European Space Agency. The funding was made available by the Joint Research Centre of the European Commission through a Ph.D. grant and by the "Bundesministerium für Wissenschaft, Forschung, und Kunst" of the Austrian Federal Republic through the "Kurt Gödel Stipendium".

In the first place, I would like to thank Karl Kraus, Hugo de Groof, Paul Vossen, and Josef Noll. Without their interest and support this work would not have been possible.

I am especially grateful to Helmut Rott and Guido Lemoine for carefully following my work and for their useful comments and corrections.

For fruitful discussions and their help, I thank Maurice Borgeaud, Bertram Arbesser-Rastburg, Alan Robock, Konstantin Vinnikov, Pavel Groisman, Richard Kidd, Iwan Supit, Steve Peedell, Javier Gallego, Andreas Hirscheider, Stefan Sommer, Luca Montarella, Jürgen Vogt, Ted Engman, Klaus Scipal, and Andrea Bellinzaghi.

ERS Scatterometer data were kindly provided by CERSAT. Most of the reference data were drawn from the archives of the Space Applications Institute.

## Preface

Being trained in physics, my interest has been to understand the physical mechanisms that determine the signal measured by the ERS Scatterometer, and to develop a method to retrieve soil moisture from the signal based on this understanding. However, I have always been aware that remote sensing by itself is not the goal, but rather a means to obtain information about geophysical processes that is of use in applications. Keeping this in mind I have tried to write this thesis in such a way that it is not only understandable by remote sensing experts, but also by scientists from other fields who might be interested in using the derived information in their field of interest.

The subject of the study is necessarily interdisciplinary and I have tried my best to integrate the knowledge from many different fields including electrical engineering, physics, statistics, image processing, hydrology, meteorology, ecology, and soil science into one consistent thesis.

Many parts of the text have been published previously in a number of journal papers, reports, and conference contributions. A list of these publications is given below:

**Journals:**

Wagner, W., J. Noll, M. Borgeaud, H. Rott, Monitoring Soil Moisture over the Canadian Prairies with the ERS Scatterometer, *IEEE Trans. Geosci. Remote Sensing*, in press.

Wagner, W., G. Lemoine, M. Borgeaud, H. Rott, A Study of Vegetation Cover Effects on ERS Scatterometer Data, *IEEE Trans. Geosci. Remote Sensing,* in press.

Wagner, W., G. Lemoine, H. Rott, A Method for Estimating the Profile Soil Moisture Content from ERS Scatterometer and Soil Data, *Remote Sens. Environ.*, submitted.

Supit, I., W. Wagner, Analysis of yield, sowing and flowering dates of barley of field survey results in Spain, *Agro. Systems.*, in press.

**Conferences and Periodicals:**

Wagner, W., M. Borgeaud, J. Noll (1996) Soil Moisture Mapping with the ERS Scatterometer, *Earth Observation Quarterly*, No. 54, December 1996, pp. 4-7.

Wagner, W., G. Lemoine (1998) Land Cover Effects on ERS Scatterometer Data, *IGARSS'98*: Managing Natural Resources, Seattle, Washington, USA, July 6-10, 1998, pp. 1574-1576.

Wagner, W. (1998) ERS Scatterometer derived soil moisture maps of three climatic zones, Int. Symposium on Resource and Environmental Monitoring, ECO BP'98, ISPRS Commission VII, Budapest, Hungary, September 1-4, 1998, *International Archives of Photogrammetry and Remote Sensing*, Vol. XXXII, Part 7, pp. 573-578.

Wagner, W. (1998) A Comparison of ERS Scatterometer Retrieved Soil Moisture Data with Field Observations in the Ukraine, *Workshop on Emerging Scatterometer Applications: From Research to Operations*, ESTEC, Noordwijk, The Netherlands, 5-7 October 1998, in press.

Wagner, W. (1998) Vegetation as observed with the AVHRR and the ERS Scatterometer: A Case Study over the Iberian Peninsula, *Workshop on Emerging Scatterometer Applications: From Research to Operations*, ESTEC, Noordwijk, The Netherlands, 5-7 October 1998, in press.

Lecomte, P., W. Wagner (1998) ERS Wind Scatterometer Commissioning and in-flight Calibration, *Workshop on Emerging Scatterometer Applications: From Research to Operations*, ESTEC, Noordwijk, The Netherlands, 5-7 October 1998, in press.

**Reports:**

Wagner, W. (1996) Change Detection with the ERS Scatterometer over Land, EWP N°1896, *European Space Agency*, Noordwijk, The Netherlands, July 1996, 143 p.

Wagner, W. (1998) Vegetation Cover Effects on ERS Scatterometer Data, Technical Note No. I.98.05, *EC Joint Research Centre*, Ispra, Italy, January 1998, 193 p.

NEO (1998) Application Service Demonstrator for Drought Early Warning in Mali based on Scatterometer Information, ESA-ESRIN Data User Programme, 1st Interim Report, NEO Netherlands Geomatics & Earth Observation B. V., Lelystad, The Netherlands, 29 May 1998, 73 p.

## *Web Site*

Electronic versions (pdf files) of this thesis and many of the above listed articles and technical reports can be found on the web site:

**http://www.ipf.tuwien.ac.at/ww/home.htm**

## Contents

## List of Symbols and Acronyms

The list of symbols and acronyms is not exhaustive. Only symbols and acronyms that appear in more than one part of the text are included.

$\delta$ ..... Difference of $\sigma^0$ measured by the fore- and aft beam antennas
$\varepsilon$ ..... Relative permittivity or dielectric constant
$\varepsilon'$ ..... Real part of $\varepsilon$
$\varepsilon''$ ..... Imaginary part of $\varepsilon$
$\theta$ ..... Incidence angle (degree)
$\theta_{dry}$ ..... Crossover angle for dry soil conditions (degree)
$\theta_{wet}$ ..... Crossover angle for wet soil conditions (degree)
$\sigma^0$ ..... Backscattering coefficient ($m^2 \cdot m^{-2}$ or dB)
$\sigma^0_{dry}$ ..... Backscattering coefficient of a dry soil surface
$\sigma^0_{wet}$ ..... Backscattering coefficient of a wet soil surface
$\sigma^0(40)$ ..... $\sigma^0$ at the reference incidence angle of 40°
$\sigma'$ ..... Slope of $\sigma^0(\theta)$ (dB/deg)
$\sigma'(40)$ ..... $\sigma'$ at the reference incidence angle of 40°
$\sigma''$ ..... Curvature of $\sigma^0(\theta)$ (dB/deg$^2$)
$\sigma''(40)$ ..... $\sigma''$ at the reference incidence angle of 40°
$\tau$ ..... Optical depth or thickness (Np)
$\omega$ ..... Single scattering albedo
$\Psi'$ ..... Periodic function describing the seasonal variation of $\sigma'(40)$
$\Psi''$ ..... Periodic function describing the seasonal variation of $\sigma''(40)$

$f$ ..... Frequency (Hz)
$l$ ..... Spatial resolution (m)
$m_s$ ..... Relative moisture content in the soil surface layer (%)
$t$ ..... Time (s)

$A$ ..... Percentage area of resolution cell occupied by one land cover class (%)
$C^0_{dry}$ ..... Constant term of function describing the seasonal variation of $\sigma^0_{dry}(40)$
$C^0_{wet}$ ..... Constant term of function describing the seasonal variation of $\sigma^0_{wet}(40)$
$C^S$ ..... Constant term of function describing the seasonal variation of $S$
$C'$ ..... Constant term of function describing the seasonal variation of $\sigma'(40)$
$C''$ ..... Constant term of function describing the seasonal variation of $\sigma''(40)$
$D'$ ..... Dynamic range of the seasonal variation of $\sigma'(40)$
$D''$ ..... Dynamic range of the seasonal variation of $\sigma''(40)$
$ESD(\sigma^0)$ ..... Estimated standard deviation of $\sigma^0$ due to instrument noise, speckle and azimuthal effects
$FC$ ..... Field capacity ($m^3 \cdot m^{-3}$ or %)
$PAW$ ..... Plant available water ($m^3 \cdot m^{-3}$ or %)
$R$ ..... Correlation coefficient
$S$ ..... Sensitivity of $\sigma^0$ to changes in the surface moisture content (dB)

*SWI*..... Soil Water Index (%)

*T*..... Characteristic time length used for calculation of *SWI*

*TWC* ..... Total water capacity or porosity ($m^3 \cdot m^{-3}$ or %)

*W*..... Volumetric soil moisture content ($m^3 \cdot m^{-3}$ or %)

*WL*..... Wilting level ($m^3 \cdot m^{-3}$ or %)

AVHRR..... Advanced Very High Resolution Radiometer

CORINE..... Co-ordination of Information on the Environment

DEM..... Digital Elevation Model

ERS ..... European Remote Sensing Satellite

ESA..... European Space Agency

FAO..... Food and Agriculture Organisation of the United Nations

ITCZ..... Inter-Tropical Convergence Zone

MARS ..... Monitoring Agriculture with Remote Sensing Project

NDVI..... Normalised Difference Vegetation Index

NOAA ..... National Oceanic and Atmospheric Administration

SAR..... Synthetic Aperture Radar

# 1. Introduction

## *1.1. Soil Moisture*

Water is the most critical resource of our planet. Without it life cannot exist. About 97.2 % of the global water resources are stored in the oceans, 2.15 % in the ice sheets and glaciers, and 0.63 % is groundwater (Strahler and Strahler, 1997). Soil moisture, which is the water held in the soil within reach of the plant roots, constitutes only 0.005 %. Despite the soil water reservoir is small it exerts a prominent control on the interactions between the hydrosphere, biosphere and atmosphere. Consequently, soil moisture is of importance in a number of disciplines and applications.

The agronomist is interested in soil moisture because plant growth is limited by either too little or too much water, but mostly the former. According to Kozlowski (1968) tremendous losses in plant growth occur annually because of recurrent or sustained internal water deficits in plants. He thinks that these losses are not realised because for many areas data are not available to indicate how much more growth would occur if plants had favourable water supplies throughout the growing season. In meteorology and climate change studies soil moisture is important because it directly affects the partitioning of energy at the surface between latent and sensible heating. Therefore the hydrology of the Earth's surface needs to be incorporated into General Circulation Models (Manabe, 1969). Modelling studies show that strong perturbations in soil moisture on global and regional scales can affect atmospheric circulation, and may persist for several month (Dirnmeyer and Shukla, 1993). For example, over the North American plains there is a tendency for dry springs to be followed by hot summers, and wet springs to be followed by cool summers. Also in hydrology soil water plays an important role because excess soil moisture can lead to large runoffs and streamflows while soil water deficits can aggravate a hydrological drought (Lawford, 1992).

Traditional methods for measuring soil moisture are essentially point measurements. The thermo-gravimetric method consists of removing a soil sample and by determining its weight before and after it has been dried in an oven at 105°C for 24 hours (Hillel, 1980). It is the standard method for soil wetness determination on which all other methods are ultimately calibrated (Schulin et al., 1992). In the Time-Domain Reflectory (TDR) method the velocity of propagation of a high frequency voltage pulse in the soil is measured and related to the soil dielectric properties. Since the dielectric constant of a soil increases with the water fraction the soil moisture content can be estimated (Topp, 1992). Other measurement devices are capacitance probes, resistance probes, neutron probes, and tensiometers.

One problem of these traditional measurement techniques is the great spatial variability of soil moisture at scales[1] from millimetres to hundreds of meters and the associated question how reliable areal soil wetness values can be derived (Schulin et al., 1992). An even bigger problem may be that they are labour intensive and costly (Hollinger and Isard, 1994; Rombach and Mauser, 1997). Consequently, only relatively few programs have accumulated substantial soil moisture data (Georgakakos and Baumer, 1996). The lack of data is strongly felt by hydrologists and scientists from related subjects. Engman (1986) wrote that 'improved performance of hydrologic processes and models is pretty much at a standstill because of a lack of proper types and amounts of data'. Dirnmeyer (1995) states that 'the lack of widespread observations of soil moisture continues to hamper efforts to verify and improve hydrological models'. Blöschl and Sivapalan (1995) think that 'reliable measurements of soil moisture patterns would be ideal for model evaluation and could be the key to progress in hydrologic modelling'.

[1] In this thesis the term "scale" refers in general to a characteristic time or length.

## 1.2. Remote Sensing of Soil Moisture

Remote sensing is, broadly speaking, the collection of information about an object without coming into physical contact with it (Rees, 1990). Originally it was an offspring of photogrammetry by emphasising the interpretation of photos and descriptive analysis of the subject. The modern era of remote sensing started in July 1972 with the launch of the ERTS-A satellite which was later renamed Landsat 1 (Engman, 1986). Since then a multitude of spaceborne sensors operating in the visible, infrared and microwave range of the electromagnetic spectrum have been launched.

It was soon realised that remote sensing might be able to solve the problems of the traditional methods for measuring soil moisture. Firstly, it would naturally provide areal measures of soil moisture rather than point data. Secondly, soil moisture maps of large regions could be produced at relatively low-costs. Consequently, much effort has been put into the development of remote sensing techniques for soil moisture retrieval. Sensors operating in the visible and infrared can provide some information about soil moisture patterns because soil colour and surface temperatures are influenced by soil wetness. However, only the microwave region offers the potential for truly quantitative measurements (Engman, 1990). Microwaves are electromagnetic waves with frequencies extending from 0.3 to 300 GHz corresponding to wavelengths from 1 m to 1 mm (Ulaby et al., 1981). Especially at low microwave frequencies the dielectric properties of water and soil particles are distinctly different which is why the soil's microwave response is strongly depended on the soil moisture content. Microwaves also have the advantage to penetrate clouds, to be independent of the sun as a source of illumination, and to be able to penetrate deeper into vegetation and soil.

Microwave remote sensing encompasses two types of sensors: passive systems (radiometers), and active systems (radars). The term 'radar' stands for radio detection and ranging, and is applied to any device in which a transmitter illuminates a reflecting or scattering surface or object, and a receiver records some property of the returned wave. One can further distinguish between imaging and non-imaging radars. Synthetic Aperture Radars (SAR) are imaging radars which have been designed to achieve high spatial resolution. Scatterometers like the one on board of the European Remote Sensing Satellites ERS-1 and ERS-2 belong to the group of non-imaging radars. They are absolutely calibrated in terms of intensity.

Radiometer systems measure the intensity of the emission of the surface that is related to the temperature and emissivity of the emitting body. Over land surfaces the emitted radiation depends on the soil moisture content because the emissivity of a bare soil surface changes from about 0.95 when dry to 0.6 or less when wet (Schmugge et al., 1986). Soil moisture can be retrieved from radiometer data if the algorithm successfully accounts for vegetation, soil roughness, and surface temperature. For example, Wang et al. (1990) retrieved patterns of surface soil moisture over an area of 7 x 14 $km^2$ from airborne L-band radiometer data which compared favourable with field measurements. Griend and Owe (1993 and 1994) used the 6.6 GHz channels of the Scanning Multi-channel Microwave Radiometer (SMMR) which have a spatial resolution of about 100 km. In a case study over south-eastern Botswana they report a r.m.s. error between ground based soil moisture and satellite estimated surface moisture of only 1.2 % by volume.

Radar systems measure the backscattering coefficient that is proportional to the energy scattered back from the surface. The radar signal is dependent on soil moisture because the larger the dielectric constant of the soil the stronger the scattered radiation will be as compared with the radiation entering the sub-surface medium (Schanda, 1986). Vegetation and surface roughness effects are important and need to be accounted for. The literature on soil moisture retrieval from SAR imagery is abundant and in a number of studies good results have been reported. For example, Dubois et al. (1995) report for bare soil surfaces a r.m.s. error of less than 4.2 % using spaceborne (SIR-C) and airborne (AIRSAR) imaging radar data.

Despite the progress made microwaves systems are not yet used for operational soil moisture monitoring. Engman (1990) and Wigneron et al. (1998) state that, although some case studies are promising, the future for using microwave data for operational soil moisture retrieval is somewhat uncertain. Beven and Fisher (1996) think that the optimistic view on the use of remote sensing in hydrology in the eighties has not been borne out of practice. They further state that remote sensing data have only limited direct relevance to hydrological variables and continue: "Even soil moisture estimates require an intermediate model for the interpretation of remotely-sensed fields which then introduces significant uncertainty."

## *1.3. Scope of the Work*

The objective of the study was to develop a methodology for soil moisture retrieval from ERS Scatterometer data that can be used over different regions of the world. The ERS Scatterometer is a radar operating at 5.3 GHz with a spatial resolution of 50 km. It has been flown on board of the European Remote Sensing Satellites ERS-1 (from 1991 to 1996) and ERS-2 (from 1995 onwards) and is the first spaceborne scatterometer that has been providing global coverage for several years. The measured backscattering coefficient is sensitive to vegetation and for low vegetation types like grasses and agricultural crops to the soil moisture content. This duality has lead to different types of studies: those that are concerned with using the ERS Scatterometer for vegetation application and those concerned with soil moisture monitoring. First results using the ERS Scatterometer for soil moisture retrieval are reported by Wagner et al. (1995), Pulliainen et al. (1996, 1998), and Magagi and Kerr (1997). Vegetation applications were investigated by Wiesmann (1994), Mougin et al. (1995), Wismann et al. (1996a and 1996b), Frison and Mougin (1996a and 1996b), Schmullius (1997), and Frison et al. (1998).

The choice of the study areas for this work was driven mainly by the availability of reference data sets. The main study areas are the Iberian Peninsula, the Ukraine, Mali, and the Canadian Prairies. Vegetation cover effects on ERS Scatterometer data were studied over the Iberian Peninsula for which land cover information and NDVI (Normalised Difference Vegetation Index) imagery were available. The accuracy of the soil moisture retrieval method and the question how the remotely sensed surface soil moisture estimates are related to the water content in the soil profile are investigated based on an extensive data set of gravimetric soil moisture data from the Ukraine. Other study areas are Illinois, England and Wales, and a tropical forest region in central Africa.

The thesis is structured as follows: In Chapter 2 the instrument characteristics and the data quality are discussed. The study areas and the reference data sets are presented in Chapter 3. The physical fundamentals of radar scatterometry are discussed in Chapter 4. In Chapter 5 it is investigated which surface parameters influence the backscattering signal and at which scale these parameters vary. The discussions on instrument design and backscatter mechanisms build the basis for an appropriate processing chain of ERS Scatterometer data (Chapter 6). The findings in Chapter 7 on the effects of heterogeneous land cover and vegetation phenology on the ERS Scatterometer signal lead to the definition of an algorithm to retrieve surface soil moisture in Chapter 8. In Chapter 9 a method for estimating the profile soil moisture content from the remotely sensed surface wetness values is defined and validated using the gravimetric soil moisture data from the Ukraine. In Chapter 10, finally, soil moisture maps of different climatic zones are presented.

# 2. The ERS Scatterometer

## *2.1. The ERS Active Microwave Instrument*

The European Remote Sensing Satellites ERS-1 and ERS-2 carry an Active Microwave Instrument (AMI) which combines the functions of a Synthetic Aperture Radar (SAR) and a Scatterometer (ESA, 1992 and 1993). The AMI is a radar operating at a frequency of 5.3 GHz (C-Band) using vertically polarised antennas for both transmission and reception (VV-Polarisation). It has a set of four different antennas to illuminate the Earth's surface and to receive backscattered energy. By on-board and on-ground signal processing, two-dimensional imagery is produced. In the picture elements the intensities represent the normalised radar backscattering coefficient. To meet various geophysical mission objectives the AMI has three modes of operation, namely the Image Mode, the Wave Mode, and the Wind Mode. The requirements are such that each mode should function independently. However, the Wind and Wave Modes are capable of interleaved operation, i.e. the so-called Wind/Wave Mode. Generally, the ERS AMI is operated in interleaved Wind/Wave Mode. Since the data generation rate for Wind Mode is not affected by the fact that it is operated in parallel with the Wave Mode, Scatterometer data are collected continuously over sea and land surfaces while the AMI is in Wind/Wave Mode. The operation of Image Mode excludes the operation of the other two modes. Clearly, over regions with heavy SAR operation the temporal coverage of the ERS Scatterometer can be degraded substantially.

### 2.1.1. Wind Mode

The ERS Scatterometer has been designed to obtain information on wind speed and wind direction over sea surfaces. Therefore it is often called Wind Scatterometer. It uses three sideways looking antennas, one looking to the right side of the satellite track (mid beam antenna), one looking forward at 45° azimuth projection angle with respect to the mid beam (fore beam antenna), and one looking backward at 45° azimuth projection angle with respect to the mid beam (aft beam antenna) (Figure 2-1). The three beams illuminate a 500 km wide swath as the satellite moves along its orbit. Thus three backscatter measurements are obtained at different viewing angles and separated by a short time delay. These 'triplets' are used as input into mathematical models to calculate surface wind speed and direction.

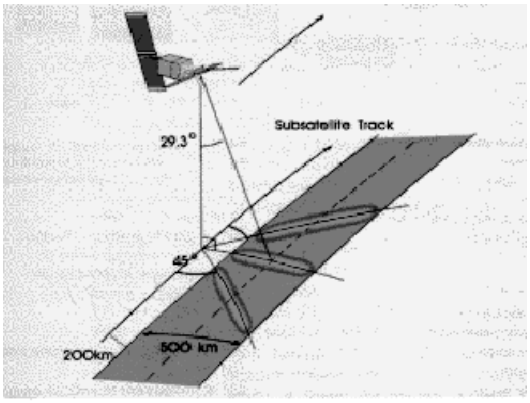


*Figure 2-1: The AMI Wind Mode. From Francis et al. (1995).*

As already mentioned, the AMI is generally operated in interleaved Wind/Wave mode. The Wind/Wave mode has to be interrupted for SAR image mode. Unfortunately, not only the period while the SAR is running is affected but also certain time periods before and after needed for switching of the modes. Would the Wind/Wave mode be continuously operated each point on the earth's surface would, on the average, be revisited every three to fours days in mid-latitudes. In practice, the number of Scatterometer measurements fluctuates strongly depending on region and latitude. The regions most affected by SAR Image Mode operation are Europe, the northern Polar Regions and North America (Wiesmann, 1994).

| | | | |
|---|---|---|---|
| Frequency | 5.3 GHz ± 52 kHz (C-Band) | | |
| Bandwidth | 15.55 Mhz | | |
| Polarisation | Linear vertical (VV) | | |
| Antenna parameters | Fore | Mid | Fore |
| Aspect angle | 45±0.5 deg | 0±0.5 deg | -45±0.5 deg |
| Length | 3.6 m | 2.5 m | 3.6 m |
| Dynamic range | 42 dB | 42 dB | 42 dB |
| Incidence angle range | 25 - 59 deg | 18 - 47 deg | 25 - 59 deg |
| Peak power | 4.8 kW | | |
| Spatial resolution | ~ 45 km (along and across track) | | |
| Swath width | ~ 500 km | | |
| Swath stand-off | 200 km to right of sub-satellite track | | |
| Localisation accuracy | ± 5 km (along and across track) | | |
| Number of pulses per 50 km | 256 | | |
| Radiometric resolution | 6 % | | |
| Cross polarisation | ≥ 15 dB | | |
| Spacecraft altitude | 785 km | | |

*Table 2-1: ERS Scatterometer engineering parameters. From ESA (1992, 1993).*

### 2.1.2. Image Mode

In Image Mode the Synthetic Aperture Radar (SAR) provides two dimensional images with a ground resolution of about 30 m. The 10 m long SAR antenna is aligned parallel to the flight track and images a 100 km wide strip. Power considerations limit SAR Image Mode operations to a maximum of 12 minutes per orbit. As the data rate is too high for on-board storage, images must be acquired within the reception zone of suitably equipped ground receiving stations.

### 2.1.3. Wave Mode

The SAR Wave Mode provides two-dimensional spectra of ocean surface waves. For this function the SAR records regularly spaced samples within the image swath. Images of 5 x 5 $km^2$ are generated every 200 km or 300 km. The data can be generated in stand-alone mode or interleaved with Wind Mode.

## *2.2. The ERS Scatterometer Instrument Description*

The three antennas of the ERS Scatterometer measure the backscattering coefficient from three different look directions. All three antennas form a fan beam with a narrow along-track (azimuth) pattern and a relative wide across-track (elevation) pattern in order to cover a wide swath (500 km) parallel to the subsatellite track (Brinz et al., 1989). The azimuth half-power beamwidth of the mid beam antenna[2] is about 1.3° (ESA, 1993) corresponding to a footprint size in the along-track direction of about 20 km in near range and about 30 km in far range.

While the along-track resolution is given by the antenna gain pattern, the across-track resolution is achieved by using short pulses. The Scatterometer Electronics produce short transmit pulses of constant frequency which are routed to the correct antenna by a Circulator Assembly. Series of 32 pulses are directed in turn to each of the three antennas in the sequence fore, mid, and aft beams. For the mid beam, the pulse duration is 70 μsec and the pulse-repetition frequency is 115 Hz. (A pulse duration of 70 μsec corresponds to an across-track resolution of about 30 km in near range and about 13 km in far

[2] The half-power beamwidth of an antenna is defined as the angular width of the main lobe between the two angles at which the magnitude of the azimuth antenna gain pattern is half of its peak value.

range.) For the fore- and aft-beams, the pulse duration is 130 μsec and the pulse repetition time is 98 Hz. One cycle of 32 pulses from each fore, mid, and aft beam takes 941 msec (ESA, 1993). After four of these cycles the satellite has travelled approximately 25 km.

The relatively low pulse-repetition frequency leaves sufficient space between consecutive pulses for the radar echo signals to return from the earth's surface to the satellite. Between the transmission of each pulse and the arrival of the first radar echo signal, there is additional "dead" time available for calibration and system noise measurements (Attema, 1991). The signal backscattered by the earth's surface is routed via the appropriate antenna to the Scatterometer Electronics. For the mid beam, the return echo is filtered and sampled in a complex format with a sampling rate of 30 kHz (33 μsec), while a coarse Doppler shift is applied to the fore and aft signals before filtering and sampling. The Scatterometer output signals are stored temporarily before they are transmitted to the ground station.

## 2.3. Ground Processing

The principal function of the ground processor is to transform the digital radar echo samples into backscattering coefficients on a 25 x 25 $km^2$ grid for all three antennas. According to Brinz et al. (1989) the main processing steps on the ground are:

1. *Resampling.* The data are resampled in order to avoid aliasing during the consecutive processing stages.
2. *Doppler Correction.* An on-ground Doppler Correction is performed to improve to on-board compensation of the Doppler shift of the return signal introduced by the spacecraft motion and the earth rotation.
3. *Low-Pass Filtering.* The data are low pass filtered to improve the signal to noise ratio. Until the output of the low-pass filter the data are represented in complex format.
4. *Envelope Detection.* The quantity to be detected is the instantaneous signal power.
5. *Block Averaging.* Samples with the same echo time are averaged over a 'block' of 32 pulses. Block averaging is done to reduce the data throughput for the subsequent processing steps and to reduce the variance of the signal samples. During the time it takes to transmit and receive the 32 pulses the satellite has traveled approximately 2.1 km for the mid-beam antenna and 2.5 km for the fore- and aft-beam antennas.
6. *ADC-Nonlinearity Correction*
7. *Noise Subtraction*
8. *Internal Calibration Correction.* This correction is applied to compensate for instrument gain fluctuations.
9. *Power to $\sigma^0$ Conversion*
10. *Spatial Filtering.* Echo signal samples are averaged thereby increasing the radiometric resolution of the final product $\sigma^0$ values.

## 2.4. Impulse Response Function and Spatial Resolution

An image can be thought of as being formed by the convolution of the imaging system's impulse response function with the actual scene (Marion, 1991). The impulse response function of the ERS Scatterometer is dominated by the spatial filtering process in the last processing stage (Walker, 1997). In this stage a regular grid with a 25 x 25 $km^2$ spacing is defined and the position of the grid's nodes on the earth's surface are calculated in an adequate coordinate system. After relating the block signal samples to their position on the ground, a weighted integration of block signal samples belonging to an area

around the nodes is performed. The integration area is a square with a sidelength of approximately 85 km (Pierschel et al., 1988). The weighting function is a two-dimensional Hamming window and is given by

$$w(x, y) = w(x)w(y) \; . \tag{2.1}$$

The function $w(\zeta)$ is the one-dimensional Hamming window which is defined by

$$w(\zeta) = \alpha + (1-\alpha)\cos\left(\frac{2\pi}{L}\zeta\right) \qquad \zeta \le \left|\frac{L}{2}\right| \tag{2.2}$$

and $\alpha = 0.54$ (Figure 2-2). The parameter $L$ is the width of the Hamming window and is approximately 85 km. The Hamming window is designed to have a Fourier transform with low sidelobes (Harris, 1978).

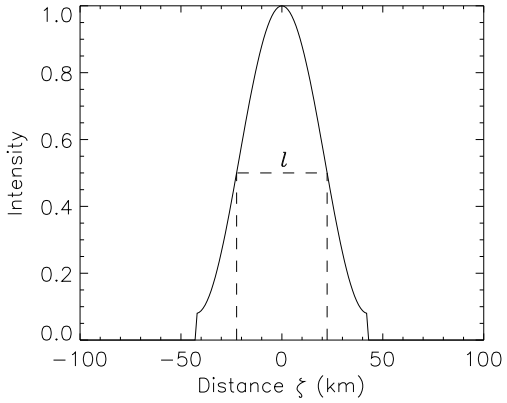


*Figure 2-2: The Hamming window with a sidelength of 85 km. The dashed lines explain the definition of the spatial resolution l*

According to Pierschel et al. (1988) the spatial resolution is defined by the width of the impulse response function where the function reaches fifty percent of its peak value. For the Hamming window used the spatial resolution is 45 km. The antenna gain patterns, the complex frequency response of the on-board instrument, and the on-ground processor function (except, of course, the spatial filtering stage) further decrease the resolution to about 50 km. In the processing chain described in Chapter 6, the data are interpolated to a regular grid using either a box window with a radius of 36 km or a Hamming window with a width of 72 km. The final spatial resolution of the data is approximately 80 km if the box window is used, and 60 km when the Hamming window is used (Wagner, 1996).

Because a spatial resolution of 50 km is a constraint in land application it has been investigated if the resolution of the ERS Scatterometer images can be improved by means of resolution enhancement techniques. Long et al. (1994) describe an algorithm to enhance the resolution of ERS Scatterometer images which was originally developed for use with the Seasat Scatterometer (Long et al., 1993). The Seasat oceanographic satellite was launched in 1978. Its scatterometer operated at a frequency of 13.9 GHz ($K_u$-band) at both horizontal and vertical polarisations. The resolution enhancement technique for the Seasat Scatterometer data takes advantage of the spatial overlap of scatterometer measurements taken at different times, and, by using an indirect reconstruction formulation, the effective resolution is improved (Long et al., 1993). Walker (1997) reviewed the technique developed by Long et al. (1993) and found that while this algorithm is appropriate for use with the Seasat Scatterometer, it is not appropriate for use with the ERS Scatterometer. The reason is that the Seasat Scatterometer images are substantially undersampled, whereas the ERS Scatterometer data are not. Walker (1997) concludes that in the ERS Scatterometer data there is virtually no information existing at frequencies above that corresponding to the sampling rate of 25 km.

## *2.5. Data Quality*

### 2.5.1. Absolute and Interbeam Calibration

The radiometric resolution of the ERS Scatterometer retrieved backscattering coefficient $\sigma^0$ is determined mainly by speckle and receiver noise contributions (Wuttge and Munz, 1995). Speckle in radar measurements of distributed targets are due to phase-interference effects (Ulaby et al., 1988). In SAR images these random variations produce a speckle appearance in the image. In the absence of additive instrument noise a theoretical estimate of the radiometric resolution $\gamma$ of a square-law detector is (Ulaby et al., 1982):

$$\gamma = 10 \cdot \log\left(1 + \frac{1}{\sqrt{N}}\right), \qquad \text{(dB)} \qquad (2.3)$$

where $N$ is the number of independent radar echo signals. During the time it takes the ERS satellites to travel 50 km each antenna has transmitted and received 8 times 32 pulses, i.e. 256 echo samples contribute to $\sigma^0$. Thus the theoretical estimate of the noise due to speckle is 0.26 dB.

In Lecomte and Attema (1992) the calibration procedures implemented by the European Space Agency are described. The objective of the engineering calibration is to ensure absolute calibration of $\sigma^0$ for all incidence angles and antennas. It is achieved by using internal and external references. Two types of external references are used: point targets (transponders) and distributed targets (areas of known constant backscatter). The tropical rain forest in South America has been used as the distributed reference and for monitoring instrument stability. The calibration is based on the assumption that the backscattering coefficient $\sigma^0$ divided by the cosine of the incidence angle $\theta$ is constant over the whole range of incidence angles. This assumption has some physical background but does not necessarily reflect the physical reality accurately. Since the shape of the function $\sigma^0(\theta)$ depends on this assumption, no physical explanations for the exact shape of $\sigma^0(\theta)$ over other regions should be sought, e.g. if the curve is concave or convex.

When ERS-1 was launched, it was agreed that an absolute radiometric calibration of 0.7 dB was enough to satisfy the geophysical data quality requirements in terms of wind speed and wind direction. Following some system anomalies it became clear that meteorologists using the derived wind field data in their routine operations can detect a bias in $\sigma^0$ corresponding to less than 0.2 dB (Lecomte and Wagner, in press). This showed that the absolute calibration of $\sigma^0$ achieved by routine monitoring of ERS Scatterometer system performance is in general better than 0.2 dB. The interbeam calibration is about 0.1 dB.

The second and the third nodes of the mid beam (which correspond to the incidence angles 19.6° and 21.7°) of ERS-2 show an exception because they are systematically higher by about 0.2 dB than the other two beams. This may point to an anomaly in the characterisation of the mid antenna pattern (Lecomte and Wagner, in press).

### 2.5.2. Instrument Switch-On/Switch-Off

A degradation of individual ERS Scatterometer measurements occurs when not all echo data contributing to the backscattering coefficient estimate are available (Wuttge and Munz, 1995). There are two possible causes which lead to the loss of entire source packets, i.e. the loss of echo samples:

1. The instrument is being switched on or off.
2. Source packets are lost during wave gaps in Wind/Wave Mode.

Wuttge and Munz (1995) made an analysis to assess the impact of missing source packets on the ERS Scatterometer product quality. In general, the fore and the aft beam measurements are affected more strongly than the mid beam measurement, and the observed relative errors decrease significantly from the near range to the far range. The most important effects are:

a) Offset in $\sigma^0$ of fore and aft beam due to missing echo samples:

   *Relative Errors:* maximum from 150 % (near range) to 12 % (far range) for instrument switch-on and switch-off
   maximum from 5 % (near range) to 0.4 % (far range) for Wind/Wave Mode

b) Offset in $\sigma^0$ of all beams due to varying backscattering characteristics of the surface:

   *Relative Errors:* depending on the observed scene, several tens of percent for the instrument switch-on and switch-off, and several percent for Wind/Wave Mode.

From this we can make a worst case estimate of the relative errors in the Wind/Wave Mode and for switch-on and switch-off operations. In Wind/Wave Mode the worst relative error is about 10 % corresponding to about 0.5 dB, and for instrument switch-on and switch-off it is about 200 % corresponding to about 5 dB.

Of course, these data should be discarded from the data set. In the ERS Scatterometer Fast Delivery Product (FDP) data format, a counter for the missing source packets for each antenna can be found, thus it would be possible to discard all nodes with more than four source packets missing. Unfortunately, the number of missing source packets is not included in the Off-Line Wind Scatterometer Products generated at IFREMER which are used in this study. Fortunately, it is rather easy to discard all values succeeding an instrument switch-on and preceding an instrument switch-off, thus excluding all values affected by instrument switching from the analysis. On the other hand, without knowing the number of missing source packets, it is impossible to identify measurements affected by the Wind/Wave Mode. So every now and then an inaccurate value (relative error $\leq$ 0.5 dB) will be present in the data set.

Another reason for erroneous data are high tension arcs within the AMI instrument. In some instances the ERS Scatterometer might be unavailable due to arcing. For example, in September 1994 high tension arcs occurred three times and the Scatterometer was not available for a few hours each time (Amans, 1994). This chapter on data quality can be concluded by stating that, in general, data quality is good. However, in some instances erroneous data may occur due to missing echo samples and due to arcing.

## *2.6. Off-Line Wind Scatterometer Products*

The ERS Scatterometer data used in this study were delivered on CDROMs by the Institut Francais de Recherche pour l'Exploitation de la Mer (IFREMER). Each CDROM contains approximately three weeks of data. An ERS Scatterometer product consists of 19 x 19 pixels corresponding to a 500 x 500 $km^2$ large area on the ground. For each pixel the geographic location (longitude, latitude) and the backscattering coefficients for all three antennas are given together with the respective incidence angles and azimuth angles. A detailed description of the Off-Line ERS Wind Scatterometer Products generated at IFREMER can be found in Quilfen (1995).

# 3. Main Study Areas and Data Base

Most of the reference data used in this study were drawn from the data base build up in the framework of the MARS Project (Monitoring Agriculture with Remote Sensing). The MARS Project is implemented by the Space Applications Institute of the Joint Research Centre of the European Commission in close co-operation with national laboratories and organisations (Vossen, 1994). Reference data for the Canadian Prairies stem from the archives of the Atmospheric Environment Service Canada.

## *3.1. Iberian Peninsula*

***Physical Geography***

With the exception of the north-western coast, which is under the influence of a relatively humid marine climate, the Iberian Peninsula is characterised by a Mediterranean climate. The Mediterranean climate has an annual precipitation cycle with wet winters and dry summers (Strahler and Strahler, 1996). The reason for this precipitation cycle lies in the poleward movement of subtropical high-pressure cells during the summer season. Total annual rainfall exhibits a south-north trend with low values in the south-east (Gata, 122 mm) and high values in the north-west (Santiago, 1637 mm) (Rodriguez-Puebla et al., 1998). Natural vegetation is characterised by sclerophylls, evergreen shrubs and trees with small, hard or thick leaves that resist water loss trough transpiration. In the arid south-east vegetation is sparse which gives some regions the appearance of a semi-desert. In the absence of a protective vegetation cover soil erosion may be important leaving behind rocky and barren hillsides. Poesen (1996) notes that soils containing rock fragments in their top layers occupy more than 60 % of the land area of the Iberian Peninsula. Soil erosion is less of a problem in the humid zone of the Iberian Peninsula where organic matter plays a fundamental role in structural stabilisation of soils (Diaz-Fierros and Benito, 1996).

***ERS Scatterometer Data***

ERS Scatterometer data of the domain from 10°W to 4°E and from 36°N to 44°N for the period from September 1991 to May 1996 were extracted.

***CORINE Land Cover***

As part of the CORINE Program (Co-ordination of Information on the Environment) realised by the European Commission a land cover data base of Europe has been prepared based on Earth Observation satellite imagery and auxiliary information (European Environment Agency, 1994; Perdigão and Annoni, 1997). The CORINE nomenclature distinguishes 44 classes that are grouped into a 3-level hierarchy. Each class has a code which is a one, two, or three digit number depending on its level in the hierarchy. On the first level, the CORINE nomenclature distinguishes “Artificial surfaces”, “Agricultural areas”, “Forest and semi-natural areas”, “Wetlands”, and “Water bodies”.

***Advanced Very High Resolution Radiometer***

For the study of vegetation phenology the Normalised Difference Vegetation Index (NDVI) was calculated from AVHRR (Advanced Very High Resolution Radiometer) imagery. Pre-processing of AVHRR data is done at the Space Applications Institute and includes standard calibration procedures, atmospheric correction, cloud detection, geometric registration by matching vector coastline segments, and resampling to build a European mosaic (Millot, 1994). For the comparison with the ERS Scatterometer data the spatial resolution of daily NDVI scenes from the period September 1991 to September 1994 was degraded to match the resolution of the ERS Scatterometer.

***Meteorological Observations***

Daily meteorological observations from twelve inland stations in Spain (Albacete, Burgos, Caceres, Ciudad Real, Cordoba, Granada, Logrono, Madrid, Salamanca, Sevilla, Valladolid, Zaragoza) and four in Portugal (Beja, Braganca, Coimbra, Portalegre) were available in the MARS archive. Extracted parameters include precipitation, minimum and maximum temperatures, and sunshine duration.

***Digital Elevation Model***

A digital elevation model (DEM) given in geographical coordinates compiled by the National Oceanic and Atmospheric Administration (NOAA) is available (Row et al., 1995). The DEM is in raster format with a spacing of 5′. Although the original sources for the DEM and processing procedures are not documented, the original data for the DEM have probably been spatially downgraded from more detailed DEMs developed by the former U.S. Army Map Service.

## *3.2. Ukraine*

***Physical Geography***

The Ukraine covers a total area of 603,700 $km^2$, its landscape is dominated by vast flat plains with elevations generally below 300 m. The Carpathian Mountains (highest point, Howverla Mt., 2061 m) extend into the westernmost part of the country. On the southernmost point are the mountains of the Crimean Peninsula (highest point, Roman-Kosh Mt., 1545 m). The climate is temperate continental, with a Mediterranean climate prevalent in the extreme south. Precipitation generally decreases from north (> 600 mm) to south (< 400 mm). It is greatest in the Carpathians and lowest in the coastal lowlands of the Black Sea. The natural vegetation formed three broad belts that crossed the territory latitudinally. Mixed forest vegetation occupied the north, forest-steppe the middle portion, and steppe the southern third of the country. Nowadays, about 70 % of the total area is cultivated land. Woodland and minor forest occupy an estimated 17 %.

***ERS Scatterometer Data***

ERS Scatterometer data of the domain from 21.5°E to 40.5°E and from 44°N to 53°N for the period from September 1991 to November 1997 were extracted.

***Gravimetric Soil Moisture Data***

In the former Soviet Union an agrometeorological network has been build up starting in the 1930's. Regular measurements are now carried out at approximately 3000 stations (Vinnikov and Yeserkepova, 1991). The soil moisture content is measured by the gravimetric method three times per month (normally on the $8^{th}$, $18^{th}$, and $28^{th}$ of each month) during the warm season, specifically for each crop. For this study, a soil moisture data set covering five years (1992-1996) with data from 99 agrometeorological stations were available (Groisman, 1998). At these stations measurements are carried out at maize, spring wheat, or winter wheat fields, or any combinations of these crops. Table 3-1 shows the number of maize, spring wheat, and winter wheat fields and the respective period of observation. In total, observations from 211 fields for the 0-20 cm and the 0-100 cm soil layers are available. The distance from the station to the fields is as a rule not more than 3 km. If a horse or a car are available then the distance may be up to 5 to 10 km.

In the monitoring program the gravimetric method is employed, i.e. the water content is measured by removing a soil sample from which the moist and dry weight are determined. At each field soil samples are taken at least at four different points within a probe area of about 0.1 hectare. Cores of soil are

extracted in 10 cm segments, and samples from these segments are weighted, dried, and weighted again (Robock et al., 1995). For each 10 cm segment the water available to plants expressed as depth of liquid water is calculated by converting the gravimetric wetness to volumetric wetness and by subtracting the wilting level. For the 0-20 cm and 0-100 cm layers the results for the individual segments are summed up. The data set contains in total 14,293 average field wetness values for the 0-20 cm layer and 12,835 for the 0-100 cm layer. Throughout the text soil water values are presented as % volumetric soil moisture.

| Crop | Number of Stations | Period of Observation |
|---|---|---|
| Maize | 70 | April - September |
| Spring wheat | 70 | April - July |
| Winter wheat | 71 | April - July and September - November |

*Table 3-1: Period of soil moisture observation and number of stations for maize, spring wheat and winter wheat.*

For each field auxiliary information encompassing soil type, soil texture, bulk density in $g \cdot cm^{-3}$, wilting level in both gravimetric and volumetric units, field capacity in mm, and porosity (also called total water capacity) in mm is available for the 0-10 cm, 0-20 cm, and 0-100 cm layers. When a field is spatially inhomogeneous, several cross sections were made to secure this information. *Bulk density* is measured by cutting a known volume of the soil, drying it completely, weighting it, and calculating the ratio of the weight to the preselected volume. The *wilting level* is determined in the laboratory by placing a plant (often oats) in a soil that is initially well saturated and then the water supply is shut down. When the plants show clear signs of mortification the soil moisture content, which defines the wilting level, is measured. The *field capacity* is the water content when deep percolation has nearly stopped after the soil was thoroughly wetted by heavy rain or irrigation. In the Former Soviet Union field capacity is defined in field conditions. A large portion of undisturbed soil in the field is well saturated and then sealed from the atmosphere. A portion of the water drains and the residual provides the estimate. The *porosity* is the relative pore volume of the soil. It is supposed that all soil pores can be filled with water and this justifies the porosity measurement in mm of water. Therefore the porosity is also called the *total water capacity*.

***FAO-Unesco Soil Map of the World***

The FAO (Food and Agriculture Organisation of the United Nations) Soil Map of the World at a scale 1:5,000,000 was available (FAO 1974 and 1988). The map was prepared on the basis of the topographic map series of the American Geographical Society of New York. The original soil map comprises an estimated 4930 different map units, which consists of soil units or associations of soil units. The legend comprises 106 soil units grouped into 26 major soil groupings which are: Acrisols, Cambisols, Cernozems, Podzoluvisols, Rendzinas, Ferralsols, Gleysols, Phaeozems, Lithosols, Fluvisols, Kastanozems, Luvisols, Greyzems, Niotsols, Histosols, Podzols, Arenosols, Regosols, Solonetz, Andosols, Rankers, Vertisols, Planosols, Xerosols, Yermosols, Solonchaks. For each soil unit the texture, the slope class, and the phases are given.

Three texture classes are recognised: coarse texture with less than 18 % clay and more than 65 % sand, medium texture with less than 35 % clay and less than 65 percent sand, and fine texture with more than 35 % clay. Slope classes indicate the slope that dominates in the area of soil association. Three slope classes are distinguished: level to gently undulating, with generally less than 8 % slope, rolling to hilly with slopes between 8 and 30 % slope, and steeply dissected to mountainous, with more than 30 % slope.

***Meteorological Observations***

Daily temperature and precipitation measurements from 35 synoptic station for the period from June 1, 1991 to December 31, 1997 were available.

***Digital Chart of the World***

The Digital Chart of the World is a comprehensive 1:1,000,000 scale vector basemaps of the world (ESRI, 1993).The database was originally developed for the United States Defence Mapping Agency (DMA). The primary source is the DMA Operational Navigation Chart (ONC). The ONCs were designated to meet the needs of pilots and air crews in medium- and low-altitude en route navigation by visual and other techniques. The ONC series was also designed to support military operational planning, intelligence briefings, preparation of visual cockpit displays, and other DMA uses. In this study the Land Cover layer of the Digital Chart of the World is utilised. The map is of interest because it depicts that in the northernmost part of the country at the border to Byelarus extensive wetlands can be found. No distinction about the wetland type is made.

## *3.3. Mali*

Mali, situated in western Africa, was included in the list of study areas because of its distinctly different climatic and environmental conditions. Mali experiences a marked seasonal change between a dry season during the winter months and a rainy season during the summer months. The driving force for this change is the yearly northward migration of the Inter-Tropical Convergence Zone (ITCZ) which reaches its northernmost position around 20°N in August. This northward movement of the ITCZ brings rain to the savanna and sahelian zones of Mali during summer. The first rainfalls over an area are associated with localised and scattered thunderstorms. After these first rains follow irregular, short and intense showers, and in a last stage steady rains with extensive could cover. From the humid south to the arid north the character of rainfall events changes (Barth, 1986):

- Decrease of the mean annual rainfall amount: 1257 mm at Sikasso (11.4°N) and 201 mm at Tombouctou (16°N);
- Shorter rainfall season;
- More localised and singular showers;
- Higher intensity of individual rainfall events;
- Higher relative variability of rainfall.

Temperatures and solar radiation are high in the study area. Average annual solar radiation received on the ground range from about 200 $Wm^{-2}$ in the south to 260 $Wm^{-2}$ in the north of Mali (Christopherson, 1997). Mean annual temperatures are between 25 and 29°C. Both parameters show a maximum shortly before and at the beginning of the rainy season. The highest mean monthly temperatures and the maximum temperatures are observed in May. Surface temperatures may easily surpass 50°C (Vogt, 1992). With the progress of the rainy season cloud cover and air humidity increase which lead to a decrease of temperature, incoming solar radiation, and consequently potential evapotranspiration.

ERS Scatterometer data of the domain from 13°W to 5°E and from 9°N to 16.5°N for the period from September 1991 to January 1998 were extracted. Rainfall data from thirteen stations were available.

### 3.4. Canadian Prairies

The Canadian Prairie Provinces Alberta, Saskatchewan, and Manitoba served as study area for initial algorithm development and testing. These provinces occupy the southern interior of Western Canada. With the exception of the Rocky Mountains in the western part of Alberta, the terrain is mostly a vast, gently sloping plain. The dominant vegetation regions are grassland, parkland (a mixture of grassland and woodland), and boreal forest. The forest distribution in this region is controlled by chronic soil moisture deficits and the boreal forest is generally restricted to areas where there is a surplus of precipitation over potential evapotranspiration (Hogg, 1997). The forested foothills of the Rocky Mountains are dominated by conifers (perialpine forest). The climate is purely continental with low annual precipitation totals between about 300 to 500 mm.

ERS Scatterometer data from the years 1992 and 1993 were extracted. Archived climate data were made available by the Atmospheric Environment Service Canada for eighteen synoptic weather stations in the southern part of the Canadian Prairie Provinces and comprise daily temperatures, rainfall, snowfall, snow depth, and soil temperature.

# 4. Physical Principles of Radar Scatterometry

## 4.1. Introduction

Radar scatterometers like the Scatterometer on board of the ERS satellites are non-imaging systems that provide a quantitative measure of the backscattering coefficient $\sigma^0$. They are working in the microwave part of the electromagnetic spectrum extending from about 0.3 to 300 GHz. Because we humans have no sensory perception of microwaves it is often quite difficult for us to understand the information content of $\sigma^0$ measurements. It is only through empirical observations and theoretical considerations that one starts to learn what $\sigma^0$ tells us about the observed target. In this chapter some principles of radar scatterometry are presented. It is shown that the backscattering coefficient is determined by the structure and the dielectric properties of the observed target. Then the dielectric properties of natural media including soil, vegetation, and snow are discussed. This discussion shows that the dielectric properties are to a large extent determined by the fraction of water within these media which explains the very important role of water in microwave remote sensing.

## 4.2. Radar Equation

A radar scatterometer transmits an electromagnetic wave and measures the energy of the wave that is scattered backwards from the illuminated object. The received power depends on the technical characteristics of the radar, the distance between the radar and the object, and on the properties of the object itself. This is expressed in the (monostatic) *radar equation* (Ulaby et al., 1982):

$$P_r = \frac{P_t A_{eff}^2}{4\pi\lambda^2 R^4}\sigma \tag{4.1}$$

where
- $P_r$ = received power;
- $P_t$ = transmitted power;
- $A_{eff}$ = effective area of the antenna;
- $\lambda$ = radar wavelength;
- $R$ = range (distance) between radar and object;
- $\sigma$ = cross section of the object.

In Equation (4.1) the technical characteristics of the radar are described by the transmitted power $P_t$, the effective area of the antenna $A_{eff}$, and the wavelength $\lambda$. This radar equation is not formulated for area-extensive targets (Fung, 1994). For the case of scatterometer measurements of the earth's surface let us consider the illuminated surface as composed of an infinite collection of targets with a cross section of differential size $d\sigma$. Then we rewrite $d\sigma$ as the product of the *backscattering coefficient* $\sigma^0$ times the differential area $da$ occupied by the target. The backscattering coefficient is such defined as the radar cross section per unit area. The unit of $\sigma^0$ is $m^2m^{-2}$ but it is commonly expressed in decibels (dB):

$$\sigma^0(\text{dB}) = 10 \cdot \log \sigma^0(\text{m}^2\text{m}^{-2}) \tag{4.2}$$

Applying (4.1) to an area extensive target with an area $A$, the received power is equal to:

$$P_r = \iint_A \frac{P_t A_{eff}^2}{4\pi\lambda^2 R^4}\sigma^0 da \tag{4.3}$$

As the objective of the radar measurements is to obtain information about the observed target, the power measurements are converted to the backscattering coefficient $\sigma^0$. For the ERS Scatterometer this is done in the ground segment (Chapter 2.3).

## 4.3. Scattering and Absorption of Electromagnetic Waves

In the radar equation it is assumed a priori that an object can scatter an incident wave into all directions. But what are the physical reasons of the scattering phenomenon? Let us consider an electromagnetic wave which is characterised by the electric and magnetic field vectors **E** and **B**[3]. According to Lorentz force law an electromagnetic field exerts a force **F** on a charge *Q* moving with a velocity **v:**

$$\mathbf{F} = Q(\mathbf{E} + \mathbf{v} \times \mathbf{B}) \tag{4.4}$$

When the wave is incident on an object then the positive and negative charges of which any material is made up will be accelerated into different directions. The induced microscopic currents will reradiate electromagnetic waves into all directions thereby modifying the original field. The amount of energy scattered backwards into the direction of the incident wave therefore depends on the geometrical and electromagnetic properties of the illuminated object. A mathematical description of these processes, which is provided by electromagnetic theory, is presented below. The treatment follows mainly Jackson (1983) and Ishimaru (1978).

### 4.3.1. Maxwell's Equations

The basic equations of electromagnetic theory in macroscopic media are Maxwell's equations:

$$\begin{aligned} \nabla \cdot \mathbf{D} &= \rho & \nabla \cdot \mathbf{B} &= 0 \\ \nabla \times \mathbf{E} &= -\frac{\partial \mathbf{B}}{\partial t} & \nabla \times \mathbf{H} &= \frac{\partial \mathbf{D}}{\partial t} + \mathbf{J} \end{aligned} \tag{4.5}$$

where **E** = electric field intensity (voltage/distance);
**H** = magnetic field intensity (current/distance);
**D** = electric displacement (charge/area);
**B** = magnetic induction (voltage×time/area);
ρ = volume charge density (charge/volume);
**J** = volume current density (current/area).

For linear, isotropic and homogenous media the electric field variables **E** and **D** are related via:

$$\mathbf{D} = \varepsilon \varepsilon_0 \mathbf{E}, \tag{4.6}$$

where $\varepsilon_0$ is the permittivity of the vacuum ($\varepsilon_0 = 8.854 \cdot 10^{-12}$ As/Vm) and $\varepsilon$ is the relative permittivity of the medium. The corresponding relation for the magnetic field variables **B** and **H** is:

$$\mathbf{B} = \mu \mu_0 \mathbf{H}, \tag{4.7}$$

where $\mu$ is the relative permeability and $\mu_0$ is the permeability of vacuum ($\mu_0 = 4\pi \cdot 10^{-7}$ Vs/Am). $\varepsilon$ and $\mu$ are empirical parameters that describe the interaction of electromagnetic fields and media. All substances show magnetic effects but only for ferromagnetic and ferrimagnetic materials $\mu$ takes on values significantly different from one (Duffin, 1965). Water, for instance, has a relative permeability of 0.999988 (Mätzler, 1987). Therefore, in remote sensing, the small magnetic interaction can be neglected and $\mu$ can be set equal to one. The relative permeability $\varepsilon$ is also called the dielectric constant and is in general a complex quantity to account for losses in the media. Amongst natural media water plays a very important role because of its distinct dielectric properties. For example, at frequencies below 2 GHz the dielectric constant of liquid water is around 80, while for other natural media like soil particles, dry vegetative matter, or rocks it rarely exceeds 7 (Ulaby et al., 1986). The dielectric properties of natural media will be discussed in more detail in Chapter 4.4.

[3] The bold letters indicate vector quantities.

### 4.3.2. Wave Propagation

The propagation of waves in macroscopic media in the absence of sources is described by the wave equation. The wave equation can be directly derived from Maxwell's equations:

$$\nabla^2 \mathbf{E} = \frac{\varepsilon}{c^2} \frac{\partial^2 \mathbf{E}}{\partial t^2}, \tag{4.8}$$

where $c$ is the speed of light in vacuum which is equal to $(\varepsilon_0 \cdot \mu_0)^{-1/2}$. The equation for **B** has exactly the same form. One solution of (4.8) is the plane wave which is given by

$$\mathbf{E} = \mathbf{E}_0 e^{j(\pm \mathbf{kx} - \omega t)}, \tag{4.9}$$

where $\mathbf{E}_0$ is a constant vector, $\omega$ is the angular frequency, **k** is the propagation vector, and **x** is the displacement vector. The magnitude of the propagation vector is called the wave number $k$. Expression (4.9) is recognised as two waves propagating in directions defined by the unit vectors $\pm\mathbf{k}/k$. The vectors **E**, **B**, and **k** are mutually perpendicular such that the vector $\mathbf{E} \times \mathbf{B}$ points along the direction of propagation. When (4.7) is substituted into (4.6) it can be seen that

$$k = \sqrt{\varepsilon} \cdot \frac{\omega}{c} = n \cdot k_0, \tag{4.10}$$

where $k_0 = \omega/c$ is the wave number in vacuum, and $n$ is the refractive index. As already mentioned above, to account for losses in the medium the dielectric constant and the refractive index are complex quantities:

$$n = n' + jn'' = \sqrt{\varepsilon' + j\varepsilon''}. \tag{4.11}$$

The amplitude of the wave decreases exponentially which can be readily seen if the direction of propagation of the plane wave is chosen, for example, to be along the z-axis:

$$\mathbf{E} = \mathbf{E}_0 e^{-n'' k_0 z} e^{\mathrm{j}(\mathrm{n}' \mathrm{k}_0 \mathrm{z} - \omega t)} \tag{4.12}$$

The distance at which the power of the wave $|\mathbf{E}|^2$ decreases by $e^{-1}$ is called the penetration depth $L_p$:

$$L_p = \frac{1}{2n'' k_0}. \tag{4.13}$$

Another solution of the wave equation (4.6) is a spherical wave which is of the form:

$$\mathbf{E} = \mathbf{E}_0 \frac{e^{j(\pm kr - \omega t)}}{r} \tag{4.14}$$

where $r$ is the radius of the spherical coordinate system. A spherical wave travels along the radiusvector. As is the case for plane waves, **E**, **B** and the direction of propagation are mutually perpendicular.

### 4.3.3. Scattering of a Wave by a Particle

In this chapter the scattering of a plane wave by a single particle is described in mathematical terms. The objective is to demonstrate that scattering arises from microscopic currents which are generated by the incoming wave, and that this phenomenon is accounted for by describing the object in terms of its geometrical and dielectric properties. The treatment follows closely the introductory chapter in Ishimaru (1978).

Let us consider a particle whose dielectric constant is a function of the position within the body. It occupies a volume $V$ and is surrounded by a medium with a dielectric constant $\varepsilon_0$. It is illuminated by a plane wave of frequency $\omega$. With the understanding of a time factor $\exp(-j\omega t)$ the incident wave $\mathbf{E}_i$ is given by:

$$\mathbf{E}_i(\mathbf{x}) = \hat{\mathbf{e}}_i e^{jk\hat{\mathbf{i}}\mathbf{x}} \tag{4.15}$$

where $\hat{\mathbf{i}}$ is the unit vector in the direction of propagation. The amplitude of $\mathbf{E}_i$ is chosen to be one. The direction of polarisation is given by $\hat{\mathbf{e}}_i$. The electric field induces microscopic currents within the particle which reradiate electromagnetic fields. In the far field of the object, i.e. at distances much larger than the wavelength and the diameter of the volume *V*, the scattered field $\mathbf{E}_s$ behaves like a spherical wave. The total field is such given by:

$$\mathbf{E}(\mathbf{x}) = \mathbf{E}_i(\mathbf{x}) + \mathbf{E}_s(\mathbf{x}) \underset{kr\to\infty}{=} \hat{\mathbf{e}}_i e^{jk\hat{\mathbf{i}}\mathbf{x}} + \mathbf{f}(\hat{\mathbf{i}},\hat{\mathbf{o}})\frac{e^{jkr}}{r} \tag{4.16}$$

where $\mathbf{x} = r\hat{\mathbf{o}}$. The parameter $\mathbf{f}(\hat{\mathbf{i}},\hat{\mathbf{o}})$ is called the scattering amplitude. The ratio of power of the scattered and incident waves define the differential cross section $\sigma$ of the particle (see also Equation 4.1) which is given by

$$\sigma(\hat{\mathbf{i}},\hat{\mathbf{o}}) = \lim_{r\to\infty} \frac{4\pi r^2 |\mathbf{E}_s|^2}{|\mathbf{E}_i|^2} = 4\pi \left|\mathbf{f}(\hat{\mathbf{i}},\hat{\mathbf{o}})\right|^2 \tag{4.17}$$

The problem is determined by Maxwell's equation in the absence of free currents and charges:

$$\begin{aligned} \nabla\cdot\mathbf{E} &= 0 & \nabla\cdot\mathbf{H} &= 0 \\ \nabla\times\mathbf{E} &= j\omega\mu_0\mathbf{H} & \nabla\times\mathbf{H} &= -j\omega\varepsilon(\mathbf{x})\varepsilon_0\mathbf{E} \end{aligned} \tag{4.18}$$

Let us rewrite Ampère's Law in the following manner:

$$\nabla\times\mathbf{H} = -j\omega\varepsilon_0\mathbf{E} + \mathbf{J}_{eq}, \tag{4.19}$$

where

$$\mathbf{J}_{eq} = \begin{cases} -j\omega\varepsilon_0[\varepsilon(\mathbf{x})-1]\mathbf{E} & \text{in } V \\ 0 & \text{outside} \end{cases} \tag{4.20}$$

Ampère's Law would take on exactly the same form if the problem of finding the radiation field of a localised oscillating current embedded in vacuum is considered. The only difference would be that instead of $\mathbf{J}_{eq}$, Equation (4.19) would contain the free current source **J**. This shows that $\mathbf{J}_{eq}$ represents an equivalent current source which generates the scattered wave. The solution of the equation system (4.18) is given by

$$\begin{aligned} \mathbf{E} &= \mathbf{E}_i + \mathbf{E}_s \\ \mathbf{H} &= \mathbf{H}_i + \mathbf{H}_s \end{aligned} \tag{4.21}$$

where the field ($\mathbf{E}_i$, $\mathbf{H}_i$) represents the homogenous solution. In our case ($\mathbf{E}_i$, $\mathbf{H}_i$) can be identified with the incident plane wave given by (4.13). The field ($\mathbf{E}_s$, $\mathbf{H}_s$) is the scattered field generated by the microscopic currents within *V*. It is given by:

$$\begin{aligned} \mathbf{E}_s &= \nabla\times\nabla\times\mathbf{A} \\ \mathbf{H}_s &= -j\omega\varepsilon_0\nabla\times\mathbf{A} \end{aligned} \tag{4.22}$$

where **A** is the Hertz vector:

$$\mathbf{A}(\mathbf{x}) = \frac{1}{4\pi}\int_V [\varepsilon(\mathbf{x}')-1]\mathbf{E}(\mathbf{x}')\frac{e^{jk|\mathbf{x}-\mathbf{x}'|}}{|\mathbf{x}-\mathbf{x}'|}d^3x'. \tag{4.23}$$

In the far field we can make the approximation

$$\frac{e^{jk|\mathbf{x}-\mathbf{x}'|}}{|\mathbf{x}-\mathbf{x}'|} \underset{kr\to\infty}{=} \frac{e^{jkr}}{r}e^{-jk\hat{\mathbf{o}}\mathbf{x}'} \tag{4.24}$$

so that $\mathbf{E}_s$ can be written as:

$$\mathbf{E}_s = \mathbf{f}(\hat{\mathbf{i}},\hat{\mathbf{o}})\frac{e^{jkr}}{r} \tag{4.25}$$

with

$$\mathbf{f}(\hat{\mathbf{i}},\hat{\mathbf{o}}) = \frac{k^2}{4\pi}\int_V \{-\hat{\mathbf{o}}\times\hat{\mathbf{o}}\times\mathbf{E}(\mathbf{x}')\}\{\varepsilon(\mathbf{x}')-1\}e^{-jk\hat{\mathbf{o}}\mathbf{x}'}d^3x' \tag{4.26}$$

Equation (4.26) represents only a formal solution to our problem because, in general, the electric field **E** within the body is not known. However, for our purpose this solution is sufficient because it shows that the scattered amplitude depends on the dielectric properties of the medium and its geometrical arrangements or structure.

## *4.4. Dielectric Properties of Natural Media*

The dielectric behaviour of media arises because positive and negative charges move into opposite directions when an **E** field is applied, a phenomenon that is referred to as polarisation. Let us consider a perfect insulator. Insulators are build up from groups of atoms or ions which we shall call here for convenience a "molecule". In an inert gas our "molecule" would be a single atom, while in a solid such as potassium chloride a single KCl group may be considered as a "molecule" even though the structure is an ionic framework in which molecules do not exist. When an external field is applied then the positive and negative charges within our "molecules" move into opposite directions forming electric dipoles. There are three ways in which polarisation may arise, two involving distortion and one orientation (Duffin, 1965). If the "molecule" has no permanent dipole then polarisation may be due to the relative movement of nuclei and electrons (electronic polarisation) or of positive and negative ions in a solid (ionic polarisation). If the "molecule" has a permanent dipole then the external field imposes a preferential direction. This orientational polarisation is temperature dependent since thermal agitation randomises the directions of the dipoles. In an oscillating field the molecules will never be quite in phase with the applied field, and for high frequencies will not follow it at all. At low frequencies the three polarisation mechanisms may occur together. The orientational distribution disappears in general in the microwave region, ionic polarisation in the infrared, and electronic polarisation in the visible and infrared.

### 4.4.1. Water

Amongst natural media only liquid water shows orientational polarisation. The permanent dipole moment of water is due to the triangular structure of the $H_2O$ molecules[4]. Above a certain frequency, called relaxation frequency, the dipoles cannot follow the oscillations of the applied **E** field any longer and thus $\varepsilon'$ decreases. At the relaxation frequency the molecules behave like harmonic oscillators at resonant frequency and absorption ($\varepsilon''$) is highest. The dielectric constant of pure water obeys the relaxation spectrum of the Debye type, which is given by a three parameter expression (Ulaby et al., 1986):

$$\varepsilon = \varepsilon' + j\varepsilon'' = \varepsilon_\infty + \frac{\varepsilon_s - \varepsilon_\infty}{1 - j\, f / f_0}, \tag{4.27}$$

where $f$ is the frequency, $f_0$ is the relaxation frequency, $\varepsilon_s$ is the static dielectric constant, and $\varepsilon_\infty$ is the dielectric constant in the high frequency limit. The parameters are temperature dependent. Table 4.1 lists the parameters for 0°C and 20°C and the resulting values of the dielectric constant at 5.3 GHz. Figure 4-1 shows the frequency dependency of $\varepsilon$ at 20°C.

| Temperature | $f_0$ (GHz) | $\varepsilon_s$ | $\varepsilon_\infty$ | $\varepsilon'$ | $\varepsilon''$ |
|---|---|---|---|---|---|
| 0°C | 9 | 88.3 | 5.3 | 66.9 | 36.2 |
| 20°C | 17 | 80 | 4.9 | 73.3 | 21.3 |

*Table 4-1: Parameters of the Debye equation at 0°C and 20°C and the obtained values of the dielectric constant of pure water at 5.3 GHz.*

[4] The axes joining the two hydrogen nuclei to the oxygen form an angle of about 104º (Schanda, 1986).

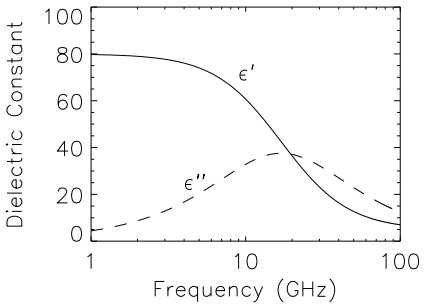


*Figure 4-1: Dielectric constant ε of pure water versus frequency at 20°C.*

### 4.4.2. Soil

The term soil refers to the weathered and fragmented outer layer of the earth's terrestrial surface (Hillel, 1980). Soils consist of three phases: a solid phase made up of mineral and organic matter, a liquid phase consisting of soil water, and a gaseous phase. In the absence of water the real part of the dielectric constant $\varepsilon'$ varies over the range from two to four (Ulaby et al., 1986). The imaginary part $\varepsilon''$ is typically lower than 0.05. For explaining the dielectric behaviour of wet soil the soil water is usually divided into two fractions according to the forces that are acting on the water molecules (Hallikainen et al., 1985; Dobson et al., 1985). The water molecules contained in the first molecular layers surrounding the soil particles are tightly held due to matrix and osmotic forces. This fraction is referred to as bound water and exhibits a dielectric dispersion spectrum that is very different from that of free water. The dielectric properties of bound water are not known quantitatively, but it is apparent that with an increasing fraction of bound water $\varepsilon'$ decreases. Therefore $\varepsilon$ depends on the textural composition of the soil which determines the specific surface area of the soil particles (Koorevar et al., 1983). The term soil texture refers to the size range of particles in the soil. The array of possible particle sizes is divided into three fractions, namely sand, silt, and clay. In the definition of the U.S. Department of Agriculture (USDA) sand are particles falling in the range from 2000 µm down to 50 µm, silt from 50 to 2 µm, and clay from 2 µm downwards. For several frequencies Hallikainen et al. (1985) generated empirical expressions for $\varepsilon$ as a function of the volumetric water content $W$ and the sand ($Sa$) and clay ($Cl$) components in percent of weight. For 6 GHz their best fit polynom is:

$$\begin{aligned}\varepsilon' &= (1.993 + 0.002Sa + 0.015Cl) + (38.086 - 0.176Sa - 0.633Cl)\cdot W + \\ &\quad +(10.720+1.256Sa+1.522Cl)\cdot W^2 \\ \varepsilon'' &= (-0.123+0.002Sa + 0.003Cl) + (7.502 - 0.058Sa - 0.116Cl)\cdot W + \\ &\quad +(2.942 + 0.452Sa + 0.543Cl)\cdot W^2\end{aligned} \tag{4.28}$$

Figure 4-2 shows the dependence of the dielectric constant on soil wetness for a loamy soil with $Sa$ = 40 % and $Cl$ = 20 %. It can be seen that $\varepsilon'$ increases from about 2.3 for a dry soil to 40 for a saturated soil surface.

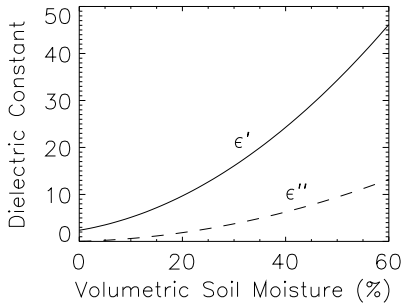


*Figure 4-2: Dielectric constant ε of a loamy soil versus the volumetric soil moisture content in %.*

When soil temperature drops below 0°C the dielectric constant decreases strongly because when water freezes polarisation by orientation is not possible any longer. However, some soil water does not freeze even at temperatures around -50°C and therefore $\varepsilon$ of frozen soil still shows some dependency on the moisture content before freezing. Hallikainen et al. (1984) made dielectric measurements of soils in the 3 GHz to 37 GHz band between -50°C and 23°C. For several soil types, two samples with a volumetric water content of 5 % and 25 % were prepared in the laboratory and quickly frozen. For silt loam at -2°C Hallikainen et al. (1984) found $\varepsilon'$ to be about 3.3 and 5.5 for the dry and wet samples respectively. Despite these values are slightly larger than for a completely dry soil sample it can be concluded that the dielectric properties of a dry and frozen soil are similar.

### 4.4.3. Vegetation

Direct measurements of oven-dried samples of various types of vegetation material show that the real part of the dielectric constant $\varepsilon'$ is generally between 1.5 and 2, and $\varepsilon''$ is below 0.1 (Ulaby and El-Rayes, 1987). Water may constitute between about 80 % and 90 % of the fresh weight of leave like plants (Börner, 1996, after Kramer, 1983). Even woody plants contain more than 50 % water. Therefore also $\varepsilon$ of vegetation increases strongly with the water content. El-Rayes and Ulaby (1987) and Ulaby and El-Rayes (1987) investigated the dielectric properties of vegetation and developed an empirical formula to model $\varepsilon$ as a function of the volumetric water content of vegetation matter alone. They state that the model is capable of reproducing $\varepsilon$ of various vegetation elements, leaves, stalks, branches, trunks, with an relative error of ±5 %. In the model it is distinguished between bound water that is held tightly by the organic compounds and free water that can move within the plants with relative ease. To estimate $\varepsilon$ of both the bound and free water components a dispersion model of the Debye type is employed. While the relaxation frequency of the free water component was assumed to be equal to that of pure water (17 GHz at 20°C), the relaxation frequency of the bound water component was estimated to be about 0.18 GHz by conducting dielectric measurements for sucrose-water mixtures.

To account for temperature effects a slightly modified version of the model is presented in Ulaby et al. (1990). Figure 4-3 shows how $\varepsilon$ varies with the volumetric moisture content of vegetation according to this model at 20°C and 5.3 GHz. The model suggests that for a gravimetric vegetation moisture content around 80 % $\varepsilon'$ takes on values above 40.

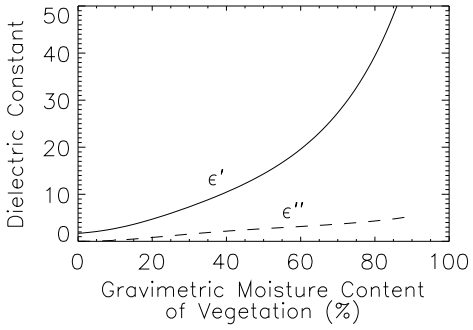


*Figure 4-3: Dielectric constant ε of vegetation versus the gravimetric soil moisture content in %.*

### 4.4.4. Ice and Snow

Over the whole microwave frequency range $\varepsilon'$ of ice is relatively constant, $\varepsilon' = 3.17 \pm 0.03$ (Mätzler, 1987). Ice has a remarkable property in the microwave range. For frequencies below 10 GHz $\varepsilon''$ is lower than $10^{-3}$. These losses are amongst the lowest of condensed matter and consequently the penetration depth of microwaves into ice is on the order of meters.

Snow is a mixture of ice, air, and water, depending on the temperature. For dry snow $\varepsilon'$ is lower than about 1.7. The magnitude of the imaginary part $\varepsilon''$ of dry snow is not much different from that of ice. When temperatures approach 0°C, liquid water is formed and the dielectric properties are changed significantly. Figure 4-4 shows how $\varepsilon$ of snow changes with the volume fraction of liquid water in the snow pack according to the formulas given by Mätzler (1987). The penetration depth decreases rapidly with increasing water content and consequently dry and wet snow show distinctly different backscattering behaviour.

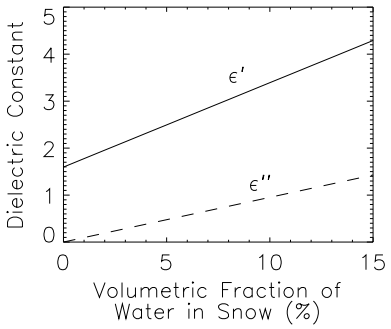


*Figure 4-4: Dielectric constant ε of snow versus the volume fraction of water in %.*

# 5. Backscatter from Natural Surfaces and Scaling Issues

## *5.1. Backscatter from Bare Soil*

When an electromagnetic wave impinges on a soil surface a part of the energy is scattered at the boundary surface in all directions and the rest is transmitted forward into the soil. The penetration depth of the transmitted wave is limited by absorption and scattering losses in the inhomogeneous soil medium. Considering only absorption losses (Equation 4.13) the penetration depth of C-band microwaves into the soil varies from about 10 cm when dry to less than 1 cm when wet. In most circumstances the layer accessible to C-band microwaves is about 0.5 cm to 2 cm thick (Schmugge, 1983 after Wilheit, 1978 and Newton et al., 1982; Ulaby et al., 1978; Boisvert et al., 1997). Therefore scatter from a bare soil surface is determined mainly by the dielectric properties of the upper few centimetres of the soil (and hence the soil moisture content in this layer) and by the geometrical structure or roughness of the soil surface. Although some scatter may arise due to inhomogeneities within the soil medium (Schanda, 1987) these may be ignored in favour of the surface scattering contribution (Ulaby et al., 1982).

To explain the influence of surface roughness on scattering let us consider Figure 5-1 from Schanda (1986). When a wave is incident on a plane surface then it is specular reflected in the forward direction. In this case no energy is scattered backwards to the sensor, except for normal incidence. A concise mathematical solution to this problem exists and the formulas for calculating the reflected and transmitted waves are known as Fresnel's formulas (Jackson, 1983). When the surface is slightly rough the incident wave will partly be reflected into the specular direction and partly be scattered in all directions. The first component is called the coherent component because the phase front of the coherent wave is conserved. The diffusely scattered component is called the non-coherent scattering component because the phase coherence is deteriorated or even destroyed. As the surface becomes rougher, more and more energy is scattered diffusely while the coherent component becomes negligible. This means that for incidence angles away from nadir (greater than about 10°) the energy scatted in the backwards directions increases with increasing surface roughness (Ulaby and Batlivala, 1976; Ulaby et al., 1982).

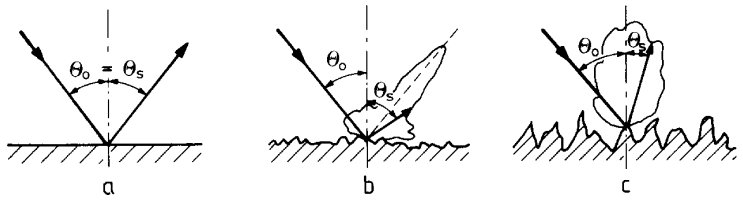


*Figure 5-1: Specular and diffuse components of the radiation scattered at **a** perfect plane, **b** slightly rough, **c** very rough surfaces. $\theta_o$ and $\theta_s$ are the incidence and scattering angles. From Schanda (1986).*

When the dielectric constant of the soil increases then the ability of the soil surface to reradiate electromagnetic waves also increases, which is why $\sigma^0$ and the soil moisture content are positively correlated. In numerous field experiments it was found empirically that $\sigma^0$ expressed in dB is in a first approximation linearly related to the volumetric soil moisture content *W* (e.g. Champion, 1996):

$$\sigma^0(\text{dB}) = A + B \cdot W \,, \tag{5.1}$$

where by definition *A* is the backscattering coefficient of a completely dry soil surface and *B* is the sensitivity of $\sigma^0$ to changes in the surface soil moisture content. The regression coefficients *A* and *B* are dependent on soil surface roughness, incidence angle, and soil texture (Dobson and Ulaby, 1986). *A* is primarily controlled by surface roughness and the incidence angle. For the incidence angle range covered by the ERS Scatterometer, *A* increases with increasing roughness and decreases with increasing

incidence angles. The sensitivity $B$ is dependent on soil texture because for constant volumetric soil moisture levels $\varepsilon$ varies with soil texture. In addition, $B$ may be dependent on incidence angle but the literature is contradictory about this question (Ulaby and Batalivala, 1976; Bertuzzi et al., 1992; Autret et al, 1989; Champion and Faivre , 1997).

Theoretical research on scattering of electromagnetic waves by rough surfaces has been extensive (Tsang et al., 1985; Fung, 1994). These studies show that backscatter is dependent on the r.m.s. height of the surface and the autocorrelation function of the surface height variations. In well defined situations, such as in controlled laboratory experiments, theoretical models like the Integral Equation Method (IEM) model show good agreement with experimental results. As shown in Fung (1994) the IEM is very sensitive to the choice of the autocorrelation function. In fact, the IEM stands for a multitude of models with each prototype representing different surface roughness types (Fung, 1997; personal communication). This makes the use of these models in practice quite difficult because the statistical properties of the surface are in general not known. For this reason empirical models that explain the variation of $\sigma^0$ with the soil dielectric properties, the r.m.s. height, frequency, and incidence angle were developed based on field experiments (Oh et al., 1992; Dubois et al., 1995; Champion, 1996). However, like the theoretic models, the empirical models often fail to provide results in good agreement with field observations. One reason might be that the parameters that have been used to describe surface roughness (r.m.s. height, correlation length) are not well representing the statistical characteristics of area extensive targets (Davidson et al., 1998). Lersch et al. (1988a) studied the spatial variability of various surface roughness parameters derived from 1 m long surface profiles and found that these parameters are most commonly spatially independent. Research to define a scale independent description of surface roughness is on-going (Manninen et al., 1998).

### 5.2. Backscatter from Vegetated Surfaces

Vegetation canopies are inhomogeneous media comprising scattering elements with many different sizes, shapes, orientations, and permittivities. Usually, the vegetation constitutes 1 % or less of the canopy volume (Attema and Ulaby, 1978) and the penetration depth is on the order of meters (Ulaby et al., 1982). Scattering is caused mainly by the dielectric discontinuities within the canopy volume (volume scattering) and, for vegetation canopies of low height, by the underlying soil surface (surface scattering). Scattering from vegetation is a complex phenomenon and elaborated models have been developed to model $\sigma^0$ in terms of vegetation and soil surface parameters (Ulaby et al., 1990; Karam et al., 1992; Saatchi et al., 1994). These models have been used to simulate $\sigma^0$ of various vegetation canopies with some success (e.g. Touré et al, 1994) but, unfortunately, their input data requirements are very demanding. For example, to model $\sigma^0$ of an aspen canopy the Michigan Microwave Canopy Scattering Model (MIMICS) requires 19 parameters like leaf diameter, branch length, or trunk moisture and three probability functions representing the orientational distribution of leaves, branches, and trunks.

For the discussion of backscatter from vegetation a simple model based on radiative transfer theory is useful. Radiative transfer theory formulates the problem of absorption, scattering, and creation of radiation within a volume filled with particles (Chandrasekhar, 1960). The first-order radiative transfer solution of the problem of scattering of vertically polarised radiation by a vegetation canopy consists of three terms[5] (Fung, 1994):

[5] In this formulation it is assumed that the vegetation elements are isotropic scatterers and that only single scattering is important. Further it is assumed that the reflection at the surface for the interaction term can be calculated using the Fresnel power reflection coefficient.

$$\sigma^0_{can} = \sigma^0_{vol} + \sigma^0_{sur} + \sigma^0_{int} = \frac{\omega \cos\theta}{2}(1 - e^{-\frac{2\tau}{\cos\theta}}) + \sigma^0_s(\theta) e^{-\frac{2\tau}{\cos\theta}} + 2\Gamma_v(\theta)\omega\tau e^{-\frac{2\tau}{\cos\theta}} \qquad (5.2)$$

where
$\sigma^0_{can}$ = backscattering coefficient of the vegetation canopy;
$\sigma^0_{vol}$ = volume scattering term;
$\sigma^0_{sur}$ = surface scattering term;
$\sigma^0_{int}$ = surface-volume interaction term;
$\sigma^0_s$ = backscattering coefficient of soil surface;
$\omega$ = single-scattering albedo of the canopy;
$\tau$ = optical depth or thickness of the canopy;
$\Gamma_v$ = Fresnel power reflectivity for vertically polarised radiation.

The volume scattering term $\sigma^0_{vol}$ is that contribution to total backscatter which is due to direct backscatter of the incoming wave by the vegetation elements. It is proportional to the single scattering albedo $\omega$ which is a measure of the scattering efficiency of the vegetation elements. The surface scattering term $\sigma^0_{sur}$ represent direct backscattering from the soil surface attenuated by the vegetation layer. It can be seen in Equation (5.2) that the term

$$\gamma^2(\theta) = e^{-\frac{2\tau}{\cos\theta}} \qquad (5.3)$$

controls the relative contributions of the vegetation layer and the soil surface. $\gamma^2$ is called the two-way transmissivity of the vegetation layer as it describes the attenuation that a wave experiences when it travels two times through the canopy. With increasing incidence angle the path length increases and consequently $\gamma^2$ decreases. As a result the vegetation contribution becomes more important at large incidence angles. Dense forest canopies are not transparent for C-band microwaves and are such representative of pure volume scatterers (Figure 5-2). It is noted that ERS Scatterometer measurements of tropical rainforest are used for sensor calibration to show exactly the incidence angle behaviour of the volume scattering term (Chapter 2.5.1)

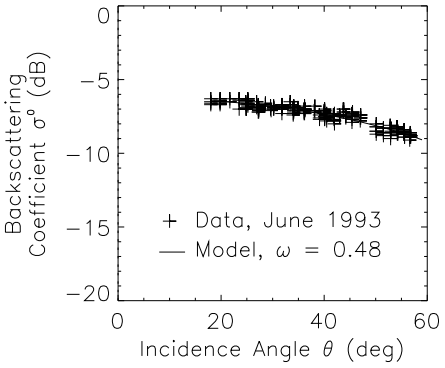


*Figure 5-2: ERS Scatterometer data acquired during June 1993 over tropical forest in Congo (2°N, 17°E). Also shown is the fitted volume scattering term of Equation (5.2).*

The interaction term $\sigma^0_{int}$ accounts for multiple scattering by the vegetation and the soil surface. For vertical polarisation the interaction term is in general much smaller than the volume and surface scattering terms (Ulaby et al., 1986). However, it may be important for wet soil surface conditions and relatively small values of the optical thickness. Under these conditions the interaction term partly compensates for the attenuation of the soil contribution by the vegetation layer, especially at high incidence angles. This implies that the interaction term tends to reduce the loss in sensitivity to soil moisture as the optical depth increases (Fung and Eom, 1985).

The Cloud Model developed by Attema and Ulaby (1978) is of the same form as Equation (5.2), but without the interaction term. This model was employed in numerous studies to simulate $\sigma^0$ of various vegetation cover types: alfalfa (Attema and Ulaby, 1978), barley (Bouman, 1991), beet (Bouman, 1991; Clevers and Leeuwen, 1996, Leeuwen et al., 1996), boreal forest (Pulliainen et al., 1994 and 1996), corn

(Attema and Ulaby, 1978), grass (Mo et al., 1984), milo (Attema and Ulaby, 1978), potato (Bouman, 1991), savanna vegetation (Magagi and Kerr, 1997), and wheat (Attema and Ulaby, 1978; Bouman, 1991; Champion and Guyout, 1991; Prévot et al., 1993a and 1993b; Taconet et al., 1994 and 1996). Extensions to the Cloud Model can for example be found in Ulaby et al. (1984) and Paris (1986). To simulate vegetation growth the optical depth $\tau$ was related to vegetation parameters like plant water content, plant height or leaf area index (LAI). In the majority of the studies the single-scattering albedo $\omega$ was kept constant.

Despite its theoretical background the Cloud Model may be considered to be an empirical model whose parameters, i.e. the single scattering albedo and optical depth, may be tuned to fit observations. For example, Wigneron et al. (1996) introduce an incidence angle dependency for $\omega$ and $\tau$ to account for vegetation structure in radiometric measurements. However, the relatively successful application of radiative transfer theory to a wide variety of vegetation types and radar systems shows that the main phenomena involved in the problem of backscattering from vegetation can be well described by the interplay of surface and volume scattering effects.

To illustrate principle backscattering trends in ERS Scatterometer data over vegetated land surfaces a simple model based on radiative transfer theory is used (Table 5-1). The model is discussed in detail in Wagner (1998). It was developed by postulating its general form and by identifying the possible ranges of model parameters based on a literature review and on a comparison of model simulations with ERS Scatterometer data acquired under known conditions in the Canadian Prairies and over tropical rain forest. A final set of vegetation and surface parameters was chosen to achieve an agreement of model simulations and ERS Scatterometer measurements over the Iberian Peninsula. The major characteristics of the model are:

- The ERS Scatterometer measured backscattering coefficient is modelled as a mixture of non-transparent (forests, bushes, shrubs) and translucent (grassland, agricultural land) vegetation. This formulation was adopted because the literature review showed that the single scattering albedo of translucent vegetation types like grasses or agricultural crops is in general smaller than the single scattering albedo of non-transparent vegetation like forests. It will be shown in Chapter 7.2.1 that, indeed, the percentage area of non-transparent respectively translucent vegetation within one ERS Scatterometer pixel is important to explain the backscatter behaviour. The percentage area of one ERS Scatterometer pixel covered by non-transparent vegetation is denoted by $A_{nt}$.
- Because currently available empirical models describing backscatter from bare soil surfaces (Oh et al., 1992; Dubois et al., 1995; Champion, 1996) fail to reproduce the observed incidence angle behaviour of ERS Scatterometer measurements, a simple model assuming a linear relationship between $\sigma^0$ in decibels and $\theta$ is used.
- Model simulations show that the slope of $\sigma^0(\theta)$ in the logarithmic range varies strongly with changing soil dielectric properties if the interaction term given in Equation (5.2) is used. Since this is not in line with empirical observations (Chapter 6.3.4) a new solution for the surface-volume interaction term was proposed. This solution is based on the assumption that the soil surface is perfectly rough instead of assuming a perfectly flat soil surface which leads to the interaction term given in (5.2). Unfortunately, the proposed formulation of the interaction term contains a multiplier that depends on the exact form of the ground scattering phase and the phase function of the vegetation canopy, which are unknown. Therefore this multiplier could only be determined empirically, which is why it cannot be said if it is physically meaningful or not. However, the new term is used to improve the agreement of model simulations with observations. Only for incidence angles greater than 40° and wet soil conditions it contributes more than 1 dB to total backscatter.

$$\sigma^0 = (1 - A_{nt}) \cdot \sigma^0_{tr} + A_{nt} \cdot \sigma^0_{nt}$$

$$\sigma^0_{nt} = \frac{\omega_{nt} \cos\theta}{2}$$

$$\sigma^0_{tr} = \frac{\omega_{tr} \cos\theta}{2}(1 - e^{-\frac{2\tau_{tr}}{\cos\theta}}) + \sigma^0_s(\theta) e^{-\frac{2\tau_{tr}}{\cos\theta}} + 2\chi\Gamma_0\omega_{tr}\tau_{tr}e^{-\frac{2\tau_{tr}}{\cos\theta}}$$

$$\sigma^0_s = \sigma^0_{s,dry}(40) + \sigma'_s \cdot (\theta - 40) + S_s m_s \quad \text{in dB}$$

| Symbol | Name | Unit | Range of Values | Value used in Simulation |
|---|---|---|---|---|
| $\sigma^0$ | ERS Scatterometer backscattering coefficient | $m^2m^{-2}$ | | |
| $\sigma^0_{nt}$ | $\sigma^0$ of non-transparent vegetation | $m^2m^{-2}$ | | |
| $\sigma^0_{tr}$ | $\sigma^0$ of translucent vegetation | $m^2m^{-2}$ | | |
| $A_{nt}$ | *Percentage area* of non-transparent vegetation | - | 0 – 1<br>(0 – 100 %) | 0 – 1<br>(0 – 100 %) |
| $\theta$ | Incidence angle | deg | 18 – 59 | 18 – 59 |
| $\omega_{nt}$ | Single scattering albedo of non-transparent vegetation | - | 0.38 – 0.48 | 0.45 |
| $\omega_{tr}$ | Single scattering albedo of translucent vegetation:<br>*Winter* (dormant vegetation)<br>*Summer* (fully grown vegetation canopy) | - | <br>0.05 – 0.1<br>0.05 – 0.3 | <br>0.06<br>0.1 |
| $\tau_{tr}$ | Optical depth of translucent vegetation:<br>*Winter* (dormant vegetation)<br>*Summer* (fully grown vegetation canopy) | Np | <br>0.05 – 0.15<br>0.05 – 2 | <br>0.1<br>0.3 |
| $\chi$ | Empirical multiplier | - | | 3 |
| $\Gamma_0$ | Fresnel power reflectivity at nadir | - | 0.05 – 0.5 | 0.05 – 0.5 |
| $\sigma^0_s$ | $\sigma^0$ of soil surface | dB | | |
| $\sigma^0_{s,dry}(40)$ | $\sigma^0_s$ of a dry soil surface at $\theta = 40°$ | dB | -18 – -16 | -16 |
| $\sigma'_s$ | Slope of $\sigma^0_s(\theta)$ at $\theta = 40°$ | dB/deg | -0.3 – -0.4 | -0.36 |
| $S_s$ | Sensitivity of $\sigma^0_s$ to changes in the surface soil moisture content | dB | 7 – 8 | 7 |
| $m_s$ | Degree of saturation of soil surface layer<br>*Dry* conditions<br>*Wet* conditions | - | 0 – 1 | <br>0<br>1 |

*Table 5-1: Backscattering model for ERS Scatterometer data over vegetated land surfaces from Wagner (1998). The forth column shows the estimated range of possible values based on a literature review and a comparison with ERS Scatterometer measurements over the Canadian Prairies, the Iberian Peninsula, and tropical rain forest. The last column shows the values used in simulation.*

Figure 5-3 shows how $\sigma^0(\theta)$ varies according to the model from grassland to densely forested areas (increase of $A_{nt}$), from dry to wet soil conditions (increase of soil moisture), and from winter to summer (decrease of the optical depth of translucent vegetation types). The following trends are evident in the model simulations:

- With increasing percentage area of non-transparent vegetation $A_{nt}$ the backscattering coefficient in general increases, the slope of the curve $\sigma^0(\theta)$ becomes less steep, and the difference of $\sigma^0$ for wet and dry soil conditions decreases.
- Except for complete coverage by non-transparent vegetation types, $\sigma^0$ increases with increasing soil moisture.
- The growth of translucent vegetation types such as grasses or agricultural crops results in a less steep decline of $\sigma^0$ with the incidence angle, and may increase or decrease $\sigma^0$ depending on the incidence angle and soil wetness.

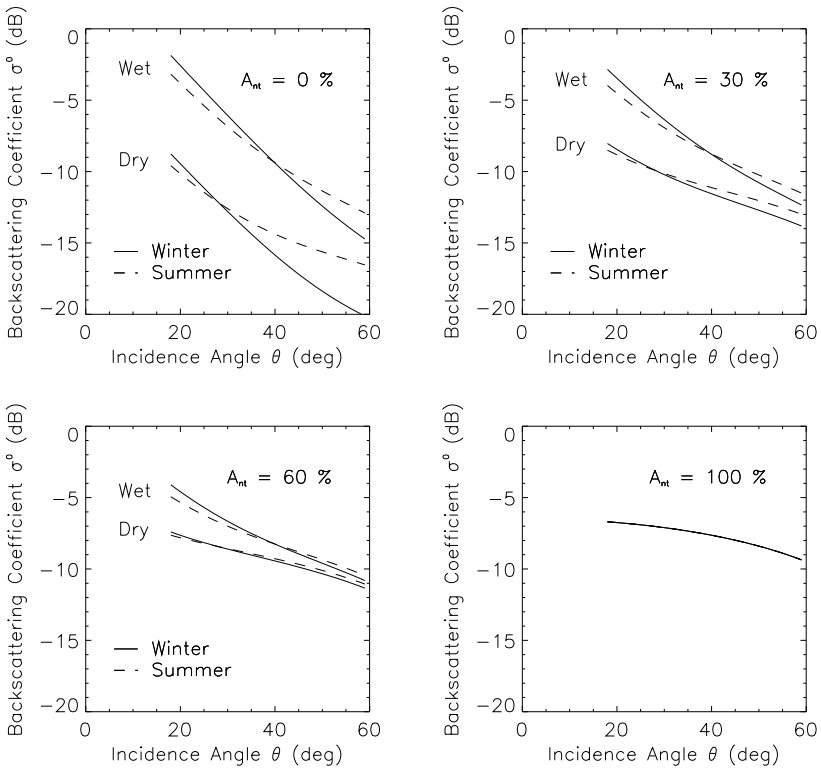


*Figure 5-3: Simulated backscattering coefficient for increasing percentage area of non-transparent vegetation $A_{nt}$ within one ERS Scatterometer pixel, and for dry/wet soil conditions and winter/summer conditions. The model and parameters used for the simulation are given in Table 5-1.*

## 5.3. Backscatter from Dry and Wet Snow

Dry snow is a horizontally stratified medium which can be thought of consisting of ice particles of various shapes embedded in air. Although the grain clusters in coarse spring snow can exceed 5 mm in radius, snow grain radii normally vary between 50 μm and 1000 μm representing a range from new snow to spring snow (Dozier, 1989). The scattering efficiency of snow grains is proportional to the third power of the ice grain radii (Mätzler, 1986). Therefore the largest grains are responsible for most of the cross section. When two snow layers are considered the layer with the largest particles determines $\sigma^0$ (West et al., 1993). At C-band dry snow is highly transparent (Rott, 1993; Mätzler and Schanda, 1984) because of the small scattering efficiency and negligible absorption capacity of the snow grains at this frequency. A study of ERS Scatterometer data over the Canadian Prairies has shown that a dry shallow snow pack overlying a bare soil is almost identical to $\sigma^0$ of the snow free situation (Wagner, 1995; Wagner et al., 1995).

If liquid water is present in the snow layer then absorption increases by orders of magnitude and dominates all other snow-microwave interactions. According to Weise (1996) a water layer with a column height as small as 0.001 mm is detectable. The radar return of a wet snow layer is thus dominated by scattering of the air-snow boundary. If the snow surface is smooth then $\sigma^0$ of a wet snow surface may be lower than $\sigma^0$ of bare soil (Rott and Nagler, 1993 and 1994; Kosokowsky et al., 1993). If, however, the surface is very rough then $\sigma^0$ of wet snow is comparable to $\sigma^0$ of bare soil and it is not possible anymore to detect the presence of wet snow. For example, it was not possible to identify wet snow in the Canadian Prairies with the ERS Scatterometer (Wagner, 1995; Wagner et al., 1995). The reason is thought to be that the generally shallow snow pack exhibits a rough surface because it follows the underlying ground and dormant vegetation.

## 5.4. Backscatter from Water Surfaces

The penetration depth of C-band microwaves into water is less than about 2 mm and therefore, as is the case for bare soil and wet snow, $\sigma^0$ of water is dependent on the roughness of the surface. When the water surface is calm then specular reflection occurs and $\sigma^0$ at off-nadir angles is very low. Wind generates water waves that increase scattering into the backward direction. The main contributions do not come from large ocean waves, even if they are many meters in height. Rather, scattering is dominated by short waves that ride on the top of the larger waves (Ulaby et al., 1982). The radar return is highest when the radar looks into the upwind or downwind direction and is smallest when it looks normal to the wind vector. Therefore $\sigma^0$ of water surfaces depends on the azimuthal look direction. These dependencies allow to estimate the direction and speed of wind from the backscatter triplet measured with the ERS Scatterometer.

## 5.5. Scale Issues

In a wide spectrum of environmental disciplines like hydrology, meteorology, and ecology 'scale issues' have been recognised to be of great importance (Blöschl, 1996; Blöschl and Sivapalan, 1995; Assivar, 1995; Raupach and Finnigan, 1995). The term 'scale' refers to a characteristic time or characteristic length. The problem at hand is that different physical processes tend to dominate at different scale levels ('process scale') which is why the extrapolation of models that have been formulated at a given scale to other scales is not always meaningful (Klemeš, 1983). One example from hydrology is flow of water in soils which is dominated at small scales (1 $dm^2$) by soil matrix flow, while at larger scales (1 $km^2$) preferential flow in macropores may become important (Blöschl, 1996). Another problem is that natural processes, models that are describing these processes, and measurements used as input into these models may all have different characteristic scales. In other words, the 'model scale' and the 'measurement scale' might not be compatible with the 'process scale' which would lead to a mediocre representation of the physical process.

'Scale issues' are also of great importance for the interpretation of ERS Scatterometer data. Our present understanding of backscattering phenomena stems to a large extent from the study of ground based measurements (Ulaby et al., 1981). This knowledge is often directly applicable to the interpretation of SAR imagery because the spatial resolution of SAR systems is comparable to the footprint size of ground based scatterometers. However, the spatial resolution of the ERS Scatterometer is on the order of tens of kilometres and it is by no means obvious what are the dominating processes at this scale? It is clear that only processes that act on scales comparable to the measurement scale and/or which generate features that are present within extended areas of the resolution cell of the ERS Scatterometer are important. Unfortunately, the identification of important processes is not always easy. For example, let us consider ERS Scatterometer measurements of a dry shallow snow pack in the Canadian Prairies that are discussed in Wagner (1995). Although in some situations ice crusts, which should increase $\sigma^0$, were known to be present in the snow pack, no such effects were visible in the ERS Scatterometer data. The most likely explanation is that ice crust formed only in a small part of the area. Or let us consider the action of strong wind that bends the stalks and branches of vegetation. On a field scale, $\sigma^0$ may change by several dB (Ulaby et al., 1986; Brisco et al., 1993), but is it also reasonable to assume that wind can change the average backscattering coefficient of a 50 x 50 $km^2$ large region?

The literature review has shown that over land surfaces the main geophysical parameters influencing the backscattered signal are soil moisture, surface roughness, and vegetation. Various processes that act on different space and time scales control these parameters. Therefore they exhibit a high degree of variability over a large range of scales. If the processes that are important at the measurement scale can be identified then it would become clearer what the terms 'soil moisture', 'surface roughness', and 'vegetation' actually mean in our context.

## 5.6. Spatial and Temporal Variability of Soil and Vegetation Parameters

### 5.6.1. Soil Moisture

Water is constantly added and withdrawn from the soil water reservoir. The main processes affecting the water balance are precipitation, surface runoff, evaporation from the soil surface, transpiration by the plants, vertical and lateral flow, and snowmelt (Hillel, 1980). Due to the dynamic nature of these processes, soil moisture is highly variable in space and time (Saddiq et al., 1985; Schmugge and Jackson, 1996, Western et al., 1998).

***Temporal Patterns***

Delworth and Manabe (1988) studied the temporal variability of model computed moisture content in the soil profile to understand the physical mechanisms controlling the time scales of this variability. They viewed anomalies in soil moisture as a response of the soil layer to short time-scale rainfall forcing damped by evapotranspiration. Rainfall has a spectrum close to white, i.e. it can be represented by a purely random stochastic process. They described the profile soil moisture content $W$ by a random process with:

$$\frac{dW}{dt} = -\frac{1}{T}W(t) + z(t), \tag{5.4}$$

where $t$ is the time, and $T$ is a constant. $z(t)$ is white noise that accounts for rainfall and runoff. The autocorrelation function $\rho(\tau)$ of this process is:

$$\rho(\tau) = e^{-\frac{\tau}{T}}, \tag{5.5}$$

where $\tau$ is the time lag, and $T$ is the scale of this variability. Delworth and Manabe (1988) also showed that

$$T \approx \frac{FC}{ET_0}, \tag{5.6}$$

where $FC$ is the field capacity of the soil and $ET_0$ is the potential evapotranspiration. In words, the temporal variability of soil moisture is controlled by the capacity of soil to store water and by the evaporative demand. Hence, soil moisture varies more slowly at high latitudes where the energy available for evapotranspiration is small. This hypothesis was empirically confirmed by Vinnikov and Yeserkepova (1991) who analysed 1 m soil moisture data from sites with natural vegetation in the Soviet Union. Vinnikov et al. (1996) found that $T$ of this soil layer is approximately three months at midlatitudes.

The degree of variability depends on the depth of the considered soil layer. Especially the top few centimetres of the soil, which are accessible to C-band microwaves, exhibit a high degree of variability because this is the active layer for evaporation. Evaporation is influenced by the level of irradiance, wind speed, air temperature, soil infiltration capacity, and leaf area of the vegetation canopy (Keulen and Seligman, 1992). For high levels of evaporation, such as in a savanna region, the surface soil moisture content is highly variable on time scales of less than one day, and rainfall events have a persistence at the surface up to only about three to five days (Wallace et al., 1993; Whitelaw and Howes, 1995; Braud, 1998). It can be concluded that due to the high temporal variability of the moisture content in the topsoil layer a large day to day variability should be observed in the ERS Scatterometer data.

***Spatial Patterns***

Let us now consider spatial patterns of the soil moisture field. On scales from centimetres to tens of meters, the variability of soil moisture is high due to the micro-topography and variations in soil properties at the meter scale which influence the vertical and lateral redistribution. At larger scales from meters to tens of kilometres differences in soil, vegetation, geology, and topography account for

variations in surface runoff, evapotranspiration, and consequently soil moisture. At even larger scales up to hundreds of kilometres, soil moisture patterns are related to the atmospheric conditions, i.e. the characteristics of precipitation, temperature, solar radiation, and atmospheric moisture. According to Vinnikov et al. (in press) the spatial autocorrelation function of the soil moisture content $W$ may be expressed as:

$$\rho(d) = \eta e^{-\frac{d}{L_s}} + (1-\eta) e^{-\frac{d}{L_a}}, \tag{5.7}$$

$$\eta = \frac{\sigma_s^2}{\sigma_s^2 + \sigma_a^2} \tag{5.8}$$

where
$d$ = distance
$L_s$ = scale of the land-surface related variability
$L_a$ = scale of the atmosphere related variability
$\sigma_s^2$ = variance of land-surface related variability
$\sigma_a^2$ = variance of atmosphere related variability

Based on field measurements in Illinois, USA, Vinnikov et al. (in press) found for the soil moisture field in this region: $\eta$ = 0.3–0.35, $L_a$ = 380–490 km for the top 10 cm soil layer, and $\eta$ = 0.3–0.35, $L_a$ = 510–670 km for the top 1 m soil layer. Also for Russia, $L_a$ of the first meter was found to be about 500 km (Vinnikov et al., 1996). For low-latitude regions $L_a$ may be less due to higher potential evapotranspiration and different weather systems. The scale of the land-surface related component $L_s$ will depend on the regional characteristics, but will always be much smaller than the scale of the atmospheric-forcing related component $L_a$.

The measurement process averages over the resolution cell and therefore high frequency components of the soil moisture field are filtered out. The measurement process can be described by following one-dimensional integral:

$$\overline{W}(x) = \frac{1}{l} \int_{x-\frac{l}{2}}^{x+\frac{l}{2}} W(x')dx'', \tag{5.9}$$

where $\overline{W}$ is the soil moisture content at the position $x$ averaged over the resolution cell of width $l$. Under the assumption of a stationary soil moisture field, the variance of $\overline{W}$ is independent of $x$ and is given by:

$$Var(\overline{W}) = E\{\overline{W}^2\} - E\{\overline{W}\}E\{\overline{W}\}, \tag{5.10}$$

where $E$ is the expectation. Substituting Equation (5.9) into (5.10) gives:

$$Var(\overline{W}) = E\left\{\frac{1}{l^2}\int_{x-\frac{l}{2}}^{x+\frac{l}{2}} W(x')dx' \int_{x-\frac{l}{2}}^{x+\frac{l}{2}} W(x'')dx''\right\} - E\left\{\frac{1}{l}\int_{x-\frac{l}{2}}^{x+\frac{l}{2}} W(x')dx'\right\} E\left\{\frac{1}{l}\int_{x-\frac{l}{2}}^{x+\frac{l}{2}} W(x'')dx''\right\} \tag{5.11}$$

Exchanging the order of the integral sign and the expectation symbol (Journel and Huijbregts, 1978), and rearranging the integrals yields:

$$Var(\overline{W}) = \frac{1}{l^2}\int_{x-\frac{l}{2}}^{x+\frac{l}{2}} dx' \int_{x-\frac{l}{2}}^{x+\frac{l}{2}} dx''\left[E\{W(x')W(x'')\} - E\{W(x')\}E\{W(x'')\}\right]. \tag{5.12}$$

Recognising that the term in the angle brackets is the covariance, a relationship between the variance $\overline{W}$ and the autocorrelation function $\rho$ has been established (Journel and Huijbregts, 1978):

$$Var\left(\overline{W}\right) = \frac{\sigma_s^2 + \sigma_a^2}{l^2} \int_{x-\frac{l}{2}}^{x+\frac{l}{2}} dx' \int_{x-\frac{l}{2}}^{x-\frac{l}{2}} dx'' \rho\left(\left|x' - x''\right|\right) , \tag{5.13}$$

where $|x' - x''|$ is the absolute distance between the points $x'$ and $x''$. Substituting Equation (5.7) into (5.13), and carrying out the integration gives:

$$\frac{Var\left(\overline{W}\right)}{\sigma_s^2 + \sigma_a^2} = \eta \cdot \left[ \frac{2L_s}{l} - \frac{2L_s^2}{l^2} \left( 1 - e^{-\frac{l}{L_s}} \right) \right] + (1-\eta) \cdot \left[ \frac{2L_a}{l} - \frac{2L_a^2}{l^2} \left( 1 - e^{-\frac{l}{L_a}} \right) \right]. \tag{5.14}$$

The term

$$\frac{Var\left(\overline{W}\right)}{\sigma_s^2 + \sigma_a^2} = \frac{Var\left(\overline{W}\right)}{Var\left(W\right)} \tag{5.15}$$

is the ratio of the variance of the original soil moisture field *W* and the variance of the measured quantity $\overline{W}$ . It is a measure for the loss of information in the measurement process. The first term on the right hand side of Equation (5.14) describes the loss of information on the land-surface related variability of *W* with increasing size of the resolution cell *l*, and the second term the loss of information about the atmospheric-forcing related component.

Figure 5-4 shows the result for a variable size of the resolution cell for assumed values $\eta$ = 0.3, $L_s$ = 1 km, and $L_a$ = 500 km. Although these parameters differ for different regions, it can nevertheless be concluded that at an observation scale of 50 km the small-scale land-surface related variability of *W* is effectively suppressed. On the other hand, the large-scale atmospheric-forcing related variability is preserved, i.e. this is the component of the soil moisture field that is recorded by the ERS Scatterometer.

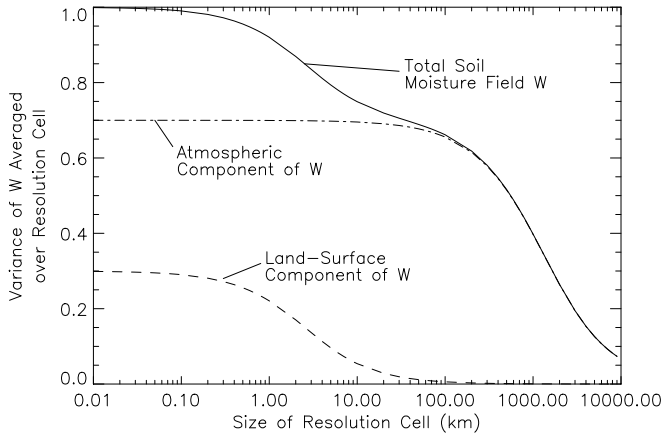


*Figure 5-4: Reduction of the variance of the soil moisture field W according to Equation (5.14). Assumed values are $\eta$ = 0.3, $L_s$ = 1 km, and $L_a$ = 500 km.*

These considerations are also of importance for the design of future sensors, because they suggest that any sensor with a spatial resolution between about 5 and 50 km will effectively suppress the land-surface related component of *W*, while providing comparable information about the atmospheric-forcing related component. To obtain a good picture of the small-scale land-surface related variability of the soil moisture field the footprint size should not be larger than 1 km.

### 5.6.2. Surface Roughness

Backscatter from bare soil surfaces is sensitive to surface height variations on scales comparable to the wavelength of the radar system. The term surface roughness therefore refers to the microrelief of the soil surface representing a scale range from millimetres to decimetres. The surface height may vary

considerably over short distances and within fields parameters describing surface roughness show little spatial dependency (Lehrsch et al., 1988a).

The processes by which soils are formed are known as pedogenic processes, including additions, transformations, transfers, and losses (Ellis and Mellor, 1995). The factors controlling these processes encompass climate, organisms, relief, parent material, and time. The structure (e.g. horizon differentiation) and the composition (e.g. texture, organic matter content) of soils are determined by these pedogenic processes, and hence also surface roughness. For example, poorly developed soils with frequent rock outcrops and gravel surface such as lithosols can be expected to have a rougher soil surface in terms of radar backscatter than highly developed soils. Consequently, on larger scales surface roughness patterns should reflect differences in climate, vegetation, relief, and parent material.

Soil formation processes usually act on time scales from decades to several thousands of years (Wild, 1993) and therefore, for the short time span considered in this investigation, surface roughness should be expected to be a relatively stable factor over time. Nevertheless, on relatively short time scales surface roughness characteristics may be changed by human activities like tillage of agricultural fields. Subsequent rainfall may smooth the so disturbed surface (Lehrsch et al., 1987 and 1988b). However, it is questionable if such changes occur over large enough areas to be detectable with the ERS Scatterometer. Consider the following example: Let the area within the resolution cell of the ERS Scatterometer be divided by half in grassland and agricultural fields. Before harvest the average backscatter from the grassland area is -16 dB and $\sigma^0$ of the agricultural area is -13 dB. During harvest about 20 % of the fields are ploughed which doubles backscatter from these fields to -10 dB. The soil moisture content is assumed to be the same before and after harvest. Before harvest $\sigma^0$ of the ERS Scatterometer is -14.3 dB and after harvest -13.7 dB. Although the assumed changes are rather on the high side the difference in $\sigma^0$ before and after harvest is only about 0.6 dB. It can be assumed that in reality variations due to changes in the microrelief are even smaller. For these reasons it will be assumed that temporal changes in the backscattering characteristics are solely due to changes in soil moisture and vegetation, keeping in mind that in some situations this assumption may not be strictly valid.

### 5.6.3. Vegetation Structure

The structure of vegetation strongly influences the scattering characteristics from vegetated terrain. Depending on the “distance” of the observer different levels of homogeneity become apparent (Klijn et al., 1995) resulting in different schemes of vegetation classification. On a global scale it is distinguished between biomes which are named for their dominant vegetation (Christopherson, 1997): forest, savannah, grassland, shrubland, desert, and tundra. The distribution of these major vegetation types largely reflects the global patterns of precipitation and temperature (Perry, 1994). “Zooming” into a more local scale the distribution of plant communities becomes a function of soils, landforms, and historical factors, and the number of vegetation classes increases. At the smallest possible scale, i.e. at the level of an individual plant, the structural complexity of vegetation is expressed by 270,000 plant species. Based on the general form and structure of the plants, it is distinguished on the highest level between trees, shrubs, herbs, and other life forms such as lianas (woody climbers and vines) or bryophytes (nonflowering, spore-producing plants including e.g. mosses) (Strahler and Strahler, 1996). Trees have a large woody main trunk and usually exceed three meters in height. Shrubs are smaller woody plants that have several stems branching from the base near the soil surface. Herbs are small plants without woody stems and as a group embrace grasses and other non-woody vascular plants.

For explaining the spatial variability of ERS Scatterometer data, the distribution of plant communities within one pixel needs to be considered. As reference vegetation map the CORINE land cover was chosen which has an appropriate scale (1:100,000) for studying subpixel effects.

### 5.6.4. Water Content of Vegetation

Plants are living entities that need water to sustain their living functions. According to Perry (1994, after Bradford and Hsiao, 1982) plants must maintain at least 75 % water content in functional cells. This is accomplished by three basic means: absorption, transpiration, and internal redistribution of water (Kozlowski, 1968). During dry periods, when water uptake cannot keep up with losses, plants close their stomates with a consequent reduction in $CO_2$ uptake. The closure of the stomata may be triggered by chemical signals of the plant roots which means that the soil water status may be more important than leaf water to control this process (Perry, 1994, after Schulze et al., 1987). Under normal conditions, the water status of plants should therefore be relatively stable. Kim et al. (1989) reported that the leaf water potential of cereal crops did not decrease below a critical value under sufficient water supply. Böhner (1996) conducted dielectric measurements of a beech for 48 hours and found some diurnal variations in $\varepsilon$ of the stem, but $\varepsilon$ of the tree leaves was more or less constant.

When plants experience water stress for longer time periods, the leaf tissues dehydrate (Keulen and Seligman, 1992) and backscatter decreases. The effects of changing soil moisture and vegetation moisture content on the backscattering signal can nevertheless be distinguished because of the different time scales involved. While the surface moisture content varies on scales of less than one day, the vegetation moisture content varies on much longer scales because it is coupled to the water content of the root zone, and because of the ability of plants to counteract for some time the effects of water stress.

# 6. Normalisation of ERS Scatterometer Data

## *6.1. Introduction*

The discussion so far has shown that the main parameters affecting the backscattering coefficient $\sigma^0$ of vegetated surfaces are the moisture content of the soil surface, the roughness of the soil surface, and the structure and water content of the vegetation. These parameters act on different time scales: surface soil moisture on scales of one day or less, vegetation on scales from several days to weeks, and surface roughness should in general be stable. The spatial variability of the ERS Scatterometer recorded $\sigma^0$ should reflect the atmospheric-forcing related soil moisture signal and the local variability of vegetation and surface roughness related to differences in soils, topography, and land use.

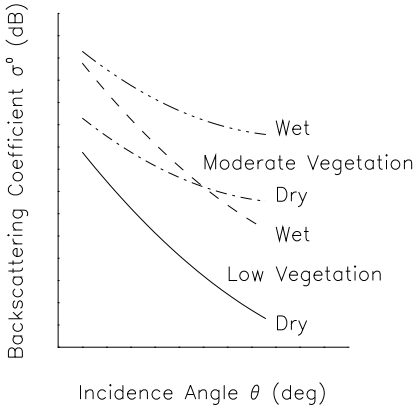


*Figure 6-1: Characteristic angular dependence of the backscattering coefficient of vegetated surfaces for different moisture conditions. See also Figure 5-3.*

The problem when dealing with ERS Scatterometer data is that $\sigma^0$ depends also strongly on the incidence angle $\theta$. Figure 6-1 gives an overview of the principle backscattering behaviour of vegetated terrain (Chapter 5.2). Increasing soil moisture and vegetation biomass tend to increase $\sigma^0(\theta)$. The incidence angle of the ERS Scatterometer varies from acquisition to acquisition and therefore it is not possible to compare consecutive $\sigma^0$ measurements. To overcome this problems the methodology most often used has been to fit simple models to $\sigma^0$ measurements acquired over longer time periods, normally one month (Wiesmann, 1994; Mougin et al., 1995; Wismann et al., 1996a; Frison and Mougin, 1996a). Messeh and Quegan (1997) investigated the goodness of the fit of such models and found that in general only about 50 % of the variability is explained. Over tropical forest where $\sigma^0$ is rather stable the model could explain up to 79 %. The problem with this approach is that soil moisture and vegetation cover effects on the signal cannot be distinguished afterwards.

The approach taken here is similar in the sense that a simple model is fitted to ERS Scatterometer observations to account for varying incidence angles. However, instead of averaging $\sigma^0$, a model is fitted to the slope $\sigma'(\theta)$ which is defined:

$$\sigma'(\theta) = \frac{d\sigma^0(\theta)}{d\theta}. \qquad (6.1)$$

The advantage is that, other than $\sigma^0$, the slope is not or only little affected by the higly variable surface soil moisture content (Chapter 6.3.4). Knowing the incidence angle behaviour of $\sigma^0$, ERS Scatterometer measurements can be extrapolated to a reference angle which is chosen to be 40° (Chapter 6.4.1). As a result, the normalised backscattering coefficient $\sigma^0(40)$ is obtained which retains information on the vegetation and soil state.

The ERS Scatterometer measures the backscattering coefficient from three different azimuthal angles and two different incidence angles. These multiple viewing capabilities are used in the three-step analysis of the ERS Scatterometer data. In each step different antenna combinations are employed

(Figure 6-2). In the first step (Chapter 6.2) the azimuthal dependence of $\sigma^0$ is analysed using the fore and aft beam antennas. Land surfaces are found to be slightly anisotropic with respect to the azimuth angle. It is proposed to consider the azimuthal anisotropy as an additional error source to $\sigma^0$, and a model is developed to estimate the standard error $ESD(\sigma^0)$ due to instrument noise, speckle, and azimuthal effects. In the second step (Chapter 6.3) the incidence angle behaviour is studied by calculating the slope $\sigma'$ using the combinations mid and fore receptively mid and aft beam antennas. In the last step the normalised backscattering coefficient $\sigma^0(40)$ is obtained using the average of all three beams (Chapter 6.4).

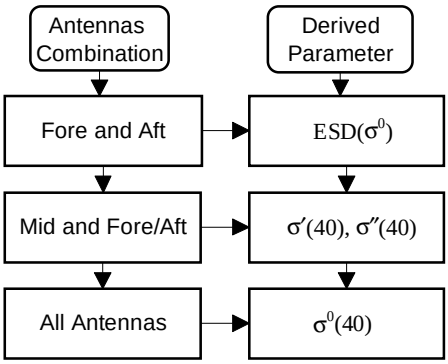


*Figure 6-2: Flow chart of processing steps for the analysis of ERS Scatterometer data. In the processing four parameters are obtained: The estimated standard deviation of $\sigma^0$, $ESD(\sigma^0)$, the slope $\sigma'(40)$ and the curvature $\sigma''(40)$, and the normalised backscattering coefficient $\sigma^0(40)$.*

## *6.2. Azimuthal Anisotropy and Noise Model*

### 6.2.1. Azimuthal Anisotropy

Backscatter from water surfaces and ice sheets depends on the azimuthal look direction. In the case of water the orientation of the water ripples with respect to the look direction of the sensor is important, and in the case of ice the morphology of the surface and the top few meters of the snow and ice volume (Rott et al., 1993). On a field scale backscatter from vegetation might also exhibit an azimuthal dependence, but on larger scales these effects should not be important. Nevertheless, slight azimuthal effects have been observed in the ERS Scatterometer data also over land surfaces (Wismann and Boehnke, 1994). To investigate these effects in more detail, the data acquired with the forward and backward looking antennas are analysed. These two antennas look at the surface with the same incidence angle, but from two different azimuth angles. Let us denote the backscattering coefficients acquired with the fore and the aft beam antennas with $\sigma^0_{fore}$ and $\sigma^0_{aft}$ respectively and let us take their difference:

$$\delta = \sigma^0_{fore} - \sigma^0_{aft} . \qquad (6.2)$$

Since $\sigma^0_{fore}$ and $\sigma^0_{aft}$ are measured at the same incidence angle the difference $\delta$ depends on the noise level of individual $\sigma^0$ measurements and on the azimuthal dependence of $\sigma^0$, but not on the backscattering characteristics of the target (Early and Long, 1997). If a large number of measurement pairs $\sigma^0_{fore}$ and $\sigma^0_{aft}$ are available then the noise can be averaged out and the resulting mean value of $\delta$ shows the magnitude of azimuthal effects. Colour Figure 1 shows the average value of $\delta$ for ascending passes based on data from the period September 1991 to May 1996 over the Iberian Peninsula. The map of $\delta$ is laid over the digital elevation model (DEM) of the Iberian Peninsula. In the view of Colour Figure 1 the look direction of the fore beam antenna is approximately perpendicular to the plane of the page (south-west to north-east), and the look direction of the aft-beam antenna is approximately in the plane of the page from the left to the right (north-west to south-east). It can be observed that $\delta$ is positive over southward facing slopes where the local incidence angle of the forward looking antenna is smaller than the incidence angle of the backward looking antenna. The difference is positive because $\sigma^0$

decreases in general with the incidence angle and thus $\sigma^0_{fore}$ is larger than $\sigma^0_{aft}$. Over northward facing slopes the reverse is true. This shows that azimuthal effects as observed with the ERS Scatterometer are to a large extent incidence angle effects. Over the Iberian Peninsula the highest values of $\delta$ are around 0.4 dB, which is generally the case. In certain instances, such as close to large water bodies or in the Canadian Prairies, $\delta$ may exceed 0.6 dB.

### 6.2.2. Estimated Standard Deviation of the Backscattering Coefficient

Over land the variation of $\sigma^0$ with the azimuth angle does not convey important information and thus one may treat these rather modest variations as noise and the azimuth angle as "unknown". Let us assume that in the logarithmic range $\sigma^0_{fore}$ and $\sigma^0_{aft}$ are normally distributed variables with equal means and with a standard deviation $SD(\sigma^0)$ (Early and Long, 1997). The means of $\sigma^0_{fore}$ and $\sigma^0_{aft}$ are determined by target characteristics and the standard deviation is due to all possible noise sources. The most important noise sources are speckle and instrument noise (Wuttge and Munz, 1995) and, in the present model, azimuthal effects. If we blindly take the difference $\sigma^0_{fore}$-$\sigma^0_{aft}$ or $\sigma^0_{aft}$-$\sigma^0_{fore}$ from both ascending and descending passes then we simulate the impact of an "unknown" azimuth angle on $\sigma^0$. The standard deviation of the resulting values that are stored in the random variable $\vartheta$ is

$$SD(\vartheta) = \sqrt{2} \cdot SD(\sigma^0) \tag{6.3}$$

because the variance of a linear combination of mutually independent, normally distributed variables is the sum of their variances (Johnson and Leone, 1978). The observation that $\vartheta$ is normally distributed in the logarithmic range is the justification for the assumption that $\sigma^0_{fore}$ and $\sigma^0_{aft}$ are normally distributed (Figure 6-3).

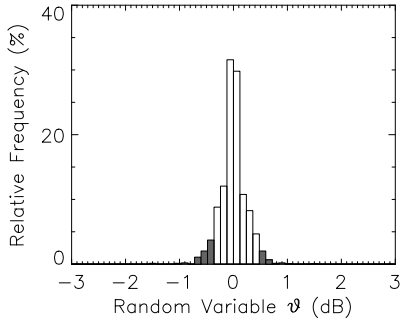


*Figure 6-3: Histogram of the random variable $\vartheta$ which has been calculated by first calculating the difference $\delta = \sigma^0_{fore}$-$\sigma^0_{aft}$ for both ascending and descending passes and then multiplying $\delta$ with +1 or -1 in a random fashion. Data for this example were taken from Beja, southern Portugal.*

Since, in reality, the azimuth angle is not random but is determined by the orbit characteristics of the ERS satellites, Equation (6.3) is not entirely correct. To express this fact we call the derived value for the standard deviation of $\sigma^0$ the *estimated* standard deviation, $ESD(\sigma^0)$:

$$ESD(\sigma^0) = \frac{SD(\vartheta)}{\sqrt{2}} \tag{6.4}$$

It should be stressed that $ESD(\sigma^0)$ is only an estimate of the real standard deviation of $\sigma^0$. One reason already mentioned is that the fore and aft beam antennas illuminate one point on the earth's surface only from four different directions. Other reasons are: The fore and aft beam antennas do not illuminate exactly the same area because of different antenna patterns on the ground. Geolocation errors may occur because of uncertainties in the spacecraft orbital characteristics and because the pixel location algorithm uses a reference spheroid to represent the Earth's surface. Interbeam calibration inaccuracies contribute to the standard deviation. These effects add to those contributions of the standard deviation of $\sigma^0$ resulting from instrument noise, speckle, and azimuthal effects.

Nevertheless, $ESD(\sigma^0)$ is useful to explain site to site differences and to estimate the worst case error of parameters derived from the ERS Scatterometer data. In Colour Figure 2, the overlay of $ESD(\sigma^0)$ over

the DEM of the Iberian Peninsula is shown. About half of the values of $ESD(\sigma^0)$, which can mainly be found in more gently sloping terrain, are in the range 0.15 - 0.2 dB and the other half is above 0.2 dB with the highest values found in the Pyrenees. In general, $ESD(\sigma^0)$ is found to be smaller than 0.4 dB. Higher values are observed over the Canadian test site, where $ESD(\sigma^0)$ ranges between 0.2 to 0.4 dB in the boreal forest zone, between 0.35 and 0.6 dB in the prairies, and may be as high as 0.8 dB in the Rocky mountains.

### 6.2.3. Influence of Land Cover on the Noise Level

The noise level $ESD(\sigma^0)$ is not only related to large-scale terrain features but also to land cover. For example, $ESD(\sigma^0)$ is in general smaller over forested areas than over regions with low vegetation cover. This is because azimuthal effects are mainly incidence angle effects and consequently $ESD(\sigma^0)$ is lower over forested areas where $\sigma^0$ shows less dependence on the incidence angle than over grass- and agricultural land. Also, $ESD(\sigma^0)$ is observed to be high over areas with large water bodies. To investigate the dependency of $ESD(\sigma^0)$ on land cover, a multiple correlation analysis between $ESD(\sigma^0)$ and the area occupied by CORINE land cover classes is conducted for the Iberian Peninsula. For the present analysis a subset of the original 44 CORINE land cover classes was taken and grouped into only four classes: artificial surfaces including urban areas and other build-up areas, inland waters, open spaces with little or no vegetation, and low vegetation including agricultural- and grassland (Table 6-1).

| Classes | CORINE class | % of total area of the Iberian Peninsula |
|---|---|---|
| Artificial surfaces (%) | 1. | 1.3 |
| Inland waters (%) | 5.1. | 1.3 |
| Open spaces with little or no vegetation | 3.3 | 6.7 |
| Arable land and natural grassland | 2.1.1 + 3.2.1 | 24.6 |

*Table 6-1: CORINE classes used for multiple regression analysis between the percent area occupied by these classes and $ESD(\sigma^0)$.*

The area occupied by each of these classes was determined by drawing a circle with a radius of 30 km around each centre point of a 0.25° grid to which ERS Scatterometer data were interpolated. Then the area of all the inside polygons belonging to one class was summed up. The circle area roughly corresponds to the spatial resolution of the ERS Scatterometer data interpolated to the grid. As a result the area of the four classes expressed in percent of the area of the resolution cell is obtained. To make inferences about the dependency of $ESD(\sigma^0)$ on these four classes a multiple regression together with a one-sided *t*-test for each regressor is performed. The multiple coefficient of determination is low ($R^2$ = 23 %) but significant. For all classes the null hypothesis that the regressor is equal to zero can be rejected with high confidence, at the $\alpha$ = 0.5 % level for the "inland water" class and at the $\alpha$ = 0.05 % level for the other three classes. It can be concluded:

1. Most of the variation of $ESD(\sigma^0)$ is caused by terrain effects, but also land cover shows some influence.
2. The magnitude of azimuthal effects depends on how fast $\sigma^0$ decreases with the incidence angle because azimuthal effects are mainly incidence angle effects. Since $\sigma^0$ decreases quickly with the incidence angle over sparsely vegetated areas $ESD(\sigma^0)$ tends to be higher over areas with sparse to low vegetation cover than over forested regions.
3. The noise level increases with the percentage area occupied by build-up areas and water bodies.

### 6.2.4. Estimating the Relative Instrument Stability

Because values of $ESD(\sigma^0)$ lower than 0.15 dB are observed the relative radiometric stability must be even better than that. This value is on the low side of specifications found in the literature. To investigate the noise level of ERS Scatterometer measurements it is generally assumed that backscatter from tropical forests is stable. For example, by analysing $\sigma^0$ separately for each antenna and separately for ascending and descending passes Frison and Mougin (1996a) found that $\sigma^0$ is stable with an estimated standard deviation smaller than 0.22 dB for all beams and passes. However, $\sigma^0$ of tropical forests show variations in the magnitude of 0.5 to 1 dB due to precipitation (Wismann et al., 1996b) and other environmental effects. Therefore this classical approach overestimates the relative noise level of ERS Scatterometer measurements. On the other side, environmental factors play no role in the calculation of $ESD(\sigma^0)$ thus allowing a better estimate of the standard deviation of $\sigma^0$ due to instrument noise (thermal and processing noise) and speckle. Azimuthal effects are not important over tropical forests because $\sigma^0$ decreases only slightly with the incidence angle.

In Figure 6-4 $ESD(\sigma^0)$ is shown for a tropical forest region in Africa. It can be seen that the minimum values of $ESD(\sigma^0)$, which are found over dense forest tracts, are around 0.13 dB which means that the relative radiometric stability is about 0.13 dB. Strictly speaking the conclusion is only valid for the relative and interbeam calibration of the fore and aft beam antennas, but it is assumed that it also applies to the mid beam antenna.

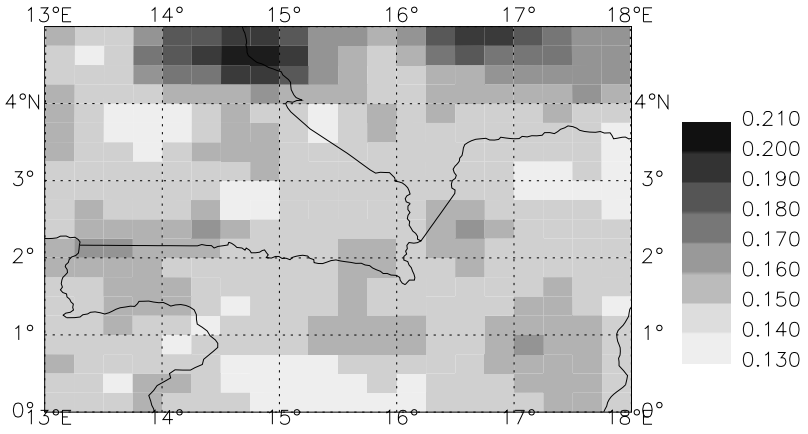


*Figure 6-4: The estimated standard deviation of $\sigma^0$, $ESD(\sigma^0)$, in dB over tropical forest in Africa (13°E-18°E, 0°N-5°N). The shown area partly covers Congo, Cameroon, Central African Republic, and Gabon. The map is based on ERS Scatterometer measurements from the year 1993.*

## *6.3. Incidence Angle Dependency*

### 6.3.1. Determination of the Slope

For each ERS Scatterometer pixel backscatter measurements are taken at two incidence angles. The difference of the incidence angles for the mid beam and the fore/aft beam varies over the swath from about 7° in the near range to about 12° in the far range. For the centre incidence angle the local slope can be estimated from each backscatter triplet:

$$\sigma'_m\left(\frac{\theta_{mid}+\theta_{f/a}}{2}\right)=\frac{\sigma^0_{mid}(\theta_{mid})-\sigma^0_{f/a}(\theta_{f/a})}{\theta_{mid}-\theta_{f/a}} \qquad \text{(dB/deg)} \qquad (6.5)$$

where the index '*mid*' stands for the mid beam antenna, and the index '*f/a*' stands for either the fore or the aft beam antenna. The index '*m*' of $\sigma'_m$ indicates that this is a *measured* quantity, which deviates from the true slope value $\sigma'_t$ by the noise $\sigma'_n$:

$$\sigma'_m = \sigma'_t + \sigma'_n . \tag{6.6}$$

The ensemble average of $\sigma'_m$ is equal to $\sigma'_t$, and its standard deviation is equal to the standard deviation of $\sigma'_n$. The noise of $\sigma'_m$ is caused by the noise of $\sigma^0$ due to instrument noise, speckle, and azimuthal effects. The azimuthal dependence is important because the azimuthal look direction is different for each antenna. The standard deviation of $\sigma'_m$ can therefore be estimated using $ESD(\sigma^0)$:

$$SD(\sigma'_m) = SD(\sigma'_n) \approx \frac{\sqrt{2}}{\theta_{mid} - \theta_{f/a}} ESD(\sigma^0) . \tag{6.7}$$

For $ESD(\sigma^0)$ = 0.3 dB and $\theta_{mid}$ - $\theta_{f/a}$ = 10° the standard error of $\sigma'_m$ is 0.04 dB/deg. This is a high value considering that the mean slope varies from about -0.27 dB/deg for sparsely to about -0.08 dB/deg for densely vegetated areas (Frison and Mougin, 1996b). Because the noise is so large and to ensure that the slope values are evenly distributed over the entire incidence angle range several dozens of data points must be used to obtain characteristic $\sigma'(\theta)$ curves. Unfortunately, the temporal sampling rate of the ERS Scatterometer is too low to obtain sufficient data points within time periods comparable to time scales characteristic for vegetation growth. Therefore, to determine characteristic $\sigma'(\theta)$ curves for a particular period of the year data from several years need to be used. In Figure 6-5 typical scatter plots of $\sigma'_m$ versus the incidence angles are shown for four months: January, April, July, and October. The data are taken from the station Zitomir in the Ukraine from the period September 1991 to November 1997. It can be observed that the $\sigma'(\theta)$ curves would probably best be reproduced by second order polynoms. However, if second order polynoms are fitted to the data unrealistic solutions occur quite frequently. Therefore $\sigma'(\theta)$ is approximated by a linear model

$$\sigma'(\theta) = \sigma'(40) + \sigma''(40) \cdot (\theta - 40) , \tag{6.8}$$

where $\sigma'(40)$ and $\sigma''(40)$ are the slope and curvature of $\sigma^0(\theta)$ at the reference angle at 40°.

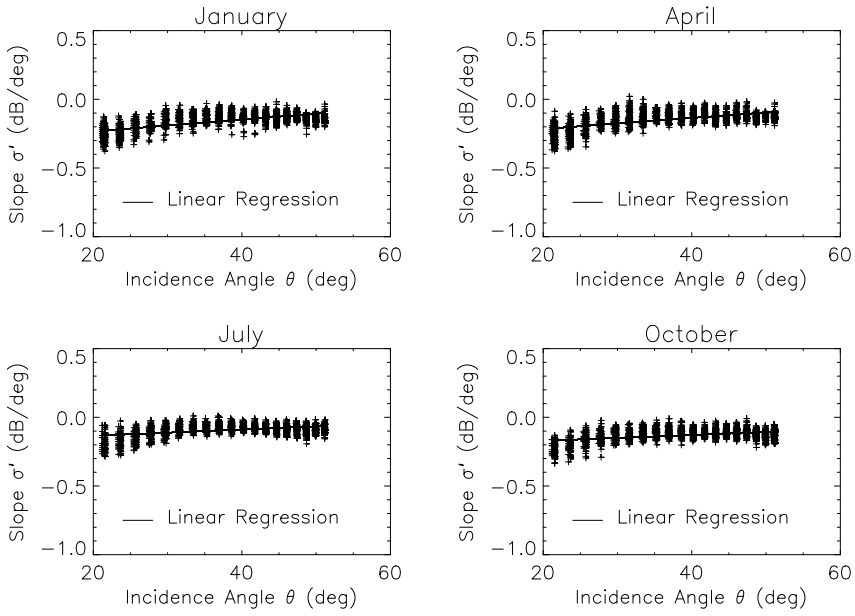


*Figure 6-5: Scatter plot of the slope versus the incidence angle for Zitomir, Ukraine (28.6°E, 50.27°N). The line is obtained by means of a regression analysis.*

From Equation (6.8) follows that $\sigma^0(\theta)$ is represented by a second order polynom:

$$\sigma^0(\theta) = \sigma^0(40) + \sigma'(40)\cdot(\theta - 40) + \frac{1}{2}\sigma''(40)\cdot(\theta - 40)^2 . \qquad \text{(dB)} \qquad (6.9)$$

In other studies it has most often been assumed that $\sigma^0(\theta)$ can be satisfactorily represented by a linear model (Wiesmann, 1994; Mougin et al., 1995; Wismann et al., 1996a).

### 6.3.2. Seasonal Variation of the Slope

The seasonal variation of the function $\sigma'(\theta)$ can be studied by fitting the regression line (6.8) to monthly data. In general, the slope $\sigma'(40)$ exhibits a seasonal cycle which is modelled using a function of the form:

$$\sigma'(40,t) = C' + D'\cdot\Psi'(t) , \qquad (6.10)$$

where $C'$ is a constant slope value, $D'$ is the dynamic range of the slope and $\Psi'(t)$ is an empirical periodic function[6]. The function $\Psi'(t)$ is dependent on the region. For example, a simple sinus model results in a satisfying fit over the Iberian Peninsula:

$$\Psi'(t) = \tfrac{1}{2}\sin\left(\tfrac{2\pi}{12}(t-3)\right). \qquad (6.11)$$

where the time $t$ is given in months. In the Ukraine a more complicated model is used (Figure 6-6):

$$\begin{aligned} \Psi'(t) &= \frac{1}{2}\left(\Psi'_1(t) + \Psi'_2(t)\right) \\ \Psi'_1(t) &= \frac{1}{2}\sin\left(\tfrac{2\pi}{12}(t-4)\right) \\ \Psi'_2(t) &= \frac{1}{4}\left(\sin\left(\tfrac{2\pi}{12}(t-3.5)\right) + \left|\sin\left(\tfrac{2\pi}{12}(t-3.5)\right)\right|\right) \end{aligned} \qquad (6.12)$$

where the vertical bars || represent the absolute value. The seasonal behaviour of the slope for various regions is discussed in more detail in Chapter 7.1.

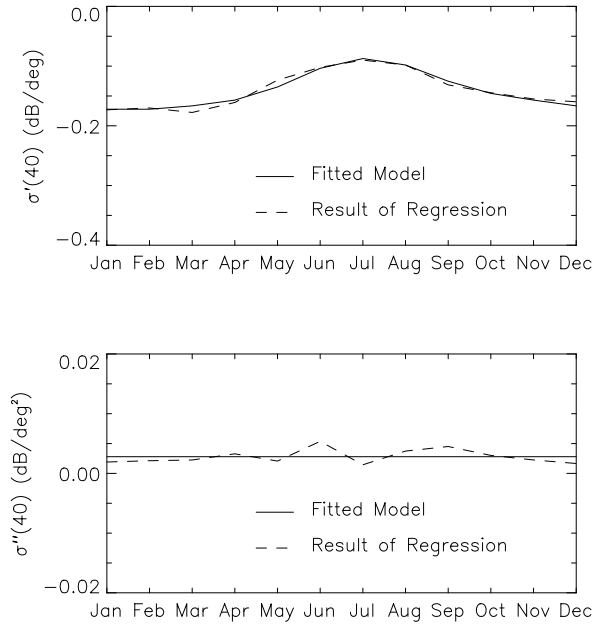


*Figure 6-6: Seasonal variation of the slope and curvature $\sigma'(40)$ and $\sigma''(40)$ for Poltava, Ukraine (34.55°E, 49.6°N) based on data from the period September 1991 to November 1997. Shown are the estimates obtained by use of the regression analysis and the fitted models.*

[6] In the text, *C* and *D* will always stand for a constant and the dynamic range of some variable that is indicated in the superscript of *C* and *D*.

Like the slope the curvature can be modelled with:

$$\sigma''(40,t) = C'' + D'' \cdot \Psi''(t)\,. \tag{6.13}$$

With only few exceptions, no seasonal cycle can be depicted in the curvature and $\sigma''$(40,t) is thus equal to a constant value $C''$.

A measure for the fit of the models (6.10) and (6.13) is the standard deviation of the residuals between the models and the values obtained by means of the regression analysis. For the seasonal slope model the root mean square error is denoted by $s'$, and for the seasonal curvature model by $s''$. Typically, $s'$ is in the order of 0.01 dB/deg and $s''$ is in the order of 0.001 dB/deg$^2$. Because of the more complex seasonal cycle both $s'$ and $s''$ tend to be higher over grassland than over forested areas.

### 6.3.3. Goodness of Fit of the Slope Model

To retrieve the function $\sigma'(\theta,t)$ a lot of averaging is done to the data. Firstly, by performing a linear regression on monthly data from several years, and secondly, by fitting the seasonal models (6.10) and (6.13) to the results of the regression analysis. The averaging is beneficial in that it suppresses the noise of $\sigma'_m$ derived from the backscatter triplet, but nevertheless it must be asked how well the *modelled* slope $\sigma'(\theta,t)$ reproduces the temporal dynamics of the *true* slope $\sigma'_t(\theta,t)$. In this section, quantities without any index refer to modelled quantities.

A measure for the fit of the model is the difference between the measured slope $\sigma'_m$ and the modelled slope $\sigma'$:

$$e'(\theta,t) = \sigma'_m(\theta,t) - \sigma'(\theta,t)\,. \tag{6.14}$$

Rewriting Equation (6.14) and substituting (6.6) gives:

$$e' = \sigma'_m - \sigma'_t - (\sigma' - \sigma'_t) = \sigma'_n - (\sigma' - \sigma'_t)\,. \tag{6.15}$$

It can be seen that the sources to $e'$ are the measurement noise $\sigma'_n$ and the error of the model represented by the difference $\sigma'$-$\sigma'_t$. As mentioned above, the averaging serves to suppress the noise term $\sigma'_n$, and therefore we are only interested in the magnitude of the difference $\sigma'$-$\sigma'_t$. The variance of $e'$ is given by:

$$Var(e') = Var(\sigma'_m) + Var(\sigma' - \sigma'_t)\,. \tag{6.16}$$

where $Var(\sigma'_m)$ can be estimated from Equation (6.7):

$$Var(\sigma'_m) \approx \frac{2}{100}\left(ESD(\sigma^0)\right)^2. \tag{6.17}$$

where the difference $\theta_{mid} - \theta_{f/a}$ was set equal to its average value of 10°. Consequently, the variance of the difference $\sigma'$-$\sigma'_t$ can be estimated from:

$$Var(\sigma' - \sigma'_t) \approx Var(e') - \frac{2}{100}\left(ESD(\sigma^0)\right)^2. \tag{6.18}$$

Uncertainties in the computation of $Var(\sigma'$-$\sigma'_t)$ arise because $ESD(\sigma^0)$ is only an estimate of the real standard deviation of $\sigma^0$ due to instrument noise, speckle, and azimuthal effects with a tendency to overestimate the real value[7] (Chapter 6.2.2). As a result, $Var(\sigma'$-$\sigma'_t)$ calculated with (6.18) may be negative, especially for large values of $ESD(\sigma^0)$, which obviously should not be the case. However, for $ESD(\sigma^0)$ values below about 0.3 dB we can put some confidence into the estimate because azimuthal effects are modest in this range. It is found that $Var(\sigma'$-$\sigma'_t)$ is in general around 0.0005 dB$^2$deg$^{-2}$ and smaller than about 0.001 dB$^2$deg$^{-2}$.

[7] One problem is that the measurements of the mid beam antenna, which are acquired at azimuthal angles intermediate to the azimuthal angles of the fore and aft beam antenna, are used for the calculation of the slope but not of $ESD(\sigma^0)$.

### 6.3.4. Dependence of the Slope on Soil Moisture

The question if soil moisture causes variations of the slope is of interest because it is connected to the question if the sensitivity of $\sigma^0$ (in decibels) to changes in the soil moisture content is dependent on the incidence angle or not. As discussed above, the sources contributing to the difference $e'$ are the measurement noise and the lack of fit of the model. The lack of fit of the model can in turn be attributed to a number of reasons: lack of fit of the seasonal models (6.10) and (6.13); variations of the true slope $\sigma'_t$ on weekly time scales due to vegetation growth; year to year differences in $\sigma'_t$; and day to day variability of $\sigma'_t$ due to soil moisture changes. The problem is that none of the noise sources can be quantified accurately. Only the spatial trend of the measurement noise can be characterised using $Var(\sigma'_m)$, and the spatial trend of error of the seasonal models (6.10) and (6.13) can be characterised by the root mean square errors $s'$ and $s''$ (Chapter 6.3.2). However, the following argument allows to determine if soil moisture has an effect on the slope or not: Forested areas are characterised by their stable backscatter, which is why the tropical rainforest is used as a distributed reference to calibrate the ERS Scatterometer data (Lecomte and Attema, 1992). On the other hand, over regions with low vegetation cover, the influence of soil moisture on the slope may be prominent (Ulaby et al., 1986). Therefore, if it is found that the variance of $e'$ over regions with low vegetation is increased above the contribution of the other scattering sources then soil moisture effects would be important.

It is tested how much of the spatial variability of $Var(e')$ can be explained by each of the parameters $Var(\sigma'_m)$, $s'^2$, and $s''^2$ alone, and by a multiple regression model of the kind:

$$Var(e') = c_0 + c_1 \cdot Var(\sigma'_m) + c_2 \cdot s'^2 + c_3 \cdot s''^2 \qquad (6.19)$$

The results for the main study areas can be seen in Table 6-2. Except for the Iberian Peninsula, the correlations are relatively high. For example, already 88 % of the variability of $Var(e')$ can be explained by $Var(\sigma'_m)$ for the Mali study area. The low correlations over the Iberian Peninsula stem probably from the fact that the dynamic range of $Var(e')$ is lower than over the other study areas. Although all parameters contribute significantly, it can be said that most of the spatial variability of $Var(e')$ can in general be explained by $Var(\sigma'_m)$, i.e. by the varying degree of azimuthal effects.

| Study area | $Var(\sigma'_m)$ | $s'$ | $s''$ | $Var(\sigma'_m)$, $s'$, $s''$ |
|---|---|---|---|---|
| Canadian Prairies | 63 | 20 | 41 | 86 |
| Iberian Peninsula | 17 | 13 | 2 | 35 |
| Mali | 88 | 36 | 29 | 91 |
| Ukraine | 53 | 40 | 73 | 82 |

*Table 6-2: Coefficient of determination $R^2$ in % between $Var(e')$ and the parameters $Var(\sigma'_m)$, $s'$, and $s''$ alone and according to Equation (6.19) for the main study areas.*

Given that $Var(\sigma'_m)$, $s'^2$, and $s''^2$ are only indicators, and given that the effects of vegetation dynamics are not considered, the relatively high correlations obtained by use of Equation (6.19) suggest that the slope is not or only weakly dependent on the surface soil moisture content. This means that in the logarithmic range the sensitivity of $\sigma^0(\theta)$ to soil moisture is approximately constant over the whole range of incidence angles from 18° to 59°. It further means that in natural units the sensitivity decreases approximately exponential with the incidence angle due to the more pronounced attenuation of microwaves at higher incidence angles by the vegetation canopy.

This finding is confirmed by the following examples from the Iberian Peninsula, Ukraine, and Canada where exceptional circumstances allow to demonstrate that the slope is independent of soil moisture respectively dielectric properties of the soil surface. In Figure 6-7 ERS Scatterometer measurements of two periods from a region around Beja in southern Portugal are shown. The radar signal is low during

the first period, July and August 1995, because hardly any rain had fallen before and during these two months. The second period, January 1996, is characterised by high $\sigma^0$ values, because high rainfall amounts in December 1995 (223 mm monthly rainfall) and January 1996 (282 mm) resulted in consistently wet soil conditions. One can see that both curves are clearly separated over the entire incidence angle range, but the slope is somewhat steeper during the winter period than during the summer period. However, this is not related to soil moisture effects on the slope, but differences in vegetation cover. The slope model (6.10) gives slope values of –0.11 dB/deg for the summer period and –0.16 dB/deg for the winter period, which fit well to the $\sigma^0(\theta)$ curves from Figure 6-7.

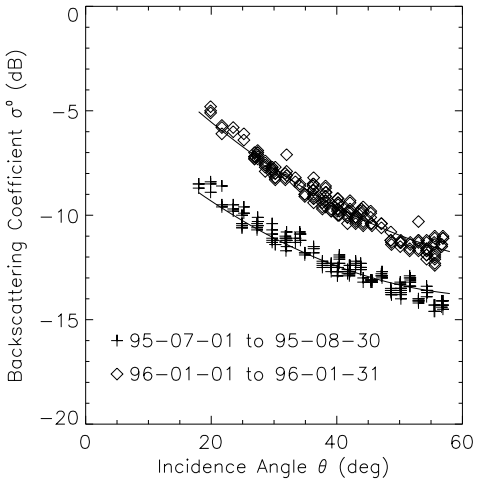


*Figure 6-7: ERS Scatterometer data for two periods from Beja (7.87°W, 38.02°N), Portugal. The full lines represent $\sigma^0(\theta)$ according to the slope model fitted to the backscatter measurements from the two periods.*

The second example in Figure 6-8 comes from the Ukraine and shows ERS Scatterometer data acquired over a region around Vladimir Volynskij in the second half of January 1994. During this time, the ERS Satellite was operated in a three days repeat cycle orbit which allowed to see the same location on the earth's surface every three days from the same incidence angles. Therefore the effect of varying dielectric properties can be observed at two different incidence angles (corresponding to mid and fore/aft beams). It can be seen in Figure 6-8 that there is some scattering in the data caused by the land-surface heterogeneity of the area from which the data are taken. However, it is evident that changes in the dielectric properties due to changes in soil moisture and/or freezing conditions have the same effect on $\sigma^0$ at the two incidence angles.

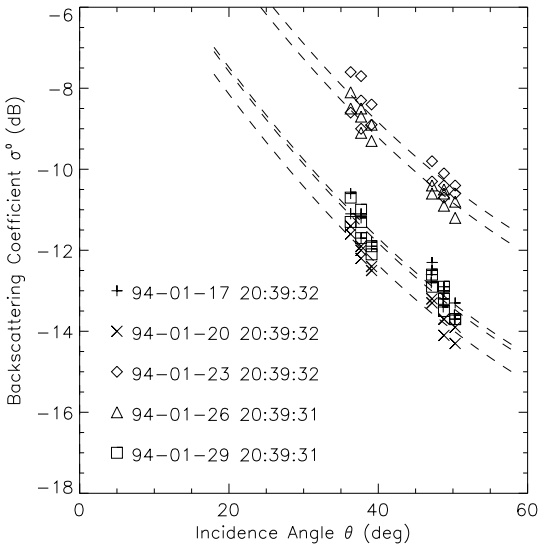


*Figure 6-8: ERS Scatterometer measurements from five days in January 1994 from Vladimir Volynskij (24.32°E, 50.83°N), Ukraine. The dotted lines represent $\sigma^0(\theta)$ according to the slope model fitted to the daily backscatter measurements.*

Finally, in Figure 6-9 backscattering measurements of a grassland and a parkland site in Saskatchewan, Canada, are shown for two periods in winter 1992/93. Again, it can be observed that the difference of the two $\sigma^0(\theta)$ curves is more or less constant for all incidence angle ranges. All over Saskatchewan these two time periods were characterised by mean temperatures below -10°C. The ground was frozen and covered by a dry snow layer with a depth between about 5 and 50 cm. Because dry snow is highly transparent at C-band the $\sigma^0(\theta)$ curves in Figure 6-9 are representative for the backscattering behaviour of snow free terrain. Higher backscatter intensities in the second period were caused by an extensive snow melt end of January 1993 which lead to an increase in the dielectric constant of the soil due to wetting of the soil and possibly also due to changes in the freezing conditions. The backscatter behaviour in winter 1992/93 is discussed in more detail in Wagner et al. (1995).

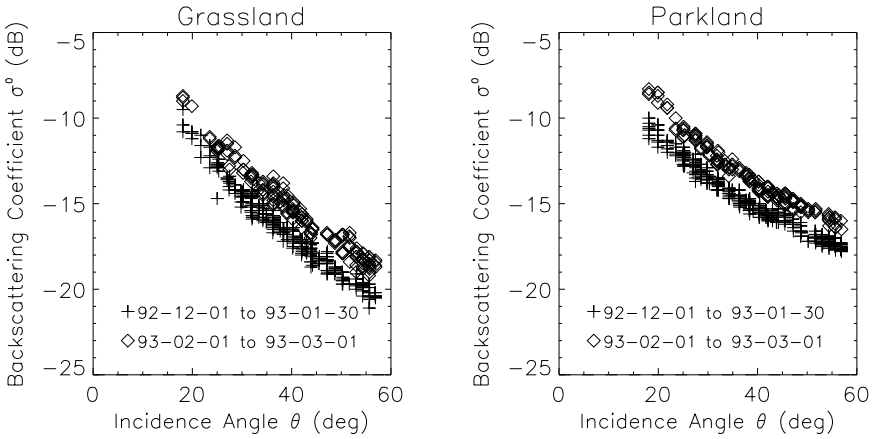


*Figure 6-9: ERS Scatterometer data for two periods in winter 1992/93 from a grassland (107°W, 49°N) and a parkland site (110°W, 53°N) in Saskatchewan, Canada.*

## *6.4. Normalised Backscattering Coefficient*

### 6.4.1. Extrapolation of the Backscattering Coefficient

With the knowledge of the spatial and temporal patterns of the slope it is possible to extrapolate ERS Scatterometer measurements to the reference angle at 40° according to

$$\sigma_i^0(40,t) = \sigma_i^0(\theta,t) - \sigma'(40,t)(\theta - 40) - \frac{1}{2}\sigma''(40,t)(\theta - 40)^2 \qquad (6.20)$$

where the index *i* stands for one of the three beams. Equation (6.20) is applied to the backscatter measurements of each antenna and then the average of the available beams is taken:

$$\sigma^0(40) = \frac{1}{3}\sum_{i=1}^{3}\sigma_i^0(40) \qquad (6.21)$$

Averaging over the three beams has the effect that the variance of the noise due to instrument noise, speckle, and azimuthal effects is lowered by a factor of three. It does however not lower the error due to the lack of fit of the slope model.

So far it has not been explained why the reference angle was chosen to be 40°. Because the sensitivity of $\sigma^0$ to soil moisture is not or only little dependent on the incidence angle, any choice of the reference angle retains information about the vegetation and soil moisture conditions. The choice of the reference angle should therefore be such that the error made when extrapolating the ERS Scatterometer measurements is smallest. For any reference angle $\theta_r$ the incidence angle dependency of $\sigma^0$ is given by:

$$\sigma^0(\theta_r) = \sigma^0(\theta) - \sigma'(\theta_r)(\theta - \theta_r) - \frac{1}{2}\sigma''(\theta_r)(\theta - \theta_r)^2 \tag{6.22}$$

The variance of $\sigma^0(\theta_r)$ is given by:

$$Var\left(\sigma^0(\theta_r, \theta)\right) = Var(\sigma^0) + (\theta - \theta_r)^2 Var(\sigma') + \frac{1}{4}(\theta - \theta_r)^4 Var(\sigma'') \tag{6.23}$$

A measure for the error made when extrapolating $\sigma^0(\theta)$ to $\sigma^0(\theta_r)$ is the integral over the variance of $\sigma^0(\theta_r)$:

$$\mathrm{IN}(\theta_r) = \int_{\theta_1}^{\theta_2} Var\left(\sigma^0(\theta_r, \theta)\right) d\theta \tag{6.24}$$

where $\theta_1$ and $\theta_2$ are the lower and upper limits of the incidence angle range. In the case of the ERS Scatterometer, $\theta_1$ and $\theta_2$ are 18° and 59° respectively. The optimum reference angle can be found where:

$$\frac{d\mathrm{IN}(\theta_r)}{d\theta_r} = 0\,. \tag{6.25}$$

Substituting (6.23) and (6.24) into (6.25) leads to the identity:

$$Var(\sigma') \cdot \left[(\theta_2 - \theta_r)^2 - (\theta_1 - \theta_r)^2\right] = -Var(\sigma'') \cdot \left[(\theta_2 - \theta_r)^4 - (\theta_1 - \theta_r)^4\right]. \tag{6.26}$$

Since $Var(\sigma')$ and $Var(\sigma'')$ can vary independently, Equation (6.26) can only be solved by setting the square brackets on the left and the right hand side to zero. The solution is

$$\theta_r = \frac{\theta_1 + \theta_2}{2}, \tag{6.27}$$

which gives $\theta_r$ = 38.5°. For a better comparison with results published in the literature the reference angle was chosen to be 40°, which is only slightly larger than the optimum reference angle.

### 6.4.2. Error Estimation

The error sources contributing to the r.m.s. error of $\sigma^0(40)$ are the measurement noise (instrument noise, speckle, azimuthal effects) and the extrapolation error. The latter error is caused by the uncertainties related to the description of the incidence angle behaviour of $\sigma^0(\theta)$. In a more general form the normalised backscattering coefficient is given by:

$$\sigma^0(40, \theta) = \sigma^0_m(\theta) - \int_{40}^{\theta} \sigma'(\zeta)\, d\zeta \tag{6.28}$$

where $\sigma^0(40,\theta)$ is the calculated backscattering coefficient at $\theta_r$ = 40° obtained by use of the slope model $\sigma'(\theta)$. $\sigma^0{}_m(\theta)$ is an ERS Scatterometer measurement. In $\sigma^0(40,\theta)$ the incidence angle is explicitly written down because the magnitude of the error of the model depends on the distance of $\theta$ from the reference angle. The true value $\sigma^0{}_t(40)$, which is of course independent of $\theta$ of an ERS Scatterometer measurement, would be given by:

$$\sigma^0_t(40) = \sigma^0_t(\theta) - \int_{40}^{\theta} \sigma'_t(\zeta)\, d\zeta \tag{6.29}$$

Taking the difference of the two equations above gives:

$$\sigma^0(40, \theta) - \sigma^0_t(40) = \sigma^0_n + \int_{40}^{\theta} \left[\sigma'(\zeta) - \sigma'_t(\zeta)\right] d\zeta\,. \tag{6.30}$$

where $\sigma^0{}_n$ is the noise level of individual ERS Scatterometer measurements due to instrument noise, speckle, and azimuthal effects. The second term describes the extrapolation error. Taking the variance gives

$$Var\left(\sigma^0(40,\theta)-\sigma_t^0(40)\right)=Var(\sigma_m^0)+Var\int_{40}^{\theta}[\sigma'(\zeta)-\sigma_t'(\zeta)]d\zeta \qquad (6.31)$$

If it is assumed that the difference $\sigma'(\theta)$-$\sigma'_t(\theta)$ is independent of $\theta$ then the variance of the integral becomes:

$$Var\int_{40}^{\theta}[\sigma'(\zeta)-\sigma_t'(\zeta)]d\zeta=(\theta-40)^2\cdot Var(\sigma'-\sigma_t') \qquad (6.32)$$

Since this assumption will in some cases lead to an overestimation of the integral and in some cases to an underestimation, Equation (6.32) is believed to be a good estimate of the real value of the variance of the integral. The random error of $\sigma^0(40)$ is thus given by:

$$Var\left(\sigma^0(40,\theta)-\sigma_t^0(40)\right)\approx Var(\sigma^0)+(\theta-40)^2\cdot Var(\sigma'-\sigma_t'). \qquad (6.33)$$

The variance is highest when $\theta$ is in the near or in the far range, and is lowest when around 40°. For each of the 38 (19 for the mid beam antenna and 19 for the fore/aft mean antennas) possible incidence angles it may be assumed that $\sigma^0(40,\theta)$-$\sigma^0{}_t(40)$ is normally distributed (Figure 6-10) with the variance given by Equation (6.33). For each point on the Earth's surface, the incidence angle varies from acquisition to acquisition depending on the orbit characteristics. For the 35 days and 168 days repeat cycles (but not for the 3 days repeat cycle) this variation happens in a rather random fashion and the distribution function of the overall error, i.e. the difference $\sigma^0(40)$-$\sigma^0{}_t(40)$[8], can be assumed to be the sum of the distribution functions of $\sigma^0(40,\theta)$-$\sigma^0{}_t(40)$. The resulting error is approximately normally distributed with a variance in between the variance of $\sigma^0(40,\theta)$-$\sigma^0{}_t(40)$ for $\theta$ = 40° and for $\theta$ in the near and far range. Computations show that the upper limit of the variance of $\sigma^0(40)$-$\sigma^0{}_t(40)$ can be estimated with:

$$Var\left(\sigma^0(40)-\sigma_t^0(40)\right)<Var(\sigma_m^0)+100\cdot Var(\sigma'-\sigma_t') \qquad (6.34)$$

which corresponds to setting $\theta$ equal to 30° or 50° in Equation (6.33), i.e. choosing an incidence angle in the middle of the ranges 18° to 40° or 40° to 59° respectively.

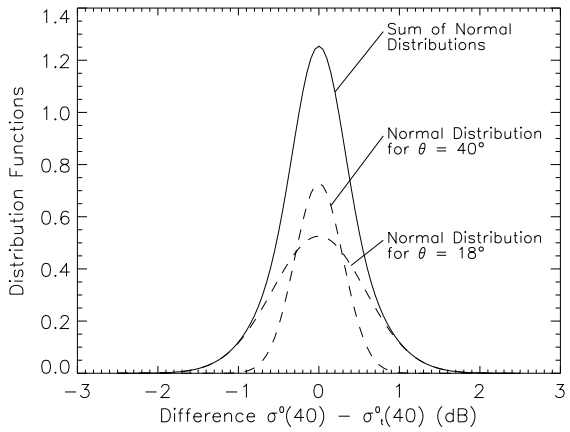


*Figure 6-10: Distribution functions of $\sigma^0(40,\theta)$-$\sigma^0{}_t(40)$ (Dashed Lines) and $\sigma^0(40)$-$\sigma^0{}_t(40)$ (Full Line). For clarity only the distribution functions of $\sigma^0(40,\theta)$-$\sigma^0{}_t(40)$ for $\theta$ = 18° and $\theta$ = 40° are shown.*

Since in the computation of $\sigma^0(40)$ the average over all three beams is taken the variance due to measurement noise of one beam is reduced by a factor of three:

$$Var\left(\sigma^0(40)-\sigma_t^0(40)\right)<\frac{1}{3}Var(\sigma_m^0)+100\cdot Var(\sigma'-\sigma_t') \qquad (6.35)$$

[8] Note that $\sigma^0(40)$ is not written as a function of $\theta$.

In Figure 6-11 the r.m.s. error of $\sigma^0(40)$, which is the square root of $Var(\sigma^0(40)-\sigma^0_t(40))$ is shown in dependence on the measurement noise and the extrapolation error. The measurement noise is expressed by the variance $Var(\sigma^0_m)$ respectively by the standard deviation $SD(\sigma^0_m)$ of a single beam, and the extrapolation error is represented by $Var(\sigma'-\sigma'_t)$. Because $SD(\sigma^0_m)$ is generally below 0.6 dB and $Var(\sigma'-\sigma'_t)$ below 0.001 $dB^2deg^{-2}$, the r.m.s. error of $\sigma^0(40)$ will in general be smaller than 0.4 dB (Figure 6-11).

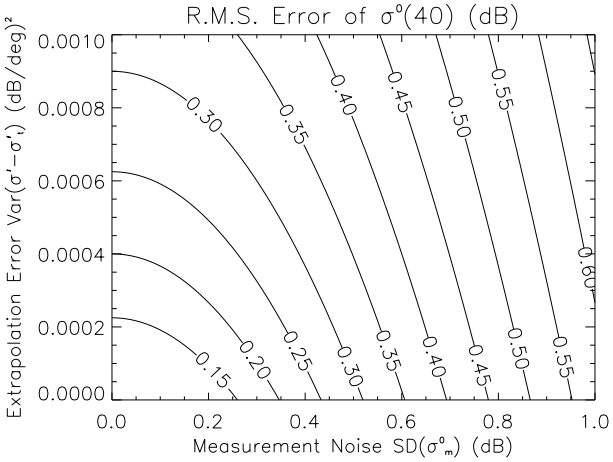


*Figure 6-11: R.m.s. error of the normalised backscattering $\sigma^0(40)$ in dependence on the measurement noise of a single beam and the extrapolation error.*

One example of a $\sigma^0(40)$ series taken from a region in western Mali is shown in Figure 6-12. It can be observed that during the dry season from about December to May $\sigma^0(40)$ is very stable. The standard deviation of $\sigma^0(40)$ in this period is, for this particular example, 0.17 dB, only 0.04 dB higher than the noise level of $\sigma^0$ due to instrument noise and speckle alone. This not only means that during the dry season the surface characteristics do not change in this region, but also that the extrapolation procedure yields good results. In addition, Figure 6-12 demonstrates the excellent stability of the sensor.

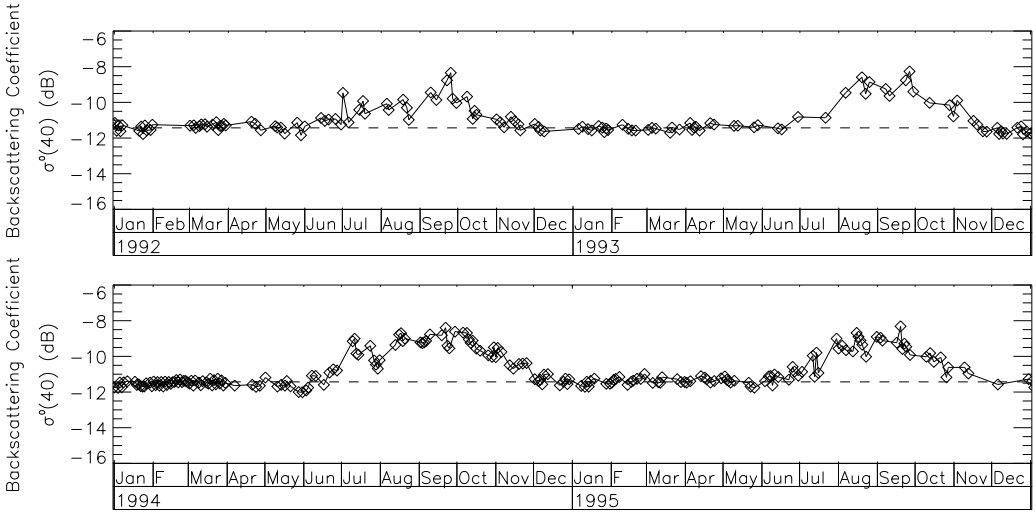


*Figure 6-12: Time series of normalised backscattering coefficient $\sigma^0(40)$ for a region in western Mali (11.8°W, 13.6°N). The dotted line shows the mean value of $\sigma^0(40)$ during the dry season.*

# 7. Vegetation Cover Effects

## *7.1. Vegetation Dynamics*

### 7.1.1. Influence on the Slope

The dominant mechanisms contributing to the backscattering coefficient of surfaces covered by vegetation are volume scattering in the vegetation canopy and surface scattering from the underlying soil surface. The incidence angle behaviour of the volume and the surface scattering terms are distinctly different. With the exception of very rough surfaces the bare soil backscattering coefficient decreases rapidly with the incidence angle. For example, scientists from the University of Bern have collected a large number of ground-based scatterometer measurements of agricultural fields at frequencies between 2 and 12 GHz and incidence angles between 10° and 70°, together with detailed ground truth information including surface roughness profiles (Wegmüller et al., 1994). An analysis of the data reported in the "Active and Passive Microwave Signature Catalogue (2-12 GHz)" by Wegmüller and Mätzler (1993) shows that $\sigma^0$ at 4.6 GHz vertical polarisation decreases in general strongly with the incidence angle for bare agricultural fields with r.m.s. heights in the range 0.4 – 2 cm. Also, ground based radar measurements of five bare soil fields with r.m.s. heights of 1.1, 1.8, 2.2, 3.0, and 4.1 cm carried out by Ulaby et al. (1978) showed, with the exception of the roughest field, a strong decrease of $\sigma^0$ at 4.25 GHz for incidence angles between 0° and 30°. Because many land cover classes have a smoother surface than agricultural fields and because of the large footprint size of the sensor the contribution of the soil surface to ERS Scatterometer retrieved $\sigma^0$ should therefore in general decrease strongly with the incidence angle.

In contrast, the contribution from the vegetation canopy is fairly uniform over a large range of incidence angles. If the transmissivity of the vegetation canopy decreases then volume scattering is enhanced with respect to the surface scattering contribution and the slope becomes less steep. Because transmissivity is related to the product of the volumetric water content of the vegetation and the plant height (Attema and Ulaby, 1978) the slope $\sigma'(40)$ should be lowest (high gradient) in winter, and highest in summer when vegetation has reached its maximum wet biomass (low gradient)[9].

In Figure 7-1 the seasonal variation of $\sigma'(40)$ for four sites located in different climatic regions is shown: Iberian Peninsula (Mediterranean climate), Ukraine (temperate continental), Canadian Prairies (dry continental), and Mali (wet-dry tropical). As the rate of net photosynthesis is strongly dependent on light intensity and duration of daylight vegetation tends to reach its maximum height during the high-sun season (Strahler and Strahler, 1996). However, water availability and temperatures are important factors influencing plant growth. Therefore climographs showing mean monthly temperatures and mean monthly rainfall are also displayed in Figure 7-1[10].

Let us first compare the temporal evolution of $\sigma'(40)$ for the sites in Spain, Ukraine, and Canada. It can be observed that the highest slope values (lowest gradients) are around July for all three regions. However, the slope starts increasing earliest in Spain, followed by Canada and the Ukraine. This is most likely related to the temperature cycles with below zero temperatures hindering plant growth in the Ukraine until March and until April in Canada. The early vegetation development in Spain is also probably a consequence of winter rainfall and summer drought which gives an advantage to plants that

[9] The slope is defined as the first derivative of $\sigma^0$ with respect to the incidence angle. Because $\sigma^0$ decreases in general from the near to the far range, the slope is in general negative.

[10] The climate data were extracted from the Web site "http://www.worldclimate.com/".

develop early in the year. In Mali plants cannot grow during the dry period from November to May. Only in the beginning of July, some weeks after the initiation of the rainfall season, enough vegetation biomass has developed to prompt an increase of $\sigma'(40)$. The maximum $\sigma'(40)$ values coincide with the end of the rainfall season in September.

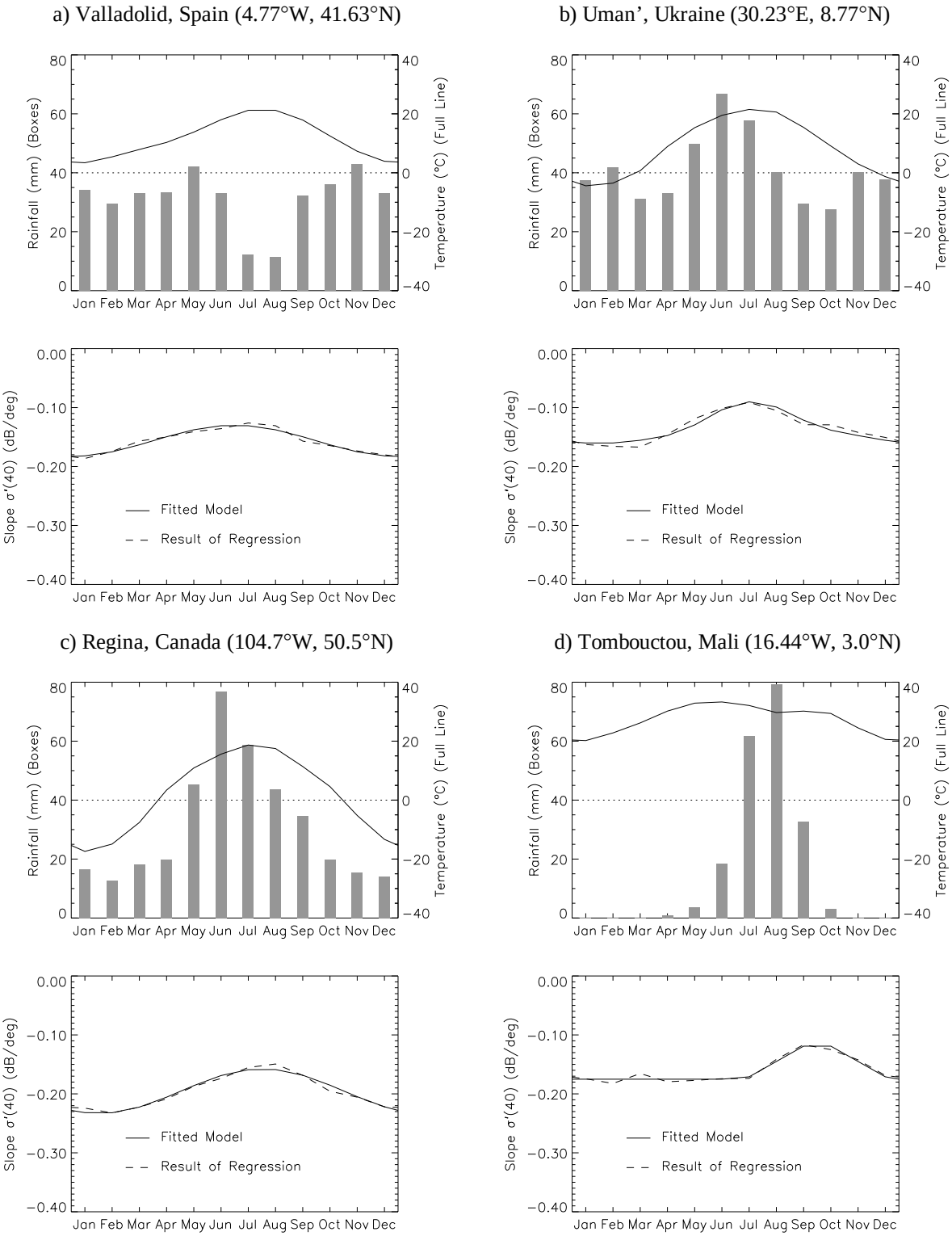


*Figure 7-1: Climographs and seasonal variation of the slope $\sigma'(40)$ for four sites in a) Spain, b) Ukraine, c) Canada, and d) Mali.*

A spatial picture of the seasonal cycle of the slope is given in Colour Figure 3 which shows monthly $\sigma'(40)$ images over the Iberian Peninsula. Over the entire region the slope is steepest around December/January and weakest around July. When compared to mean monthly NDVI images (Colour Figure 4) it can be recognised that the peak of $\sigma'(40)$ occurs with a certain time delay after the peak of the NDVI. In the south of the Iberian Peninsula the time delay is about three months and in the north about one month. A possible explanation is that while the vegetation is photosynthetically most active in spring (as indicated by the NDVI) it reaches its maximum wet biomass only in summer (as indicated by the slope).

These examples suggest that the slope is related to vegetation biomass. However, it is very unlikely that changes in biomass over one season can be estimated because $\sigma'$ derived from one backscatter triplet is very noisy. Only if $\sigma'$ values are averaged over several years then the measurement noise is suppressed, and the resulting mean values may be useful for the study of vegetation phenology. Another limitation is that the slope exhibits a clear annual cycle only over regions with low vegetation such as grassland or agricultural areas (Chapter 7.2).

### 7.1.2. Influence on the Backscatter Intensity

After the analysis of the seasonal variation of the slope the impact of vegetation growth and senescence on the temporal variability of the backscatter intensity $\sigma^0(40)$ is investigated by comparing $\sigma^0(40)$ time series to daily NDVI values and rainfall observations. In Figure 7-2 the evolution of these parameters is shown for an agricultural region around Beja in the south of Portugal. For the discussion on the temporal variability of the lowest and highest $\sigma^0(40)$ measurements, a second $\sigma^0(40)$ time series from a region about 150 km west of Beja is shown in Figure 7-2d.

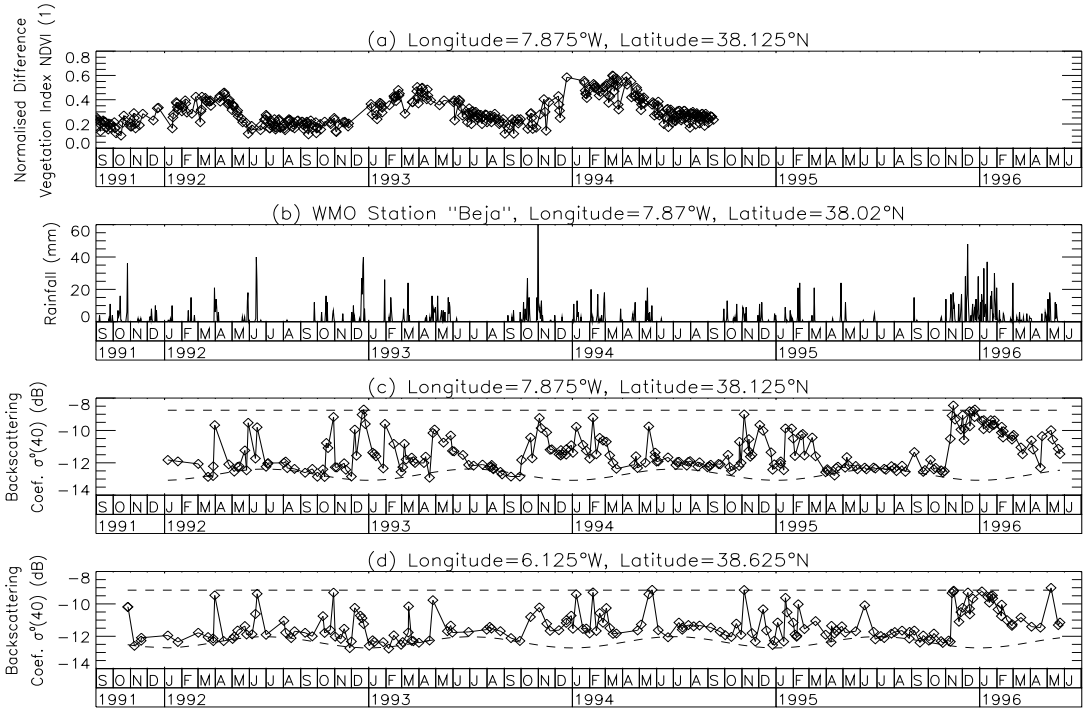


*Figure 7-2: Temporal evolution of the NDVI, rainfall observations, and the backscattering coefficient, $\sigma^0(40)$ over an agricultural region around Beja in southern Portugal. (a) Daily NDVI values degraded to match the resolution of the ERS Scatterometer. (b) Rainfall recorded at the synoptic station "Beja". (c) $\sigma^0(40)$ time series over Beja. The dotted lines show the backscattering coefficient for dry soil conditions, $\sigma^0_{dry}(40,t)$, and the backscattering coefficient for wet soil conditions, $\sigma^0_{wet}(40)$. (d) $\sigma^0(40)$ series over a region about 150 km east of Beja. The dotted lines represent $\sigma^0_{dry}(40,t)$ and $\sigma^0_{wet}(40)$.*

When comparing Figures 7-2a and 7-2c it can be observed that $\sigma^0(40)$ varies on much shorter time scales than the NDVI (day to day changes in the NDVI are mainly due to noise). Therefore it must be concluded that the direct relationship between $\sigma^0(40)$ and NDVI is either very weak or non-existent. It is noted that Frison and Mougin (1996b), who compared ERS Scatterometer data to NDVI values over a wide range of vegetation types, found a substantial agreement between vegetation development as indicated by the NDVI and $\sigma^0$, especially at large incidence angle. This disagreement can possibly be explained by the unique character of the Mediterranean climate where the annual vegetation and precipitation cycle are well separated and by the different approaches to process the ERS Scatterometer data. Nevertheless, these results demonstrate that the NDVI, which is a measure of vegetation "greenness" rather than of plant water content or height, is not important for the explanation of the backscattering behaviour.

On the other hand, the comparison of Figures 7-2b and 7-2c shows that rainfall has a pronounced effect on the backscatter intensity. Regardless of the season, the short term variability of $\sigma^0(40)$ can be explained if the changes in $\sigma^0(40)$ are interpreted as surface soil moisture changes.

How vegetation phenology affects the backscatter intensity is not obvious from the $\sigma^0(40)$ series which is why a more detailed discussion is required. Because of the distinct incidence angle behaviour of the volume and the surface scattering terms, the effects of vegetation growth and senescence should be reflected in both $\sigma^0$ and $\sigma'$, and a change in one parameter should condition a change in the other. As a growing vegetation canopy becomes less transparent, $\sigma^0$ may decrease or increase depending on whether the attenuation of the soil contribution is more important than the enhanced contribution from the vegetation canopy or vice versa. This can be seen when the first derivative of the radiative transfer solution of the backscattering coefficient of a vegetation canopy (Equation 5.2) with respect to the optical depth $\tau$ is calculated:

$$\frac{\partial \sigma^0_{can}}{\partial \tau} = \frac{\partial}{\partial \tau}\left( \frac{\omega \cos\theta}{2}\left(1 - e^{-\frac{2\tau}{\cos\theta}}\right) + \sigma^0_s(\theta) e^{-\frac{2\tau}{\cos\theta}} \right) = \left[ \frac{\omega \cos\theta}{2} - \sigma^0_s(\theta) \right] \cdot \frac{2}{\cos\theta} \cdot e^{-\frac{2\tau}{\cos\theta}} \qquad (7.1)$$

Because the interaction term is small it is neglected in Equation (7.1). If the bare soil backscattering coefficient is high compared to the contribution from the vegetation canopy, i.e.

$$\frac{\omega \cos\theta}{2} < \sigma^0_s(\theta), \qquad (7.2)$$

then the attenuation of the soil contribution is the dominant effect and $\sigma^0$ decreases. It is more likely that this situation is encountered in the near range than in the far range. For example, Prévot et al. (1993b) and Taconet et al. (1996) studied the backscattered signal at C-band from wheat fields and found that for an incidence angle of 20° the effect of vegetation is mainly attenuation of the signal returned by the underlying soil. Because of the rapid drop-off of the bare soil backscattering coefficient the situation may be reversed at high incidence angles and $\sigma^0$ increases. Therefore at some incidence angle the $\sigma^0(\theta)$ curves of a developing and a full grown vegetation canopy should cross over, or in other words, there should be an incidence angle at which $\sigma^0$ is rather stable despite vegetation growth. Mathematically speaking this angle is defined where

$$\frac{\omega \cos\theta}{2} = \sigma^0_s(\theta) \qquad (7.3)$$

If such a "crossover angle" exists then it is dependent on the soil moisture conditions. For dry soil conditions the crossover angle should be found at lower incidence angles than for wet conditions (Figure 7-3 and Chapter 5.2).

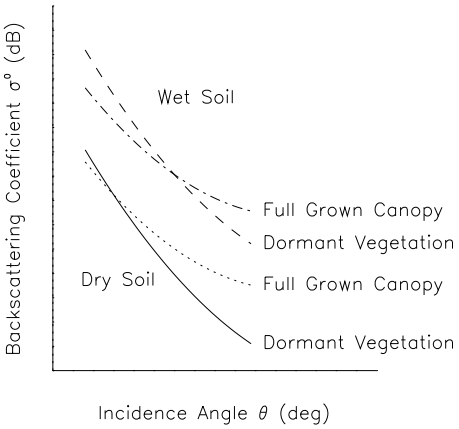


*Figure 7-3: Illustration of the concept of the "crossover angle". See the text for discussion. See also Figure 5-3.*

Let us assume that such a crossover angle exists. For a dry soil surface the backscattering coefficient is denoted by $\sigma^0_{dry}$ and the crossover angle by $\theta_{dry}$. If $\sigma^0_{dry}(\theta_{dry})$ is set equal to a constant value then the time dependence of $\sigma^0_{dry}$ at 40° is given by:

$$\sigma^0_{dry}(40,t) = C^0_{dry} - D'\Psi'(t)(\theta_{dry} - 40) - \frac{1}{2}D''\Psi''(t)(\theta_{dry} - 40)^2, \quad (7.4)$$

where $D'$ and $D''$ are the dynamic terms of the slope $\sigma'(40)$ and the curvature $\sigma''(40)$, and $\Psi'(t)$ and $\Psi''(t)$ are the empirical functions describing their time dependence (Equations 6.10 and 6.13). $C^0_{dry}$ is a constant that is equal to:

$$C^0_{dry} = \sigma^0_{dry}(\theta_{dry}) - C'(\theta_{dry} - 40) - \frac{1}{2}C''(\theta_{dry} - 40)^2, \quad (7.5)$$

where $C'$ and $C''$ are the constant terms of $\sigma'(40)$ and $\sigma''(40)$. These equations were obtained by substituting (6.10) and (6.13) into (6.9) and separating the time dependent and constant terms. The same reasoning can be applied for wet soil conditions:

$$\sigma^0_{wet}(40,t) = C^0_{wet} - D'\Psi'(t)(\theta_{wet} - 40) - \frac{1}{2}D''\Psi''(t)(\theta_{wet} - 40)^2, \quad (7.6)$$

where $\sigma^0_{wet}$ is the backscattering coefficient of vegetation with an underlying wet soil surface, $\theta_{wet}$ is the crossover angle for wet conditions, and $C^0_{wet}$ is a constant given by:

$$C^0_{wet} = \sigma^0_{wet}(\theta_{wet}) - C'(\theta_{wet} - 40) - \frac{1}{2}C''(\theta_{wet} - 40)^2. \quad (7.7)$$

As mentioned in Chapter 6.3.2, $D''$ is with few exceptions equal to zero, but is considered in Equations (7.4) and (7.6) for the sake of generality. In the following $D''$ is set equal to zero.

The crossover angles $\theta_{dry}$ and $\theta_{wet}$ can be determined by comparing the functions (7.4) and (7.6) to the minimum and maximum values of $\sigma^0(40)$ in multi-year backscatter series. A visual analysis of $\sigma^0(40)$ series over the Iberian Peninsula and the other study areas showed that setting $\theta_{dry}$ equal to 25° results in a good fit. Figures 7-2c and 7-2d show how the minimum values of $\sigma^0(40)$ follow the seasonal variation of $\sigma^0_{dry}(40,t)$. Especially in the drought year 1995 the comparison is favourable. The minimum values are somewhat higher in summer than in winter. This effect is observed to be more pronounced in areas where the dynamic range of the slope is high thus confirming the relationship between the dynamic range of $\sigma^0_{dry}$ and $D'$. Since no clear seasonal trend can be discerned for the maximum values of $\sigma^0(40)$ (Figure 7-2d) the crossover angle $\theta_{wet}$ is set equal to 40° and $\sigma^0_{wet}(40,t)$ thus becomes a constant $C^0_{wet}$.

The values $\theta_{dry}$ = 25° and $\theta_{wet}$ = 40° are estimates of the real crossover angles and the question is what is the magnitude of the associated error? From Equation (7.4) one can derive the error $\Delta\sigma^0_{dry}$ due to the uncertainties related with the estimated crossover angle for dry soil conditions $\theta_{dry}$:

$$\Delta\sigma^0_{dry}(t) = D'\Psi'(t)\Delta\theta_{dry}\,, \tag{7.8}$$

where $\Delta\theta_{dry}$ is the difference between the estimated and the true crossover angle. The maximum error of $\Delta\sigma^0_{dry}$ is obtained by setting $\Psi(t)$ equal to one:

$$Max\left(\Delta\sigma^0_{dry}\right) = D' \cdot \Delta\theta_{dry}\,. \tag{7.9}$$

One can see in Equation (7.9) that the error depends on the dynamic range of the slope $D'$ which, depending on the region, takes on values between 0 and about 0.16 dB/deg. Values of $D'$ up to 0.16 dB/deg are observed in the Canadian Prairies, Ukraine, and Mali, over the Iberian Peninsula the highest values are around 0.08 dB/deg. In Figure 7-4 the maximum error of $\Delta\sigma^0_{dry}$ in dependence on $D'$ and $\Delta\theta_{dry}$ is displayed. It can be seen that the error $\Delta\sigma^0_{dry}$ is in general relatively small. Only over regions with $D'$ values higher than 0.1 dB/deg and $\Delta\theta_{dry}$ larger than 3° the maximum error of $\sigma^0_{dry}$ may exceed 0.3 dB. The same argument applies for the wet soil case.

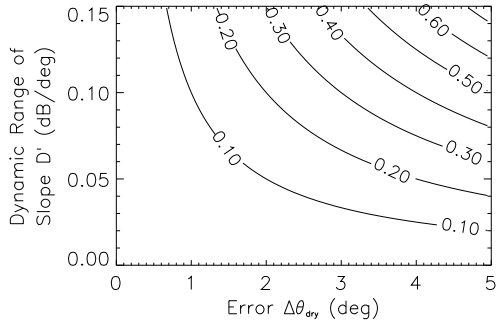


*Figure 7-4: Contour plot of the maximum error of the backscattering coefficient of a dry soil, Max($\Delta\sigma^0_{dry}$) in dB, in dependence on the dynamic range of the slope $D'$ and the deviation of the estimated $\theta_{dry}$ value from its real value, denoted by $\Delta\theta_{dry}$.*

Having estimates for $\theta_{dry}$ and $\theta_{wet}$, the constant terms $C^0_{dry}$ and $C^0_{wet}$ can be estimated for each pixel by fitting Equations (7.4) and (7.6) to the minimum and maximum values of the $\sigma^0(40)$ series. It is then straight forward to calculate the sensitivity of $\sigma^0$ to changes in the surface soil moisture content. The sensitivity $S(t)$ is defined as:

$$S(t) = \sigma^0_{wet}(40) - \sigma^0_{dry}(40,t) \tag{7.10}$$

and can be written as the sum of a constant, $C^S$, and a time variant term:

$$S(t) = C^S - D'\Psi'(t)(\theta_{wet} - \theta_{dry}) \tag{7.11}$$

The sensitivity exhibits the expected temporal behaviour with lower values in summer than in winter. The extracted values of $C^0_{dry}$, $C^0_{wet}$, and $C^S$ over the Iberian Peninsula can be seen in Colour Figures 6c, 6d, and 6e. Colour Figure 6 also shows the spatial distribution of $C'$ and $D'$, and land cover percentages derived from the CORINE land cover. The comparison of the backscattering parameters and the land cover will be the topic of the next chapter.

Using the concept of the crossover angle the impact of vegetation growth and senescence on $\sigma^0$ can be estimated at any incidence angle. The magnitude of soil moisture and seasonal vegetation cover effects on $\sigma^0$ can directly be obtained from Equation (7.11) by setting $\Psi'$ equal to one. The magnitude of soil moisture effects is represented by $C^S$, and seasonal vegetation cover effects by $D'\cdot(\theta_{wet}-\theta_{dry})$. Figure 7-5 shows a scatter plot of these two terms based on the entire data set from the Iberian Peninsula. It can be seen that the sensitivity to soil moisture is always greater than 1.5 dB, whereas the changes in $\sigma^0$ due to seasonal vegetation development are in general smaller than 1 dB. Over the other test sites, where $D'$ values up to 0.16 dB/deg are observed, vegetation may change $\sigma^0(40)$ by about 2.4 dB. However $C^S$ and $D'$ are correlated with each other, and therefore any increase in vegetation cover effects is associated by

an increase of the sensitivity to soil moisture. It can be concluded that independent of land cover the temporal variability of $\sigma^0(40)$ is mainly caused by changes in the soil moisture content rather than by changes in vegetative status.

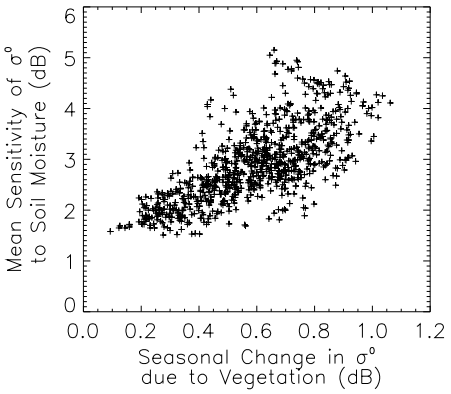


*Figure 7-5: Soil moisture versus seasonal vegetation cover effects on the backscattering coefficient $\sigma^0$ based on the data set from the Iberian Peninsula.*

## *7.2. Land Cover*

### 7.2.1. Comparison with CORINE Land Cover

The influence of land cover on the backscattering behaviour is analysed by comparing ERS Scatterometer parameters with the percentage area occupied by CORINE land cover classes within one ERS Scatterometer pixel over the Iberian Peninsula. The area occupied by each CORINE land cover class was determined by drawing a circle with a radius of 30 km around each centre point of the 0.25° grid and by summing up the area of all the internal polygons belonging to one class. The circle area roughly corresponds to the spatial resolution of the ERS Scatterometer data interpolated to the grid. As a result the area $A_i$ of the CORINE class $i$ expressed as a percentage of the area of the resolution cell is obtained. The subscript is the CORINE code which can either be a one, two, or three digit number depending on the level in the hierarchy. The original 44 CORINE land cover classes are grouped into 16 classes considering all classes that occupy more than 3 % of the total area of the Iberian Peninsula and the land cover classes "artificial surfaces", "inland waters", and "open spaces with little or no vegetation" (Table 7-1). Some minor classes were not considered and the total area occupied by the 16 classes is 97.6 %. To see how each of these classes influence ERS Scatterometer parameters, a multiple regression analysis between each parameter and the percentage area occupied by the 16 classes, is performed:

$$x = \sum_i A_i x_i \qquad i = 1, 33, 51, 211, 212, \ldots \qquad (7.12)$$

where $x$ stands for one ERS Scatterometer parameter ($C'$, $D'$, $C^0{}_{dry}$, or $C^S$). The basic assumption is that each of the 16 classes can be represented by a single parameter value $x_i$. This is a strong simplification because e.g. a field planted with olive trees is a member of the CORINE class "olive grove" no matter how densely the trees are planted and no matter if the soil surface is bare or covered by high grass. To make inferences about the significance of the 16 classes a one-sided *t*-test is performed (McCave et al., 1997). In Table 7-1 the results of the *t*-test are shown for the mean slope $C'$, the dynamic range of the slope $D'$, the mean backscattering coefficient of vegetation under dry soil conditions $C^0{}_{dry}$, and the mean sensitivity $C^S$. Because $D'$ and $C^S$ show the opposite trends to $C'$ and $C^0{}_{dry}$ the first two parameters are multiplied by -1. This allows to identify land cover classes with common behaviour more easily.

| Name of CORINE Land Cover Class | CORINE Code | Total Area (%) | $C'$ (dB/deg) | $-D'$ (dB/deg) | $C^0_{dry}$ (dB) | $-C^S$ (dB) |
|---|---|---|---|---|---|---|
| Artificial surfaces | 1 | 1.3 | + | + | + | • |
| Open spaces with little or no vegetation | 33 | 6.7 | + | + | + | – |
| Inland waters | 51 | 1.3 | – | • | – | – |
| Non-irrigated arable land | 211 | 20.6 | – | – | – | – |
| Permanently irrigated land | 212 | 3.1 | • | • | + | • |
| Olive groves | 223 | 8.9 | + | – | + | • |
| Annual crops associated with permanent crops | 241 | 3.1 | • | • | • | • |
| Complex cultivation patterns | 242 | 4.2 | • | • | + | • |
| Land principally occupied by agriculture with significant areas of natural vegetation | 243 | 5.9 | + | + | • | + |
| Agro-forestry areas | 244 | 7.2 | • | – | – | • |
| Broad-leaved forest | 311 | 9.5 | + | + | + | + |
| Coniferous forest | 312 | 7.2 | + | + | – | + |
| Mixed forest | 313 | 3.9 | + | + | + | + |
| Natural grassland | 321 | 4 | – | – | – | – |
| Sclerophyllous vegetation | 323 | 6.7 | + | + | + | + |
| Transitional woodland-shrub | 324 | 4 | • | • | + | + |

*Table 7-1: Results of a multiple regression analysis between ERS Scatterometer parameters ($C'$, $D'$, $C^0_{dry}$, and $C^S$) and the percentage area occupied by the 16 classes listed in the first column. The third column shows how many percent of the total area of the Iberian Peninsula is occupied by each land cover class. A one tailored t-test was performed for each regression coefficient. The symbols + and – indicate that the t-test suggests that the given class is significant for the explanation of the respective ERS Scatterometer parameter at the $\alpha = 0.01$ level. The symbol + signifies positive correlation and the symbol – negative correlation. The symbol • indicates that the null hypothesis cannot be rejected at this $\alpha$ level.*

It can be concluded:

1. Despite the fact that only about 1.3 % of the land is build-up, urban, industrial and the like areas have a noticeable effect on backscatter characteristics. These areas tend to increase the backscatter intensity $C^0_{dry}$ and the slope $C'$. The dynamic range of the slope $D'$ decreases.

2. Open spaces with little or no vegetation including bare rock surfaces and sparsely vegetated areas also tend to increase $C'$ and $C^0_{dry}$. This means that these surface types are typically rough for C-band microwaves. As expected $D'$ decreases and the sensitivity $C^S$ increases.

3. Also inland water occupy a total area of 1.3 % of the Iberian Peninsula and have a noticeable impact on the backscattering behaviour. As expected, both $C^0_{dry}$ and $C'$ decrease.

4. Land cover classes that are characterised by a mixture of grassland, agricultural land, bushes, shrubs, and forests have no clear impact on ERS Scatterometer parameters. Examples are “Olive groves”, “Complex cultivation patterns”, etc.. Only land cover classes which are predominantly occupied by typically low or high vegetation exhibit clear tendencies.

5. Translucent vegetation as represented by the CORINE land cover classes “Non-irrigated arable land” and “Natural grassland” decrease $C'$ and $C^0_{dry}$ and increase $D'$ and $C^S$.

6. Non-transparent vegetation as represented by the CORINE land cover classes “Broad-leaved forests”, “Coniferous forest”, “Mixed forest”, and “Sclerophyllous vegetation” increase $C'$ and $C^0_{dry}$ and decrease $D'$ and $C^S$. The parameter $C^0_{dry}$ of coniferous forests shows an exception.

Although the assumption that each land cover class can be represented by a single parameter value appeared to be strong, between 52 % and 73 % of the variability of the backscatter parameters can be explained (Table 7-2). The rest of the variability should be mainly due to in-class differences including surface roughness effects. It is tested how much of the variability is explained by using only those classes that exhibit clear trends and by grouping them together into three generalised classes representing non-vegetated surfaces, translucent vegetation, and non-transparent vegetation. The non-vegetated class is defined as the sum of the area of CORINE classes 1 and 33, $A_{no} = A_1+A_{33}$. The translucent class is represented by $A_{tr} = A_{211}+A_{321}$, and the non-transparent class by $A_{nt} = A_{31}+A_{323}$. The total area occupied by these three classes is about 60 %. In principle, it might be possible to use the other CORINE classes to improve the estimates of the area occupied by these three generalised classes, e.g. by attributing 50 % of the area occupied by the “Agro-forestry area” class to the non-transparent class and the other 50 % to the translucent class. However, any such “improvement” would introduce uncertainties and therefore this idea was rejected.

| Number of Classes | $C'$ (dB/deg) | $D'$ (dB/deg) | $C^0_{dry}$ (dB) | $C^S$ (dB) |
|---|---|---|---|---|
| 16 | 68.0 | 52.6 | 61.7 | 72.7 |
| 3 | 60.9 | 35.4 | 39.5 | 64.2 |
| 1 ($A_{tr}$) | 52.0 | 27.9 | 29.4 | 56.8 |
| 1 ($A_{nt}$) | 35.5 | 18.0 | 15.0 | 32.4 |

*Table 7-2: Multiple coefficient of determination, $R^2$, between ERS Scatterometer parameters ($C'$, $D'$, $C^0_{dry}$, or $C^S$) and the percentage area occupied by 16, 3 or 1 land cover class(es). See Table 7-1 for the definition of the 16 classes. The three classes comprise non-vegetated surfaces, translucent and non-transparent vegetation. In the third row $R^2$ for translucent vegetation ($A_{tr}$) is shown and in the last row $R^2$ for non-transparent vegetation ($A_{nt}$).*

By using the three classes the multiple coefficient of determination $R^2$ decreases by about 8 % for $C'$ and $C^S$ when compared to the 16 classes case (Table 7-2). For $C^0_{dry}$ and $D'$ it decreases more significantly and takes on values between 35 % and 40 %. The spatial distribution of $A_{no}$, $A_{tr}$, and $A_{nt}$ is shown in Colour Figure 6 together with the ERS Scatterometer parameters $C'$, $D'$, $C^0_{dry}$, $C^0_{wet}$, and $C^S$. With the exception of $C^0_{wet}$ the vegetation patterns are well reflected in the ERS Scatterometer parameters. For example, the high plains of Castillia Y Leon, Castilla La Mancha, and Extremadura, which are predominately occupied by agricultural- and grassland, are characterised by a high sensitivity to soil moisture, a steep slope, and a high dynamic range of the slope.

On top of this vegetation pattern some secondary effects can be recognised. Madrid, which can be identified in Colour Figure 6h by the yellow-green pixels in the centre of the Iberian Peninsula, has a slight impact on all ERS Scatterometer parameters. Mountainous regions and regions with scarce vegetation cover have a more pronounced effect, especially on $\sigma^0_{dry}$. For example, in the very south-east of the Iberian Peninsula $C'$ is high with values around -0.12 dB/deg, $D'$ and $C^S$ are low with values around 0.02 dB/deg and 2 dB respectively, and $C^0_{dry}$ is very high with values around -10 dB. These backscatter characteristics suggest a high forest cover percentage, while in fact, vegetation is scarce in many parts of this region. These effects are probably caused by the frequent occurrence of soils containing rock fragments in their top layer causing a rough surface for C-band microwaves.

Finally, it is tested how much of the variability of the ERS Scatterometer parameters can be explained by using either the translucent class or the non-transparent class. Table 7-2 shows that for $D'$ and $C^0{}_{dry}$ the multiple coefficient of determination is less than 30 %. For the slope and the sensitivity $R^2$ is higher than 50 % for the translucent class and higher than 30 % for the non-transparent class. These correlations are still relatively high especially when compared to the $R^2$ values obtained for the original 16 classes. This suggests that the sensitivity and the slope are useful indicators of the percentage area occupied by translucent or non-transparent vegetation respectively.

### 7.2.2. Discussion of Backscattering Characteristics

In this chapter the relationship of ERS Scatterometer parameters and the percentage area occupied by non-transparent vegetation, $A_{nt}$, is discussed. In the following figures, only those pixels where less than 1 % of the area is occupied by build-up areas, water surfaces, and open spaces with little or no vegetation are shown. In Figure 7-6 the scatter plot of $\sigma'(40)$ versus $A_{nt}$ can be seen. Slope values for January 1 and July 1 are displayed which are representative for winter and summer conditions. Since the maximum value of $A_{nt}$ is about 60 % a linear model is fitted to the data to indicate the trend towards higher values. While non-transparent vegetation is characterised by a high and stable slope, $\sigma'$ of translucent vegetation is typically low and exhibits a seasonal cycle. Higher summer values are caused by volume scattering effects in the vegetation canopies of translucent vegetation types. This explains why the spatial variability of the slope is higher in winter than in summer. Over the Iberian Peninsula $\sigma'(40)$ values range from -0.22 dB/deg to -0.1 dB/deg in winter and from -0.14 dB/deg to -0.07 dB/deg in summer. It also explains why the dynamic range of the slope is high over regions predominantly occupied by translucent vegetation and low over forested areas (Figure 7-7).

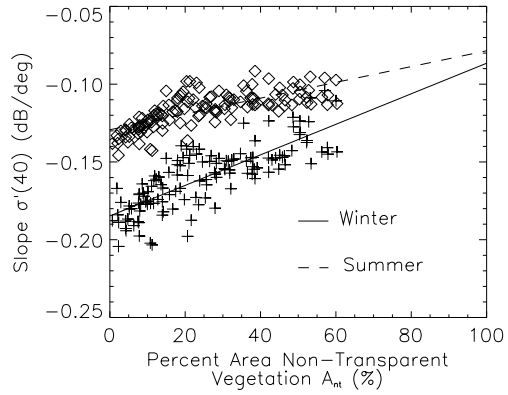


*Figure 7-6: Scatter plot of the slope at 40°, $\sigma'(40)$, versus the percentage area occupied by non-transparent vegetation types, $A_{nt}$. Slope values for t = January 1 represent winter conditions and are indicated by a cross. Slope values for t = July 1 represent summer conditions and are indicated by a diamond.*

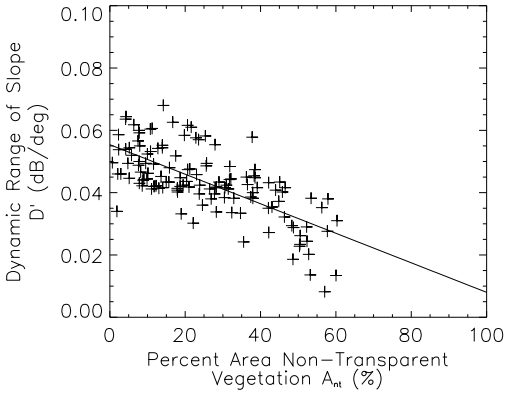


*Figure 7-7: Scatter plot of the dynamic range of the slope, $D'$, versus the percentage area occupied by non-transparent vegetation types, $A_{nt}$.*

Similar statements as for the slope can be made for the backscatter intensity $\sigma^0(40)$. As the slope, $\sigma^0(40)$ is high and stable over forests, bush- and shrubland (Figure 7-8). If the soil surface is dry $\sigma^0(40)$ is lower over agricultural- and grassland, but if wet $\sigma^0(40)$ of the translucent and non-transparent class

are comparable. As already discussed in Chapter 7.1.2, the increase of $\sigma^0(40)$ due to vegetation growth from winter to summer is relatively small. This implies that the sensitivity $S$ is only somewhat smaller in summer than in winter (Figure 7-9). The sensitivity $S$ decreases strongly with increasing $A_{nt}$ and becomes zero for $A_{nt}$ = 100 %. For $A_{nt}$ = 50 % the sensitivity is still about 2.5 dB.

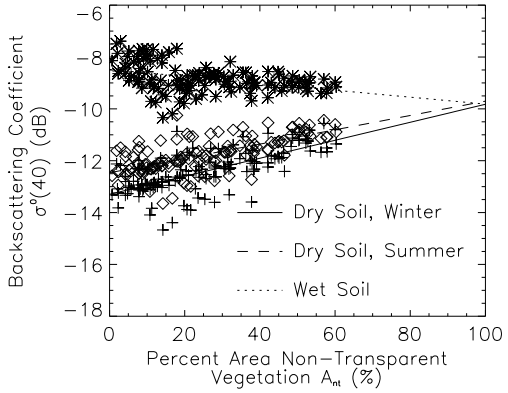


*Figure 7-8: Scatter plot of the backscattering coefficient, $\sigma^0(40)$, versus the percentage area occupied by non-transparent vegetation types, $A_{nt}$. $\sigma^0(40)$ values for dry and wet conditions are distinguished. For wet conditions $\sigma^0(40)$ is very stable and indicated by the symbol ✳. For dry conditions $\sigma^0(40)$ is somewhat higher in summer (symbol ◊) than in winter (symbol +).*

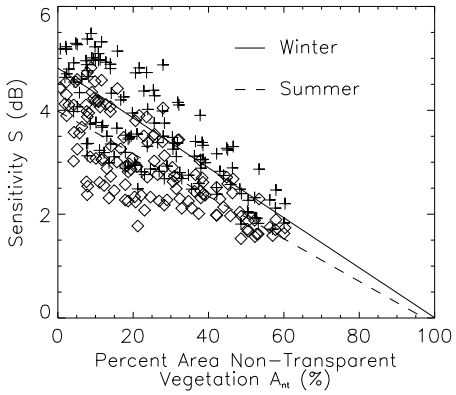


*Figure 7-9: Scatter plot of the sensitivity S versus the percentage area occupied by non-transparent vegetation types, $A_{nt}$. Sensitivity values for t = January 1 represent winter conditions (symbol +) and for t = July 1 summer conditions (◊).*

In Figure 7-10 the relationships discussed above are simulated with the model given in Table 5-1. A comparison of Figure 7-10 with Figures 7-6 to 7-9 shows that the model simulations differ somewhat from the empirical observations in absolute term and that the simulated parameters show a non-linear dependence on the percentage area $A_{nt}$. However, the general trend of the model is in reasonable agreement with observations.

Finally, it is noted that because of the similar behaviour of $\sigma'$ and $\sigma^0$ all ERS Scatterometer parameters are correlated. Table 7-3 shows the correlations based on the entire data set of the Iberian Peninsula.

| $R^2$ | $C'$ | $D'$ | $\sigma^0_{dry}$ | $C^S$ |
|---|---|---|---|---|
| $C'$ | - | 65.1 | 53.3 | 62.0 |
| $D'$ | - | - | 53.5 | 49.6 |
| $\sigma^0_{dry}$ | - | - | - | 58.5 |
| $C^S$ | - | - | - | - |

*Table 7-3: Coefficient of determination $R^2$ in % for a combination of ERS Scatterometer parameters.*

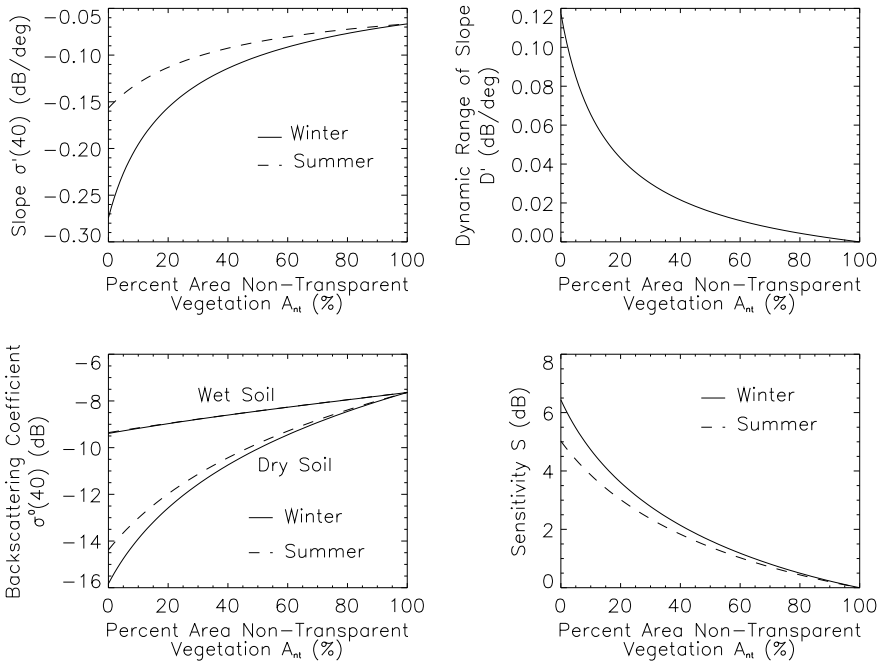


*Figure 7-10: Simulated dependence of the slope* $\sigma'(40)$*, dynamic range of slope D′, backscattering coefficient* $\sigma^0(40)$*, and sensitivity S on the percentage area occupied by non-transparent vegetation* $A_{nt}$ *using the model given in Table 5-1.*

# 8. Surface Soil Moisture Retrieval

## *8.1. Method*

The discussion of vegetation cover effects provided the necessary foundations for a simple soil moisture retrieval method. The algorithm is in principle a change detection method that compares $\sigma^0(40)$ to the lowest and highest values that have ever been recorded. The minima and maxima are denoted by $\sigma^0_{dry}(40,t)$ and $\sigma^0_{wet}(40)$, and are extracted automatically from the backscatter series. While $\sigma^0_{wet}(40)$ is more or less independent of vegetation status, $\sigma^0_{dry}(40,t)$ increases from winter to summer due to vegetation growth (Chapter 7.1.2). In Figures 8-1 and 8-2 time series of these parameters are compared to meteorological observations recorded at the synoptic stations Sarny and Simferopol in the Ukraine. Sarny is located in the more humid northern part of the country (51.35°N), and Simferopol in the more arid south on the Crimean Peninsula (45.02°N). It can be observed that the $\sigma^0(40)$ values are near $\sigma^0_{dry}(40,t)$ after dry periods of little or no rainfall, or during cold spells. In both cases, very little water is present in the upper soil layer and the dielectric properties are similar. The $\sigma^0(40)$ values are near the $\sigma^0_{wet}(40)$ line during periods of rainfall.

Assuming a linear relationship between $\sigma^0(40)$ and the surface soil moisture content (Ulaby et al., 1982) the relative soil moisture content in the surface layer, $m_s$, may be estimated with:

$$m_s(t) = \frac{\sigma^0(40,t) - \sigma^0_{dry}(40,t)}{\sigma^0_{wet}(40,t) - \sigma^0_{dry}(40,t)} . \qquad (8.1)$$

It is required that the ground is not frozen or covered with wet snow. The obtained quantity, $m_s$, is a relative measure of the soil moisture content in the first few centimetres of the soil that are accessible to C-band microwaves (0.5 - 2 cm). In the next chapter, some examples of $m_s$ series and maps are given.

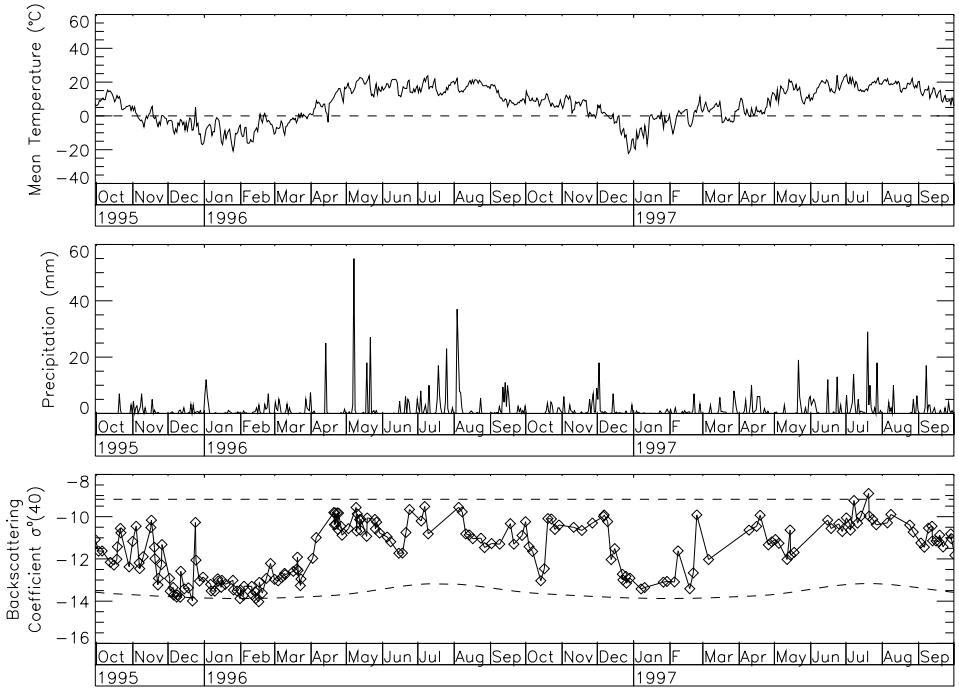


*Figure 8-1: Time series of mean temperature, precipitation and $\sigma^0(40)$ for the station Sarny (26.62°E, 51.35°N) for the period October 1995 to September 1997. In the bottom figure the backscattering coefficient of a dry and wet surface, $\sigma^0_{dry}(40,t)$ and $\sigma^0_{wet}(40)$ are indicated by dashed lines.*

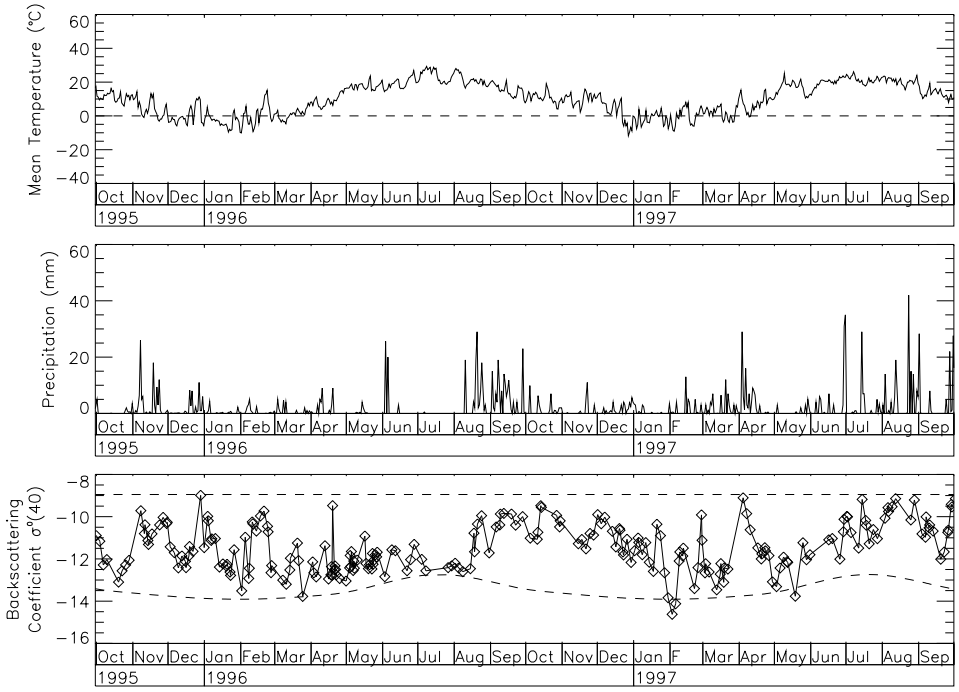


*Figure 8-2: Same as Figure 8-1 but for the station Simferopol (33.98°E, 45.02°N).*

## 8.2. Comparison with Rainfall Observations

In Figures 8-3 and 8-4 and Colour Figure 7 ERS Scatterometer retrieved $m_s$ series and maps are compared to rainfall observations over the Iberian Peninsula and Mali. Figure 8-3 shows $m_s$ and rainfall series for Sevilla, Spain, for the years 1994 and 1995. High $m_s$ values are associated with rainfall events and low $m_s$ values occur after some time without rain. Unfortunately, the temporal sampling rate of the ERS Scatterometer is not high enough to detect all rainfall events. For example, the 20 mm rainfall in the last week of April 1995 is not visible anymore in the ERS Scatterometer data acquired on May 4. If a rainfall is followed by a dry period, a quasi-exponential decrease can be observed, for example in January and November 1994, and in November 1995. This behaviour can be explained by the redistribution of the water in the wetted surface layer into the relatively dry deeper layers (Hillel, 1980).

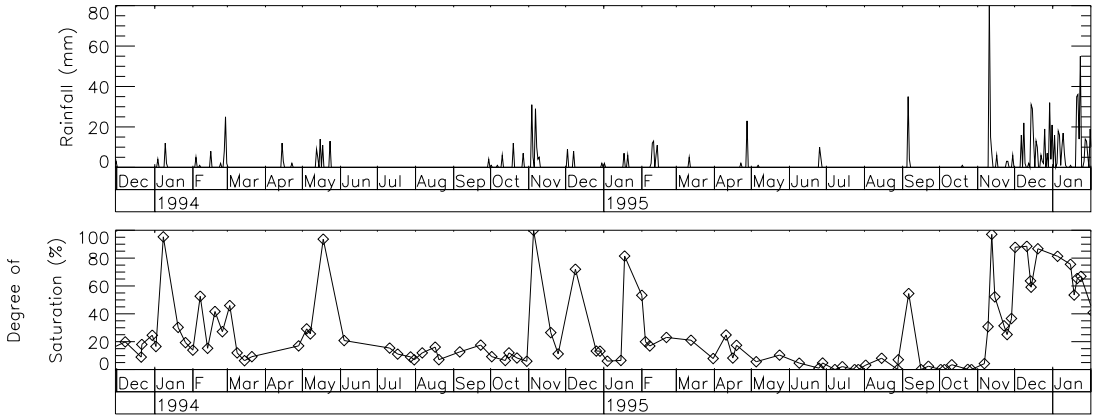


*Figure 8-3: Time series of the ERS Scatterometer retrieved $m_s$ (degree of saturation), and rainfall observations for Sevilla, Spain (5.88°W, 37.42°N) for the period December 1992 to January 1996. At this station the mean monthly temperature hardly ever falls below 5°C in winter.*

In Colour Figure 7 maps of monthly averaged $m_s$ data for the months December and January are compared to monthly rainfall recorded at 16 synoptic stations over the Iberian Peninsula. Due to SAR operations the number of $m_s$ values per month is variable. Therefore the values are not always representative for the full month, but should at least be able to describe the general wetness trend between the years. According to Christopherson (1997) at least 70 % of the precipitation in Mediterranean climates occurs during the winter months. However, rainfall is quite variable from year to year and sometimes, the weather patterns that provide winter precipitation fail to appear, leading to drought (Strahler and Strahler, 1996). When the soil moisture maps are compared, large year to year differences can indeed be observed. For example, while in January 1993 mean monthly $m_s$ values are below about 50 %, this value is exceeded over almost the entire peninsula in January 1996. This big difference is also evident in the rainfall data. In January 1993 the mean monthly rainfall of the 16 stations was only 10 mm, while in January 1996 it was 163 mm. Although there is no direct relationship between monthly rainfall and average surface soil moisture conditions, the spatial comparison reveals many similar patterns. For example, in January 1995 a west-east trend in humidity is evident in both data sources.

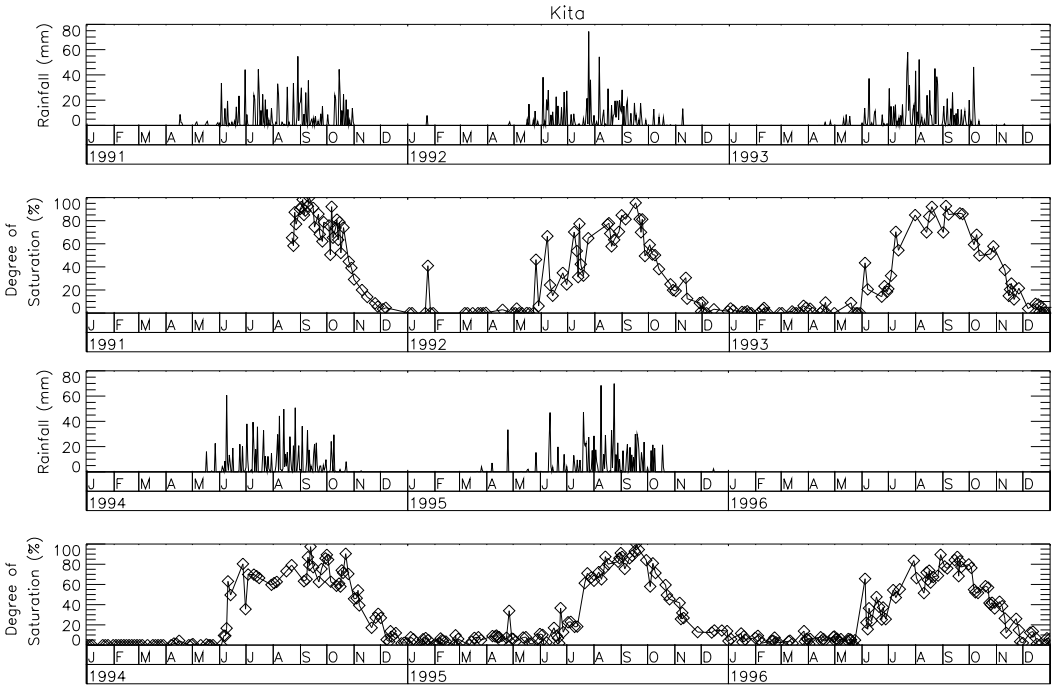


*Figure 8-4: Rainfall and ERS Scatterometer retrieved $m_s$ (degree of saturation) for Kita, Mali (9.28°W, 13.04°N) for the years 1991 to 1996. Rainfall data for the year 1996 are missing.*

Finally, in Figure 8-4 ERS Scatterometer retrieved surface wetness values are compared to rainfall recorded at Kita, Mali. During the dry season the ERS Scatterometer retrieved soil moisture values correctly depict the dry soil conditions. A remarkable feature during the dry season 1991/92 is the rainfall event in January 1992 that can be observed in both the ERS Scatterometer and the rainfall series. The beginning of the rainy season is indicated by the first rainfall observations at the meteorological station. Some of these initial rainfall events are not observed by the ERS Scatterometer because the sampling interval is longer than the persistence of these localised and singular showers at the soil surface. Only when rainfall becomes more frequent a lasting increase of the $m_s$ values can be observed. Soil moisture values reach their highest levels in general at the end of the rainfall season in September and decrease after that to reach their lowest levels in December.

## 8.3. Validation

In general it can be said that the qualitative comparison with meteorological observations and auxiliary information indicates a good quality of the remotely sensed surface wetness value. However, a thorough validation of the method would require a quantification of the error. Unfortunately, because of the lack of appropriate ground data, a truly quantitative validation of the ERS Scatterometer retrieved surface soil moisture estimates appears to be hardly feasible. For example, Schmugge and Jackson (1996) suggest that there is a limit to the accuracy which can be expected when ground samples are used to verify remotely sensed value because of the high temporal and spatial variability of the soil moisture content in the remotely sensed topsoil layer. In order to obtain a good estimate of the soil moisture content in the topmost 0.5 – 2 cm of the soil averaged over an area of about 50 x 50 $km^2$ from field observations, several dozens if not several hundreds of soil samples would have to be taken. Also, the field surveys would need to be conducted around the time of the satellite overpass, because the surface soil moisture conditions may change significantly within a few hours. The high costs of such field surveys do certainly not allow a truly quantitative validation of the remotely sensed surface values at this scale.

When the soil moisture content in layers of greater depth is considered then a quantitative validation appears to be more promising. This is because, due to the higher spatial correlation, fewer samples are required. Also, the exact timing of the field survey is less critical because of the higher temporal correlation. In fact, the results of a method to estimate the soil moisture content in the 0-20 cm and 0-100 cm layers from ERS Scatterometer and soil data will be validated by means of the gravimetric soil moisture data in Chapter 9. Although a quantitative validation of the retrieved surface wetness values appears hardly feasible, the relationship of $m_s$ with soil properties and climatic conditions is discussed in the following to gain a better understanding of the physical meaning of $m_s$.

## 8.4. Dependence on Soil Physical Properties

An absolute wetness value could be derived from $m_s$ if "calibration" points for the dry and wet case are available. Such an approach was for example used by Wang et al. (1990) to estimate soil moisture from NASA's L-band pushbroom microwave radiometer data. For clarity, some definitions of soil physics are reviewed here (Hillel, 1980, Koorevaar, 1983).

A soil is a heterogeneous system that, in general, consists of solid particles (mineral and organic), water and air. The solid particles constitute the matrix or 'skeleton' of the soil and occupy a volume $V_s$. The pore spaces between the soil particles have a volume $V_p$ and are filled with varying portions of water $V_w$ and air $V_a$. The total volume of the soil $V_t$ is equal to the sum $V_s$ and $V_p$. One way to express the amount of water in the soil is the volumetric water content $W$, which is defined as:

$$W = \frac{V_w}{V_t} = \frac{V_w}{V_s + V_p} \tag{8.2}$$

When all the soil pores are filled with air then $W$ is zero. When all the pores are filled with water then the soil is said to be saturated. The water content at saturation is called the total water capacity *TWC* and is equal to the relative pore volume $V_p/V_t$, also called porosity. In general, *TWC* takes on values between 30 % and 60 %.

The wilting point *WP* and the field capacity *FC* are two soil constants that, although not clearly defined in physical terms (Hillel, 1980), are commonly supposed to apply to critical thresholds in soil moisture content (Jones, 1997). The concepts of *WP* and *FC* can be explained by the different forces that act on the water molecules in a soil: Soil water is most strongly held when absorbed into colloidal particle surfaces in the form of thin films only a few molecules in thickness (hygroscopic water), or when it is bound up in mineral structures (structural water) (Ellis and Mellor, 1995). Further away from the particle surfaces, water is held in small micropores by capillary forces. Much of this water can be lost

though evaporation and plant uptake. Water held in the macropores usually drains rapidly from the soil under the influence of gravity. A soil which has lost most of its 'gravitational' water after two days of drainage is said to be at field capacity. The wilting point, on the other hand, is the soil moisture content at which the suction to remove the remaining water from the soil is too great for plants to exert. These two parameters are not independent of the way they are measured (Hillel, 1980), but are still useful because they provide indirect information about the strength of the various forces acting on the water molecules, which in turn are related to the textural and structural properties of the soil.

Several years of ERS Scatterometer data are already available, and the question is how $\sigma^0_{dry}$ and $\sigma^0_{wet}$ are related to the above discussed soil constants. According to Hillel (1980) the driest possible condition in nature is a state called air-dryness, at which there is still some water (hygroscopic and structural) in the soil. This means that $\sigma^0_{dry}$ corresponds to some water content $W_{min}$ which is somewhere between zero wetness and wilting level. However, considering that the remotely sensed surface layer (0.5–2 cm) is the active layer for evaporation, $W_{min}$ may be expected to be closer to zero than to the wilting point. If deeper soil layers would be considered this situation may be reversed because once the top few centimetres are completely dry, the upward capillary movement of water is slow, and the water in the subsoil is preserved (Ellis and Mellor, 1995).

The wettest possible condition is that of saturation, but there will always be some air trapped in the soil (Hillel, 1980). Therefore $\sigma^0_{wet}$ corresponds to some wetness value $W_{max}$ that is between field capacity and total water capacity. $W_{max}$ can be expected to closer to *TWC* than to *FC* because it is very likely that some ERS Scatterometer data were acquired during rainfall events. Also in this case, the reverse might be true for deeper layers. With increasing soil wetness the infiltration capacity decreases, and the rainfall in excess of the infiltration rate will result in surface runoff (Jones, 1997). Therefore only the upper soil layers will be saturated, and the depth of the wetted zone will depend on the infiltration rate and the duration of the rainfall event.

For these reasons, the best working assumption appears to be to relate $\sigma^0_{dry}$ to a completely dry soil surface, and $\sigma^0_{wet}$ to a saturated soil surface. In this case, $m_s$ is equal to the degree of saturation which is defined as the ratio of *W* and *TWC*. It must be noted that this definition strictly applies only to the case when the mineral soil horizon constitutes the topmost soil layer. The definition of $m_s$ is less clear when an organic layer consisting of undecomposed litter and/or partly decomposed debris is overlying the mineral soil horizons.

## 8.5. Dependence on Climate Type

The existence of spatially uniform "calibration" points for the dry and wet case is a necessary condition to allow a spatial comparison of the $m_s$ values. In the last chapter, it was assumed that $\sigma^0_{dry}$ and $\sigma^0_{wet}$ can be related to a completely dry and saturated soil surface, without considering the climatic conditions. Nevertheless, it is clear that, for example, in a wet equatorial climate the soil surface may never dry out completely, or that in a desert, the soil may never become saturated. The assumption that $m_s$ is an approximate measure of the degree of saturation of the soil surface layer can therefore be valid only for a limited range of climatic conditions. The hypothetical difference between the ERS Scatterometer estimate and the real value of the degree of saturation, $\Delta m_s$, is given by:

$$\Delta m_s = \frac{W - W_{min}}{W_{max} - W_{min}} - \frac{W}{TWC} \tag{8.3}$$

where $W_{min}$ and $W_{max}$ are the soil moisture values that correspond to $\sigma^0_{dry}$ and $\sigma^0_{wet}$ respectively. Figure 8-5 shows the difference $\Delta m_s$ for dry, moist, and wet soil conditions. A number of observations can be made:

1. Uncertainties related to $\sigma^0_{dry}$ introduce the largest errors when the soil moisture content of a dry soil is estimated. This means that in humid climates, where the largest uncertainties with respect to $\sigma^0_{dry}$ can be expected, the bias $\Delta m_s$ may be large during (less frequently occurring) dry periods, and smaller for the 'normal' weather conditions. In dry climates, this error is probably less important, because $\sigma^0_{dry}$ can be expected to be close to the real backscattering coefficient of a completely dry soil surface.
2. Uncertainties related to $\sigma^0_{wet}$ introduce the largest errors when the soil is wet. Following the argumentation in the previous point, the largest error can be expected during wet periods in dry climates.
3. In general, the errors caused by the uncertainties related to $\sigma^0_{dry}$ and $\sigma^0_{wet}$ tend to cancel each other out for moist conditions. For example, if both $W_{min}$ and $TWC\text{-}W_{max}$ are around 5 % then $\Delta m_s$ is zero.

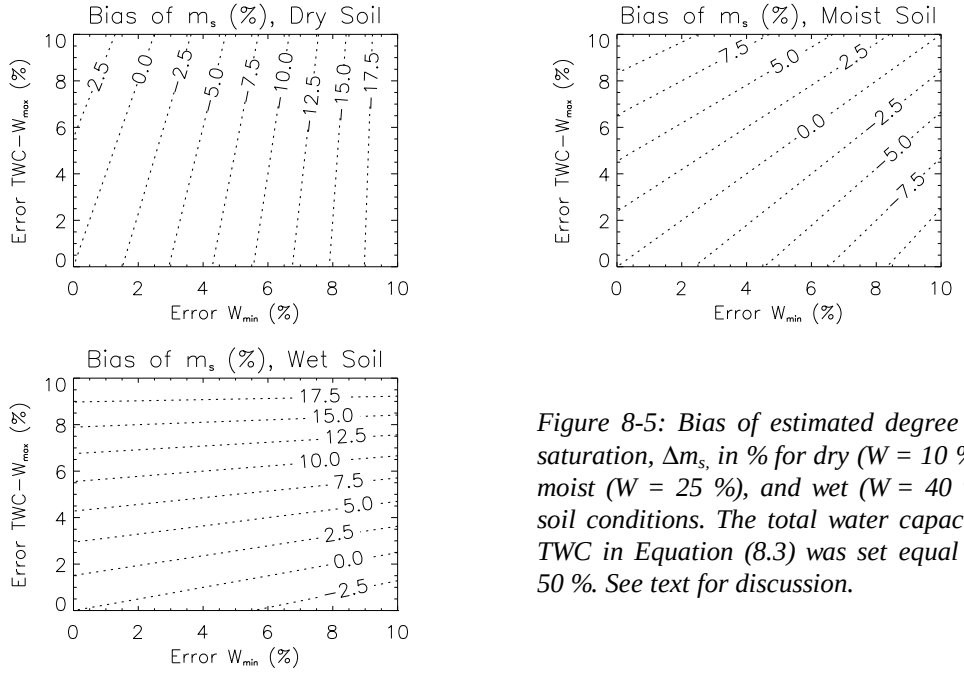


*Figure 8-5: Bias of estimated degree of saturation, $\Delta m_s$, in % for dry (W = 10 %), moist (W = 25 %), and wet (W = 40 %) soil conditions. The total water capacity TWC in Equation (8.3) was set equal to 50 %. See text for discussion.*

It can be concluded that in climates where during drought or freezing periods the liquid water content in the topmost centimetres of the soil (0.5 – 2 cm) may fall below about 5 % and where rainfall may be sufficient to saturate the soil surface the error will be less than about 10 %. The question is now, in which climates can these conditions be met? Of course, no unique relationship between climate type and soil moisture extremes can be established because this will always depend on the occurrence of extreme hydrological events. However, it should be possible to give some general guidelines in which climates it may at least be possible to meet the criteria above.

The condition of dryness is most easily fulfilled in climates with a dry season and/or high temperatures. According to Strahler's climate classification system, examples for such climates are: dry tropical, dry subtropical, wet-dry tropical, mediterranean, dry-midlatitude, and monsoon and trade-wind coastal climate. The fact that a frozen soil, which may be covered by dry snow or not, has a backscattering coefficient similar to that of snow-free dry soil probably allows to extend the range of validity to more moist climates: moist continental, marine west-coast, and boreal forest. On the other hand, the condition of saturation is most easily met in climates where ample precipitation may occur, including all moist and wet-dry climates of Table 8-1. For the dry climatic types, rainfall may not be sufficient to saturate the soil surface, a situation that is aggravated for sandy soils and high potential evaporation.

| | Climate Type | | |
|---|---|---|---|
| *Climate group* | *Moist* | *Dry* | *Wet-Dry* |
| *Low-latitude climates* | Wet equatorial<br>**Monsoon and trade-wind coastal** | Dry tropical | **Wet-dry tropical** |
| *Midlatitude climates* | Moist subtropical<br>**Marine west coast**<br>**Moist continental** | Dry subtropical<br>**Dry midlatitudes** | **Mediterranean** |
| *High-latitude climates* | **Boreal forest**<br>Tundra | Ice sheet | |

*Table 8-1: Moist, dry, and wet-dry climates after Strahler and Strahler (1996). For the climates shown in bold letters, the ERS Scatterometer retrieved wetness values $m_s$ may possibly be identified with the degree of saturation of the soil surface layer.*

As an example, let us regard the Mali study area. In the south of the study area (9°N) about 1500 mm of rain falls in the period from March to October, and hardly any rain occurs between November and February. In the north (16.5°N) mean annual rainfall, which is concentrated in the months July to September, is less than 400 mm. Because of the long dry period, which is at least four months, one can be confident that $\sigma^0_{dry}$ corresponds to a completely dried out soil surface. Also, saturation is certainly reached in the south of the domain, but in the north this is less clear. In Colour Figure 5 it can be seen that in the southern half of the study area, $\sigma^0_{wet}$ is fairly constant with values between about –7.5 dB and –9 dB. In the north, $\sigma^0_{wet}$ decreases quickly from –9 to -15 dB. The high $\sigma^0_{wet}$ values around 4.5°W and 15°N are the exception. This area is the Niger Delta which is flooded annually by the rivers Niger and Bani (Bart, 1986). A comparison of the $\sigma^0_{wet}$ map with maps of mean annual precipitation reveals similar patterns. For example, the -10 dB contour line corresponds roughly with the 600 mm isohyet. Because $\sigma^0_{wet}$ was found to show little dependence on vegetation cover (Chapter 7.2.2), it can be concluded that, although soil effects may also play a role, the decrease of $\sigma^0_{wet}$ in the northern part of the study area is associated with the failure to saturate the soil surface. With additional assumptions one might still be able to compare $m_s$ values from the south and the north. For example, one might assume that $\sigma^0_{wet}$ does not decrease below –9 dB, and consequently set all $\sigma^0_{wet}$ values below –9 dB to this threshold value. Of course, this will introduce errors, especially for wet soil conditions, but it will depend on the kind of application if this error is acceptable or not.

# 9. Profile Soil Moisture Retrieval

Remote sensing techniques provide information about the soil surface layer. To infer the water content in the soil profile, auxiliary data on soil characteristics are needed. In this chapter a simple method for estimating the profile soil moisture content from ERS Scatterometer and soil data is developed and validated with an extensive data set of gravimetric field measurements in the Ukraine. Before the method is introduced the properties of Ukrainian soils are discussed.

## *9.1. Properties of Ukrainian Soils and Spatial Representativity*

The Ukraine lies in the soil fertile triangle of the former Soviet Union. Many of its fertile soils developed on loess deposits which cover much of the Ukraine (Christopherson, 1997). Russians refer to their fertile soils as chernozems. Information on soils is drawn from two sources: the FAO-Unesco Soil Map of the World at the scale 1:5,000,000 and the agrometeorological network in the Ukraine of which data from 211 measurement fields are available.

### 9.1.1. Soil Type

The FAO-Unesco soil map of the Ukraine is shown in Colour Figure 8. The dominant soils are Chernozems, which occupy most of the interior of the Ukraine, and Kastanozems, which can be found in the south. In the northern and western part of the country Luvisols and Podzoluvisols can often be found. Chernozems and Kastanozems are soils conditioned by the steppe environment (FAO, 1993). The climate of these soils is characterised by relatively low rainfall (250 – 600 mm per year) concentrated in spring and early summer, with cold to very cold winters and short, warm to hot summers. The rainfall is sufficiently limited to prevent excessive leaching. The natural vegetation is dominated by grass species, producing a mass of fine fibrous root in the upper horizon. This results in soil characterised by a thick, dark, humus- and nutrient rich surface horizon. The surface horizon may extent down to a depth of two meters and the organic matter content may be as high as 16 %. While Chernozems developed in the colder areas of the steppe under a tall grass prairie, Kastanozems are soils of the drier and warmer areas of the steppe. Luvisols and Podzoluvisols can be considered as the moist version of the steppe soils. The climate is cold temperate or colder with evenly distributed precipitation of between 500 and 1000 mm a year. Trees are the natural vegetation. Other soil types found in the Ukraine are in order of significance Greyzems, Cambisols, Fluvisols, Gleysols, Histosols, Lithosols, Phaeozems, Planosols, Podzols, and Solonetz.

### 9.1.2. Spatial Representativity

For studying the spatial trend of soil physical properties, the soil data from the agrometeorological network were plotted on the FAO-Unesco soil map. For example, in Colour Figure 8 mean values of the wilting level for the 0-100 cm layer reported at the agrometeorological stations are shown. The comparison makes clear that there are not sufficient data (one station per ca. 6100 $km^2$) to characterise the real spatial distribution of the soil physical properties. Therefore geostatistical methods (Isaaks and Srivastava, 1989; Kitanidis, 1997) for estimating spatial patterns from point values cannot be meaningfully applied because these methods assume that the properties vary in an arbitrary way between the sample points. Blöschl (1996) calls this the ‘disorderly assumption’ which states that no order exists beyond what is known from the data. As a consequence, maps of soil constants (e.g. wilting level) will be produced by using nearest neighbourhood interpolation.

Also, for lack of any better alternative, the field measurements of soil moisture are therefore directly compared to the nearest ERS Scatterometer pixel. This introduces the problem of scale matching as data representing an area of 0.1 hectare are compared to data representing 60 x 60 $km^2$. Under 'nearest' pixel the pixel closest to the agrometeorological stations is understood. If however, the station is located at the coast or close to a large water body then a pixel further inland is used to avoid the disturbing influence of water on the ERS Scatterometer signal.

### 9.1.3. Soil Texture and Soil Constants

Soil texture reported at the 211 fields of the agrometeorological network encompass the classes sandy, loamy sand, light loamy, mid loamy, heavy loamy, clayey, light clayey, and clayey sand. The great majority of the fields (92 %) have a light loamy to heavy loamy soil texture. The texture or particle size distribution of mineral soils determines to a large extent the physical and chemical behaviour. Figures 9-1 to 9-3 show how wilting level, field capacity, and total water capacity (porosity) change with soil texture for the 0-10 cm, 0-20 cm, and 0-100 cm layers for the 211 measurement fields in the Ukraine. Because of higher soil matrix forces the wilting level and field capacity increase with increasing clay content. Also, the clayey soils in the Ukraine tend to have a higher total water capacity, as is generally the case (Koorevaar et al., 1983).

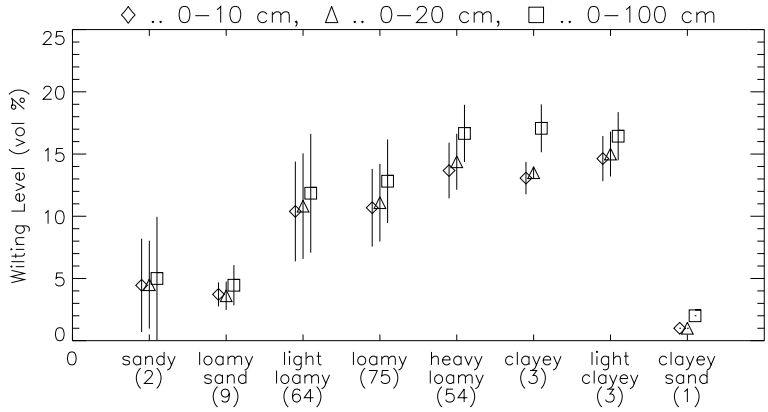


*Figure 9-1: Wilting level, WL, in % for different soil textures and for three soil layers (0-10 cm, 0-20 cm, 0-100 cm) based on measurements on 211 fields in the Ukraine. The mean value and a bar representing the range mean value ± standard deviation are shown. The numbers of field measurements on which these values are based are shown in brackets below the texture classes.*

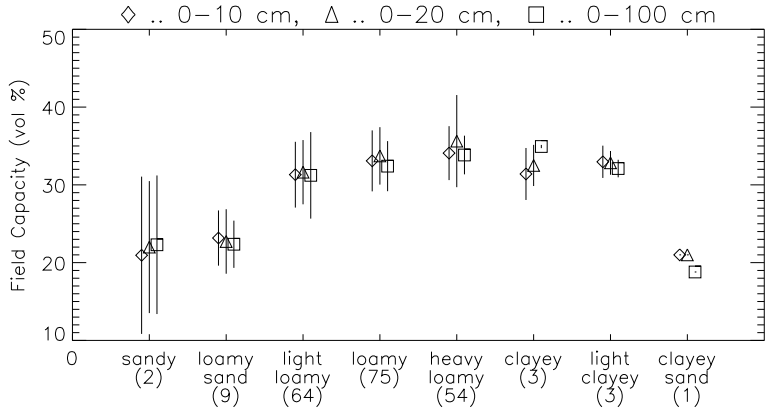


*Figure 9-2: Same as Figure 9-1, but for the field capacity FC.*

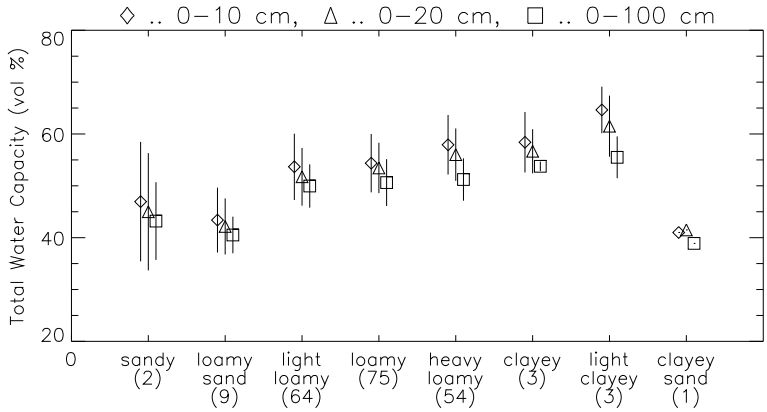


*Figure 9-3: Same as Figure 9-1, but for the total water capacity TWC.*

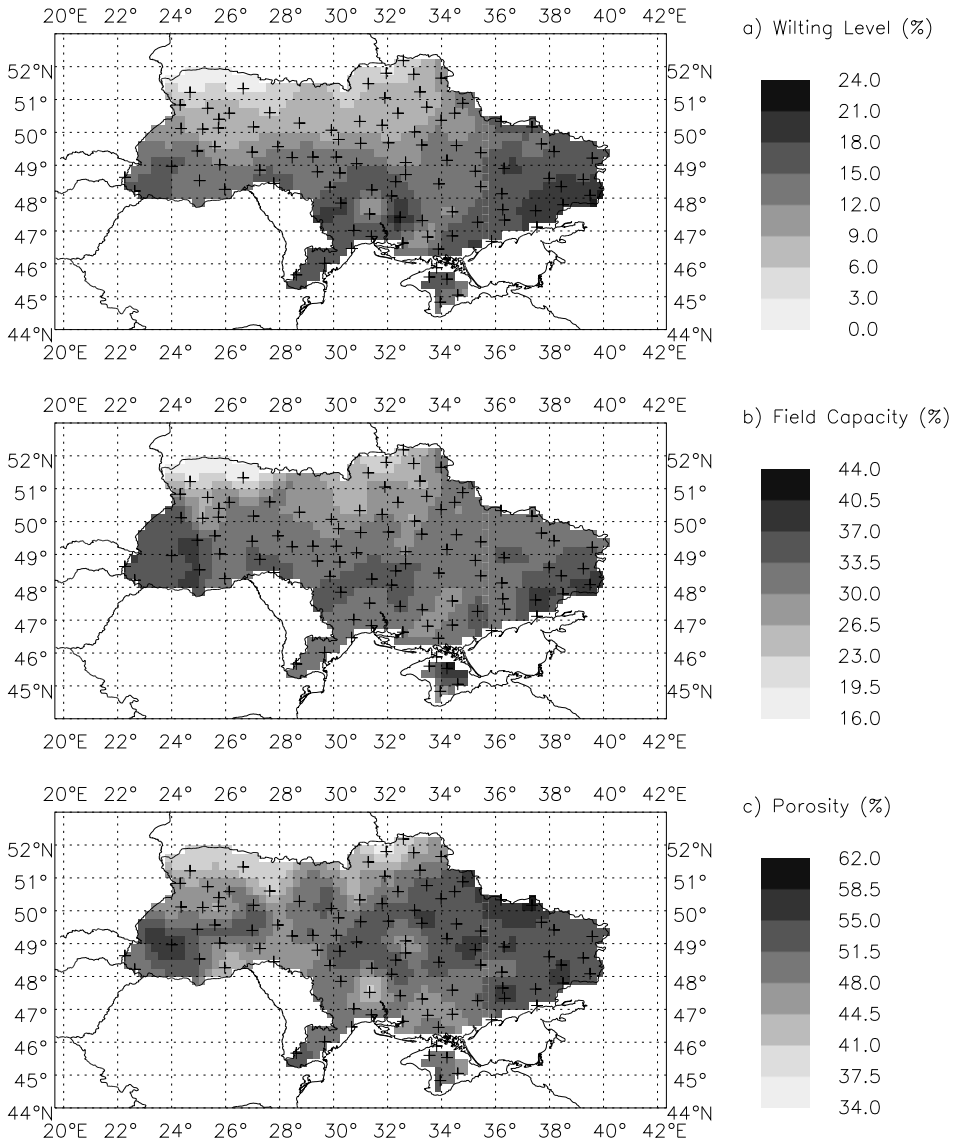


*Figure 9-4: Soil constants for 0-100 cm soil layer interpolated to a 0.25° grid. The crosses indicate the location of the agrometeorological stations. a) Wilting level; b) Field capacity; c) Porosity or total water holding capacity. All constants are expressed in volumetric percent.*

A spatial analysis of texture shows that there is a north-south trend with more sandy soils in the north and more clayey soils in the south. This trend finds its expression in the spatial variability of soil constants. In Figure 9-4 maps of the wilting level, field capacity, and porosity of the 0-100 cm layer are shown. These maps were obtained by calculating the mean value of the fields at each station, interpolating these values to a 0.25° grid using the nearest neighbourhood method, and by smoothing the resulting maps with a 3 x 3 pixels window. The wilting level is low with values around 5 % in the northern part of the Ukraine where Luvisols and Podzoluvisols are the dominating soils. Towards the south the clay content and consequently the wilting level increase with maximum values of about 20 %. Along the river Dnepr wilting levels are somewhat lower than in the surrounding areas due to fluvial processes. The spatial patterns of field capacity are similar with minimum values of about 20 % for the more sandy soils and maximum values of about 40 % for the more clayey soils. The porosity or total water capacity shows somewhat different patterns with most values falling in the range from 40 to 60 %.

Also pedotransfer functions might be useful for deriving spatially integrated soil properties based on the FAO-Unesco soil map. However, since field measurements will be directly compared to the nearest ERS Scatterometer pixels, the values determined with the method described above are preferred because the average station data represent the best available estimates in the vicinity of the agrometeorological stations. Further away from the stations the maps contain errors due to the small number of stations, but to produce overview maps they were found to be useful.

## *9.2. Method*

### 9.2.1. Soil Water Index

In a number of studies the question how to estimate the moisture content in the soil profile from surface measurements has been investigated (Jackson, 1986; Ragab 1992 and 1995; Entekhabi et al., 1994; Shutko et al., 1994). The proposed methods range from simple statistical relationships to physically based retrievals. The problem of using these methods for ERS Scatterometer data analysis is that most of the studies were conducted on small areas and that the models require empirical parameters as input that vary with soil type and vegetation cover. The input parameters to these models are often site specific and were not available to this study. Another drawback of some of these methods is that they relate the instantaneous value of surface moisture to the profile moisture assuming for example a linear relation between the surface and profile soil moisture or hydraulic equilibrium conditions (Kondratyev et al., 1977; Jackson, 1980). Because of these problems and because of the good temporal resolution of the ERS Scatterometer it was decided to develop as a first step a simple empirical method for estimating the profile moisture from the $m_s$ series.

It can be assumed that the time series of surface wetness observations from the ERS Scatterometer gives an indication about the wetting and drying trend of the moisture content in the soil profile. This is because the profile moisture content is affected by the weather patterns during the preceding few days to weeks which are reflected in the $m_s$ series. Since the soil moisture content integrated over deeper layers exhibits much smaller variations than in the topmost layer, it appeared sensible to use a filter which smoothes the $m_s$ series to reproduce the trend in deeper layers.

To define an appropriate low-pass filter a simple two-layer water balance model is considered. The first layer represents the remotely sensed topsoil layer, and the second layer which extends downwards from the bottom of the surface layer is assumed to be a reservoir that has no contact to the outside world other than via the surface layer. In this model, the water content in the surface layer is highly dynamic due to various processes such as precipitation, evaporation, and surface runoff. The water content in the reservoir varies only slowly because its rate of change is limited by the amount of water that can be

exchanged with the surface layer. The water flux between the two layers is assumed to be proportional to the difference of the volumetric water content in the surface layer and in the reservoir. Under this assumptions the water balance equation for the reservoir is:

$$L\frac{dW}{dt} = C \cdot (W_s - W) \tag{9.1}$$

where $W$ is the volumetric moisture content of the reservoir, $W_s$ of the surface, $t$ is the time, $L$ is the depth of the reservoir layer, and $C$ is a pseudo-diffusivity coefficient that depends on the soil properties. Setting $T = L/C$ gives following solution of this differential equation:

$$W(t) = \frac{1}{T}\int_{-\infty}^{t} W_s(\tau) e^{-\frac{t-\tau}{T}} d\tau \tag{9.2}$$

In this model the water content in the reservoir is fully explained by the past dynamics of the surface soil moisture content. More recent events have a stronger impact on the reservoir water because of the exponential weighting function. Equation (9.2) may be viewed as the description of the redistribution process of the water in the surface layer into the deeper layers. The parameter $T$ represents a characteristic time length and increases with the depth of the reservoir $L$ and decreases with the pseudo-diffusivity constant $C$. It is noted that

$$T = \int_{-\infty}^{t} e^{-\frac{t-\tau}{T}} d\tau \,. \tag{9.3}$$

Many important processes like transpiration are not considered in this abstract water balance. Also, it is assumed that soil hydraulic conductivity is constant while in reality it may vary over orders of magnitude depending on soil moisture conditions (Hillel, 1980). However, it is still useful as a general concept for estimating the profile soil moisture content, accounting for the decreasing influence of measurements with increasing time. In addition, the model provides some physical insight into the characteristic time length $T$. Thus a Soil Water Index $SWI$ is defined:

$$SWI(t) = \frac{\sum_i m_s(t_i)\, e^{-\frac{t-t_i}{T}}}{\sum_i e^{-\frac{t-t_i}{T}}} \qquad \text{for } t_i \le t \tag{9.4}$$

where $m_s$ is the surface soil moisture estimate from the ERS Scatterometer at time $t_i$. The $SWI$ is calculated if there is at least one ERS Scatterometer measurement in the time interval [$t$,$t$-$T$] and at least three measurements in the interval [$t$,$t$-5$T$].

The parameter $T$ was determined by calculating the correlation between $SWI$ and the ground observations in the 0-20 cm and 0-100 cm layers from the 211 fields for $T$ values ranging between one and one hundred days and by determining $T$ where the highest correlation is observed. Initially, ERS Scatterometer data from the morning passes (around 10:30 h, descending node) and evening passes (22:30 h, ascending node) were kept separate. The highest correlations were obtained if the $SWI$ was based on descending passes only. But since very few acquisitions have been taken during the morning passes it was decided to use all ERS Scatterometer data to calculate the $SWI$. The best correlation between the remotely sensed and the 0-20 cm field data is observed if $T$ is set equal to 15 days. For the 0-100 cm layer setting $T$ equal to 20 days gave the best results. How different choices of $T$ would affect the accuracy of the retrieved soil moisture data will be discussed in more detail in Chapter 9.3.2.

### 9.2.2. Merging Soil and Remote Sensing Data

The Soil Water Index *SWI* is a trend indicator ranging between 0 and 1. For estimating the water in deeper layers auxiliary information about the soil physical properties is needed. The idea is to define calibration points for dry and wet conditions. Let us assume that $W_{min}$ and $W_{max}$ are the minimum and maximum soil wetness values that can occur in a particular soil. Assuming further a linear relationship, the profile soil moisture content *W* at the time *t* may be estimated from *SWI* with:

$$W(t) = W_{min} + SWI(t) \cdot (W_{max} - W_{min}) \tag{9.5}$$

The soil parameters commonly used to define critical soil moisture values are the wilting level *WL*, the field capacity *FC*, and the total water capacity *TWC*. To investigate how $W_{min}$ and $W_{max}$ are related to these soil parameters, the frequency distribution of the gravimetric measurements on the 211 fields was analysed for both layers.

Figures 9-5 and 9-6 show the histograms of *W* for the 0-100 cm layer for two fields with very different characteristics. The first field (Figure 9-5) has heavy loamy texture and the great majority of the measured soil moisture values is relatively evenly distributed in the range from wilting level (18 %) to field capacity (33 %). Some *W* values are above field capacity. On the other hand, the loamy sand field in Figure 9-6 has low values for both the wilting level (2 %) and the field capacity (16 %), and the frequency distribution of *W* resembles a log-normal distribution with the centre near the field capacity. A considerable percentage of the values are above field capacity, but all are lower than 30 %.

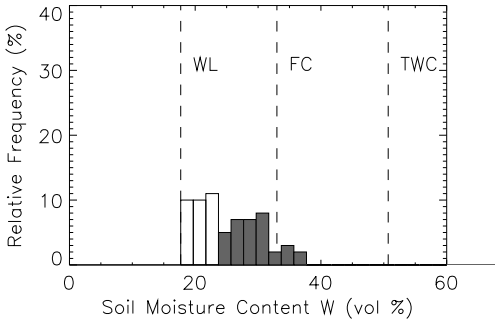


*Figure 9-5: Histogram of soil moisture content W in % of the 0-100 cm layer at the winter wheat field at the station Belovodsk (39.58°E, 49.21°N). The field has a chernozem soil with a heavy loamy texture. The wilting level WL, field capacity FC, and total water capacity TWC are indicated by the dashed lines.*

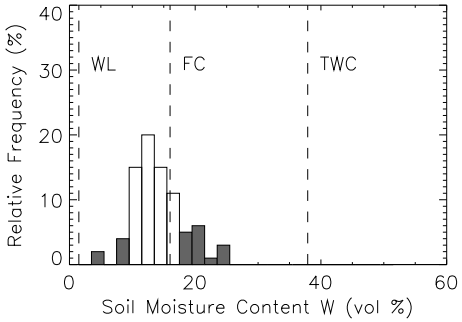


*Figure 9-6: Histogram of soil moisture content W in % of the 0-100 cm layer at the winter wheat field at the station Sarny (26.65°E, 51.33°N). The field has a dark grey podzolic soil with a loamy sand texture. The wilting level WL, field capacity FC, and total water capacity TWC are indicated by the dashed lines.*

A summary statistics for all 211 fields is prepared by dividing the range of possible soil moisture values into three classes: from zero wetness to wilting level, from wilting level to field capacity, and from field capacity to total water capacity; and by calculating the frequency distributions within these three classes separately. The resulting histograms for the 0-20 cm and 0-100 cm layers are shown in Figure 9-7. It can be seen that the minimum values are at *WL* and the maximum values above *FC*. The histogram for the 0-20 cm layer shows a peak at *WL*, which prompted me to inquire at the data providers. According to Zabeline (1998) in only very few cases soil wetness is below wilting level. Usually, in such situations a

crust is formed at the top that prevents further evaporation, and the moisture below the crust is preserved. The maximum soil wetness measurements exceed *FC* in 10.4 % of the cases for the 0-20 cm layer, and in 8.5 % for the 0-100 cm layer. The upper limit is roughly half way between *FC* and *TWC*.

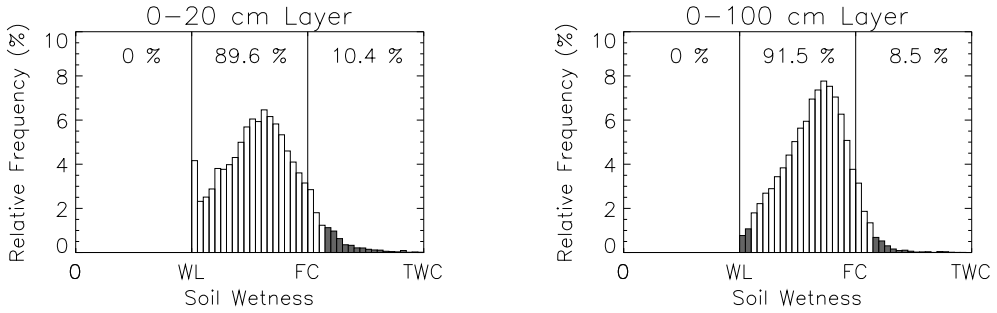


*Figure 9-7: Histogram of soil moisture content in 0-20 cm layer (left side) and 0-100 cm layer (right side) based on measurements on 211 fields in the Ukraine. WL is the wilting level, FC the field capacity, and TWC the total water capacity*

The choice of $W_{min}$ and $W_{max}$ for Equation (9.5) is based on the results of the statistics. This requires that the *SWI* is capable of accounting for very different frequency distributions of *W* which depend on the soil type and the climatic conditions. Let us set $W_{min}$ equal to *WL* and $W_{max}$ to the arithmetic mean of *FC* and *TWC* and substitute these values into Equation (9.5):

$$W(t) = WL + SWI(t) \cdot \left( \frac{FC + TWC}{2} - WL \right). \tag{9.6}$$

The water content available to plants, *PAW*, which is defined as the water content exceeding the wilting level, can be directly derived from (9.6):

$$PAW(t) = SWI(t) \cdot \left( \frac{FC + TWC}{2} - WL \right). \tag{9.7}$$

Values for *WL*, *FC*, and *TWC* for the 0-20 cm and 0-100 cm layers are taken from the maps as described in Chapter 9.1.3. This means that for the ERS Scatterometer pixels nearest to the agrometeorological stations the employed soil constants are essentially the mean values over the fields at these stations, which represent the best available estimates of *WL*, *FC*, and *TWC* for these pixels

### 9.2.3. Discussion

An example how plant available water *PAW* estimated with Equation (9.7) compares to the field measurements can be seen in Figure 9-8. The example is taken from a region in south-eastern Ukraine for the period from March to December 1996. The figure shows mean temperature in °C (top) and precipitation in mm (second from top) recorded at the station Dnepropetrovsk, ERS Scatterometer retrieved surface soil moisture values $m_s$ (third from top), and plant available water for the 0-20 cm (second from bottom) and for 0-100 cm layers (bottom) measured at maize, spring wheat, and winter wheat fields and estimated from ERS Scatterometer and soil data. Until May 1996 both ERS-1 and ERS-2 were in operation and the resulting high temporal sampling rate allows to detect many individual rainfall events. As has already been observed previously the temporal behaviour of $m_s$ resembles a sawtooth line: jumps and quasi-exponential declines of $m_s$ are caused by rainfall events and consecutive drying periods.

In March and December temperatures fell below 0°C resulting in unrealistic low values of $m_s$. These values associated to freezing and/or wet snow conditions should be discarded, but unfortunately, based on the backscattering series alone, it is difficult to define criteria for detecting frozen soil or wet snow in this region.

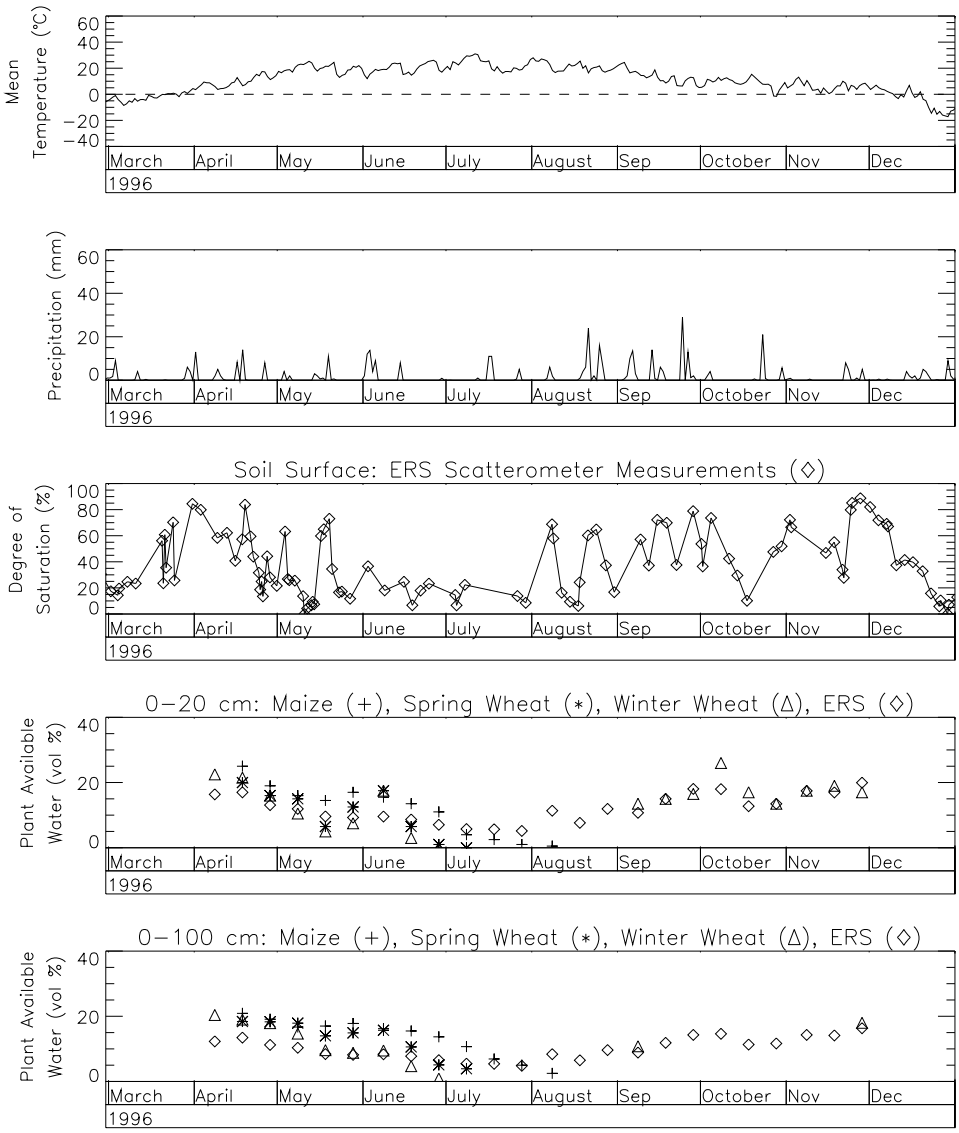


*Figure 9-8: Meteorological observations, field measurements of soil moisture, and remotely sensed wetness values for Dnepropetrovsk (35.08°E, 48.37°N) for the year 1996. The third diagram from the top shows ERS Scatterometer retrieved surface moisture $m_s$. The two diagrams on the bottom show plant available water content in % for the 0-20 cm and 0-100 cm layers measured on maize (cross), spring wheat (asterix), winter wheat (triangle) fields and the remotely sensed soil wetness values (diamond) according to Equation (9.7).*

In the two bottom diagrams of Figure 9-8 it can be seen that the remotely sensed soil moisture values agree reasonable well with the field measurements; the differences between the measurements on the various fields are comparable to the deviations between the remote sensing and field data. For the 0-100 cm layer, the correlation coefficient *R* (based on all six years of data for this station) between the remotely sensed *PAW* and the maize field is 0.44, 0.56 for spring wheat, and 0.5 for winter wheat. The bias, which is the systematic difference of the field measurements minus the remote sensing measurements, is 4.8 % for maize and spring wheat, and 3.9 % for winter wheat, i.e. the moisture content on the fields is overestimated for this station. The r.m.s. errors are 6.3 % for maize, 5.9 % for spring wheat, and 5.6 % for winter wheat.

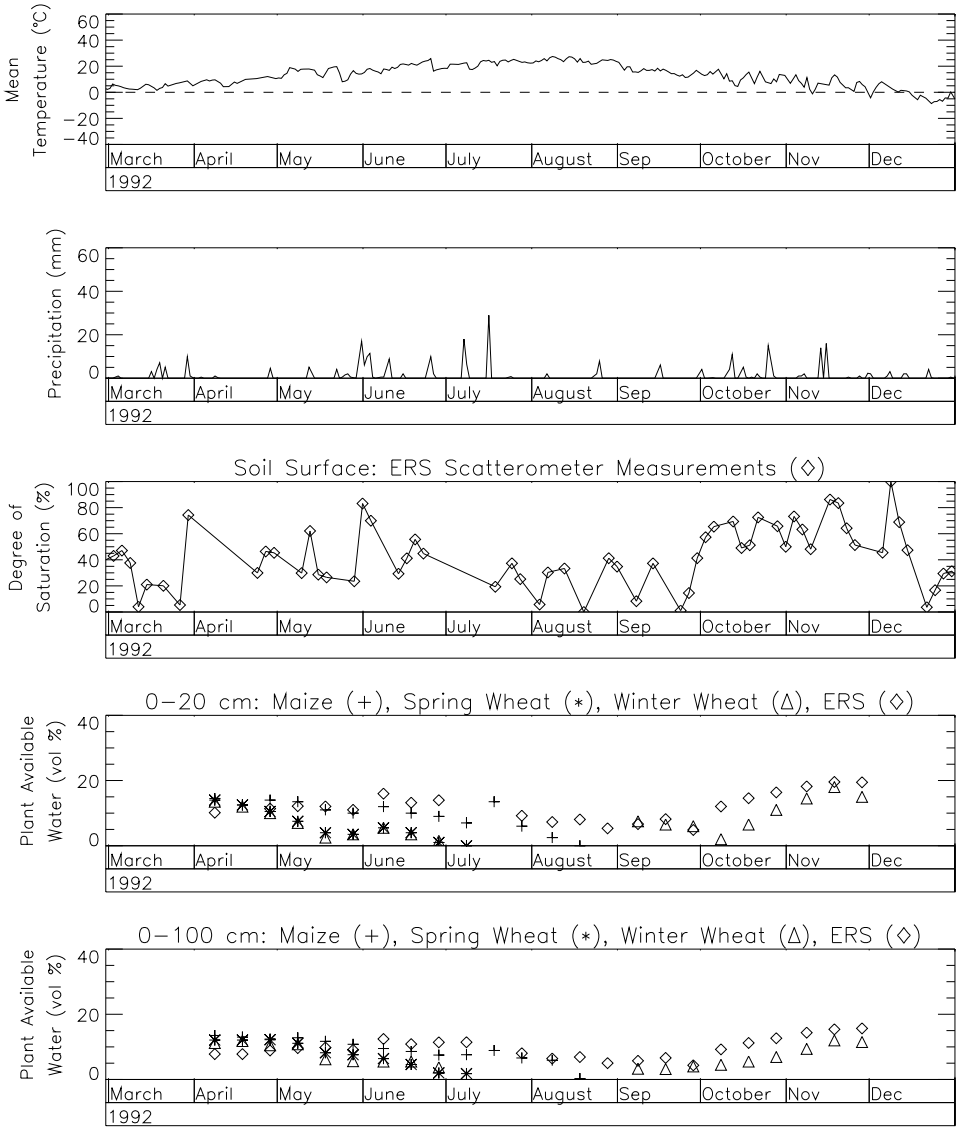


*Figure 9-9: Meteorological observations, field measurements of soil moisture, and remotely sensed wetness values for Odessa (36.67°E, 46.47°N) for the year 1992. The third diagram from the top shows ERS Scatterometer retrieved surface moisture $m_s$. The two diagrams on the bottom show plant available water content in % for the 0-20 cm and 0-100 cm layers measured on maize (cross), spring wheat (asterix), winter wheat (triangle) fields and the remotely sensed soil wetness values (diamond) according to Equation (9.7).*

Another example, where the correlations are considerable less than in the previous one, is given in Figure 9-9 that shows time series for Odessa for the year 1992. The site is characterised by relatively modest variations in soil moisture conditions which is possibly the reason why the correlations are low: $R$ = 0.18 for maize, 0.09 for spring wheat, and 0.26 for winter wheat. However, the r.m.s. errors are less than in the previous example: 3.8 %, 5.0 %, and 4.8 % respectively.

In the calculation of *SWI* it is not corrected for the irregular sampling rate of the ERS Scatterometer. Figure 9-10 shows an example where this leads to a large error. In this particular case, three measurements of a dry soil were acquired in short time intervals around May 20. In the last days of May some 60 mm of rainfall fell, but the next ERS Scatterometer image was acquired only one week after, when

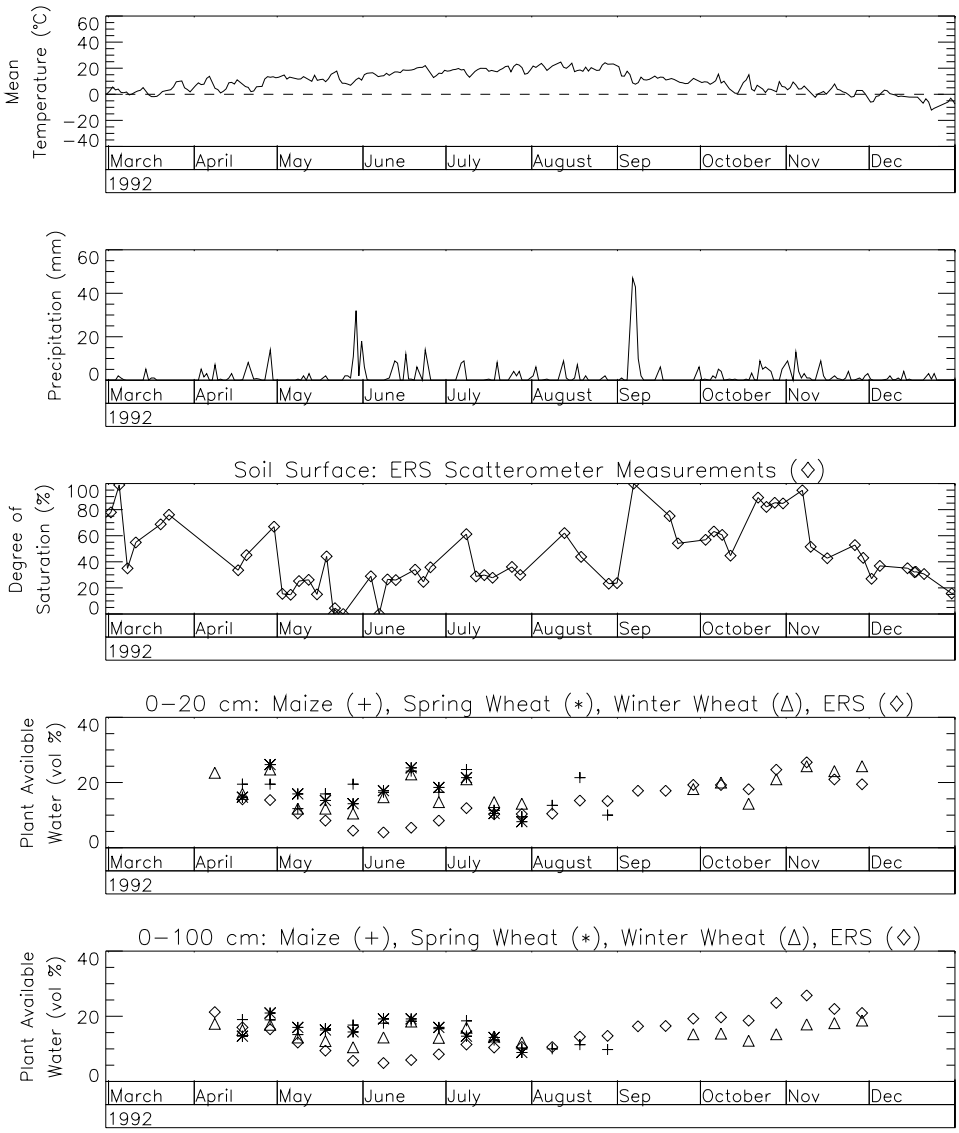


*Figure 9-10: Meteorological observations, field measurements of soil moisture, and remotely sensed wetness values for Ternopol (25.6°E, 49.6°N) for the year 1992. The third diagram from the top shows ERS Scatterometer retrieved surface moisture $m_s$. The two diagrams on the bottom show plant available water content in % for the 0-20 cm and 0-100 cm layers measured on maize (cross), spring wheat (asterix), winter wheat (triangle) fields and the remotely sensed soil wetness values (diamond) according to Equation (9.7).*

the soil had already dried again. Because this rainfall event was completely missed soil moisture levels in June are underestimated by around 20 %. As a last example, time series from the same station but a different year are displayed in Figure 9-11. Now, an excellent agreement between the remote sensing and soil data can be observed.

In Colour Figure 9 spatial patterns of soil moisture in the 0-100 cm layer derived from ERS Scatterometer data and the agrometeorological network are compared for three dates for wet (April 18, 1993), humid (June 8, 1993), and dry (June 18, 1996) soil conditions. The remotely sensed maps are based on the soil maps from Figure 9-4. The field maps were obtained by averaging the soil moisture measurements from all fields at one station and by using nearest neighbourhood interpolation.

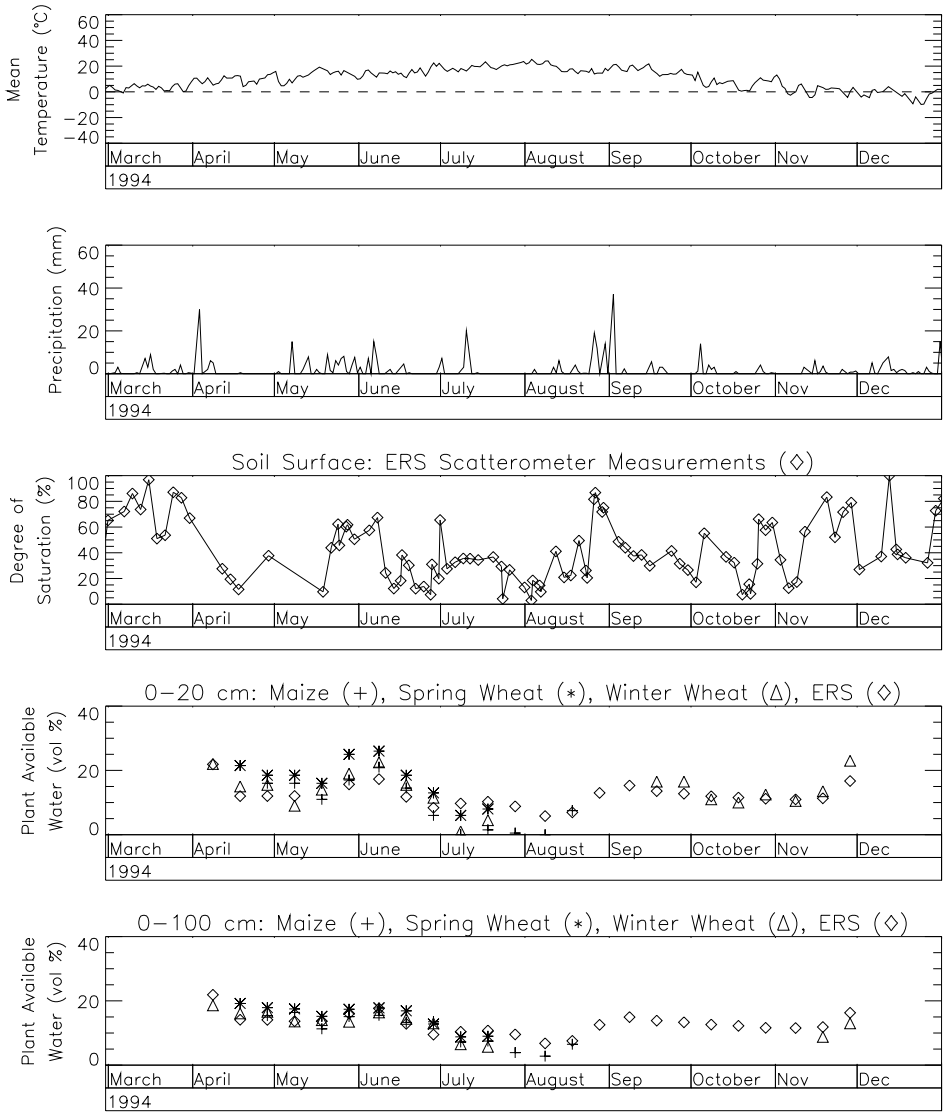


*Figure 9-11: Meteorological observations, field measurements of soil moisture, and remotely sensed wetness values for Ternopol (25.6°E, 49.6°N) for the year 1994. The third diagram from the top shows ERS Scatterometer retrieved surface moisture $m_s$. The two diagrams on the bottom show plant available water content in % for the 0-20 cm and 0-100 cm layers measured on maize (cross), spring wheat (asterix), winter wheat (triangle) fields and the remotely sensed soil wetness values (diamond) according to Equation (9.7).*

The maps pick up differences in soil wetness conditions from date to date quite well. The field maps show less homogeneous soil moisture patterns as the remote sensing maps. In the region at the border to Byelarus soil moisture levels derived from the ERS Scatterometer are in general higher than suggested from the interpolated field measurements. This reflects the physical reality as extensive wetlands can be found in this area. The Carpathian Mountains in the south-western corner of the Ukraine also show up in the remote sensing maps quite often. In April soil moisture levels there are often too low because of the presence of wet snow. In later months soil moisture levels are often higher due to the later snow melt compared to the plains.

## *9.3. Error Analysis*

### 9.3.1. Area-Extensive versus Field Measurements

Because no improvements can be expected by extrapolating the gravimetric measurements from the individual fields to the large footprints of the ERS Scatterometer using geostatistical methods, the remotely sensed area-extensive *PAW* values are directly compared to the field observations. Since the ERS Scatterometer is primarily sensitive to the atmospheric-forcing related component of the soil moisture field, differences of the two data sets should be caused mainly by the land-surface related variability and the retrieval error. Scatter plots of the field versus the area-extensive remote sensing values are shown for the stations Khmelink (27.9°E, 49.6°N) and Prikolotnoye (37.4°E, 50.1°N) in Figures 9-12 and 9-13 for the 0-100 cm layer. The scattering of the data points is relatively high and consequently the correlations are low. In the case of the station Khmelink (Figure 9-12) the correlation coefficient *R* between the remote sensing value and field measurements is 0.60 for maize, 0.50 for spring wheat, and 0.48 for winter wheat. For the station Prikolotnoye (Figure 9-13) the respective values are even lower: 0.20 for maize, 0.16 for spring wheat, and 0.43 for winter wheat.

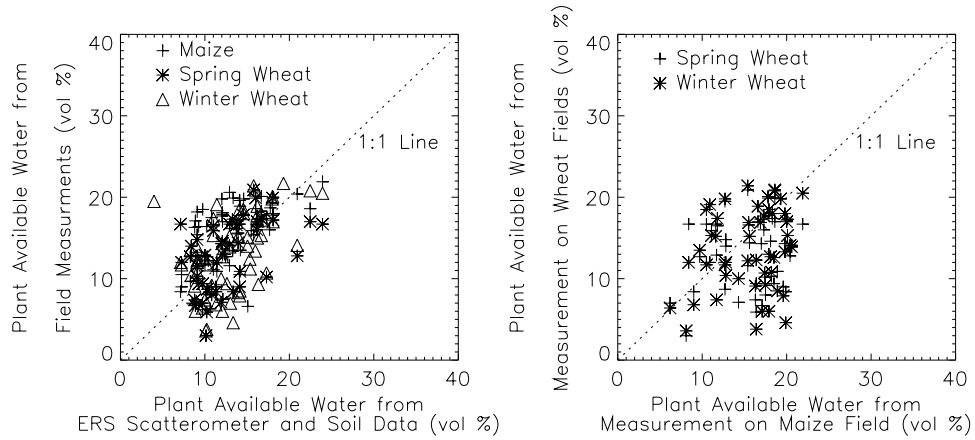


*Figure 9-12: Scatter plots of plant available water PAW in % from ERS Scatterometer and field measurements for the station Khmelnik (27.9°E, 49.6°N). The figure on the left-hand side shows the measurements on the maize (cross), spring wheat (asterix), and winter wheat (diamond) fields versus the area-extensive remote sensing estimates. The figure on the right shows the measurements on the spring (cross) and winter wheat (asterix) fields versus the measurements on the maize field for this station.*

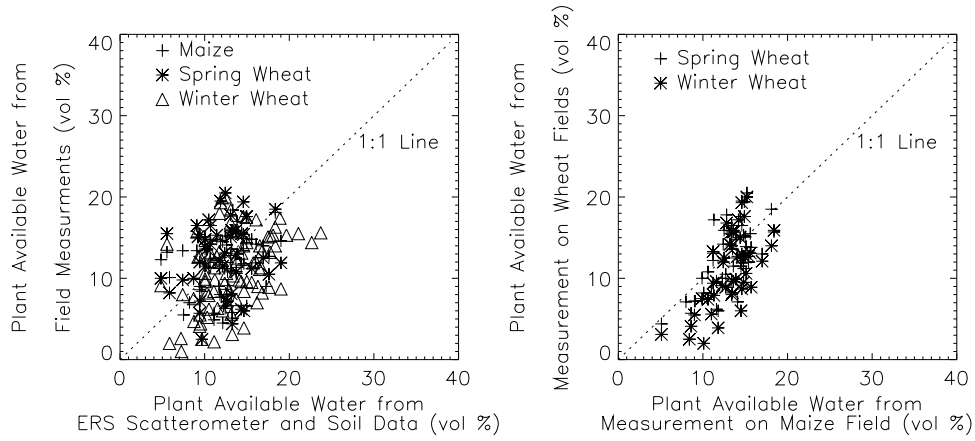


*Figure 9-13: Scatter plots of plant available water PAW in % from ERS Scatterometer and field measurements for the station Prikolotnoye (37.4°E, 50.1°N). See caption of Figure 9-12.*

In the second column of Table 9-1, which summarises the results for all 211 fields, the minimum, mean, and maximum values of *R* between the remote sensing estimates and the 70 maize, 70 spring wheat, and 71 winter wheat fields are shown for the two layers. The numbers for the different crop types are calculated separately because of their different periods of observation. As could be expected from the previous examples, *R* may vary significantly from field to field. For example, for the 0-100 cm layer *R* is 0.76 for the winter wheat field at the station Zhitomir (28.73°E, 50.28°N), while for the winter field at the station Bolgrad (28.62°E, 45.67°N) the correlation is not significant (*R* = 0.05). The mean correlation *R* for the 71 winter wheat fields is about 0.5, 0.4 for spring wheat, and 0.35 for maize. The correlation is probably best for winter wheat because on these fields the surveys are also conducted in the usually wetter period from September to November. There is no apparent dependence of *R* on layer depth.

| | Correlation Coefficient *R*<br>Minimum<br>**Mean**<br>Maximum | Bias (vol %)<br>Minimum<br>**Mean**<br>Maximum | R.M.S. Difference (vol %)<br>Minimum<br>**Mean**<br>Maximum | R.M.S. Error (vol %)<br>Minimum<br>**Mean**<br>Maximum |
|---|---|---|---|---|
| **0-20 cm Layer** | | | | |
| Maize | -0.09<br>**0.35**<br>0.68 | -7.54<br>**-1.32**<br>4.75 | 3.87<br>**5.59**<br>6.96 | 4.68<br>**6.16**<br>9.03 |
| Spring Wheat | -0.11<br>**0.42**<br>0.68 | -6.38<br>**-0.82**<br>8.72 | 4.24<br>**5.62**<br>9.76 | 4.40<br>**6.30**<br>10.64 |
| Winter Wheat | -0.16<br>**0.53**<br>0.71 | -6.10<br>**-1.23**<br>6.52 | 4.29<br>**5.37**<br>7.20 | 4.45<br>**6.06**<br>8.90 |
| **0-100 cm Layer** | | | | |
| Maize | -0.08<br>**0.33**<br>0.71 | -4.17<br>**0.85**<br>14.04 | 2.78<br>**4.31**<br>6.86 | 2.92<br>**4.91**<br>15.63 |
| Spring Wheat | -0.14<br>**0.40**<br>0.78 | -4.55<br>**0.15**<br>5.95 | 2.42<br>**4.24**<br>6.70 | 2.92<br>**4.84**<br>7.58 |
| Winter Wheat | 0.05<br>**0.49**<br>0.76 | -4.60<br>**-0.57**<br>6.36 | 3.20<br>**4.18**<br>8.75 | 3.37<br>**4.84**<br>8.94 |

*Table 9-1: Summary statistics of a direct comparison of ERS Scatterometer retrieved profile soil moisture estimates and gravimetric measurements made on 70 maize, 70 spring wheat, and 71 winter wheat fields.*

As mentioned above, the high degree of scattering is caused on the one hand by the retrieval error and on the other hand by the land-surface related variability of the soil moisture field. Since the true area-extensive soil moisture values are not known, it is not possible to quantify the magnitude of these two sources for the deviations. However, to get an impression about the small-scale variability, the field measurements for the stations Khmelink and Prikolotnoye are plotted versus each other on the right hand side of Figures 9-12 and 9-13. While for the station Prikolotnoye the correlations are 0.69 between maize and spring wheat, and 0.66 between maize and winter wheat, the correlations between the fields at the station Khmelink are actually lower than between the field and the remote sensing values: 0.18 and 0.23 respectively. In Table 9-2 the results of the comparison of the gravimetric data measured at the various fields at the 99 stations are summarised. Although the fields are within a distance of a few kilometres and may even lay side by side, *R* may take on negative values and the mean ranges between 0.49 and 0.72.

This suggests that the observed low correlations between the area-extensive remote sensing data and the field observations are to a considerable extent caused by the small-scale variability of the soil moisture field.

| | | Maize - Spring Wheat | Maize - Winter Wheat | Spring Wheat - Winter Wheat |
|---|---|---|---|---|
| Number of stations with these two fields | | 51 | 45 | 55 |
| Common period of observation | | April - July | April - Sept. | April - July |
| **0-20 cm Layer** | Minimum | 0.09 | -0.06 | 0.10 |
| | **Mean** | **0.62** | **0.55** | **0.72** |
| | Maximum | 0.91 | 0.89 | 0.95 |
| **0-100 cm Layer** | Minimum | -0.03 | -0.01 | 0.10 |
| | **Mean** | **0.52** | **0.49** | **0.72** |
| | Maximum | 0.94 | 0.90 | 0.96 |

*Table 9-2: Correlation coefficient R between gravimetric measurements on maize, spring and winter wheat fields for the agrometeorological stations in the Ukraine.*

Other statistical parameters for assessing the quality of the retrieval method are the bias, the r.m.s. difference, and the r.m.s. error. The bias is the systematic deviation of the field measurements from the remote sensing estimates. The standard deviation of this difference is called here the r.m.s. difference and is a measure of the random deviations from the common trend. The r.m.s. error is the square root of the mean squared deviations and accounts for both the bias and the random deviations from the common trend. Together with the correlation coefficient *R* the results for the 211 fields are summarised in Table 9-1. The bias is roughly normally distributed with the mean slightly negative for the 0-20 cm layer and close to zero for the 0-100 cm layer. Although in certain instances the bias may be significant, 96 % of the values are within ± 5 %. No systematic dependence of the bias on latitude can be observed, i.e. the method correctly depicts the generally more humid conditions in the north and the more arid conditions in the south. The r.m.s. difference varies between 3.9 % and 9.8 % with a mean of 5.5 % for the 0-20 cm layer, and between 2.4 % and 8.8 % with a mean of 4.2 % for the 0-100 cm layer. The r.m.s. error is the most important parameter for assessing the quality of the soil moisture retrieval method and is given here in % volumetric soil moisture. 95 % of the values are below 8.1 % for the 0-20 cm layer and below 6.4 % for the 0-100 cm layer. The mean errors are 6.2 % and 4.9 % respectively. Recalling again that areal data are directly compared to field observations these values are surprisingly low.

Only if the true areal soil moisture values were available then the real accuracy of the ERS Scatterometer based estimates could be assessed. However, since both the field data and the remote sensing data represent only approximations of the true areal values the error of the remote sensing method should be smaller than indicated by the direct comparison with the field observations. The average of the gravimetric measurements at the maize, spring wheat, and winter wheat fields at one station should better represent the true areal value than the measurements from one field alone, and therefore the deviations between the remote sensing and these average values should be smaller. In fact, if the average soil moisture value is calculated in those cases where measurements are available from all three fields at one station then the mean r.m.s. error for the 0-20 cm layer is 5.35 % and for the 0-100 cm layer 4.18 %. It can be concluded that the presented method to estimate the profile soil moisture content from ERS Scatterometer and soil data allows to distinguish at least five soil moisture classes: very dry, dry, medium, wet, and very wet. (The total water capacity divided by two times the r.m.s. error gives a number of about five).

### 9.3.2. Dependence of the Error on the Characteristic Time Length

As described above, the characteristic time length *T* for the calculation of the *SWI* was chosen to maximise the correlation with the field data. The question is how would a different choice of *T* have affected the results? To investigate this question, the mean values of the correlation coefficient, the bias, the r.m.s. difference, and the r.m.s. error were calculated for each crop, for each layer, and for *T* ranging between 1 and 100 days (Figures 9-14 and 9-15).

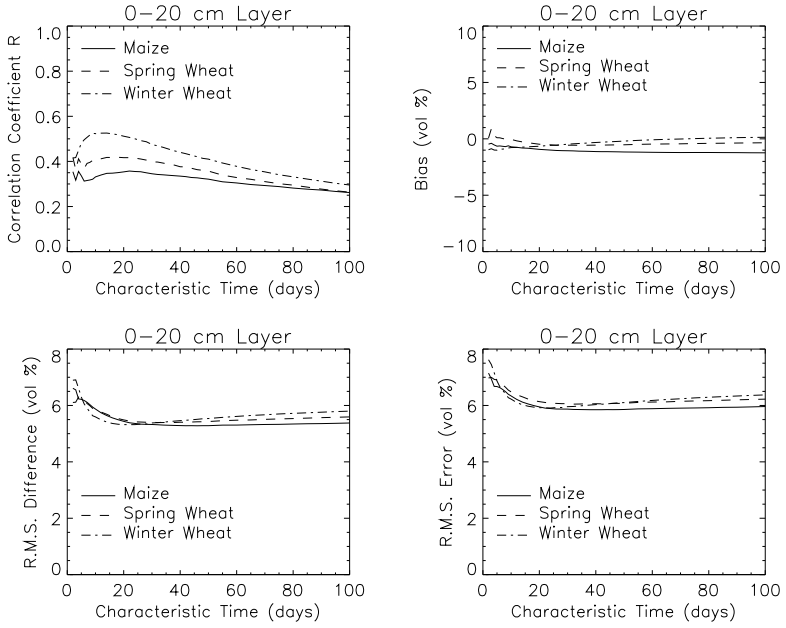


*Figure 9-14: Correlation coefficient, bias, r.m.s. difference, and r.m.s. error versus the characteristic time length T for the 0-20 cm layer. The curves represent the mean values for 70 maize, 70 spring wheat, and 71 winter wheat fields.*

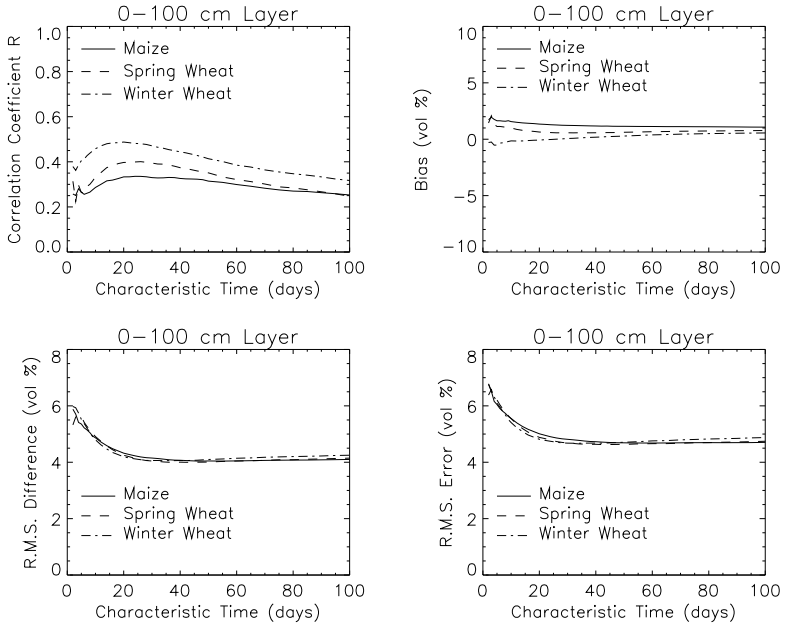


*Figure 9-15: Same as Figure 9-14 but for 0-100 cm layer.*

The results are similar for the 0-20 cm and 0-100 cm layers. In Figures 9-14 and 9-15 it can be seen that $R$ has a local maximum which is, although being shifted somewhat for the three crops, around $T$ = 15 days for the 0-20 cm layer and $T$ = 20 days for the 0-100 cm layer. With increasing $T$ values the high-frequency components of the surface soil moisture series $m_s$ are filtered out and the correlation decreases. It can also be observed that the choice of $T$ has very little influence on the bias. The r.m.s. difference and consequently the r.m.s. error are highest for small $T$ values and decrease with increasing $T$ until the local maxima of $R$ are reached. After this they remain more or less constant with a r.m.s. error of about 6 % for the 0-20 cm layer and 5 % for the 0-100 cm layer. The r.m.s. error is practically identical for all three crops. These results show that a certain degree of smoothing of the surface soil moisture series $m_s$ is necessary. However, above a certain threshold for $T$, which is about 15 and 20 days for the 0-20 cm and 0-100 cm layer respectively, the r.m.s. error is more or less insensitive to $T$, and any choice of $T$ between about 15 days to 30 days would have produced reasonable results. Higher values of $T$ should not be used because, although the mean values of *SWI* still reflect the climatic conditions, the information about the soil moisture trend is degraded. Because the method is relatively insensitive to the choice of $T$ it shows some potential to be transferred to other regions with similar soils and climate.

### 9.3.3. Dependence of the Error on Soil Properties

It has been shown that the bias between the remote sensing estimates and the field data is relatively low, but it has not been investigated if a systematic dependence on soil properties exists. To check if there is a relationship, the bias is plotted versus the wilting level in Figure 9-16. Data are taken from all 211 fields for the 0-100 cm layer. Other soil constants like field capacity could also have been used because these parameters are correlated with each other. Although a statistically significant trend is present (Table 9-3), it is very small. It can be concluded that the method successfully accounts for soil type variation.

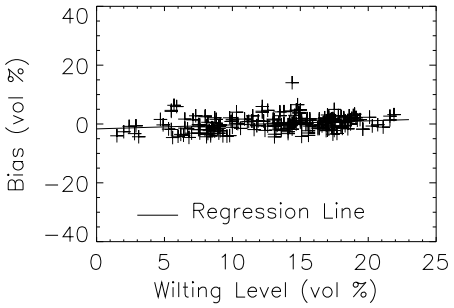


*Figure 9-16: Dependence of bias on wilting level for the 211 measurement fields in the Ukraine for the 0-100 cm layer.*

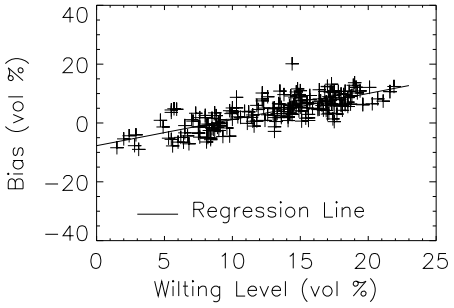


*Figure 9-17: Same as Figure 9-16 but for different assumptions on lowest and highest soil moisture levels. Here it is assumed that the lowest occurring wetness values are at zero wetness and the highest at saturation.*

The question now is what would happen if the information on the minimum and maximum occurring soil wetness values, $W_{min}$ and $W_{max}$, is not available for the study area? In order to find this out a number of assumptions on the level of $W_{min}$ and $W_{max}$ are tested. For example, let us set $W_{min}$ euqal to 0 % and $W_{max}$ equal to the total water capacity *TWC*. This would have produced a significant bias that would have

varied for different soil types (Figure 9-17). In order to compare various assumptions a linear regression line is fitted to the scatterplot of the bias versus the wilting level:

$$bias = c + d \cdot WL \tag{9.8}$$

The resulting values for the intercept *c* and the slope *d* for our original assumption and four alternatives are shown in Table 9-3. Alternative 1 ($W_{min}$ = *WL*, $W_{max}$ = *FC*) performs best when compared to the other assumptions. Its bias shows no dependence on soil type, but is around 4 %. It can be said that with decreasing likeness of the assumptions the bias becomes more dependent on soil type. Alternative 4 ($W_{min}$ = 0 %, $W_{max}$ = *TWC*) produces the poorest results.

| Assumption No. | Minimum Wetness $W_{min}$ | Maximum Wetness $W_{max}$ | Intercept of Bias *c* (vol %) ±95 % Confidence Interval | Slope of Bias *d* (vol %) ±95 % Confidence Interval |
|---|---|---|---|---|
| Original | *WL* | $\frac{FC+TWC}{2}$ | -1.66±1.05 | 0.14±0.08 |
| Alternative 1 | *WL* | *FC* | 3.90±0.98 | 0.01±0.07 |
| Alternative 2 | *WL* | *TWC* | 7.22±1.23 | 0.26±0.09 |
| Alternative 3 | 0 | *FC* | 3.41±1.08 | 0.64±0.08 |
| Alternative 4 | 0 | *TWC* | -7.72±1.39 | 0.89±0.10 |

*Table 9-3: Intercept and slope from linear regression between the bias and the wilting level for five different assumptions on the lowest and highest soil wetness levels. WL is the wilting level, FC is the field capacity, and TWC is the total water capacity or porosity.*

Because the original assumptions seem to come closest to the physical reality in the Ukraine, the error introduced by the other assumptions can be explained by the following model. Let us rewrite (9.5):

$$W = (1 - SWI) \cdot W_{min} + SWI \cdot W_{max} \tag{9.9}$$

and estimate the bias introduced by incorrect assumptions for $W_{min}$ and $W_{max}$ with:

$$bias \approx (1 - AVG(SWI)) \cdot \Delta W_{min} + AVG(SWI) \cdot \Delta W_{max} \tag{9.10}$$

where

$$\Delta W_{min} = WL - W_{min} \tag{9.11}$$

and

$$\Delta W_{max} = \frac{FC + TWC}{2} - W_{max}\,. \tag{9.12}$$

*AVG*(*SWI*) is the average *SWI* over the period from April to November which varies from about 0.3 in the south to about 0.6 in the north. $W_{min}$ and $W_{max}$ in Equations (9.11) and (9.12) are the assumed values. In Figure 9-18 the theoretical bias obtained from Equation (9.10) is compared to the observed values for Alternative 4. The points gather along the 1:1 line which shows that our reasoning has been correct. Similar results are obtained for the other assumptions.

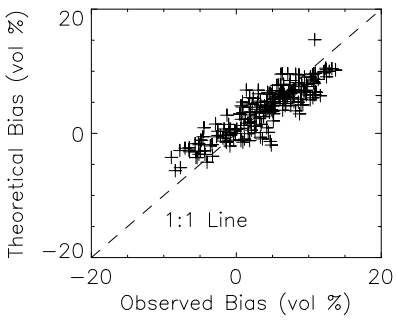


*Figure 9-18: Observed and estimated values of the bias for the 0-100 cm layer for Alternative 4 (Table 9-3). The dashed line is the 1:1 line.*

# 10. Soil Water Index Maps of Different Climatic Zones

## *10.1. Introduction*

The comparison with the gravimetric soil moisture data set from the Ukraine has shown that the Soil Water Index *SWI* is a useful trend indicator of the moisture content in the soil profile. The method shows some potential to be transferred to other regions because the *SWI* is relatively insensitive to the choice of the characteristic time length *T*, which is the only parameter needed for the calculation of *SWI*. In this chapter *SWI* maps of different climatic zones are presented: wet-dry tropical, Mediterranean, moist continental, and marine west-coast climate. The discussion of soil moisture patterns is purely qualitative, but is nevertheless included here to give a first indication of potential applications of this technique, for example in climatology.

## *10.2. Wet-Dry Tropical Climate*

Monthly *SWI* maps of southern Mali and Burkina Faso are shown in Colour Figure 10. The characteristic time length *T* was set equal to 10 days to account for sandy soils with high hydraulic conductivity. The *SWI* is calculated for the last day of each month, i.e. the maps represent the wetness conditions at the end of the month. Rainfall patterns are displayed in Figure 10-1 for comparison.

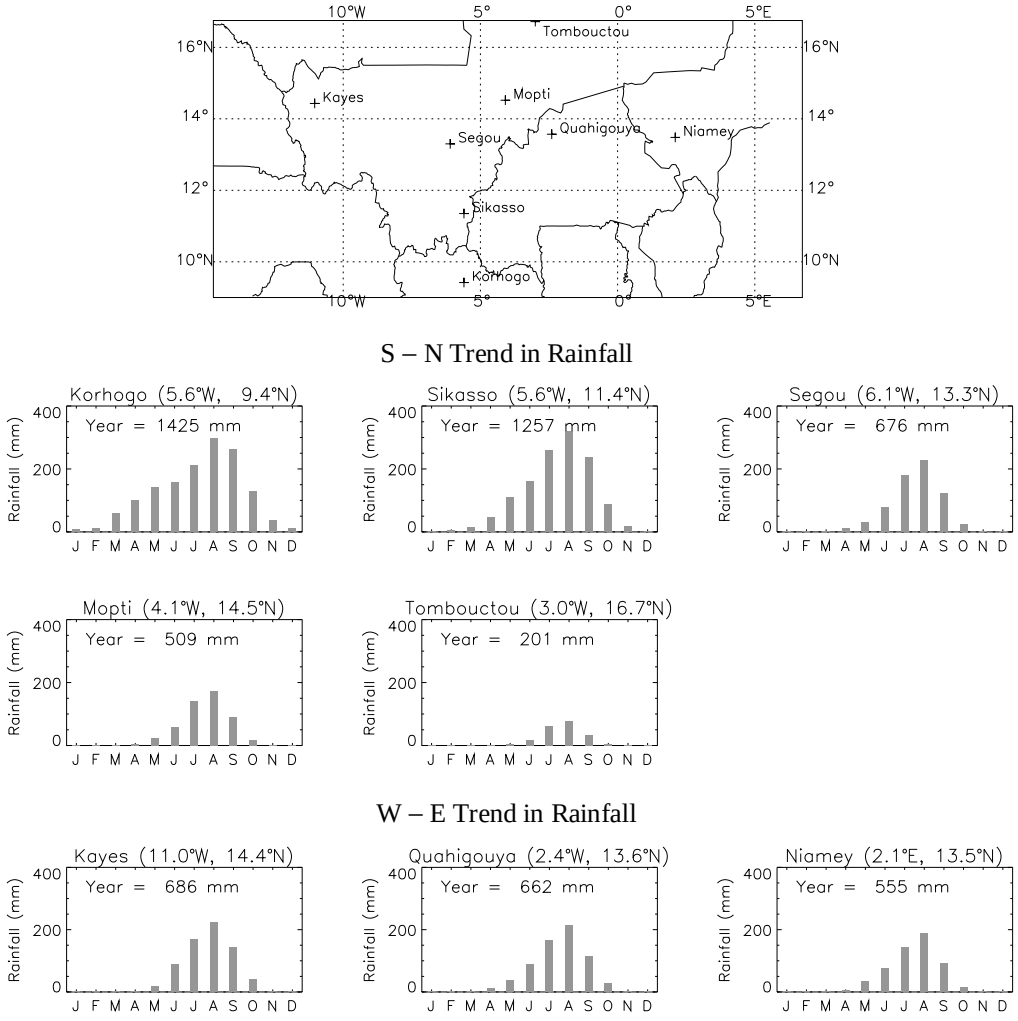


*Figure 10-1: Average monthly rainfall for eight stations in the region 13°W-5°E and 9°N-16.5°N.*

The region is under the influence of a wet-dry tropical climate. Average monthly temperatures are above 20°C all year round for the entire region. The northward movement of the Intertropical Convergence Zone (ITC), which brings rain in the high sun season, is well depicted in Colour Figure 10. In the south of the study area (10°N) the first increase of *SWI* at the beginning of the rainfall season is observed around May when monthly rainfall exceeds 100 mm. In the northern parts (16°N) rainfall may not be sufficient to lead to a significant increase of *SWI*. The highest rainfall amounts are normally observed in August leading to the highest *SWI* values at the end of August/beginning of September. Some rainfall may still occur in October but the soil is already drying. In December the soil has completely dried out and remains dry until the next rainy season. In the upper middle of the *SWI* images a spot remains visible until January. This is the Niger Delta that is flooded each year during the rainy season by the rivers Niger and Bani (Barth, 1986). The *SWI* maps suggest that the north-western part of the region receives in general more rain than the north-east. Also this pattern reflects the physical reality. For example, Kayes which is located in the western part of the region at a latitude of 14.4°N, receives an average annual rainfall of about 686 mm, while Niamy in the eastern part at latitude 13.5°N receives about 130 mm less.

## *10.3. Mediterranean Climate*

The Iberian Peninsula is characterised by a Mediterranean climate with low summer rainfall and a wet winter season. Colour Figure 11 shows monthly *SWI* maps (with $T$ = 20 days) and Figure 10-2 shows climographs for the stations Granada, Beja, Zaragoza, and Ponferrada. Monthly *SWI* values averaged over the years 1992 to 1996 are included in the climographs.

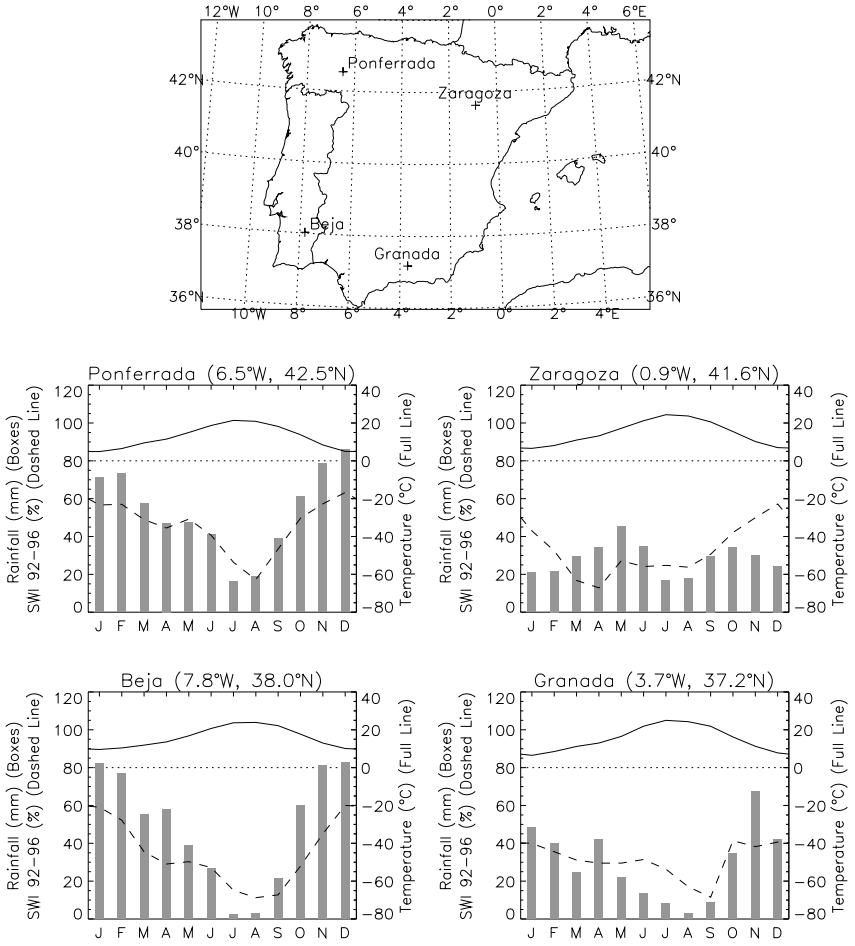


*Figure 10-2: Climographs for four stations at the Iberian Peninsula. Also shown are the mean monthly SWI values from the years 1992-1996.*

Although the annual *SWI* profile is based on only five years of data, the seasonal trends of rainfall and temperature are well reflected. Also in Colour Figure 11 the generally wet winter and dry summer conditions are evident. In a number of autumn and winter maps (e.g. December 1992 and 1993, January and February 1995) a decrease of *SWI* from the north-west to the south-east can be observed. These patterns depict the more humid conditions in the north-eastern part of the Iberian Peninsula that receives rain from the prevailing westerly winds. In the years 1992 to 1995 many regions suffered from drought. The financial losses caused by the drought in this period are estimated to be around 10 million US dollars alone in the agricultural sector (González Alonso et al., 1998). The drought ended in November 1995 when high rainfall amounts quickly saturated the soil surface (Picatoste, 1997). In Colour Figure 11 it can be seen that the rainfall front moved from west to east, leaving a small fringe of relatively dry soil on the eastern coast of Spain. In the south-east of Spain some patterns of high *SWI* emerge in June/July which cannot be related to rainfall events. With the beginning of the wet season the phenomenon disappears. In these regions the sensitivity of $\sigma^0$ to changes in the soil moisture content is only 2 dB (compare Colour Figure 6e and the July 1994 image in Colour Figure 11), i.e. these patterns are caused by $\sigma^0(40)$ values which are only about 1 dB higher than the reference backscattering value for dry soil conditions $\sigma^0_{dry}$. The reasons for this phenomenon are not known.

## *10.4. Moist Continental Climate*

As an example for a moist continental climate, ERS Scatterometer data covering the US State Illinois were processed. Colour Figure 12 shows monthly *SWI* maps ($T$ = 20 days) and Figure 10-3 shows climographs of four selected stations. The moist continental climate lies in the frontal zone between polar and tropical air masses with strong seasonal temperature contrasts (Strahler and Strahler, 1996). Ample precipitation throughout the year is increased in summer by invading tropical air masses (Figure 10-3). Because it has not been possible to exclude ERS Scatterometer measurements of frozen soil and wet snow without auxiliary data, some *SWI* images show unrealistic low values in the winter months from November to February, especially in the northern part of Illinois. This demonstrates the need to utilise other data sources to exclude such measurements in regions with cold winters.

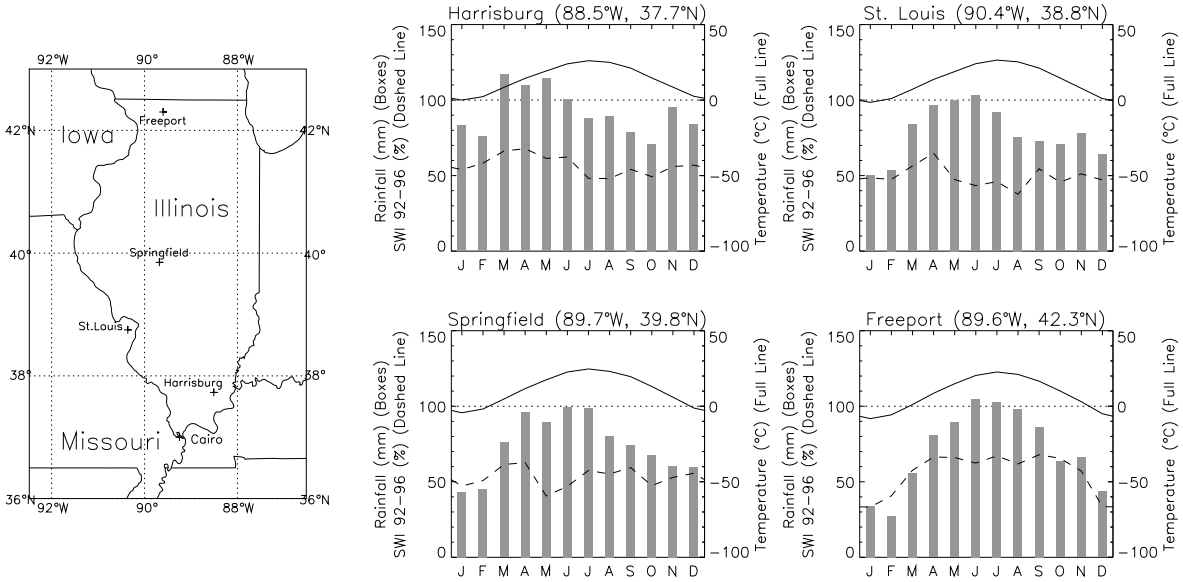


*Figure 10-3: Climographs for four stations in Illinois, USA. Also shown are the mean monthly SWI values from the years 1992 to 1996.*

The *SWI* values are generally relatively high during the summer months. Especially 1993 was a very wet year which lead to the Mississippi flood in summer 1993 that caused losses in the order of $15-20 billion

(Jones, 1993). Unfortunately, only few ERS Scatterometer data were acquired during this period, but some events as described by Jones (1993) can still be observed:

> "Springtime floods are a regular occurrence within the [Mississippi] basin, but the 1993 floods followed eight months of unusually high rainfall, with up to twice the normal amounts, plus exceptionally heavy winter snows in the Rockies. Some areas received more than 1200 mm in rain over the period. (*Note the consistently high SWI values from March to June 1993.*) … By late June the Mississippi was overbank in Minnesota, at that stage a 30-year record. Then on 8 July and 11 July, a total of 160 mm fell on saturated land in parts of Iowa. (*The July 1993 map shows SWI values well above 80 % for Iowa.*) … "Many mid-western rivers remained in flood stage till September, with levels topped up by sporadic and localised heavy rain through August in what for many upstream states was the wettest summer ever. The soils of the entire basin upstream of the Ohio River confluence at Cairo, Illinois, remained saturated into September and models at the Midwestern Regional Climate Center indicated this was likely to continue till March 1994. *(Note that in the southern part of Illinois SWI values remain indeed generally above 60 % until April 1994.)"*

## *10.5. Marine West-Coast Climate*

As a last example, monthly *SWI* maps of England and Wales are shown in Colour Figure 13. The climographs are displayed in Figure 10-4. England and Wales have a marine west-coast climate. It is a moist climate with plentiful precipitation all year round, but there is often a winter maximum (Strahler and Strahler, 1996). Marine west-coast climates are unusually mild for their latitude and may have average monthly temperatures that are above freezing throughout the year (Christopherson, 1997). As a result of the relatively mild winters, freezing and wet snow occur less often than e.g. in Illinois (last chapter). However, in a number of winter *SWI* maps (e.g. January and February 1997) the *SWI* values are also unrealistically low, which shows again that over higher latitude regions reference data are needed to decide whether the soil was frozen or if there was wet snow.

The climographs show that average monthly precipitation in summer in England and Wales is about 20 – 50 mm lower than in Illinois (Figures 10-3 and 10-4). Despite this, the low *SWI* values in the summer months of 1992-1993, and 1995-1996 are surprising. However, the years 1988-93 and 1995-97 were considered drought years (Jones, 1997, BBC News, 1997), so that the *SWI* maps probably reflect the physical reality.

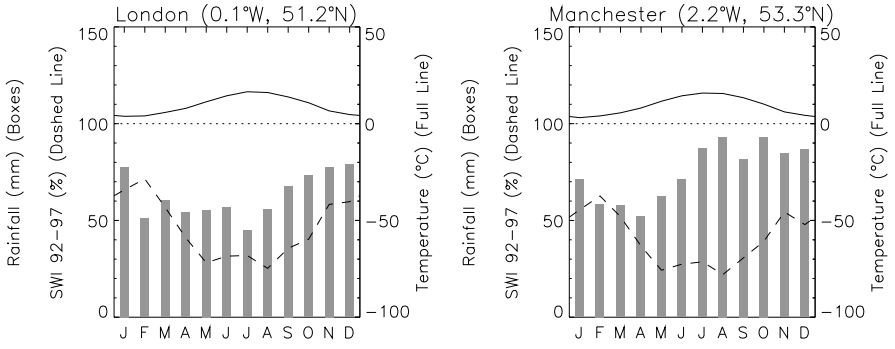


*Figure 10-4: Climographs for London and Manchester. Also shown are the mean monthly SWI values from the years 1992 to 1997.*

# 11. Summary and Conclusions

## *11.1. Executive Summary*

The study was concerned with the development of an algorithm to retrieve soil moisture from ERS Scatterometer data. The main problems to be solved were 1) how to account for the incidence angle dependency of the backscattering coefficient; 2) how to correct for vegetation cover effects; and 3) how to validate the remotely sensed soil wetness values quantitatively?

***Scaling Issues***

The main parameters affecting the backscattering signal over land surfaces are the moisture content in the top few centimetres of the soil, the roughness of the soil surface, and the absorption and scattering characteristics of the vegetation canopy. All these parameters vary at different scales, and a crucial point for the correct interpretation of the ERS Scatterometer signal is to have a good understanding of the processes that control the various parameters at the observation scale (50 km). The discussion of these processes lead to the conclusions that changes in the surface soil moisture content cause a high variability of the ERS Scatterometer signal at short time scales (minutes to days), changes in vegetation at time scales from days to weeks, and that surface roughness should in general expected to be stable over time. The spatial variability of the ERS Scatterometer signal is caused by atmospheric forcing (precipitation, evapo-transpiration) of soil moisture, patterns of vegetation as a function of soils, landforms, and land use, and by changes in the microrelief related to soil formation factors such as climate, vegetation, and topography.

***Processing Chain***

These considerations were the basis for the development of a processing chain that has the purpose of removing the incidence angle dependency of the signal while fully preserving the information about the soil moisture and vegetation status. The processing chain makes full use of the multiple viewing capabilities of the instrument and requires as input several years of ERS Scatterometer data.

In the first processing step, the azimuthal dependency of the backscattering coefficient $\sigma^0$ is determined by using the measurements of the fore and aft beam antennas. Land surfaces are slightly anisotropic in azimuth mainly due to topography. Since the effect is small it is considered as noise. An error model is used to estimate the standard error of $\sigma^0$, $ESD(\sigma^0)$, due to instrument noise, speckle, and azimuthal effects. Analysis over the tropical rainforest shows that the standard error due to instrument noise and speckle alone is 0.13 dB, and any increase above this level is due to azimuthal effects. $ESD(\sigma^0)$ is only an estimate of the real noise, but was found useful for quality control and to explain the spatial variability of the noise level of parameters derived from $\sigma^0$.

In the second processing stage, the incidence angle dependency of $\sigma^0$ is investigated. Because the ERS Scatterometer measures $\sigma^0$ at two incidence angles, it is possible to calculate the slope $\sigma'$ from each backscatter triplet. The dependency of $\sigma'$ on the incidence angle $\theta$ can be modelled using a linear relationship. Fitting a regression line to data acquired during a particular period of the year allows to calculate the slope and the curvature of $\sigma^0(\theta)$ at the reference angle of 40°, $\sigma'(40)$ and $\sigma''(40)$. Because the noise of $\sigma'$ derived from the backscatter triplet is large, and to make sure that the $\sigma'$ values are evenly distributed over the entire incidence angle range from 18° to 59°, data from several years must be used in the regression. Therefore $\sigma'(40)$ and $\sigma''(40)$ represent mean values for a particular period of the year averaged over a long period of records. Averaging of $\sigma'$ is possible without loosing substantial information, because the slope depends on vegetation and surface roughness, but it is not or only little correlated to the rapidly varying soil moisture content. While the curvature $\sigma''(40)$ is in general stable

over the year, the slope $\sigma'(40)$ exhibits a characteristic seasonal cycle. The time dependency is modelled using a function of the form $C'+D'\cdot\Psi(t)$, where $C'$ is a constant, $D'$ is the dynamic range of the slope, and $\Psi(t)$ is an empirical periodic function. Knowing the spatial and temporal behaviour of the slope, the backscattering coefficient at 40°, $\sigma^0(40)$, can be calculated from each ERS Scatterometer measurement in the last processing step.

***Vegetation Cover Effects***

The effects of land cover and seasonal vegetation development were studied by comparing the backscattering parameters with land cover information, NDVI data sets, and meteorological information. As land cover information and AVHRR imagery were readily available, the Iberian Peninsula was the principal study area. Because of the different incidence angle behaviour of the contributions from the soil surface and the vegetation volume to total backscatter, the slope varies over the year. In winter $\sigma'(40)$ is lowest (steep slope) and highest in summer (low gradient) when the vegetation has reached its maximum wet biomass. Unfortunately, vegetation development over one season cannot be monitored because the noise level of $\sigma'$ derived from one backscatter triplet is high. However, the multi year average $\sigma'(40)$ values may be useful for the study of vegetation phenology. This is because the temporal variation of the slope is linked to the wet biomass of the vegetation.

Unlike $\sigma'(40)$, no clear effects of vegetation development on $\sigma^0(40)$ could be discerned visually. However, it is clear that if the slope changes, $\sigma^0$ must necessarily change too. This consideration lead to the concept of the "crossover angle" which states that at some incidence angle the $\sigma^0(\theta)$ curves of a dormant and a full-grown vegetation canopy should cross over. If such a "crossover angle" exists then it is dependent on the surface soil moisture conditions because they affect the relative level of the surface and volume scattering contribution. For dry soil conditions the crossover angle should be found at lower incidence angles than the crossover angle for wet soil conditions. The concept of the crossover angle is important because it allows to link the temporal evolution of the slope $\sigma'$ and the backscatter intensity $\sigma^0$. To this end it allows to correct for seasonal vegetation cover effects. A visual analysis of the $\sigma^0(40)$ time series showed that the crossover angle for dry soil moisture conditions is around 25° and for wet soil conditions around 40°. Knowing the dynamic range of the slope, $D'$, and the approximate position of the crossover angles the impact of vegetation growth can be estimated at any incidence angle. At the reference angle and for dry soil moisture conditions the increase of the backscatter intensity $\sigma^0_{dry}(40)$ due to vegetation growth is about 1.5 – 2.5 dB over areas predominantly occupied by agriculture and grassland. Over densely forested areas the slope and thus $\sigma^0_{dry}(40)$ are stable over the year. For wet soil moisture conditions the crossover angle coincides with the reference angle and therefore $\sigma^0_{wet}(40)$ is more or less unaffected by vegetation growth. Knowing the temporal evolution of $\sigma^0_{dry}(40)$ and $\sigma^0_{wet}(40)$ these curves can be fitted to the minimum and maximum values of $\sigma^0(40)$ which gives for each pixel the mean value of the backscatter coefficient for dry and wet soil conditions, denoted by $C^0_{dry}$ and $C^0_{wet}$ respectively. Knowing $\sigma^0_{dry}(40,t)$ and $\sigma^0_{wet}(40,t)$ the sensitivity $S(t)$ to changes in the surface soil moisture content can be calculated. The sensitivity varies over the year and can be modelled as the sum of a constant term $C^S$ and a dynamic part that is proportional to the seasonal variation of the slope $D'\cdot\Psi(t)$.

A number of backscattering parameters are thus available that fully describe the backscattering characteristics of land surfaces: the constant and the dynamic slope terms $C'$ and $D'$, the backscattering coefficients of a dry and wet surface $C^0_{dry}$ and $C^0_{wet}$, and the sensitivity $C^S$. How various land cover classes effect these parameters was investigated by comparing them with statistics derived from the CORINE land cover. It was found that although build-up areas, inland waters, and rocky surfaces occupy only small fractions of the land surface, they have a noticeable effect on the scattering behaviour. Also it was found that only CORINE classes, where translucent and non-transparent vegetation types do not mix, exhibited a clear trend. Based on the CORINE classes "Non-irrigated arable land" and "Natural grassland" a generalised class representing translucent vegetation types was defined. The CORINE

classes “Broad-leaved forest”, “Coniferous forest”, “Mixed forest”, and “Sclerophyllous vegetation” were grouped together in a non-transparent vegetation class. By using these two classes between 50 and 60 % of the variability of $C'$ and $C^S$ and around 30 % of the variability of $D'$ and $C^0_{dry}$ could be explained. Also surface roughness effects appear to be important to explain the spatial variability. In this context especially the backscatter intensity appears to be sensitive to regional variations in the microrelief of the ground surface. Nevertheless, the results suggest that most of the spatial variability of the backscattering parameters is related to the percentage area occupied by translucent vegetation (agricultural land, grassland) and non-transparent vegetation (forests, bushes, and shrubs) respectively.

***Soil Moisture Retrieval***

Given that for each pixel a set of parameters which fully describe the backscattering behaviour is available, the surface soil moisture content can be estimated. The algorithm is in principle a simple change detection method where $\sigma^0(40)$ is compared to $\sigma^0_{dry}(40,t)$ and $\sigma^0_{wet}(40,t)$ which represent the lowest and highest values ever observed at a given pixel. Thus the algorithm accounts for the effects of heterogeneous land cover and seasonal vegetation development. As a result, a relative measure of the moisture content in the top few centimetres of the soil, denoted by $m_s$, is obtained. If it can be reasonably assumed that $\sigma^0_{dry}$ and $\sigma^0_{wet}$ represent a completely dry and saturated soil respectively, then $m_s$ can be identified with the degree of saturation of the soil surface. Qualitative comparison with rainfall and temperature data indicates a good quality of the remotely sensed surface soil moisture estimates. Unfortunately, a quantitative validation using field measurements appears hardly feasible because of the high degree of the land-surface related variability of the surface soil moisture content over small distances and because of the high costs of field surveys.

The chances for a successful validation are improved if a method for estimating the moisture content in the soil profile is available. This is because the variance of the soil moisture field due to the land-surface related variability decreases with respect to the variance due to the atmospheric related variability when the depth of the soil layer increases. Consequently, an algorithm for estimating the profile soil moisture content from ERS Scatterometer and soil data was defined and validated with an extensive set of gravimetric soil moisture measurements from the Ukraine. The reference data set encompasses data from 211 maize, spring wheat, or winter wheat fields and covers five years (1992 to 1996). In total, 14,293 average field wetness values were available for the 0-20 cm layer and 12,835 for the 0-100 cm layer.

The method for estimating the soil moisture content in the soil profile consists of two components. Firstly, a trend indicator, which was called the Soil Water Index *SWI*, is derived from the remotely sensed surface wetness values. The *SWI* takes into account that the moisture content in deeper layers is influenced by the past dynamics of the surface moisture content and that, with increasing time difference, the influence of measurements decreases. Therefore it describes in a simplified manner the propagation of water from the top soil into the profile. In a second step, auxiliary information about soil physical properties is used to determine calibration points for dry (*SWI* = 0 %) and wet (*SWI* = 100 %) soil conditions. Analysis of the field measurements in the Ukraine has shown that, for the 0-20 cm and 0-100 cm soil layers, the observed minimum moisture content is around wilting point, and the maximum is roughly half way between field capacity and total water capacity. The required soil data for estimating the moisture content are such wilting level, field capacity, and total water capacity.

Because geostatistical methods could not be meaningfully applied, the ERS Scatterometer retrieved soil moisture values were directly compared to the field measurements. Differences between the area-extensive remote sensing and field soil moisture data should mainly be due to the small-scale land-surface related variability of the soil moisture field and the retrieval error. The statistical analysis showed that in 95 % of the cases the soil moisture content on a field can be estimated with an r.m.s. error of less than 8.1 % volumetric units for the 0-20 cm layer and less than 6.4 % for the 0-100 cm layer. The expected

(mean) r.m.s. errors are 6.2 % and 4.9 % respectively. The agreement between the true areal soil moisture values, which however cannot be measured in-situ, and the ERS Scatterometer derived estimates should be better than that. This allows to distinguish about five soil moisture levels with some confidence.

The method for estimating the profile soil moisture content shows some potential to be transferred to other regions. One reason is that soil data requirements are relatively modest. In the absence of direct field observations, the range of possible soil moisture values could potentially be estimated for individual soil units of basic soil map data. For example, in Dam et al. (1994), Thomasson (1994), and King et al. (1994) it is described how soil constants such as wilting level, field capacity, and porosity are estimated from the 1:1,000,000 Soil Map of the European Union. The other reason is that the *SWI* is relatively insensitive to the characteristic time length *T*, which is the only parameter needed to calculate the former index. A qualitative analysis of *SWI* maps of such diverse regions as Mali, Iberian Peninsula, Illinois, and England and Wales shows that the maps reflect regional and temporal climatic trends quite well. Also, extreme hydrological events such as droughts and floods can be monitored. However, every effort to validate the results should be undertaken if the methodology is to be transferred. For example, if the soil characteristics are not well known then the soil moisture estimates might be biased.

## *11.2. Conclusions and Potential Applications*

The results show that the ERS Scatterometer is a powerful sensor for monitoring soil moisture conditions. The main reasons are its high temporal sampling rate and its capability to acquire measurements independent of the sun and cloud cover. This allows to follow the temporal evolution of the highly variable surface moisture content and provides an indication of the wetting and drying trend of the soil profile. Also, the multiple viewing capabilities of the instrument are important because this characteristic makes it possible to correct for the effects of vegetation growth and senescence.

The low spatial resolution of 50 km means that the small-scale variability of the soil moisture field caused by differences in soils, vegetation, and land form is averaged out in the measurement process. However, the atmospheric-forcing related variability of the soil moisture field at the synoptic scale is reflected by the ERS Scatterometer signal because the autocorrelation length of this component is several hundreds of kilometres.

Due to population growth the demand for water resources is rising in many regions of the world, most notably in Western Asia, South-Central Asia, and Northern Africa (Fischer and Heilig, 1997). Although soil moisture is not directly exploitable for water supply, it is extremely important for agriculture and natural ecosystems (Jones, 1997). Soil moisture is also recognised to be of importance for medium- to long-range weather forecasting and climate modelling. The demand and the current lack of operational large-scale soil moisture monitoring systems mean that spaceborne scatterometers could become an important source of information in soil moisture applications. For each application it needs however to be asked if the required information is contained in the signal and if the required accuracy can be achieved. It also must be realised that currently used concepts and models in hydrology, meteorology, agronomy and related fields have been developed from a point concept, while remote sensing provides spatial information. Therefore, to utilise these data, it may become necessary to develop new concepts and models to accommodate this new type of information (Engman, 1986).

The ERS Scatterometer also shows some potential in vegetation applications. The results achieved in this study suggest that it is possible to distinguish regions predominantly occupied by translucent vegetation types (agricultural land, grassland) from regions occupied by non-transparent vegetation (forest, bushed, and shrubs). Also, the study of vegetation phenology appears possible. However, more research (e.g. surface roughness effects need to be better understood) is needed to confirm these applications.

### 11.3. New Sensors and Sensor Design

ESA and EUMETSAT are cooperating in the development of a series of polar-orbiting weather satellites that will replace the meteorological satellites currently being used in weather forecasting, possibly starting in the year 2003. The METOP (Meteorological Operational) satellites will carry an Advanced Scatterometer (ASCAT) operating in C-band. The illumination geometry is similar to the ERS Scatterometer and the spatial resolution is 25 km. Because the instrument illuminates two swaths to the side of the satellite track, global coverage is achieved every second day. These characteristics make the ASCAT an ideal instrument for monitoring the atmosphere-related component of the soil moisture field. To allow soil moisture retrieval immediately after the start of METOP, the ASCAT must be calibrated to the same absolute and relative levels as the Scatterometer on board of ERS-1 and ERS-2.

The results obtained in this study clearly show that for soil moisture monitoring a high temporal sampling rate is more important than a high spatial resolution. Any sensor with a spatial resolution between about 5 and 50 km will effectively suppress the land-surface related variability of the soil moisture field, while providing comparable information about the atmospheric component. Only if the spatial resolution can be improved to about 1 km or less, while still providing measurements every second or third day, it will become possible to assess also the land-surface related variability of soil moisture.

## References


Amans, V. (1994) Wind Scatterometer Monthly Report, September 1994, *ESA, ESRIN, Doc. No. DEX/EM/VA/94/006*.

Assivar, R. (1995) Scaling of land-atmosphere interactions: an atmospheric modelling perspective, *Hydrological Processes*, Vol. 9, pp. 679-695.

Attema, E. P. W. (1991) The Active Microwave Instrument On-Board the ERS-1 Satellite, *Proceedings of the IEEE*, Vol. 79, No. 6, June 1991, pp. 791-799.

Attema, E. P. W., F. T. Ulaby (1978) Vegetation modeled as water cloud, *Radio Science*, Vol. 13, No. 2., pp. 357-364.

Autret, M., R. Bernard, D. Vidal-Madjar (1989) Theoretical study of the sensitivity of the microwave backscattering coefficient to the soil surface parameters, *Int. J. Remote Sensing*, Vol. 10, No. 1, pp. 171-179.

Barth, H. K. (1986) Mali, Eine geographische Landeskunde, Wissenschaftliche Länderkunden, Herausgeber W. Storkebaum, *Wissenschaftliche Buchgesellschaft Darmstadt*, ISBN 3-534-08157-9, 395 p.

BBC News (1997) UK Government warns of water shortages, Tuesday, November 4, 1997, http://news.bbc.co.uk.

Bertuzzi, P., A. Chànzy, D. Vidal-Madjar, M. Autret (1992) The use of a microwave backscatter model for retrieving soil moisture over bare soil, *Int. J. Remote Sensing*, Vol. 13, No. 14, pp. 2653-2668.

Beven, K. J., J. Fischer (1996) Remote Sensing and scaling in hydrology, In Scaling up in hydrology using remote sensing, edited by J.B. Steward, E.T. Engman, R.A. Feddes, Y. Kerr, *John Wiley & Sons*, New York etc., pp. 1-18.

Blöschl, G. (1996) Scale and Scaling in Hydrology, Wiener Mitteilungen, Wasser·Abwasser·Gewässer, *Institut für Hydraulik, Gewäserkunde und Wasserwirtschaft, Technische Universität Wien*, Band 132, 346 p.

Blöschl, G., M. Sivapalan (1995) Scale issues in hydrological modelling: A Review, *Hydrological Processes*, Vol. 9, pp. 251-290.

Boisvert, J. B., Q. H. J. Gwyn, A. Chanzy, D. J. Major, B. Brisco (1997) Effect of surface soil moisture gradients on modelling radar backscatter from bare fields, *Int. J. Remote Sensing*, Vol. 18, No. 1, pp. 153-170.

Börner, T. (1996) Vergleichende Analyse von Verfahren zur Bestimmung der Dielektrizitätskonstante von Bäumen, Report IN-Nr. 551-12/96, *Deutsche Luft und Raumfahrsbehörde*, Oberpfaffenhoden, Deutschland, 51 p.

Bouman, B. A. M. (1991) Crop Parameter Estimation from ground-based X-band (3-cm Wave) Radar Backscattering Data, *Remote Sens. Environ.*, Vol. 37, pp. 93-205.

Bradford, K. J., T. C. Hsiao (1982) Physiological responses to moderate water stress, In Encyclopedia of plant physiology, Vol. 12B, O. L. Lange, P. S. Nobel, C. B. Osmond, H. Ziegler (Eds.), *Springer Verlag*, Berlin, pp. 265-364.

Braud, I. (1998) Spatial variability of surface properties and estimation of surface fluxes of a savannah, *Agricultural and Forest Meteorology*, Vol. 98, pp. 15-44.

Brinz, K., L. Schmieder, S. Schuetz (1989) Description of Simulation Model (Scatterometer System Simulator), *ESA/ESTEC, Doc. No. ER-MA-DSF-SY-0006*, September 1989.

Brisco, B., D. Bedard, J. Nauheimer, R. J. Brown (1993) Environmental effects on radar data of agricultural areas, *16th Canadian Symposium on Remote Sensing*, pp. 405-410.

Champion, I. (1996) Simple modelling of radar backscattering coefficient over a bare soil: variation with incidence angle, frequency and polarization, *Int. J. Remote Sensing*, Vol. 17, No. 4, pp. 783-800.

Champion, I., G. Guyout (1991) Generalized Formulation for Semi-Empirical Radar Models Representing Crop Backscattering, *Proc. 5th International Colloquium - Physical Measurements and Signatures in Remote Sensing, ESA SP-319*, Courchevel, France, pp. 269-272.

Champion, I., R. Faivre (1997) Sensitivity of the Radar Signal to Soil Moisture: Variation with Incidence Angle, Frequency, and Polarisation, *IEEE Trans. Geosci. Remote Sensing*, Vol. 35, No. 3, pp. 781-783.

Chandrasekhar, S. (1960) Radiative Transfer, *Dover Publications*, New York.

Christopherson, R. W. (1997) Geosystems, An Introduction to Physical Geography, Third Edition, *Prentice Hall*, London etc., 656 p.

Clevers, J. G., H. J. van Leeuwen (1996) Combined Use of Optical and microwave remote Sensing Data for Crop Growth Monitoring, *Remote Sens. Environ.*, Vol. 56, pp. 42-51.

Dam, O. van, J. W. M. van der Drift, C. A. van Diepen (1994) Estimation of Available Soil Moisture Capacity for the soil units of the EC soil map, Technical Document 20, *DLO Winand Staring Centre, Wageningen*, The Netherlands, 87 p.

Davidson, M., T. Le Toan, M. Borgeaud, T. Manninen (1998) Measuring the roughness characteristics of natural surfaces at pixel scales: moving from 1 metre to 25 metre profiles, *Proc. of IGARSS'98*, Seattle, USA, 6-10 July 1998, pp. 1200-1202.

Delworth, T. L., S. Manabe (1988) The Influence of Potential Evaporation on the Variablities of Simulated Soil Wetness and Climate, *J. Climate*, Vol. 1, pp. 523-547.

Diaz-Fierros, F., E. Benito (1996) Rainwash erodibility of Spanish soils, In "Soil degradation and desertification in Mediterranean environments", Edited by J. L. Rubio and A. Calvo, *Geoforma Ediciones*, Logroño, pp. 91-103.

Dirnmeyer, A. P. (1995) Problems in Initializing Soil Wetness, *Bulletin of the American Meteorological Society*, Vol. 76, No. 11, pp. 2234-2240.

Dirnmeyer, P. A., J. Shukla (1993) Observational and modeling studies of the influence of soil moisture anomalies on atmospheric circulation (Review), *Nato ASI Series*, Vol. 16, Springer-Verlag Berlin Heidelberg, pp. 1-23.

Dobson, M. C., F. T Ulaby (1986) Active Microwave Soil Moisture Research, *IEEE Trans. Geosc. Remote Sensing*, Vol. GE-24, No. 1, pp. 23-35.

Dobson, M. C., F. T. Ulaby, M. T. Hallikainen, M. El-Rayes (1985) Microwave Dielectric Behaviour of Wet Soil - Part II: Dielectric Mixing Models, *IEEE Trans. Geosc. Remote Sensing*, Vol. GE-23, No. 1, pp. 35-45.

Dozier, J. (1989) Remote Sensing of Snow in Visible and Near-Infrared Wavelengths, In Theory and Applications of Optical Remote Sensing, Chapter 13, Editor G. Asrar, *John Wiley & Sons*, New York etc..

Dubois, P. C., J. van Zyl, T. Engman (1995) Measuring Soil Moisture with Imaging Radars, *IEEE Trans. Geosci. Remote Sensing*, Vol. 33, No. 4, pp. 915-926.

Duffin, W. J. (1965) Electricity and Magnetism, *McGraw-Hill Book Company*, London, etc., 467.

Early, D. S., D. G. Long (1997) Azimuthal Modulation of C-Band Scatterometer $\sigma^0$ Over Southern Ocean Sea Ice, *IEEE Trans. Geosci. Remote Sensing*, Vol. 35, No. 5, pp. 1201-1209.

Ellis, S., A. Mellor (1995) Soils and Environment, *Routledge*, London, 364 p.

El-Rayes, M. A., F. T. Ulaby (1987) Microwave Dielectric Spectrum of Vegetation - Part I: Experimental Observations, *IEEE Trans. Geosc. Remote Sensing*, Vol. GE-25, No. 5, pp. 541-549.

Engman, E. T. (1986) Hydrologic Research Before and After AgRISTARS, *IEEE Trans. Geosc. Remote Sensing*, Vol. GE-24, No. 1, pp. 5-11.

Engman, E. T. (1990) Progress in Microwave Remote Sensing of Soil Moisture, *Canadian Journal of Remote Sensing*, Vol. 16, No. 3, pp. 6-14.

Entekhabi, D., H. Nakamura, E. G. Njoku (1994) Solving the Inverse Problem for Soil Moisture and Temperature Profiles by Sequential Assimilation of Multifrequency Remotely Sensed Observations, *IEEE Trans. Geosci. Remote Sensing*, Vol. 32, No. 2, pp. 438-447.

ESA (1992) ERS-1 System, *ESA SP-1146*, ESA Publications Division, Noordwijk, September 1992.

ESA (1993) ERS-2 Satellite to Ground Segment Interface Specification, *ESA, ESTEC, Doc. No. ER-IS-ESA-GS-0002*, December 1993.

ESRI (1993) The Digital Chart of the World for use with ARC/INFO, Data Dictionary, *Environmental Systems Research Institute Inc.*, 380 New York Street, Redlands, CA 92373 USA.

European Environment Agency (1994) CORINE Information System, Summary Data Directory, *EEA/15/94*, 77 p..

FAO (1974) FAO-Unesco Soil Map of the World, 1:5 000 000, Unesco, Paris.

FAO (1988) FAO/Unesco Soil Map of the World, Revised Legend, with corrections and updates. World Soil Resources Report 60, FAO, Rome, Reprinted with updates as Technical Paper 20, ISRIC, Wageningen, 1997.

FAO (1993) World Soil Resources, An explanatory note on the FAO World Soil Resource Map at 1:25 000 000 scale, *World Resource Reports*, NO. 66, Rev. 1, Rome: FAO.

Fischer, G., G. K. Heilig (1997) Population momentum and the demand on land and water resources, *Phil. Trans. R. Soc. Lond. B.*, Vol. 352, pp. 869-889.

Francis, C. R., G. Graf, P. G. Edwars, M. McCaig, C. McCarrthy, A. Lefebvre, B. Pieper, P.Y. Pouvreau, R. Wall, F. Weschler, J. Louet, W. Schuman, R. Zobl (1995) The ERS-2 Spacecraft and its Payload, *ESA Bulletin*, No. 83, August 1995, pp. 13-31.

Frison, P. L., E. Mougin (1996a) Use of ERS-1 Wind Scatterometer data over Land Surfaces, *IEEE Trans. Geosc. Remote Sensing*, Vol. 34, No. 2, pp. 550-560.

Frison, P. L., E. Mougin (1996b) Monitoring global vegetation dynamics with ERS-1 wind scatterometer data, *Int. J. Remote Sensing*, Vol. 17, No. 16, pp. 3201-3218.

Frison, P. L., E. Mougin, P. Hiernaux (1998) Observations and Interpretation of Seasonal ERS-1 Wind Scatterometer Data over Northern Sahel (Mali), *Remote Sens. Environ.*, Vol. 63, pp. 233-242.

Fung, A. (1994) Microwave Scattering and Emission Models and their Applications, *Artech House*, 573 p.

Fung, A. K., H. J. Eom (1985) A Comparison Between Active and Passive Sensing of Soil Moisture from Vegetated Terrains, *IEEE Trans. Geosc. Remote Sensing*, Vol. GE-34, No. 5, pp. 768-775.

Georgakakos, K. P., O. W. Baumer (1996) Measurement and utilization of on-site soil moisture data, *J. Hydrology*, 184, pp. 131-152.

González Alonso, F., A. Calle, J. L. Casanova, J. M. Cuevas, A. Vázquez (1998) Drought monitoring in Spain using NOAA-AVHRR multitemporal images, International Symposium on Resource and Environmental Monitoring, ECO BP'98 (ISPRS Commission VII), Budapest, September 1-4, 1998, *International Archives of Photogrammetry and Remote Sensing*, Vol. XXXII, Part 7, pp. 709-712.

Griend, A. A. van de, M. Owe (1993) Determination of microwave vegetation optical depth and single scattering albedo from large scale soil moisture and Nimbus/SMMR satellite observations, *Int. J. Remote Sensing*, Vol. 14, No. 10, pp. 1875-1886.

Griend, A. A. van de, M. Owe (1994) The influence of Polarization on Canopy Transmission Properties at 6.6 GHz and Implications for Large Scale Soil Moisture Monitoring in Semi-Arid Environments, *IEEE Trans. Geosci. Remote Sensing*, Vol. 32, No. 2, pp. 409-415.

Groisman, P. (1998) Description of soil moisture data and accompanying information for the agricultural regions of Western Russia and The Ukraine, *Report of the Hydrology Science & Service Corporation, JRC Contract N.En. 9701838V*, 10 p.

Hallikainen, M. T., F. T. Ulaby, M. C. Dobson, M. A. El-Rayes, L. Wu (1985) Microwave Dielectric Behaviour of Wet Soil - Part I: Empirical Models and Experimental Observations, *IEEE Trans. Geosc. Remote Sensing*, Vol. GE-23, No. 1, pp. 25-33.

Hallikainen, M., F. T. Ulaby, M. C. Dobson, M. El-Rayes (1984) Dielectric Measurements of Soils in the 3- to 37-GHz Band between -50°C and 23°C, *Proc. IGARSS'84, ESA SP-215*, pp. 163-168.

Harris, F. J. (1978) On the Use of Windows for Harmonic Analysis with the Discrete Fourier Transform, *Proceedings of the IEEE*, Vol. 66, No. 1, January 1978, pp. 51-83.

Hillel, D. (1980) Introduction to Soil Physics, *Academic Press*, San Diego etc., 365 p.

Hogg, E. H. (1997) Temporal Scaling of soil moisture and the forest-grassland boundary in western Canada, *Agricultural and Forest Meteorology*, Vol. 84, pp. 115-122.

Hollinger, S. E., S. A. Isard (1994) A Soil Moisture Climatology of Illinois, *J. Climate*, Vol. 7, pp. 822-833.

Isaaks, E. H., R. M. Srivastava (1989) Applied Geostatistics, *Oxford University Press*, Oxford etc., 550 p.

Ishimaru, A. (1978) Wave Propagation and Scattering in Random Media, 2 Volumes, *Academic Press*, San Diego, etc., 572 p.

Jackson, J. D. (1983) Klassische Elektrodynamic, 2. verbesserte Auflage, *Walter de Gruyter*, Berlin, New York, 1020 p.

Jackson, T. J. (1980) Profile soil moisture from surface measurements, *J. Irrig. Drain. Div.*, ASCE, Vol. 106, No. IR2, pp. 81-92.

Jackson, T. J. (1986) Soil Water Modeling and Remote Sensing, *IEEE Trans. Geosc. Remote Sensing*, Vol. 24, No. 1, pp. 37-46.

Johnson, N. L., F. C. Leone (1978) Statistics and Experimental Design, In Engineering and the Physical Sciences, Volume I, *John Wiley & Sons, Inc.*, New York-London-Sydney.

Jones, J. A. A. (1997) Global Hydrology, Processes, resources and environmental management, *Addison Wesley Longman*, Essex, 399 p.

Journel, A. G., Ch. J. Huijbregts (1978) Mining Geostatistics, *Academic Press*, London etc., 598 p.

Karam, M. A., A. K. Fung, R. H. Lang, N. S. Chauhan (1992) A microwave scattering model for layered vegetation, *IEEE Trans. Geosci. Remote Sensing*, Vol. 30, No. 4, pp. 767-784.

Keulen, H. van, N. G. Seligman (1992) Moisture, nutrient availability and plant production in semi-arid environments, In "Food from dry lands", Edited by T. Alberda, H. van Keulen, N. G. Seligman, C. T de Wit, *Kluwer Academic Publisher*, Cordrecht etc., pp. 25-81.

Kim, J., A. B. Verma, N. J. Rosenberg (1989) Energy balance and water use of cereal crops, *Agriculture and Forest Meteorology*, Vol. 48, pp. 135-147.

King, D., C. Le Bas, J. Daroussin, A. J. Thomasson, R. J. A. Jones (1994) The EU map of Soil Water Available for Plants, in European land Information Systems for Agro-Environmental Monitoring, D. King, R. J. A. Jones, A. J. Thomasson (Eds.), *Publication EUR N°16232 EN of the Office for Official Publications of the European Communities*, pp. 131-142.

Kitanidis, P. K. (1997) Introduction to Geostatistics: Applications to Hydrogeology, *Cambridge University Press*, Cambridge, New York, Melbourne, 249 p.

Klemeš, V. (1983) Conceptualization and scale in hydrology, *J. Hydrology*, Vol. 65, pp. 1-23.

Klijn, F., R. W. De Waal, J. H. Oude Voshaar (1995) Ecoregions and Ecodistricts: Ecological Regionalisation for The Netherland's Environmental Policy, *Environmental Management*, Vol. 19., No. 6, pp. 797-813.

Kondratyev, K. Ya., V. V. Melentyev, Y. I. Rabinovich, E. M Shulgina (1977) Passive microwave remote sensing of soil moisture, In *Proc. 11th Symp. Remote Sensing Environment*, (Environmental Research Institute of Michigan, Ann Arbor), pp. 1641-1661.

Koorevaar, P., G. Menelik, C. Dirksen (1983) Elements of Soil Physics, Developments in Soil Science 13, *Elsevier Science Publisher B. V.*, Amsterdam etc., 228 p.

Kosokowsky, I. P., M. S. Lowings, D. E. Taylor (1993) Acquisition and Interpretation of Radar Backscatter from Snowpack and Bare Ground for Applications Involving Off-Road Vehicles, *Terrain Resources Division, Polar Sea Research Ltd.*, Lethbridge, Alberta, SSC File No. XSG91-00078-(603), March 1993.

Kozlowski, T. T. (Ed.) (1968) Water Deficits and Plant Growth, Vol. I, Development, Control, and Measurement, *Academic Press*, New York, London.

Kramer, P. J. (1983) Water Relations of Plants, *Academic Press*.

Lawford, R. G. (1992) An overview of soil moisture and its role in the climate system, *in Soil Moisture Modelling, Proc. of National Hydrology Research Centre Workshop*, March 9-10, 1992, Saskatoon, Saskatechewan, Canada, pp. 1-12.

Lecomte, P., E. P. W. Attema (1992) Calibration & Validation of the ERS-1 Wind Scatterometer, *ESA SP-359, Proc. 1st ERS-1 Symposium*, Cannes, France, 4-6 Nov 1992, pp. 19-29.

Lecomte, P., W. Wagner (1998) ERS Wind Scatterometer Commissioning and in-flight Calibration, *Workshop on Emerging Scatterometer Applications: From Research to Operations*, ESTEC, Noordwijk, The Netherlands, 5-7 October 1998, in press.

Leeuwen, H. J. C. van, J. Bakker, B. A. M. Bouman, B. van den Broek, J. G. P. W. Clevers, G. J. Rijkenberg (1996) Vegetation retrieval by combined microwave and optical remote sensing, *ESA ESTEC, Contract: 11154/94/NL/NB*, 110 p.

Lehrsch, G. A., F. D. Whisler, M. J. M. Römkens (1987) Soil Surface Roughness as Influences by Selected Soil Physical Properties, *Soil & Tillage Research*, Vol. 10, pp. 197-212.

Lehrsch, G. A., F. D. Whisler, M. J. M. Römkens (1988a) Spatial Variation of Parameters Describing Soil Surface Roughness, *Soil Sci. Soc. Am. J.*, Vol. 52, pp. 311-319.

Lehrsch, G. A., F. D. Whisler, M. J. M. Römkens (1988b) Selection of a Parameter Describing Soil Surface Roughness, *Soil Sci. Soc. Am. J.*, Vol. 52, pp. 1439-1445.

Long, D. G., D. S. Early, M. R. Drinkwater (1994) Enhanced Resolution ERS-1 Scatterometer Imaging of Southern Hemisphere Polar Ice, *Proc. IGARSS 1994*, pp. 156-158.

Long, D. G., P. J. Hardin, P. T. Whiting (1993) Resolution Enhancement of Spaceborne Scatterometer Data, *IEEE Trans. Geosci. Remote Sensing*, Vol. 31, No. 3, May 1993, pp. 700-714.

Magagi, R. D., Y.H. Kerr (1997) Retrieval of soil moisture and vegetation characteristics by use of ERS-1 wind scatterometer over arid and semi arid areas, *J. Hydrology*, No. 188-189, pp. 361-384.

Manabe, S. (1969) Climate and the Ocean Circulation I, The atmospheric circulation and the hydrology of the earth's surface, *Monthly Weather Review*, Vol. 97, No. 11, pp. 739-774.

Manninen, T., M. Rantaso, T. Le Toan, M. Davidson, F. Mattia, M. Borgeaud (1998) Multiscale Surface Roughness of Bare Soil, *Proc. of IGARSS'98*, Seattle, USA, 6-10 July 1998, pp. 1203-1205.

Marion, A. (1991) Introduction to Image Processing, *Chapman and Hall*, London a.o., 1991.

Mätzler, C. (1987) Applications of the Interactions of Microwaves with the Natural Snow Cover, *Remote Sensing Reviews*, 1987, Vol. 2, pp. 259-387.

Mätzler, C., E. Schanda (1984) Snow Mapping with Active Microwave Sensors, *Int. J. Remote Sensing*, Vol. 5, No. 2, pp. 409-422.

McClave, J. T., F. H. Dietrich, T. Sincich (1997) Statistics, 7th Edition, *Prentice-Hall International*, London etc., 823 p.

Messeh, M. A., S. Quegan (1997) The use of the ERS-1 scatterometer for global vegetation monitoring, *Proc. EARSel Symposium on Future Trends in Remote Sensing*, Lyngby, Denmark, 17-20 June 1997.

Millot, M. (1995) NOAA AVHRR Pre-Processing, Workshop on Agrometeorological Models: Theory and Applications in the MARS Project, *Publication EUR N°16008 EN of the Office for Official Publications of the European Communities*, pp. 173-179.

Mo, T., T. J. Schmugge, T. Jackson (1984) Calculations of Radar Backscattering of Vegetation-Covered Soils, *Remote Sens. Environ.*, Vol. 15, pp. 119-133.

Mougin, E., A. Lopes, P. L. Frison, C. Proisy (1995) Preliminary analysis of ERS-1 wind scatterometer data over land surfaces, *Int. J. Remote Sensing*, Vol. 16, No. 2, pp. 391-398.

Newton, R. W., Q. R. Black, S. Makanvand, A. J. Blanchard, B. R. Jean (1982) Soil moisture information and thermal microwave emission, *IEEE Trans. Geosci. Remote Sensing*, Vol. GE-20, pp. 275-281.

Oh, Y., K. Sarabandi, F. T. Ulaby (1992) An Empirical Model and an Inversion Technique for Radar Scattering from Bare Soil Surfaces, *IEEE Trans. Geosci. Remote Sensing*, Vol. 30, No. 2, pp. 370-381.

Paris, J. F. (1986) The Effect of Leaf Size on the Microwave Backscattering by Corn, *Remote Sens. Environ.*, Vol. 19, pp. 81-95.

Perdigão, V., A. Annoni (1997) Technical and methodological guide for updating CORINE land cover data base, *Publication EUR N°17288 EN of the Office for Official Publications of the European Communities*, 124 p.

Perry, D. A. (1994) Forest Ecosystems, *The John Hopkins University Press*, Baltimore and London, 649 p.

Picatose, J. R. (1997) Personal Communication, Seccion de Meteorologia Hidrologica, Instituto Nacional de Meteorologia, Ciudad Universitaria, Madrid.

Pierschel, D., AMI Team (1988) Active Microwave Instrument Requirements Specification, *ESA/ESTEC, Doc. No. ER-RS-DSF-AM-0001*, September 1988.

Poesen, J. (1996) Effects of rock fragments on soil degradation processes in Mediterranean environments, In "Soil degradation and desertification in Mediterranean environments", Edited by J. L. Rubio and A. Calvo, *Geoforma Ediciones*, Logroño, pp. 185-222.

Prévot, L., I. Champion, G. Guyot (1993b) Estimating Surface Soil Moisture and Leaf Area Index of a Wheat Canopy Using a Dual-Frequency (C and X Bands) Scatterometer, *Remote Sens. Environ.*, Vol. 46, pp. 331-339.

Prévot, L., M. Dechambre, O. Taconet, D. Vidal-Majar, M. Normand, S. Galle (1993a) Estimating the characteristics of vegetation canopies with airborne radar measurements, *Int. J. Remote Sensing*, Vol. 14, No. 15, pp. 2803-2818.

Pulliainen, J. T., K. Heiska, J. Hyyppä, M. T. Hallikainen (1994) Backscattering Properties of Boreal Forests at C- and X-Bands, *IEEE Trans. Geosci. Remote Sensing*, Vol. 32, No. 5, pp. 1041-1050.

Pulliainen, J. T., P. J. Mikkelä, M. T. Hallikainen, J. P. Ikonen (1996) Seasonal Dynamics of C-Band Backscatter of Boreal Forests with Applications to Biomass and Soil Moisture Monitoring, *IEEE Trans. Geosci. Remote Sensing*, Vol. 34, No. 3, pp. 758-769.

Pulliainen, J. T., T. Manninen, M. T. Hallikainen (1998) Application of ERS-1 Wind Scatterometer Data to Soil Frost and Soil Moisture Monitoring in Boreal Forest Zone, *IEEE Trans. Geosci. Remote Sens.*, Vol. 36, No. 3, pp. 849-863.

Pulliainen, J., J. Grandell, M. Hallikainen, M. Virtanen, N. Walker, S. Metsaemaeki, J.P. Ikonen, Y. Sucksdorff, T. Manninen (1996) Scatterometer and Radiometer Land Applications, *ESRIN Contract: 11122/94/I-HGE(SC)*, 253 p.

Quilfen, Y. (1995) ERS-1 Off-Line Wind Scatterometer Products, *IFREMER, Ref. No. C1-EX-MUT-CD0000-03-IF, Version 1.1*, December 1995.

Ragab, R. (1992) Assessment of the relationship between remotely sensed topsoil moisture content and profile moisture content, in *Soil Moisture Modelling, Proceedings of the National Hydrology Research Centre Workshop*, March 9-10, 1992, Saskatoon, Saskatchewan, Canada, pp. 141-153.

Ragab, R. (1995) Towards a continuous operational system to estimate the root-zone soil moisture from intermittent remotely sensed surface moisture, *J. Hydrology*, Vol. 173, pp. 1-25.

Raupach, M. R., J. J. Finnigan (1995) Scale issues in boundary-layer meteorology: Surface energy balances in heterogeneous terrain, *Hydrological Processes*, Vol. 9, pp 589-612.

Rees, W. G. (1990) Physical Principles of Remote Sensing, Topics of Remote Sensing 1, *Cambridge University Press*, Cambridge etc.., 247 p.

Robock, A., K. A. Vinnikov, C. A. Schlosser, N. A. Speranskaya, X. Yongkang (1995) Use of Midlatitude Soil Moisture and Meteorological Observations to Validate Soil Moisture Simulations with Biosphere and Bucket Models, *J. Climate*, Vol. 8, No. 1, pp. 15-35.

Rodriguez-Puebla, C., A. H. Encinas, S. Nieto, J. Garmendia (1998) Spatial and temporal patterns of annual precipitation variability over the Iberian Peninsula, *Int. J. Climatology*, Vol. 18, pp. 299-316.

Rombach, M., W. Mauser (1997) Multi-annual analysis of ERS surface soil moisture measurements of different land uses, *3rd ERS Symposium on Space at the service of our Environment, Florence*, Italy, 14-21 March, European Space Agency, SP-414, pp. 27-34.

Rott, H. (1993) Capabilities of Microwave Sensors for Monitoring Areal Extent and Physical Properties of the Snowpack, *Proc. of NATO Advanced Research Workgroup on 'Global Environmental Change and Land Surface Processes in Hydrology'*, Tucson AZ., USA, May 1993.

Rott, H., H. Miller, K. Sturm, W. Rack (1993) Application of ERS-1 SAR and Scatterometer Data for Studies of the Antarctic Ice Sheet, *Proc. Second ERS-1 Symposium*, 11-14 October 1993, Hamburg, Germany.

Rott, H., T. Nagler (1993) Snow and Glacier Investigations by ERS-1 SAR - First Results, *Proc. of First ERS-1 Symposium, ESA SP-359*, pp. 577-582.

Rott, H., T. Nagler (1994) Capabilities of ERS-1 SAR for snow and glacier monitoring in alpine areas, *Proc. of Second ERS-1 Symposium, ESA SP-361*, pp. 965-970.

Row, L. E., D. A. Hastings, P. K. Dunbar (1995) Terrain Base, Worldwide Digital Terrain Data, Documentation Manual, CD-ROM Release 1.0, *National Geophysical Data Center, National Oceanic and Atmospheric Administration*.

Saatchi, S. S., D. M. Le Vine, R. H. Lang (1994) Microwave Backscattering and Emission Model for Grass Canopy, *IEEE Trans. Geosci. Remote Sensing*, Vol. 32, No. 1, pp. 177-186.

Saddiq, M. H., P. J. Wierenga, J. M. H. Hendickx, M. Y. Hussain (1985) Spatial variability of soil water tension in an irrigated soil, *Soil Science*, Vol. 140, No. 2, pp. 126-132.

Schanda, E. (1986) Physical Fundamentals of Remote Sensing, *Springer Verlag*, Berlin Heidelberg etc., 187 p.

Schanda, E. (1987) On the contribution of volume scattering to the microwave backscattered signal from wet snow and wet soil, *Int. J. Remote Sensing*, Vol. 8, No. 10, pp. 1489-1500.

Schmugge, T. J. (1983) Remote Sensing of Soil Moisture: Recent Advances, *IEEE Trans. Geosci. Remote Sensing*, Vol. GE-21, No. 3, pp. 336-344.

Schmugge, T. J., T. J. Jackson (1996) Soil moisture variability. In Scaling up in hydrology using remote sensing, edited by J.B. Steward, E.T. Engman, R.A. Feddes, Y. Kerr, *John Wiley & Sons*, New York etc., pp. 183-192.

Schmugge, T., P. E. O'Neill, J. R. Wang (1986) Passive Microwave Soil Moisture Research, *IEEE Trans. Geosc. Remote Sensing*, Vol. GE-24, No. 1, pp. 12-22.

Schmullius, C. (1997) Monitoring Siberian Forests and Agriculture with the ERS-1 Windscatterometer, *IEEE Trans. Geosc. Remote Sensing*, Vol. 35, No. 5, pp. 1363-1366.

Schulin, R., H. Flühler, H. M. Selim, B. Sevruk, P. J. Wierenga, (1992) Soil Moisture, Part III, In Snow cover measurements and areal assessment of precipitation and soil moisture, edited by B. Sevruk, *WMO, Operational Hydrological Report*, No. 55, pp. 219-283.

Schulze, E. D., R. H. Robichaux, J. Grace (1987) Plant water balance, *Bioscience*, Vol. 37, pp. 30-37.

Shutko, A. M., E. A. Reutov, S. P. Golovachev (1994) Estimation of soil moisture profiles and root zone moisture content by means of microwave radiometry and a priori information, In Passive Microwave Remote Sensing of Land-Surface Interactions, B. J. Choudhury, Y. H. Kerr, E. G. Njoku, and P. Pampaloni (Eds.), *ESA/NASA International Workshop*, pp. 461-474.

Strahler, A., A. Strahler (1996) Physical Geography, Science and Systems of the Human Environment, *John Wiley & Sons Inc.*, New York etc., 637 p.

Taconet, O., D. Vidal-Majar, C. Emblanch, M. Normand (1996) Taking into account vegetation effects to estimate soil moisture from C-band radar measurements, *Remote Sens. Environ.*, Vol. 56, pp. 52-56.

Taconet, O., M. Benallegue, D. Vidal-madjar, L. Prevot, M. Dechambre, M. Normand (1994) Estimation of Soil and Crop Parameters for Wheat from Airborne Radar Backscattering Data in C and X Bands, *Remote Sens. Environ.*, Vol. 50, pp. 287-294.

Thomasson, A. J. (1995) Assessment of Soil Water Reserves Available for Plants (SWAP): a review, in European land Information Systems for Agro-Environmental Monitoring, D. King, R. J. A. Jones, A. J. Thomasson (Eds.), *Publication EUR N°16232 EN of the Office for Official Publications of the European Communities*, pp. 115-130.

Topp, G. C. (1992) The measurement and monitoring of soil water content by TDR, *in Soil Moisture Modelling, Proc. of National Hydrology Research Centre Workshop*, March 9-10, 1992, Saskatoon, Saskatechewan, Canada, pp. 155-161.

Touré, A., K. P. B. Thomson, G. Edwards, R. J. Brown, B. G. Brisco (1994) Adaptation of the MIMICS Backscattering Model to the Agricultural Context - Wheat and Canola at L and C Bands, *IEEE Trans. Geosci. Remote Sensing*, Vol. 32, No. 1, pp. 47-61.

Tsang, L., J. A. Kong, R. T. Shin (1985) Theory of Microwave Remote Sensing, *John Wiley & Sons*, New York etc., 613 p.

Ulaby, F. T., C. T. Allen, G. Eger, E. Kanemasu (1984) Relating the Microwave Backscattering coefficient to Leaf Area Index, *Remote Sens. Environ.*, Vol. 14, pp. 113-133.

Ulaby, F. T., K. Sarabandi, K. MCDonald, M. Whitt, M. C. Dobson (1990) Michigan microwave canopy scattering model, *Int. J. Remote Sensing*, Vol. 11, No. 7, pp. 1223-1253.

Ulaby, F. T., M. A. El-Rayes (1987) Microwave Dielectric Spectrum of Vegetation - Part II: Dual-Dispersion Model, *IEEE Trans. Geosc. Remote Sensing*, Vol. GE-25, No. 5, pp. 550-557.

Ulaby, F. T., P. P. Batlivala (1976) Optimum Radar Parameters for Mapping Soil Moisture, *IEEE Trans. Geosci. Electronics*, Vol. GE-14, No. 2, pp. 81-93.

Ulaby, F. T., P. P. Batlivala, M. C. Dobson (1978) Microwave Backscatter Dependence on Surface Roughness, Soil Moisture, and Soil Texture, Part I - Bare Soil, *IEEE Trans. Geosci. Remote Sensing*, Vol. GE-16, No. 4, pp. 286-295.

Ulaby, F. T., R. K. Moore, A. K. Fung (1981) Microwave Remote Sensing, Active and Passive, Volume I: Microwave Remote Sensing Fundamentals and Radiometry, *Artech House*, Norwood, 456 p.

Ulaby, F. T., R. K. Moore, A. K. Fung (1982) Microwave Remote Sensing, Active and Passiv, Volume II, Radar Remote Sensing and Surface Scattering and Emission Theory, *Artech House*, Norwood.

Ulaby, F. T., R. K. Moore, A. K. Fung (1986) Microwave Remote Sensing, Active and Passive, Volume III: From Theory to Applications, *Artech House*, Norwood.

Ulaby, F. T., T. F. Haddock, R. T. Austin (1988) Fluctuation Statistics of Millimeter-Wave Scattering from Distributed Targets, *IEEE Trans. Geosci. Remote Sensing*, Vol. 26, No. 3, May 1988.

Vinnikov, K. Y., A. Robock, N. A. Speranskaya, C. A. Schlosser (1996) Scales of temporal and spatial variability of midlatitude soil moisture, *J. Geophysical Research*, Vol. 101, No. D3, pp. 7163-7174.

Vinnikov, K. Y., A. Robock, S. Qui, J. K. Entin, M. Owe, B. Choudhury, S. E. Hollinger, E. G. Njoku, Satellite Remote Sensing of Soil Moisture in Illinois, USA, *Special GCIP Issue of J. Geophysical Research*, in press.

Vinnikov, K. Y., I. B. Yeserkepova (1991) Soil Moisture: Empirical data and model results, *J. Climate*, Vol. 4, pp. 66-79.

Vogt, J. (1992) Characterising the spatio-temporal variability of surface parameters from NOAA AVHRR data, A case study for Southern Mali, *Publication EUR N°14637 EN of the Office of Official Publications of the European Communities*, 266 p.

Vossen, P. (1994) Early Crop Production Assessment of the European Union: The System Implemented by the MARS-STAT Project, *Publication EUR N°16008 EN of the Office for Official Publications of the European Communities, Proc. Workshop on "Agrometeorological Models: Theory and Applications in the MARS Project"*, pp. 21-51.

Wagner, W. (1995) Application of Low-Resolution Active Microwave Remote Sensing (C-Band) over the Canadian Prairies, *M.Sc. Thesis, Vienna University of Technology*, April 1995, 88 p.

Wagner, W. (1996) Change Detection with the ERS Scatterometer over Land, EWP N°1896, *European Space Agency*, Noordwijk, The Netherlands, July 1996, 143 p.

Wagner, W. (1998) Vegetation Cover Effects on ERS Scatterometer Data, Technical Note No. I.98.05, *EC Joint Research Centre*, Ispra, Italy, January 1998, 193 p.

Wagner, W., A. E. Walker, H. Rott (1995) Application of Low-Resolution Active Microwave Remote Sensing (C-Band) over the Canadian Prairies, *Proc. 17th Canadian Symposium on Remote Sensing*, Saskatoon, Saskatchewan, 13-15 June, pp. 21-28.

Walker, N. P. (1997) Limitations on the Possible Resolution Enhancement of ERS-1 Scatterometer Images, *IEEE Trans. Geosci. Remote Sensing*, Vol. 35, No. 1, pp. 196-198.

Wallace, J. S., C. R. Lloyd, M. V. K. Sivakumar (1993) Measurements of soil, plant and total evaporation from millet in Niger, *Agricultural and Forest Meteorology*, Vol. 63, pp. 149-169.

Wang, J. R., J.C Shiue, T. J. Schmugge, E. T. Engman (1990) The L-Band PBMR Measurements of Surface Soil Moisture in FIFE, *IEEE Trans. Geosci. Remote Sens.*, Vol. 28, No. 5, pp. 906-913.

Wegmüller, U., C. Mätzler (1993) Active and Passive Signature Catalogue (2-12 GHz), Inst. Applied Physics, University of Bern, Switzerland, Tech. Rep., 316 p.

Wegmüller, U., C. Mätzler, R. Hüppi, E. Schanda (1994) Active and Passive Signature Catalog on Bare Soil (2-12 GHz), *IEEE Trans. Geosci. Remote Sensing*, Vol. 32, No. 3, pp. 698-702.

Weise, T. (1996) Radiometric and Structural Measurements of Snow, *Ph.D. Thesis, Institute for Applied Physics, University of Bern*, Switzerland, 159 pp.

West, R., L. Tsang, D. P. Winebrenner (1993) Dense Medium Radiative Transfer Theory for two Scattering Layers with a Rayleigh Distribution of Particle Sizes, *IEEE Trans. Geosci. Remote Sensing*, Vol. 31, No. 2, pp. 462-437.

Western, A. W., G. Blöschl, R. B. Grayson (1998) Geostatistical characterisation of soil moisture patterns in the Tarrawarra catchment, *J. Hydrology*, Vol. 205, pp. 20-37.

Whitelaw, A., S Howes (1995) Hydrology Investigations of Contemporality, Appendix B of Report "Simultaneous implementation of a Synthetic Aperture Radar and a high-resolution optical imager, *ESA Contract 10063/92/NL/SF*, ESTEC, Noordwijk, The Netherlands, 52 p.

Wiesmann, A. (1994) Remote Sensing of Land Surfaces with the ERS-1 Scatterometer, *M.Sc. Thesis, Institute of Applied Physics, University of Bern*, July 1994, 84 p.

Wigneron, J. P., B. Combal, U. Wegmüller, C. Mätzler (1996) Estimation of microwave parameters from radiometric measurements, *Int. J. Remote Sensing*, Vol. 17, No. 14, pp. 2875-2880.

Wigneron, J.-P., T. Schmugge, A. Chanzy, J.-C. Calvet, Y. Kerr (1998) Use of passive microwave remote sensing to monitor soil moisture, *Agronomie*, Vol. 18, pp. 27-43.

Wild, A. (1993) Soil and the Environment: An Introduction, *Cambridge University Press*, Cambridge, 287 p.

Wilheit, T. T. (1978) Radiative transfer in a plane stratified dielectric, *IEEE Trans. Geosci. Electron*, Vol. GE-16, pp. 138-143.

Wismann, V. R., K. Boehnke (1994) Land surface monitoring using the ERS-1 scatterometer, *Earth Observation Quarterly*, N°44, pp. 11-15.

Wismann, V., A. Cavanie, D. Hoekman, I. Woodhouse, K. Boehnke, C. Schmullius (1996a) Land Surface Observations using the ERS-1 Windscatterometer, Part I, *ESA ESTEC, Contract No. 11103/94/NL/CN*, 57 p.

Wismann, V., K. Boehnke, A. Cavanié, R. Ezraty, F. Gohin, D. Hoekman, I. Woodhouse (1996b) Land Surface Observations using the ERS-1 Windscatterometer, Part II, *ESA ESTEC, Contract No. 11103/94/NL/CN*, 59 p.

Wuttge, S., H. Munz (1995) Effects of Gaps in the Scatterometer Raw Data on $\sigma^0$-Triplets, *ESA, ESRIN, Doc. No. ER-TN-DSF-FL-0001*, May 1995, 95 p.

Zabeline, V. (1998) Personal Communication, Russian Hydrometeorological Center, Moscow.

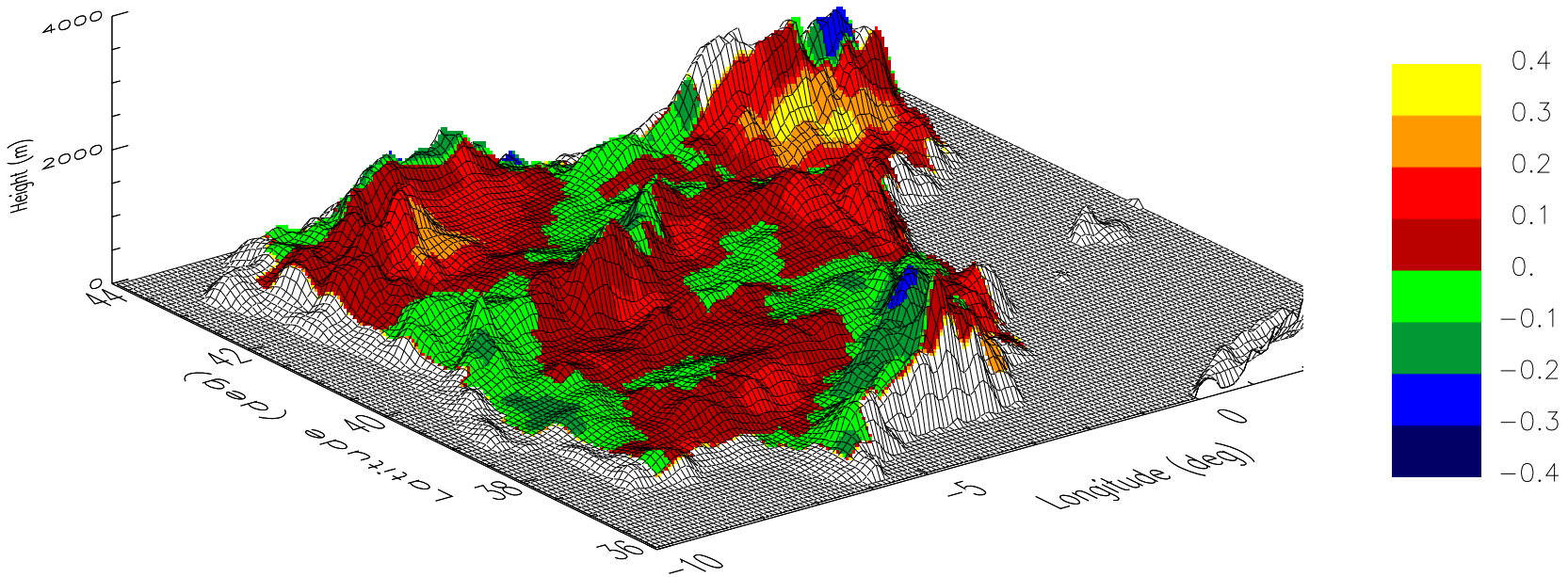


*Colour Figure 1: Overlay of $\delta$ (average value over ERS-1 mission) in dB for ascending passes over the DEM of the Iberian Peninsula.*

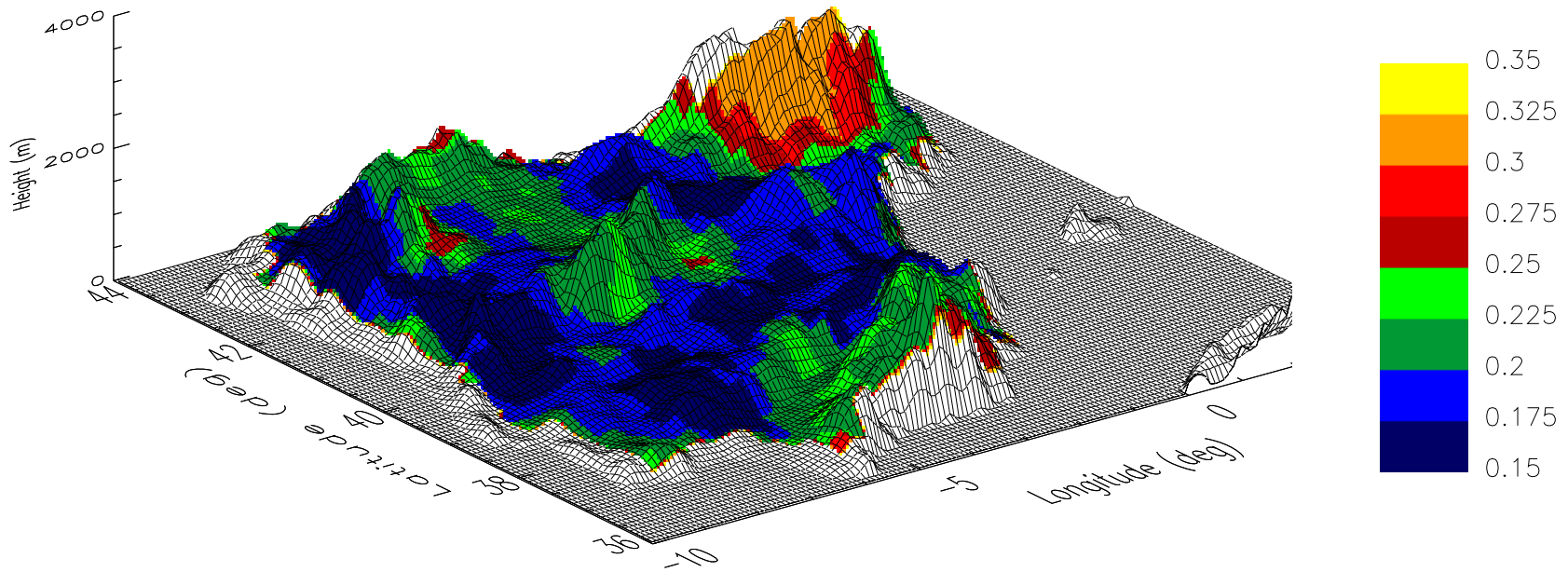


*Colour Figure 2: Overlay of ESD($\sigma^0$) in dB over the DEM of the Iberian Peninsula.*

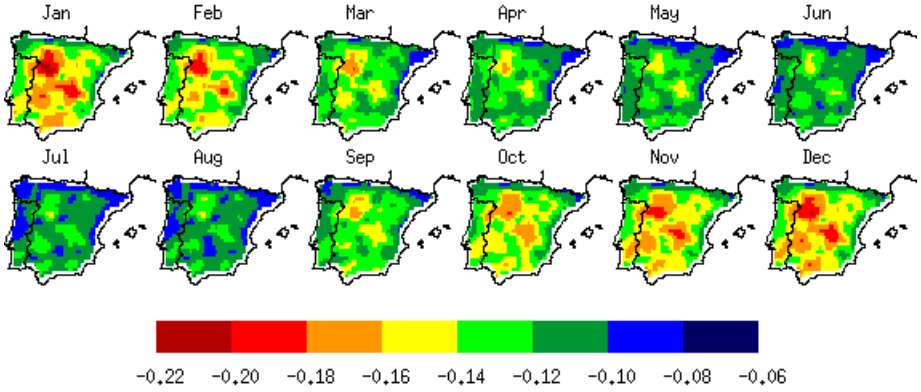


*Colour Figure 3: Seasonal variability of the slope $\sigma'(40)$ over the Iberian Peninsula derived from ERS Scatterometer data acquired during the period September 1991 to May 1996.*

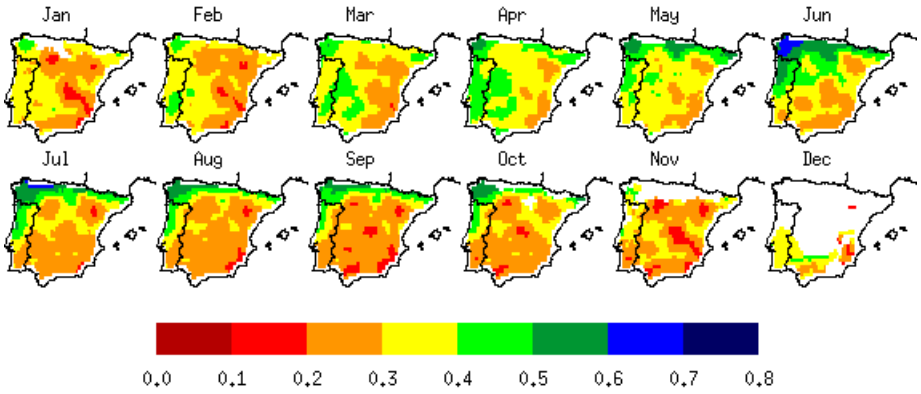


*Colour Figure 4: Mean monthly NDVI values over the Iberian Peninsula derived from AVHRR imagery acquired during the period September 1991 to September 1994. If less than 6 NDVI values per month are available then the mean value is not calculated (white areas).*

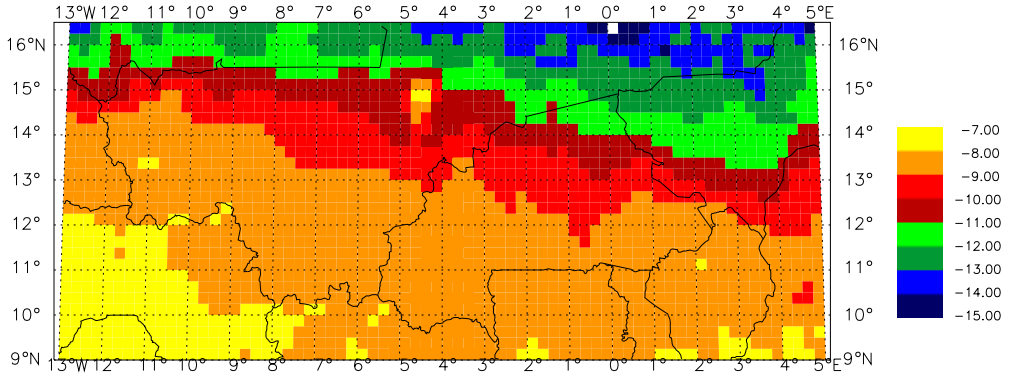


*Colour Figure 5: Spatial variation of $\sigma^0_{wet}(40)$ in dB over southern Mali and Burkina Faso derived from ERS Scatterometer data acquired during the period from September 1991 to January 1998.*

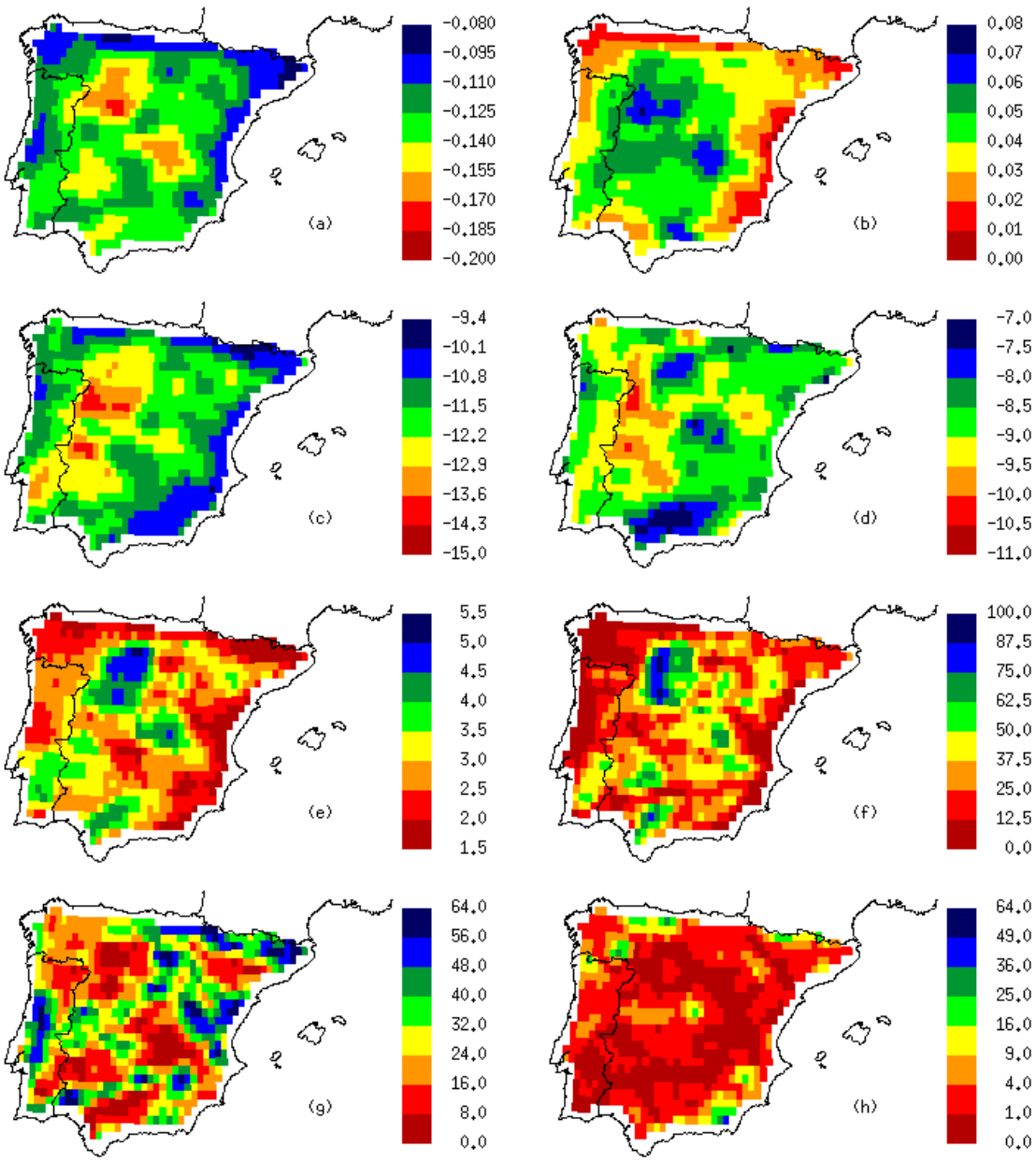


*Colour Figure 6: Comparison of backscatter parameters and generalised land cover classes based on the CORINE land cover. (a) Mean slope C´ in dB/deg. (b) Dynamic range of slope D´ in dB/deg. (c) Backscattering coefficient of vegetation under dry soil conditions* $C^0_{dry}$ *in dB. (d) Backscattering coefficient of vegetation under wet soil conditions* $C^0_{wet}$ *in dB. (e) Sensitivity* $C^S$ *in dB. (f) Percentage area of translucent vegetation* $A_{tr}$*. (g) Percentage area of non-transparent vegetation* $A_{nt}$*. (h) Percentage area of non-vegetated surfaces* $A_{no}$*. For the definition of* $A_{tr}$*,* $A_{nt}$*, and* $A_{no}$ *see Chapter 7.2.1.*

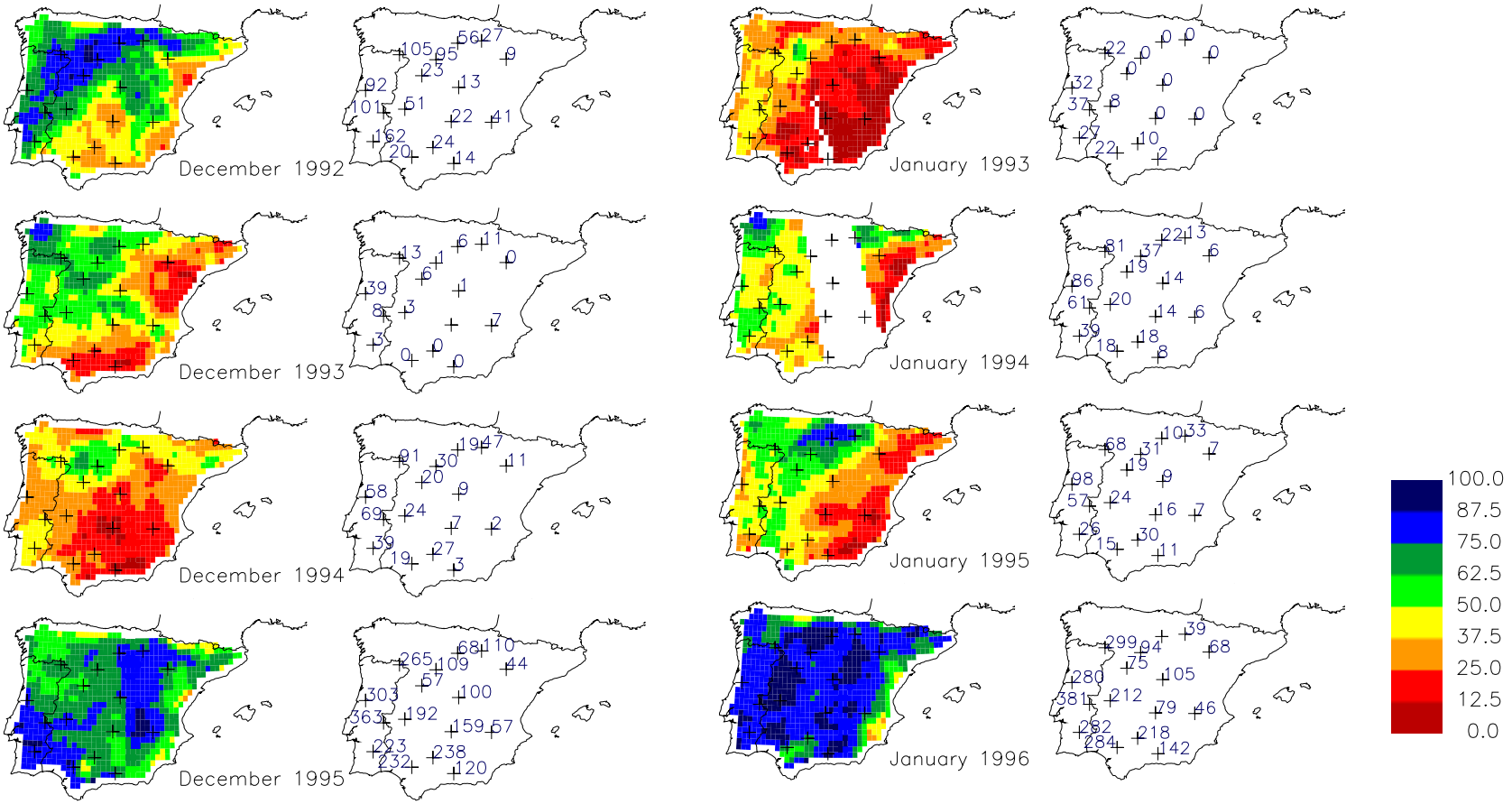


*Colour Figure 7: Comparison of mean monthly $m_s$ maps with monthly rainfall reported at 16 stations over the Iberian Peninsula for the months December and January for the years 1992 to 1996.*

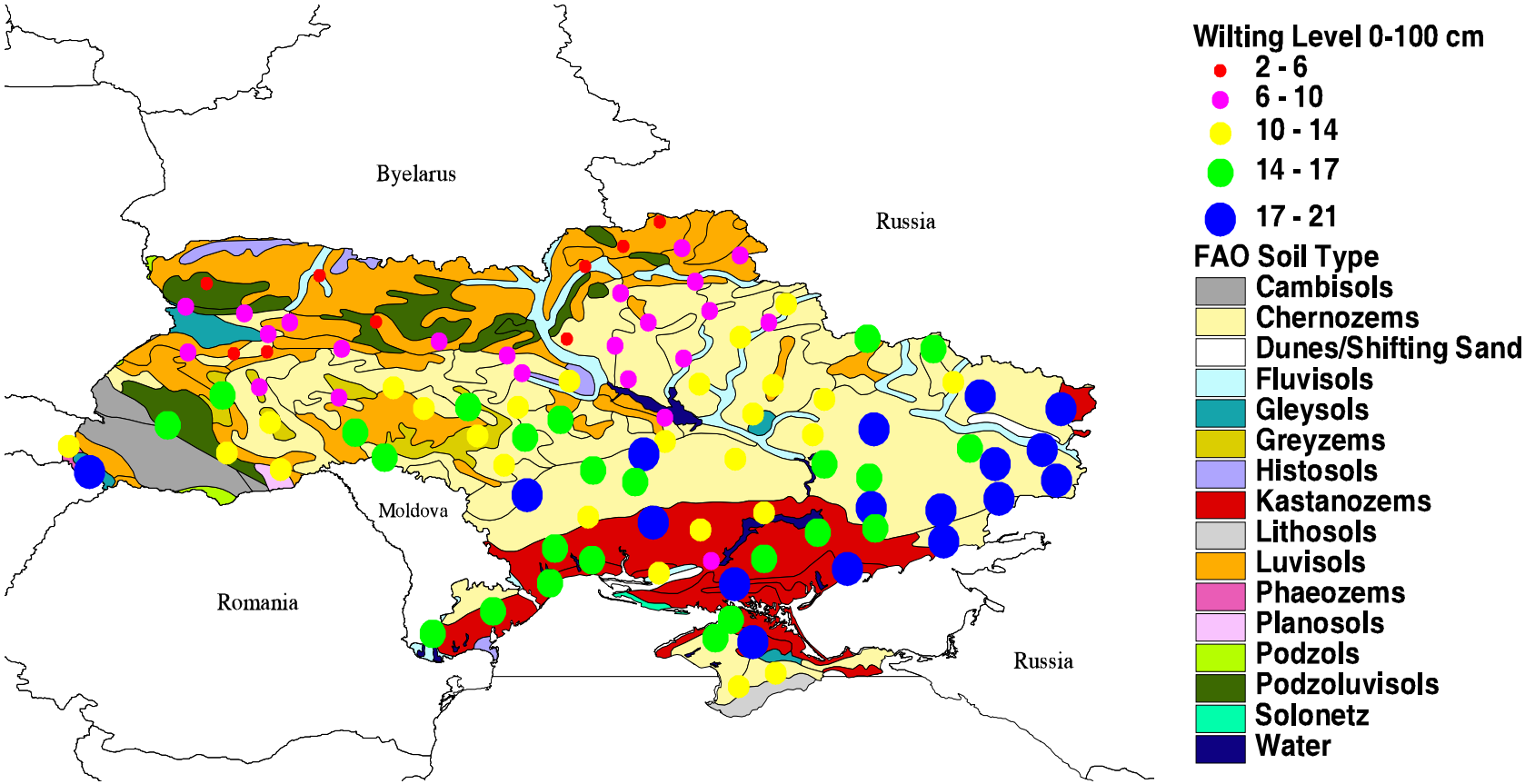


*Colour Figure 8: FAO-Unesco Soil Map of the Ukraine. The map also shows wilting levels in % for the 0-100 cm layer measured at the agrometeorological network.*

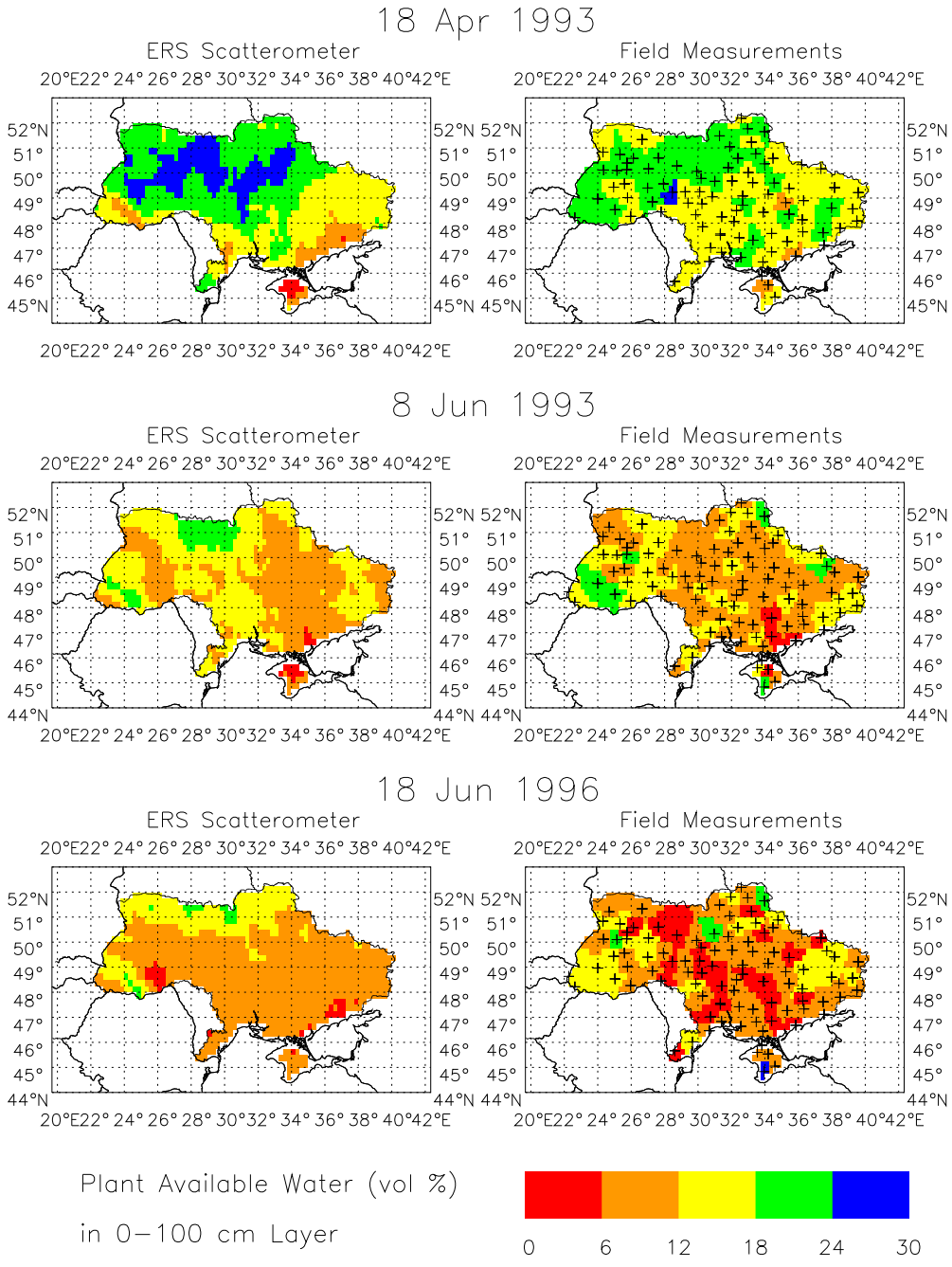


*Colour Figure 9: Maps of plant available water in the 0-100 cm layer from ERS Scatterometer and field observations for three dates. The maps on the left hand side show the remote sensing estimates. The maps on the right hand side are based on measurements on maize, spring wheat, and winter wheat fields which are interpolated using the nearest neighbourhood method. The locations of the stations are indicated by crosses.*

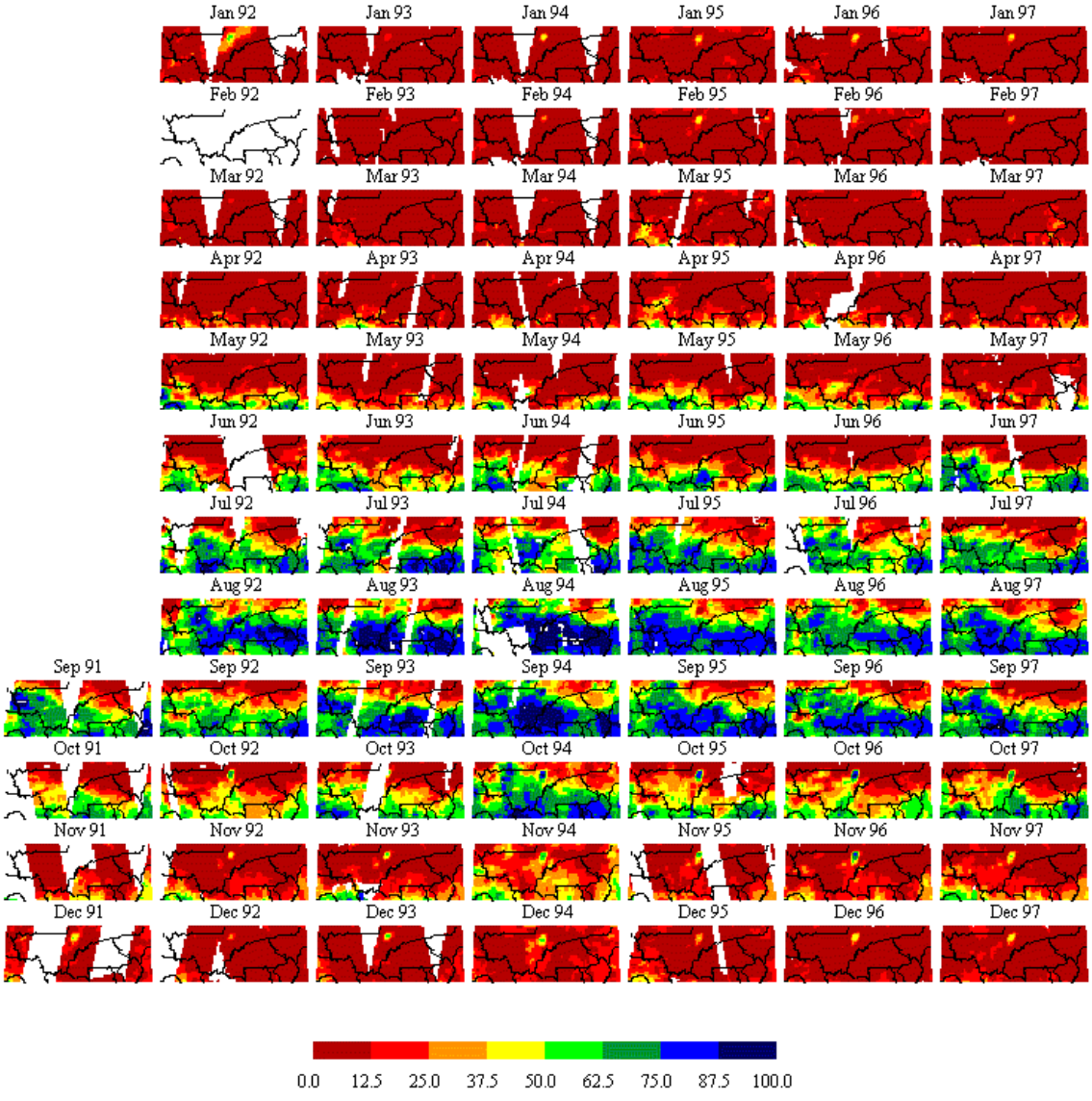


*Colour Figure 10: Monthly SWI images of southern Mali and Burkina Faso (13°W-5°E, 9°N-16.5°N) for the period from September 1991 to December 1997.*

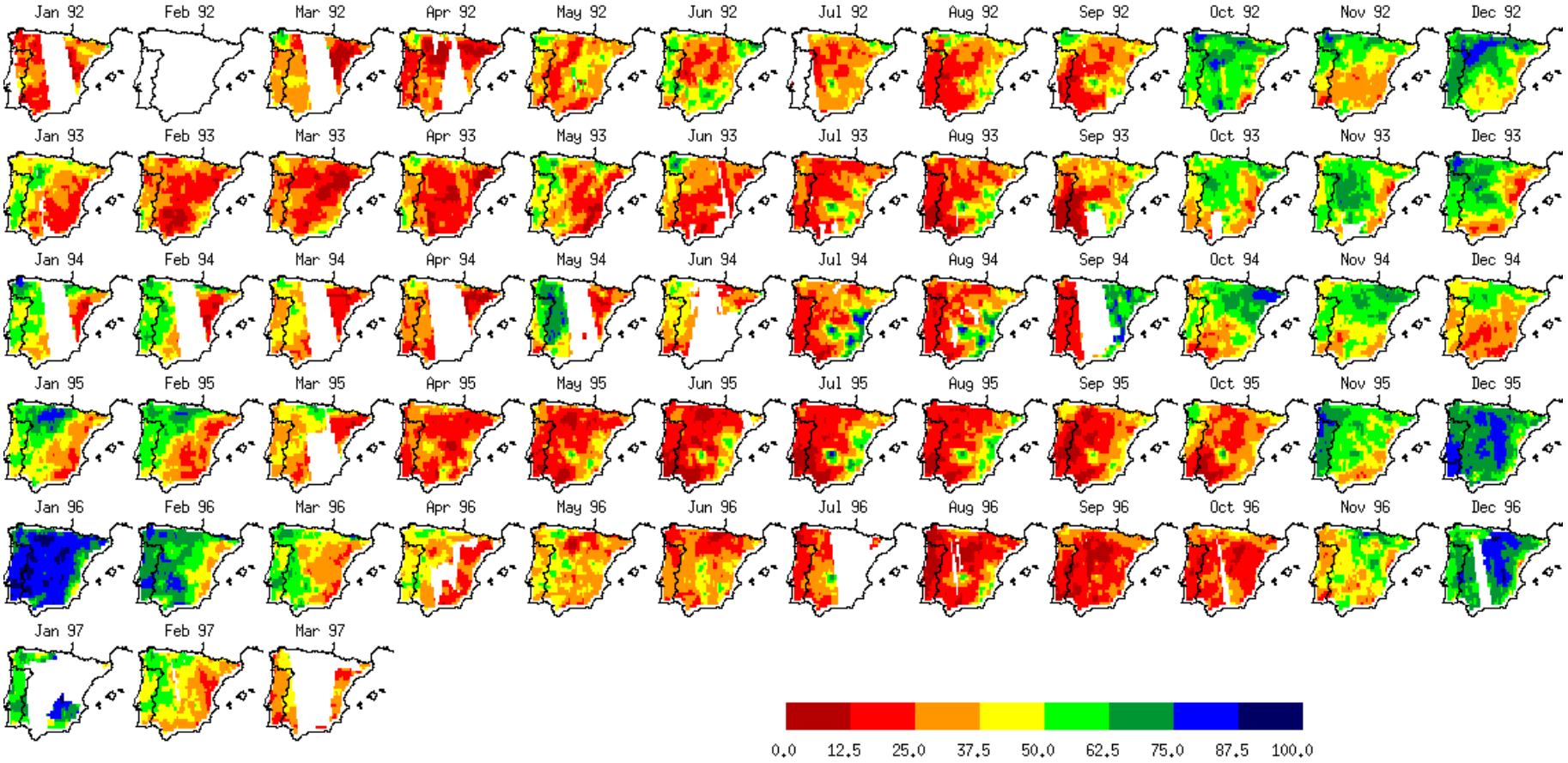


*Colour Figure 11: Monthly SWI images of the Iberian Peninsula for the period from January 1992 to March 1997.*

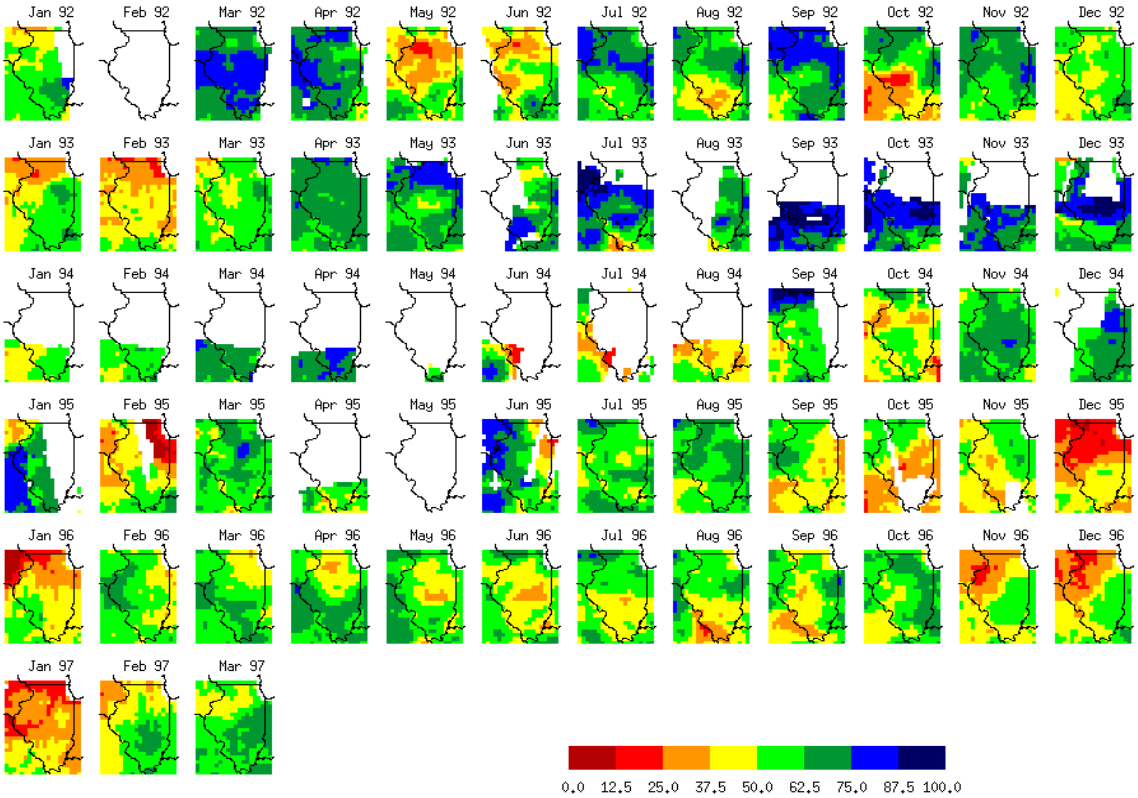


*Colour Figure 12: Monthly SWI images for Illinois, USA (36°N-43°N, 87°W-92°W) for the period from January 1992 to March 1997.*

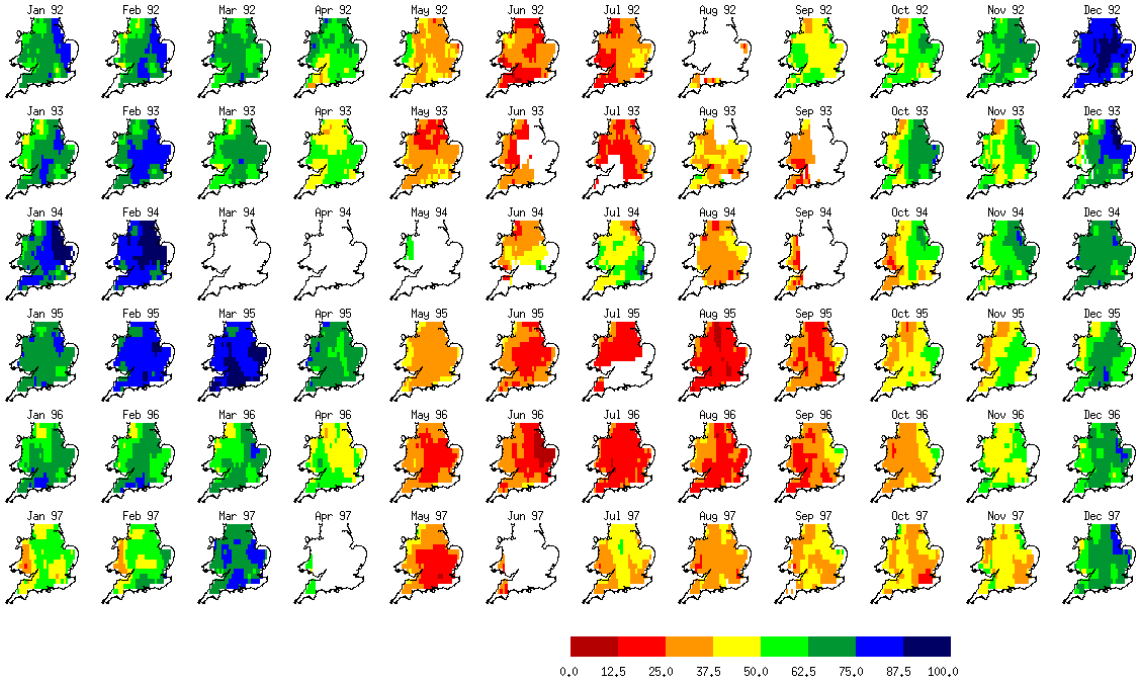


*Colour Figure 13: Monthly SWI images for England and Wales for the period from January 1992 to December 1997.*

Ispra, December 12, 1998

# Curriculum Vitae

| | |
|---|---|
| Family name | Wagner |
| First name and title | Wolfgang, Dipl.-Ing. |
| Place and date of birth | Wels, January 20, 1969 |
| Nationality | Austria |
| Parents | Alfred and Sigrid Wagner |

## School Education

On June 21, 1988 I graduated with excellence from the "Höhere Technische Bundeslehranstalt für Elektrotechnik" in Wels.

## University

From 1989 to 1990 I studied Technical Engineering at the Vienna University of Technology. Since I became interested in physics and mathematics I started to study Technical Physics on October 3, 1990. On June 29, 1995 I graduated with excellence in Technical Physics from the Vienna University of Technology. The title of my masters thesis is "Application of Low-Resolution Active Microwave Remote Sensing (C-Band) over the Canadian Prairies".

In October 1995 I started my Ph.D. study on soil moisture retrieval from ERS Scatterometer data under the supervision of Univ. Prof. Karl Kraus from the Institute for Photogrammetry and Remote Sensing of the Vienna University of Technology.

## Experience in the Field of Remote Sensing

I have been continuously working in the field of remote sensing since 1993 investigating land and snow/ice applications of microwave and optical remote sensing instruments. My main experience lies with the ERS Scatterometer. However, since I have been actively involved in a number of other research projects, I have gathered experience with a broad range of sensors and their application including ERS SAR, Landsat TM, SPOT, SMM/I, SMMR, and AVHRR.

## Remote Sensing Projects

At the following institutions I participated in various remote sensing projects:

*Institute for Photogrammetry and Remote Sensing, Vienna University of Technology, Austria*

Since 1993 continuous involvement in the activities of its remote sensing sector

1. Feasibility study on the use of high-resolution sensors to assess the areal snow water equivalent over alpine catchment areas using ERS SAR, SPOT, Landsat TM, and AVHRR. Consulting of on-going activities in this field.
2. Participation in the preparation of a number of project proposals covering microwave and optical, and low- and high-resolution remote sensing methods.

*Space Applications Institute, EC Joint Research Centre, Ispra, Italy*

From October 1, 1996 to December 31, 1998

1. Geophysical parameter retrieval from ERS Scatterometer data.
2. Crop yield assessment with AVHRR and Meteosat.

*ESTEC XEP, European Space Agency, Noordwijk, The Netherlands*
From February 1 to July 31, 1996
1. Research on land applications of the ERS Scatterometer.

*NASA Goddard Space Flight Centre, Greenbelt, Maryland, USA*
From June 18 to August 12, 1995
1. Soil moisture retrieval from SIR-SAR.
2. Study of long-term SMMR time series over Greenland.

*Vienna University of Natural Resources, Austria*
From October 1994 to February 1995
1. Participation in research project "Information Fusion and Physical Models for Image Understanding and Navigation".

*Climate Research Branch, Atmospheric Environment Service, Toronto, Canada*
From July 8 to September 30, 1994
1. Snow and soil moisture applications of ERS Scatterometer and SMM/I.

*Institute for Applied Physics, University of Bern, Switzerland*
From July 12 to September 17, 1993
1. Study of ERS Scatterometer data over the Antarctica.
2. Study of atmospheric trace gases with TOVS.

## Other Experience

In the academic year 1991/92 I was tutor for mathematics at the Vienna University of Technology.

In the period October 1997 to April 1998 I was the representative of the grant holders at the EC Joint Research Centre in Ispra.

## Military Service

From October 3, 1988 to May 31, 1989 in Vienna.

## Language Skills

German: mother language
English: fluent
Italian: reading, conversation

Bisher erschienen:

Heft 1 Kolloquium der Assistenten der Studienrichtung Vermessungswesen 1970 - 1973, Dezember 1973.

Heft 2 EGGER-PERDICH-PLACH-WAGENSOMMERER, Taschenrechner HP 45 und HP 65, Programme und Anwendungen im Vermessungswesen, 1. Auflage, März 1974, Special Edition in English, Juli 1974, 2. verbesserte Auflage, November 1974.

Heft 3 Kolloquium der Assistenten der Studienrichtung Vermessungswesen 1973 - 1974, September 1974.

Heft 4 EGGER-PALFINGER-PERDICH-PLACH-WAGENSOMMERER, Tektronix-Tischrechner TEK 31, Programmbibliothek für den Einsatz im Vermessungswesen, November 1974.

Heft 5 K. LEDERSTEGER, Die horizontale Isostasie und das isostatische Geoid, Februar 1975.

Heft 6 F. REINHART, Katalog von FK4 Horrebow-Paaren für Breiten von +30 bis +60, Oktober 1975.

Heft 7 Arbeiten aus dem Institut für Höhere Geodäsie, Wien, Dezember 1975.

Heft 8 Veröffentlichungen des Instituts für Photogrammetrie zum XIII. Internationalen Kongreß für Photogrammetrie in Helsinki 1976, Wien, Juli 1976.

Heft 9 W. PILLEWIZER, Felsdarstellung aus Orthophotos, Wien, Juni 1976.

Heft 10 PERDICH-PLACH-WAGENSOMMERER, Der Einsatz des programmierbaren Taschenrechners Texas Instruments SR-52 mit Drucker PC100 in der ingenieurgeodätischen Rechentechnik, Wien, Mai 1976.

Heft 11 Kolloquium der Assistenten der Studienrichtung Vermessungswesen 1974 - 1976, November 1976.

Heft 12 Kartographische Vorträge der Geodätischen Informationstage 1976, Wien, Mai 1977.

Heft 13 Veröffentlichung des Instituts für Photogrammetrie anläßlich des 80. Geburtstages von Prof. Dr.h.c. K. Neumaier, Wien, Januar 1978.

Heft 14 L. MOLNAR, Self Checking Analytical Relative Orientation and Strip Formation, Wien, Dezember 1978.

Heft 15 Veröffentlichung des Institus für Landesvermessung anläßlich des 80. Geburtstages von Prof. Dr. Alois Bavir, Wien, Januar 1979.

Heft 16 Kolloquium der Assistenten der Studienrichtung Vermessungswesen 1976 - 1979, Wien, November 1979.

Heft 17 E. VOZIKIS, Die photographische Differentialumbildung gekrümmter Flächen mit Beispielen aus der Architekturbildmessung, Wien, Dezember 1979.

Heft 18 Veröffentlichung des Instituts für Allgemeine Geodäsie anläßlich des 75. Geburtstages von Prof. Dipl. Ing. Dr. F. Hauer, Die Höhe des Großglockners, Wien, 1981.

Heft 19 H. KAGER, Bündeltriangulation mit indirekt beobachteten Kreiszentren, Wien, April 1981.

Heft 20 Kartographische Vorträge der Geodätischen Informationstage 1980, Wien, Mai 1982.

Heft 21 Veröffentlichung des Instituts für Kartographie anläßlich des 70. Geburtstages von Prof. Dr. Wolfgang Pillewizer: Glaziologie und Kartographie, Wien, Dezember 1982.

Heft 22 K. TEMPFLI, Genauigkeitsschätzung digitaler Höhenmodelle mittels Spektralanalyse, Wien, Mai 1982.

Heft 23 E. CSAPLOVICS, Interpretation von Farbinfrarotbildern, Wien, Novemeber 1982.

Heft 24 J. JANSA, Rektifizierung von Multispektral-Scanneraufnahmen - Entwicklung und Erprobung eines EDV-Programms, Wien, Mai 1983.

Heft 25 Zusammenfassungen der Diplomarbeiten, Dissertationen und Habilitationen an den geodätischen Instituten der TU Wien, Wien, November 1984.

Heft 26 T. WUNDERLICH, Die voraussetzungsfreie Bestimmung von Refraktionswinkeln, Wien, August 1985.

Heft 27 G. GERSTBACH (Hrsg.), Geowissenschaftliche/geotechnische Daten in Landinformationssystemen - Bedarf und Möglichkeiten in Österreich, Wien, Juni 1986.

Heft 28 K. NOVAK, Orientierung von Amateuraufnahmen ohne Paßpunkte, Wien, August 1986.

Heft 29 Veröffentlichung des Instituts für Landesvermessung und Ingenieurgeodäsie, Abteilung Ingenieurgeodäsie anläßlich des 80. Ggeburtstages von Prof. Dipl. Ing. Dr. F. Hauer, Wien, Oktober 1986.

Heft 30 K.-H. ROCH, Über die Bedeutung dynamisch ermittelter Parameter für die Bestimmung von Gesteins- und Gebirgseigenschaften, Wien, Februar 1987.

Heft 31 G. HE, Bildverbesserung mittels digitaler Filterung, Wien, April 1989.

Heft 32 F. SCHLÖGELHOFER, Qualitäts- und Wirtschaftlichkeitsmodelle für die Ingenieurphotogrammetrie, Wien, April 1989.

Heft 33 G. GERSTBACH (Hrsg.), Geowissenschaftliche/geotechnische Daten in Landinformationssystemen - Datenbestände und Datenaustausch in Österreich, Wien, Juni 1989.

Heft 34 F. HOCHSTÖGER, Ein Beitrag zur Anwendung und Visualisierung digitaler Geländemodelle, Wien, Dezember 1989.

Heft 35 R. WEBER, Lokale Schwerefeldmodellierung unter Berücksichtigung spektraler Methoden zur Geländereduktion, Wien, April 1990.

Heft 36 o.Prof. Dr. Hans Schmid zum 70. Geburtstag. Veröffentlichung der Abteilung für Landesvermessung, Wien, Oktober 1990.

Heft 37 G. GERSTBACH, H.P. HÖLLRIEGL und R. WEBER, Geowissenschaftliche Informationsbörse - Eine Nachlese zu GeoLIS II, Wien, Oktober 1990.

Heft 38 R. ECKER, Rastergraphische Visualisierungen mittels digitaler Geländemodelle, Wien, August 1991.

Heft 39 Kartographische Forschungen und Anwendungsorientierte Entwicklungen, herausgegeben von W. Stams und F. Kelnhofer zum 80. Geburtstag von Prof. Dr. W. Pillewizer, Wien, Juli 1991.

Heft 39a W. RIEGER, Hydrologische Anwendungen des digitalen Geländemodelles, Wien, Juli 1992.

Heft 40 K. STEINNOCHER, Methodische Erweiterungen der Landnutzungsklassifikation und Implementierung auf einem Transputernetzwerk, Wien, Juli 1994.

Heft 41 G. FORKERT, die Lösung photogrammetrischer Orientierungs- und Rekonstruktionsaufgaben mittels allgemeiner kurvenförmiger Elemente, Wien, Juli 1994.

Heft 42 M. und W. SCHÖNER, Photogrammetrische und glaziologische Untersuchungen am Gåsbre (Ergebnisse der Spitzbergenexpedition 1991), Wien, Februar 1996.

Heft 43 M. ROIC, Erfassung von nicht signalisierten 3D-Strukturen mit Videotheodoliten, Wien, April 1996.

Heft 44 G. RETSCHER, 3D-Gleiserfassung mit einem Multisensorsystem und linearen Filterverfahren, Wien, April 1996.

Heft 45 W. DAXINGER, Astrogravimetrische Geoidbestimmung für Ingenieurprojekte, Wien, Juli 1996.

Heft 46 M. PLONER, CCD-Astronomie von Objekten des geostationären Ringes, Wien, November 1996.

Heft 47 Zum Gedenken an Karl Killian „Ingenieur" und „Geodät" 1903-1991, Veröffentlichung der Fachgruppe Geowissenschaften, Wien, Februar 1997

Heft 48 A. SINDHUBER, Ergänzung und Fortführung eines digitalen Landschaftsmodelles mit multispektralen und hochauflösenden Fernerkundungsaufnahmen, Wien, Mai 1998